Constraints on the Shape and Scale of the Galactic Gravitational Potential

by

Mark Robert Metzger

A. B., Washington University (1988)

Submitted to the Department of Physics
in partial fulfillment of the requirements for the degree of

Doctor of Philosophy

at the

Massachusetts Institute of Technology

May 1994

Author_____
Department of Physics
May 10, 1994

Certified by_____
Paul L. Schechter
Professor of Physics
Thesis Supervisor

Accepted by_____

George F. Koster
Chairman, Graduate Committee

Science

Constraints on the Shape and Scale of the Galactic Gravitational Potential

by

Mark Robert Metzger

Submitted to the Department of Physics
on May 10, 1994, in partial fulfillment of the
requirements for the degree of
Doctor of Philosophy

Abstract

Stellar tracers are used to probe the kinematics of the Galactic disk, providing constraints on the shape of the Galactic gravitational potential. New radial velocities for faint Milky Way Cepheids are measured, and used in combination with existing Cepheid data to model the rotation curve. The new Cepheids provide a particularly good constraint on the distance to the Galactic center, R_0. The data on distant Cepheids is sparse in the northern hemisphere; therefore, to help provide future constraints on the rotation curve ellipticity, a survey was conducted for distant Cepheids near $\ell = 60°$. Photometric measurements of over 1 million stars at multiple epochs were obtained in a region covering 6 square degrees, and from this data 50 Cepheid candidates were selected. Followup photometry confirms 10 of these stars as Cepheids, one of which is the most heavily reddened Cepheid known. A separate investigation of potential rotation curve ellipticity, as reflected in a peculiar motion of the LSR, was conducted using carbon stars toward the Galactic anticenter. Radial velocities of 174 Carbon stars were measured; the net motion of the LSR with respect to these distant stars is found to be inconsistent with a rotation curve model proposed to explain measured gas kinematics. Finally, radial velocities were measured for a sample of K-dwarfs toward the south Galactic pole. An initial analysis of this data is given, providing a new measurement of the local mass density and a limit to the amount of matter present in the Galactic disk.

Thesis Supervisor: Paul L. Schechter
Title: Professor of Physics

Acknowledgments

There are many people who deserve thanks for their efforts over the years I've been working on this thesis, and I hope I am able to mention most of them in this section written in a hurry. My sincere apologies to all of the people I've inadvertantly omitted!

First I would like to thank my advisor, Paul Schechter, for his support, advise, and insight over the past several years. When I first came into his office more than five years ago, I knew little of astronomy, but what he described to me then sounded interesting enough for me to decide to go back to school. My fascination with the field has only increased since, and I have learned a lot about astronomy, science, and the rest from Paul, to whom I owe my sincere appreciation.

I also thank John Tonry for helping me out at many stages of my carreer as a graduate student through discussions and advice, and for getting me involved in instrumentation work that I have found to be great fun. I will certainly miss frequently stopping by John's office and talking shop, and the occasional intense hacking sessions. Fortunately electronic communications are very efficient these days, so I hope we will be able to keep working together in the future.

I owe more thanks than I have room to express for the assistance and friendship of Chris Naylor. Anytime something needed to get done, Chris would find some way to make it happen. He even managed to exceed his usual levels of magic during the preparation of the thesis document, and without his help I would never have been able to finish on time. Reading over the acknowledgements of other graduate students in the group, I realized that we are all indebted to Chris for his effort, and I concur with Ed Ajhar that he is the best secretary any group could have.

My former officemate, Ed Ajhar, deserves particular thanks for the many discussions we've had over the years, from science to politics. I didn't fully realize how much I appreciated our "heated debates" until he graduated and moved on, leaving a definite gap behind. He also left me alone to maintain the local computers for the group, which I may finally be getting away from at last! I also thank my current officemate, John Blakeslee, for our many discussions, and for tolerating being the

Contents

List of Figures

List of Tables

11

Chapter 1

Introduction

The focus of this thesis is to address several fundamental questions about the size and shape of the Milky Way. The method used throughout is the use of stellar kinematic tracers to determine the structure of the potential in which they move. The three topics that are given particular attention are (1) measuring the fundamental distance scale parameter in the Milky Way, the distance to the Galactic center; (2) measuring the extent to which the outer Galaxy rotation curve is axisymmetric on large scales; and (3) measuring the vertical structure of the disk gravitational potential, and inferring the amount of mass in the disk near the Sun.

The thesis consists of four mostly independent projects, and so the introductory material for each is presented within each chapter. An outline of the various projects is given below. Each chapter also contains its own conclusions.

In Chapter 2 a new body of data on Cepheid variables is presented, primarily measurements of radial velocities for a large number of known Cepheids that lack them. This new data is combined with existing data on Cepheids and used to model the rotation curve and infer the distance to the Galactic center. This distance provides a fundamental scale for many types of measurements in astronomy, and provides a basis for comparison of the size and mass of the Milky Way with other galaxies. Perhaps the most important impact of R_0 is that it provides the connection between distance and kinematics for the bulk rotation about the Galactic center. This connection can be used to infer distances to many types of objects that lack a more fundamental method, by comparing measured radial velocities with a rotation model. Distances

to objects determined in this manner scale directly with R_0.

Measurements of the distance to the Galactic center (R_0) have a long history. In 1918 Shapley deduced a distance of 13 kpc for R_0 based on the distribution of globular clusters, which are concentrated about the Galactic center. While the distance scale he adopted for the globular clusters is now thought to be too large, his work set the stage for many studies to follow. The method that we use to measure R_0 in Chapter 2 was first applied by Joy (1939), who estimated R_0 at 10 kpc. Baade (1953) pioneered the method of measuring the distance to the density maximum of RR Lyrae variables, and his estimate of 8.2 kpc would become the standard for the next 10 years. Schmidt (1965) reviewed the estimates of R_0 up to that time, and based on his recommendation the IAU adopted a standard value for R_0 of 10 kpc. This standard remained in place until 1985, when the IAU adopted a new standard of 8.5 kpc for R_0 based on the review by Kerr & Lynden-Bell (1986). A description of the more recent estimates of R_0 are described in the reveiw by Reid (1993), who concludes a "best" current estimate of R_0 of 8.0 ± 0.5 kpc based on a weighted average of measurements from several different techniques.

Our estimate of 7.75 ± 0.37 kpc, combined with a systematic error of ~ 0.5 kpc, is one of the most accurate to date and agrees well with existing measurements. One of the larger sources of systematic error involves the breakdown of one of our model assumptions that the rotation curve is axisymmetric. In Chapter 3, we present results of a survey to find additional Galactic Cepheids to help address this latter uncertainty.

Chapter 4 focuses on measuring the velocity of the local standard of rest (defined to be the frame in which the local stars are on average at rest, which has a primarily rotational velocity with respect to the Galactic center) relative to a sample of stars in the direction opposite to the Galactic center. It attempts to detect predictions of a model of the Galaxy by Blitz & Spergel (1991), which involves a non-axisymmetric distortion of the Sun's rotation about the Galactic center.

Finally, in Chapter 5 we use a new sample of K dwarfs to determine the acceleration perpendicular to the Galactic plane, and use this to infer a column density of mass in the disk near the Sun. This type of measurement was pioneered by Oort

(1932), and the local mass density near the sun is typically referred to as the "Oort limit" in his honor. Measurements of the local mass density have recently received much attention, in part due to the recent availibility of new catalogs of tracer stars useful for studying the disk potential. Our preliminary analysis indicates that there may be some amount of matter not accounted for in inventories of known populations, but a reliable estimate awaits some additional data and a more detailed analysis.

1.1 References

Baade, W. 1953, in Symposium on Astrophysics (Ann Arbor: U. of Michigan), p. 25.

Blitz, L., and Spergel, D. N. 1991a, ApJ, **370**, 205 (BS)

Joy, A. H. 1939, ApJ, **89**, 356

Kerr, F. J., and Lynden-Bell, D. 1986, MNRAS, **221**, 1023

Oort, J. H. 1932, Bull. Astr. Inst. Netherlands, **6**, 249

Reid, M. J. 1993, ARA&A, **31**, 345

Shapley, H. 1918, ApJ, **48**, 154

Schmidt, M. 1965, in Galactic Structure, eds. A. Blaauw & M. Schmidt (Chicago: U. of Chicago), p. 513.

Chapter 2

Cepheids and the Distance to the Galactic Center

2.1 Background

Cepheids have several significant advantages over other stellar tracers for determining large-scale Galactic kinematics. They are intrinsically bright ($M_V \simeq -4.1$), which in conjunction with variability makes them relatively easy to locate at large distances. Perhaps the most significant advantage of Cepheids is that distances to them can be determined extremely well: modern calibrations of the period-luminosity relation in the near infrared yield uncertainties of $< 5\%$ (Madore & Freedman, 1991). Distances to Cepheids in the Galactic disk can be best obtained from near-infrared photometry, due both to the smaller PL relation scatter and because of heavy extinction by dust in the Galactic plane.

The first use of Cepheids to measure kinematic parameters of the rotation curve was by Joy (1939), who found a distance to the Galactic center of 10 kpc; this distance was inferred from the measured shape of the rotation curve assuming a simple model. Further work was carried out by Stibbs (1956), Kraft & Schmidt (1963), and Feast (1967), using additional data on Cepheids and incorporating the use of individual reddenings in distance measurements. Their analysis was ultimately limited, however, by the small amount of available data, particularly on distant, faint Cepheids. More recently, Caldwell & Coulson (1987) made an extensive compilation

of available Cepheid photometry and radial velocities, and used this data in anaxisymmetric rotation curve model to determine, among other parameters, the distance to the Galactic center (R_0). Though a significant improvement over earlier work, their models were also limited by the available data: Caldwell & Coulson lamented that many distant Cepheids lacked good radial velocities, and there were few Cepheids known at large distances from the sun, particularly toward directions which provide the best constraints on R_0.

The work presented in this chapter is to address this lack of data, by measuring radial velocities for the large number of known distant Cepheids that lack them (§§2.2 and 2.3). We compute gamma velocities for these Cepheids in §2.4, using a new method developed to measure an accurate γ given a few individual velocities well spaced in phase.. We also measure radial velocities for several Cepheids discovered by Caldwell, Keane, & Schechter (1991) and provide a compilation of data on these Cepheids (§2.5); these stars are of particular importance for measuring the distance to the Galactic Center. We then incorporate this large body of new data into a Galactic rotation model, and make one of the most precise measurements of the distance to the Galactic center to date (§2.6). We also discuss the size of possible systematic errors, and find that they currently dominate the uncertainty in R_0.

2.2   Radial Velocities of Northern Hemisphere Cepheids

The work I discuss in this section appeared in a similar form as "Radial Velocities of 26 Northern Milky Way Cepheids" in *The Astrophysical Journal Supplement Series*, June, 1991 (Metzger *et al.* 1991). One error has been corrected in Table 1, which appears here as Table 2.1: the velocity taken at Julian date 2447018.918 of -12.21 ± 0.63 km s^{-1} is of V1726 Cyg, not V386 Cyg as published.

2.2.1   Observations

Spectra of the northern hemisphere Cepheids were obtained with the echelle spectrograph of the Palomar 60-inch telescope (McCarthy 1988) by P. Schechter and J.

17

Caldwell during runs in July and August of 1987. Spectra were projected onto a TI 800×800 CCD with a resolving power $R \sim 40,000$ per pixel (~ 7.5 km s^{-1} pixel^{-1}) and wavelength range of 4200–7500 Å. We used an entrance slit of 1$\farcs$4 which projected to ~ 2 pixels or 15 km s^{-1} in the spectrum. The slit was rotated to maintain alignment of the long dimension in the direction of atmospheric dispersion, in order to keep the star at the same relative position between the slit jaws at all wavelengths (Filippenko 1982). Calibration spectra from a Th-Ar hollow cathode tube and from Ar, He, Hg, and Ne lamps were taken to correct for instrumental drift. While Ar-He-Hg-Ne exposures were taken immediately before each observation, a Th-Ar exposure could only be taken at the end of each night, as unfortunately our runs predated the installation of an internal Th-Ar comparison source available at all zenith angles.

The observations included 26 low Galactic latitude Cepheids with longitude $15° < \ell < 140°$, and 12 radial velocity standard stars. The two runs of 5 and 6 nights were separated by 25 days in order to measure velocities over a wide range of pulsational phases for both short and long period Cepheids. Each Cepheid was observed an average of nine times. Radial velocity standards were observed throughout the runs to provide cross-correlation references and to allow a measurement of the velocity zero point. The standards also provide a statistical test of the velocities to compare with our formal error.

2.2.2   Data Reduction

Velocities were measured from the spectra using custom software developed specifically for reducing echelle data. The reduction procedure is described here, along with details specific to the 1987 Palomar run; the same software was also used to reduce echelle data from other sets of observations described below. The basic procedure is as follows: the first step was to convert the two-dimensional CCD data into individual spectra for each order. For each observation, the associated wavelength calibration lines were located and identified, and a polynomial for wavelength as a function of line position was determined. This polynomial was used to rebin the stellar spectrum to a logarithmic scale in wavelength. Each echelle order was extracted from the

rebinned image and sky-subtracted. Relative radial velocities were obtained using the Fourier quotient technique of Sargent *et al.* (1977) to find redshift between the extracted orders of the star and those of a reference star. Velocities were based on a common zero-point determined from observations of radial velocity standard stars.

2.2.2.1 Reference calibration

We used a modified version of the photometry program DoPHOT (Mateo and Schechter 1989) to find position and shape of the lines on the calibration spectra. DoPHOT's stellar point spread function was replaced with a PSF that represents the shape of the lines in the spectrum: a gaussian profile in slit width and a box with half-intensity tails in slit height. DoPHOT finds lines in the spectrum and determines centroid position, intensity, height, and width by fitting the PSF to each line. Line tilt is also determined for lines strong enough to give a good fit.

The set of lines found by DoPHOT varies from exposure to exposure, since the nonlinear least squares fitting algorithm for the PSF did not always converge on the faintest lines. To prevent a difference in matched line sets causing a large change in the wavelength solution, we chose from the set of available Ar-He-Hg-Ne lines a 100-line subset consisting of the lines located most frequently over all of the calibration exposures. The subset provides good coverage over the area of the CCD, though there are more lines toward the red due to the characteristics of the argon and neon spectra.

2.2.2.2 Wavelength solutions

To obtain a wavelength solution for each frame we fit two-dimensional Legendre polynomials third-order in λ^{-1} and $n\lambda$, where n is the echelle order number, to the x and y positions of the identified lines on the CCD. In addition, to examine the wavelength residuals we fit the inverse functions for λ^{-1} and $n\lambda$, third-order in x and y. Because the individual observation arcs have significantly fewer lines than the Th-Ar spectra, we fix the two highest-order coefficients (including cross terms) of the polynomial to the values from the wavelength solution of a Th-Ar exposure. This prevents large
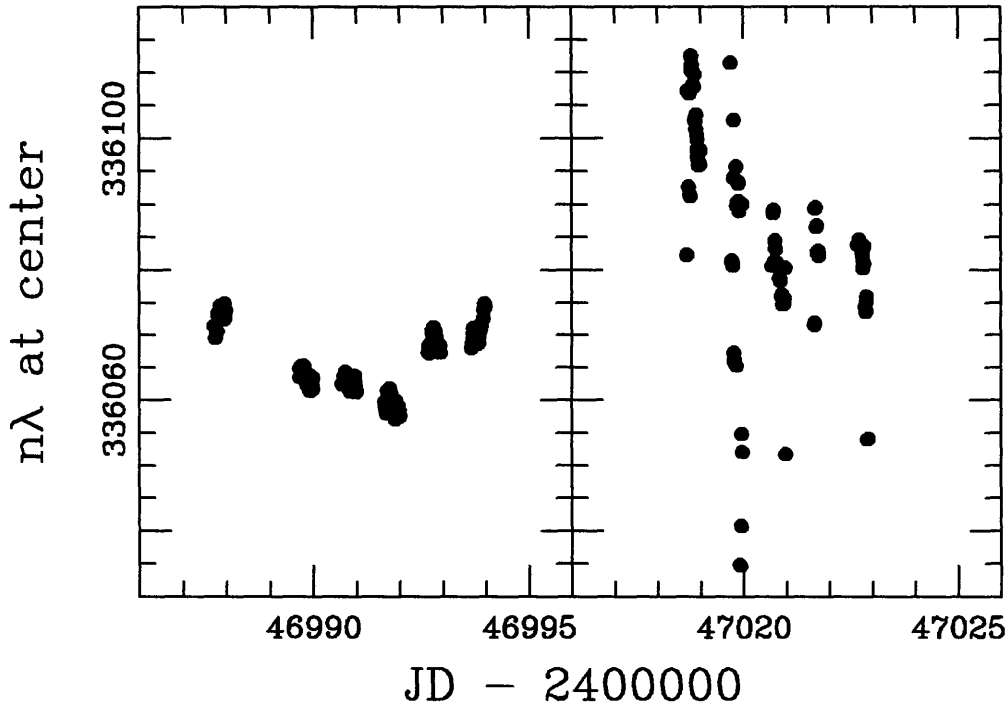
Figure 2-1: Central nλ vs. Julian date for all calibration frames. The left panel shows data from the first run, the right panel data from the second run. Each ordinate tickmark corresponds to 4.5 km s^{-1}.

variations in the solutions from observation to observation. The high-order Th-Ar coefficients are much better defined as the fit is made to over 1,000 lines.

The wavelength solution to the Th-Ar lines gives a good sense of how well the polynomial can represent the actual line positions. The residuals for the fit to the Th-Ar exposure taken at the end of the first run are $\sim$ 0.02 Å or 1 km s^{-1} rms. Hensberge and Verschueren (1989) note that eliminating blended lines reduces the rms residual of their wavelength solutions. In our case, however, we have many more unblended lines for the Th-Ar solution so that the shifted wavelengths of the blended lines are unlikely to greatly affect the wavelength solution. Indeed, of the 170 lines with wavelength residuals greater than 0.03 Å, 150 can be identified as blended lines. The rms residual computed with the unblended lines alone improves to 0.014 Å or 0.6 km s^{-1}.

Figures 2-1 and 2-2 show the calibration wavelength at the center of the CCD image and the dispersion scale, respectively, vs. time. During the first run, the

20
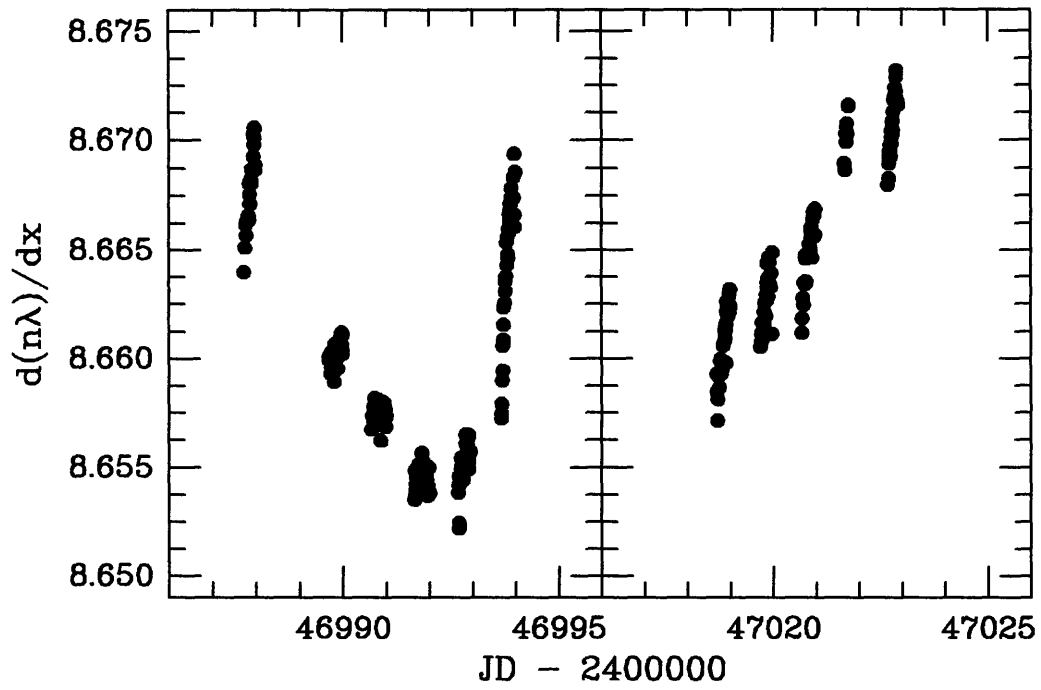
Figure 2-2: Central wavelength dispersion vs. Julian date for all calibration frames. Left and right panels are as in Fig. 2-1.
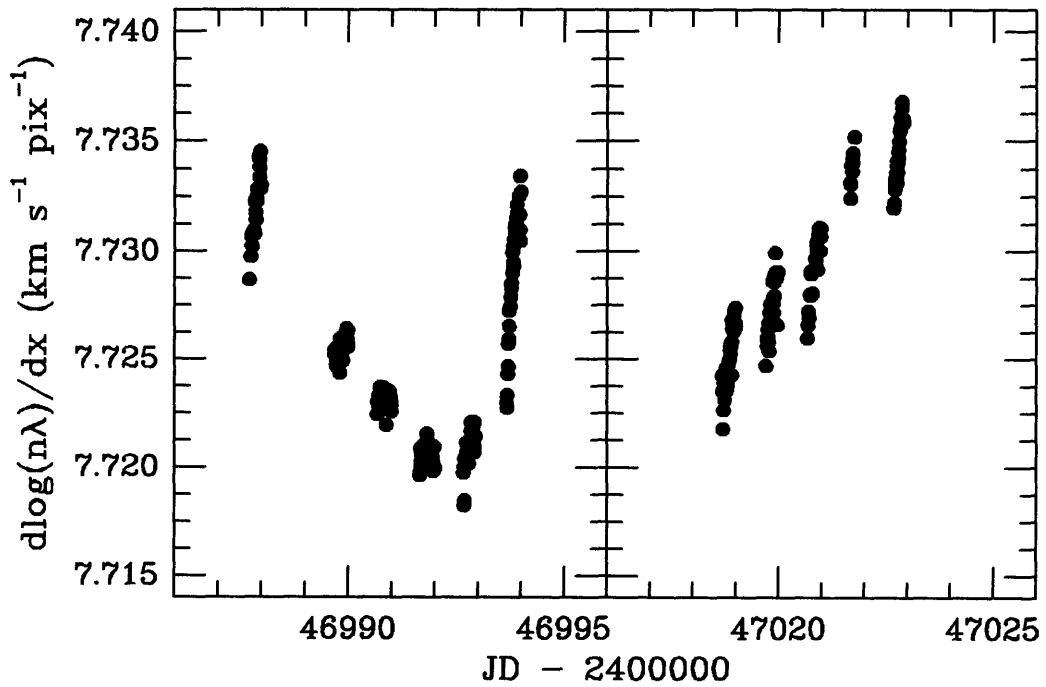
Figure 2-3: Logarithmic scale of spectrum at the center of the detector.

detector is stable at the 0.5 km s^{-1} level between observations. The large shift in the center wavelength during the second run is likely due to improper clamping of the secondary dispersion prism. The slope of the change in the coefficients indicates a worst case shift between exposures of ~ 5 km s^{-1}, though this can be mostly compensated for by use of the atmospheric B-band absorption lines (see §2.2.2.4). The changes in scale on the detector are at the 0.1–0.2% level and show a strong correlation with line width variations, thus are probably due to drift in focus of the echelle camera (perhaps with temperature). Figure 2-3 shows the effective scale at the center of the chip throughout the run expressed in km s^{-1} pixel^{-1}, which is a ratio of the data in the previous 2 plots. The coefficients show no significant trends in telescope declination, right ascension, or hour angle, which rules out instrumental flexure as a potential source of the observed drifts.

2.2.2.3 Rebinning and Extraction

We rebin each CCD spectrum to a logarithmic scale in $n\lambda$ using the calibration x, y, and tilt fits. For a given bin in log $n\lambda$, we obtain the pixel vertices corresponding to the center of the order from the $x(\lambda^{-1}, n\lambda)$ and $y(\lambda^{-1}, n\lambda)$ fits. The tilt (in pixels per pixel) polynomial gives the pixel locations away from the order center. Thus we obtain a series of two-dimensional extracted orders, with dispersion in one direction and slit height in the other. Orders were separated by ~ 10 pixels in the raw frames, but to avoid crosstalk between the orders only 4 pixels on each side of the order center were extracted.

The order strips are "collapsed" from the rebinned image by finding the centroid of the star image in the order with a gaussian fit, and for each log $n\lambda$ bin summing 5 pixels around the center and subtracting a sky level determined from the three outside pixels. Figure 2-4 shows a plot of a resulting spectrum of HD161096, a radial velocity standard of spectral class K2 III. The wavelength range is from 4300–7500 Å; the falloff on the right of the low orders is the edge of the CCD. This particular spectrum was used as the template for relative velocity measurements in our reductions. The star was chosen because it has relatively strong lines over the entire range of wavelengths
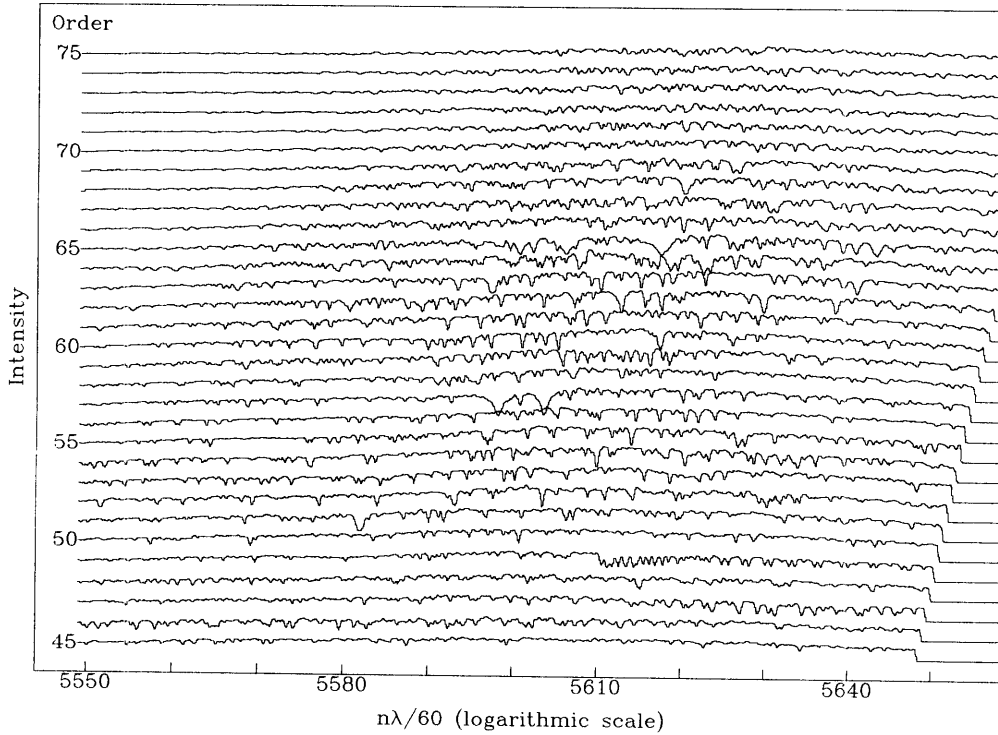
Figure 2-4: Reduced echelle spectrum of HD161096.

of our spectra, and this particular observation was chosen because it was taken on a night when the instrument was stable.

2.2.2.4 Radial Velocity Measurement

We determine radial velocities by comparing spectra to a standard star spectrum using the Fourier quotient technique described by Sargent *et al.* (1977). This method has the advantage of simultaneously solving for differences in line width and depth in addition to redshift. Depth and width of absorption lines varies substantially between stars of different spectral class, and Cepheid lines suffer further broadening (and change in profile) due to pulsation (Karp 1975; Hindsley and Bell 1986). Fourier transforms of the two spectra are computed, and the quotient of the two transforms is fit to a model with three parameters corresponding to relative line strength, broadening, and shift. We limit the comparison to the central 512 pixels of each of orders 50 through 75. The highest orders are eliminated due to the low efficiency of the instrument at these wavelengths, and the lowest orders are not used due to the presence of telluric absorption lines. In addition, the highest and lowest wavenumbers of the Fourier
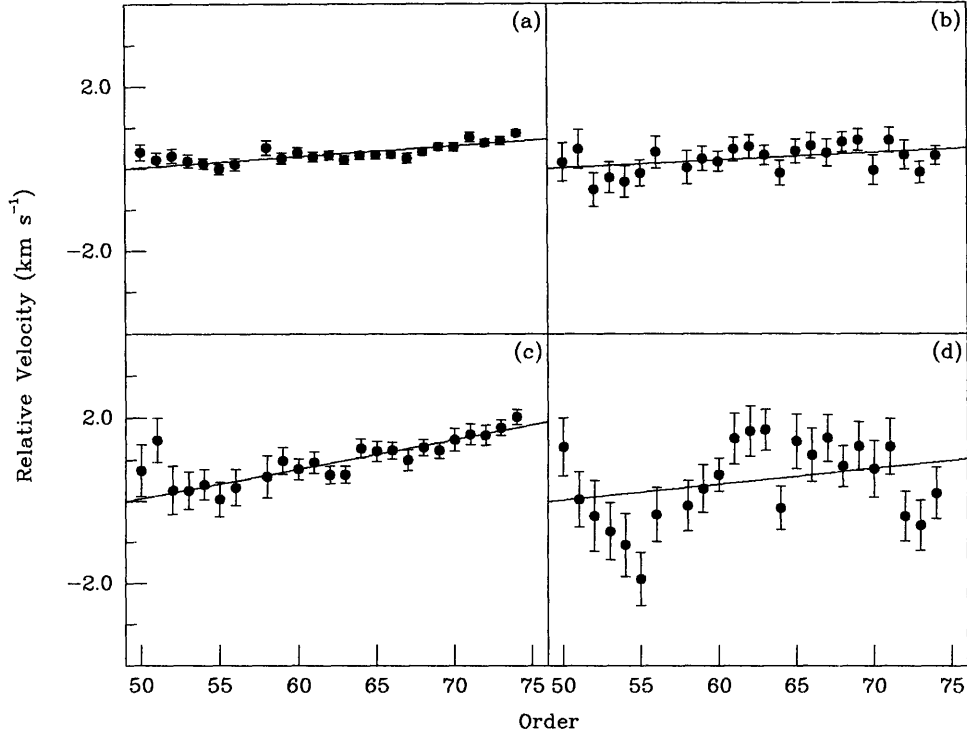
Figure 2-5: Profile of the measured relative velocity as a function of echelle order. Panels: (a) HD161096; (b) HD182572; (c) HD8779; (d) HD204867.

quotient are eliminated from the fit, as they tend to be dominated by pixel noise and continuum features.

Figure 2-5 shows typical relative velocity profiles of velocity standards across the echelle orders; panel A shows a different observation of the reference template star HD161096. Figure 2-6 shows profiles of four of the Cepheids. To remove any additional instrumental drift not taken into account with the wavelength solutions, we use the relative shifts of the atmospheric B-band absorption lines (around 6800 Å), which appear on order 49. We fit relative velocity as a linear function of order number with points weighted by the formal velocity errors. This line is shown superimposed on the profiles of Figures 2-5 and 2-6. We project a velocity back to order 49 along the line, then correct this velocity using the atmospheric lines as a zero. The atmospheric line shift is computed using 256 pixels ($\sim$45 Å) centered on the portion of the band in the order. Each computed velocity is further corrected for the Earth's orbit and rotation in the usual manner.
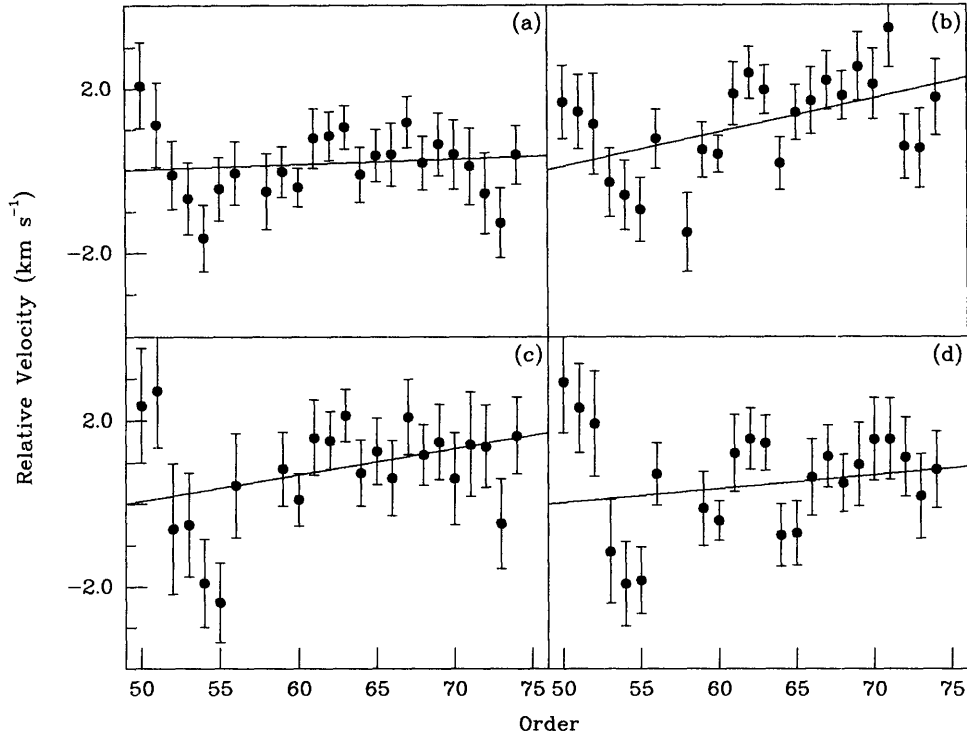
Figure 2-6: Relative velocitiy profiles of four typical Cepheids: (a) CG Cas; (b) V438 Cyg; (c) CR Cep; (d) RU Sct.

2.2.2.5 Zero point

For each observation, we measure a relative velocity $v_{rel} = v_{obs} - v_0$, where v_{obs} is the radial velocity of the star. The single value v_0, the radial velocity of the template spectrum and the effective zero point for our velocities v_{obs}, is undetermined in our observations. We determine the zero point by calculating an effective v_0 for each measured velocity of 10 reference stars (two of the observed reference stars have been eliminated, see §IV), using radial velocities of the reference stars from Latham and Stefanik (private communication, hereafter CfA velocities), v_*. Figure 2-7 shows $v_0^{eff} \equiv (v_* - v_{rel})$ for our reference star observations; here error bars represent the error of the order-to-order velocity fit added in quadrature to the formal error in comparison of the B-band absorption. The zero point v_0 is taken to be the mean of these observations, or 11.15 ± 0.09 km s^{-1}. Comparing the CfA velocities with the mean observed velocity of each reference star we find a scatter of 0.32 km s^{-1}.

25
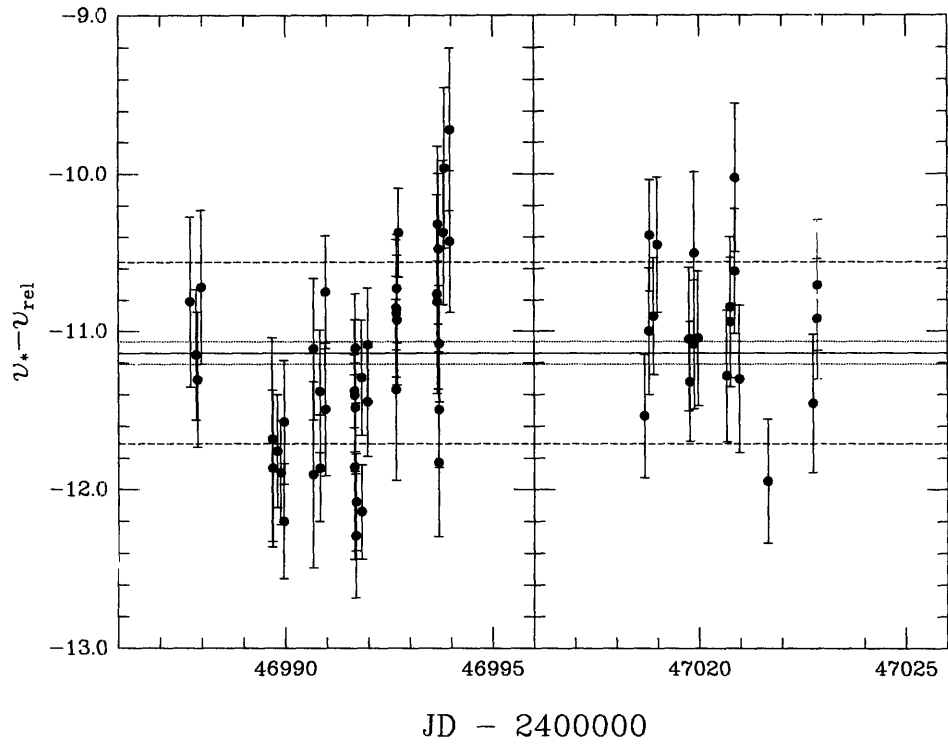
Figure 2-7: Radial velocities of the template spectrum. Each point is computed from a spectrum of a radial velocity standard star by subtracting the measured velocity relative to the template from the star's catalog velocity. Points shown use the CfA radial velocities for the standards.

26

Table 2.1: Cepheid Radial Velocities

JD -2400000	V_r km s^{-1}	σ	JD -2400000	V_r km s^{-1}	σ	JD -2400000	V_r km s^{-1}	σ
V600 Aql			47019.945	-38.86	0.70	46993.895	-23.24	0.98
46987.875	-8.57	0.54	47020.949	-44.16	0.78	47018.914	10.81	0.57
46989.813	1.80	0.40				47019.887	-20.62	0.77
46990.785	7.24	0.38	CP Cep			47020.898	-18.21	0.73
46991.809	19.19	0.48	46990.922	-39.44	0.45	47022.844	3.92	0.48
46992.844	14.01	0.53	46991.941	-34.31	0.43			
46993.809	-10.68	0.75	46992.930	-30.79	0.47	V402 Cyg		
47018.797	0.55	0.44	46993.902	-26.88	0.79	46990.840	-8.56	0.44
47019.777	6.42	0.48	47018.926	-54.99	0.67	46991.867	1.24	0.39
47021.762	16.20	0.61	47019.895	-64.07	0.75	46992.875	-18.49	0.54
47022.750	-10.71	0.76	47020.910	-64.72	0.92	46993.848	-24.95	0.84
						47018.871	-9.48	0.54
CF Cas			CR Cep			47019.828	-26.67	0.69
46989.961	-64.79	0.48	46989.949	-31.03	0.55	47020.848	-15.49	0.57
46990.941	-66.42	0.62	46990.875	-26.09	0.53	47022.789	5.80	0.73
46991.953	-91.70	0.54	46991.898	-18.64	0.55			
46992.941	-83.67	0.52	46992.918	-30.28	0.58	V438 Cyg		
47018.949	-67.88	0.55	46993.891	-43.41	0.83	46990.902	12.81	0.48
47019.910	-60.25	0.65	47018.934	-42.07	0.66	46991.934	0.98	0.42
47020.930	-92.84	0.75	47019.902	-38.64	0.67	46992.895	-14.08	0.48
47022.891	-77.03	0.50	47020.918	-33.59	0.91	46993.871	-17.30	0.69
			47022.859	-14.15	0.77	47018.891	-30.47	0.54
CG Cas						47019.852	-22.97	0.61
46989.984	-71.33	0.50	GH Cyg			47020.867	-13.29	0.48
46990.957	-62.67	0.59	46987.914	-6.93	0.69	47022.813	6.69	0.79
46991.969	-93.03	0.72	46989.840	-23.70	0.55			
46993.949	-78.18	0.78	46990.820	-19.19	0.50	V459 Cyg		
47018.961	-91.58	0.68	46991.859	-14.84	0.48	46987.961	-1.65	0.65
47019.926	-80.13	0.59	46992.867	-11.70	0.48	46989.934	-36.51	0.62
47020.945	-68.65	0.74	46993.844	-2.90	1.06	46990.859	-31.96	0.49
47022.906	-95.17	0.79	47018.832	3.86	0.64	46991.883	-24.46	0.50
			47018.859	2.81	0.53	46993.875	-13.17	0.72
DL Cas			47019.805	-24.98	0.70	47018.898	-37.16	0.63
46989.988	-41.62	0.55	47022.785	-8.06	0.83	47019.863	-32.12	0.66
46990.980	-37.61	0.56				47020.887	-25.35	0.80
46993.953	-17.33	0.81	V386 Cyg					
47018.969	-17.59	0.70	46990.883	-3.50	0.44	V492 Cyg		
			46991.906	5.63	0.41	46989.902	-4.94	0.51

27

Table 2.1—*Continued*

JD -2400000	V_r km s^{-1}	σ	JD -2400000	V_r km s^{-1}	σ	JD -2400000	V_r km s^{-1}	σ
V495 Cyg			47019.965	-42.66	0.54	TY Sct		
46987.949	-24.95	0.70	47020.973	-33.11	0.94	46987.836	36.38	0.62
46989.914	-11.99	0.47				46989.742	45.30	0.48
46990.852	-4.22	0.42	VX Per			46990.723	33.78	0.52
46991.875	1.15	0.39	46989.992	-44.64	0.60	46991.738	21.15	0.48
46992.883	0.67	0.50	46990.984	-43.52	0.61	46992.770	16.72	0.49
46993.855	-13.28	0.93	46991.996	-42.37	0.51	46993.742	13.45	0.65
47018.879	0.28	0.51	46993.965	-45.56	0.76	47019.746	25.12	0.61
47019.840	0.39	0.59	47018.973	-22.59	0.49	47020.773	33.44	0.59
47020.855	-15.47	0.66	47019.957	-16.38	0.53	47022.734	45.85	0.61
			47020.957	-19.40	0.79	47018.727	16.61	0.47
V532 Cyg								
46987.969	-11.06	0.61	X Sct			UZ Sct		
46989.941	-22.77	0.65	46987.746	-6.55	0.94	46987.766	17.64	0.61
46990.863	-14.48	0.51	46989.762	17.96	0.54	46989.777	29.02	0.52
46992.902	-22.19	0.47	46990.742	27.81	0.71	46990.758	35.18	0.45
46992.906	-21.58	0.60	46991.758	-4.50	0.75	46991.770	41.23	0.44
46993.879	-17.85	0.76	46992.793	1.13	0.57	46992.805	46.41	0.49
47018.906	-18.53	0.72	46993.766	12.81	0.68	46993.777	50.65	0.75
47019.871	-20.33	0.65	47018.754	11.41	0.58	47018.762	24.77	0.57
47020.891	-10.15	0.72	47020.695	19.69	0.78	47020.707	36.30	0.53
			47021.672	-3.80	0.69	47021.688	43.27	0.45
V1726 Cyg			47022.672	7.20	0.86	47022.684	45.35	0.77
46987.977	-15.75	0.65						
46989.945	-13.63	0.54	RU Sct			CK Sct		
46990.867	-18.59	0.54	46987.824	8.75	0.43	46987.813	-9.57	0.55
46992.910	-12.31	0.52	46989.727	16.31	0.49	46989.723	-5.98	0.39
46993.883	-14.25	0.81	46990.715	17.69	0.65	46990.707	-3.11	0.39
47018.918	-12.21	0.63	46991.719	17.55	0.50	46991.711	0.28	0.35
47019.891	-15.79	0.67	46992.754	8.97	0.49	46992.750	9.30	0.47
47020.902	-18.91	0.79	46993.727	1.89	0.53	46993.723	12.69	0.61
47022.848	-11.27	0.61	47018.711	-26.85	0.54	47018.703	-9.74	0.49
			47019.738	-22.91	0.52	47019.730	-5.73	0.47
UY Per			47020.750	-18.82	0.48	47020.742	-3.27	0.49
46990.996	-63.10	0.57	47021.727	-14.23	0.40	47021.719	3.42	0.52
46992.004	-53.74	0.51	47022.719	-8.14	0.56	47022.715	10.02	0.67
46993.988	-34.98	1.03						
47018.984	-52.71	0.57						

Table 2.1—*Continued*

JD -2400000	V_r km s^{-1}	σ	JD -2400000	V_r km s^{-1}	σ	JD -2400000	V_r km s^{-1}	σ
CM Sct			47020.734	13.81	0.69	46990.797	15.27	0.43
46987.848	23.41	0.69	47021.711	24.34	0.72	46991.820	16.56	0.44
46989.754	49.49	0.49	47022.703	12.00	1.18	46992.852	17.02	0.45
46990.734	52.19	0.52				46993.820	17.90	0.63
46991.750	24.92	0.52	V367 Sct			47018.801	11.86	0.59
46992.785	37.13	0.46	46987.781	6.92	0.72	47019.785	7.58	0.62
46993.754	48.87	0.75	46989.793	-20.32	0.58	47022.766	2.54	0.78
47018.742	27.41	0.64	46990.773	-12.28	0.52			
47019.762	29.26	0.57	46991.789	-3.62	0.48	DG Vul		
47021.750	55.20	0.52	46992.820	-0.99	0.54	46987.930	-1.38	0.60
47022.742	25.22	0.69	46993.793	-5.28	0.90	46989.828	-10.38	0.62
			47018.777	5.86	0.52	46990.813	-18.25	0.54
EV Sct			47019.703	-6.84	0.74	46991.848	-14.69	0.55
46987.793	24.73	0.76	47020.727	-18.73	0.59	46992.863	-8.54	0.45
46989.797	13.89	0.63	47021.703	-11.98	0.63	46993.832	-1.92	0.71
46990.781	24.12	0.64	47022.699	-4.92	1.39	47018.848	-17.21	0.53
46991.797	13.53	0.72				47019.793	-11.39	0.51
46993.801	22.91	1.00	GY Sge			47022.777	11.58	0.57
47018.785	24.93	0.68	46987.902	11.54	0.48			
47019.719	11.20	0.73	46989.816	14.39	0.44			

Table 2.2: Standard Star Radial Velocities

HD	V_r	ε_f	ε_V	n
8779	-3.94	0.25	0.25	3
114762	49.72	0.27	0.21	5
132737	-22.67	0.14	0.18	3
136202	54.62	0.20	0.22	6
140913	-19.39	0.22	0.18	3
144579	-58.73	0.24	0.40	3
145001	-10.31	0.18	0.37	3
154417	-16.34	0.17	0.19	5
161096	-12.02	0.14	0.39	7
182572	-100.22	0.14	0.13	9
187691	0.08	0.13	0.27	8
204867	7.34	0.20	0.76	7
212943	54.43	0.15	0.20	8
213014	-40.05	0.15	0.20	8

Table 2.3: Relative Zero Point

System	V_0	σ	n
CfA	0.00	0.32	12
Barnes	0.14	0.96	6
CORAVEL	-0.42	0.22	9
VIC	-0.44	0.62	12
DAO90	-0.17	0.20	6
Haute	-0.29	0.43	10
McClure	-0.06	0.49	7

2.2.3 Radial Velocities

Radial velocities measurements for the 26 Cepheids are given in Table 2.1. The σ column shows the total formal error, including error in determining the velocity from the linear fit across the orders, the zero-point measurement uncertainty of 0.09 km s^{-1}, and the error from the B band absorption line shift. Table 2.2 gives the radial velocities for the standard stars, where ε_f is the formal error and ε_V is the standard error of the mean of the observations. Errors for the Cepheids are somewhat larger than errors for the standards, due to a greater uncertainty in redshift from line broadening and additional error in the linear fit to the velocities of individual orders.

We computed zero-points and scatter between our velocities for the standards
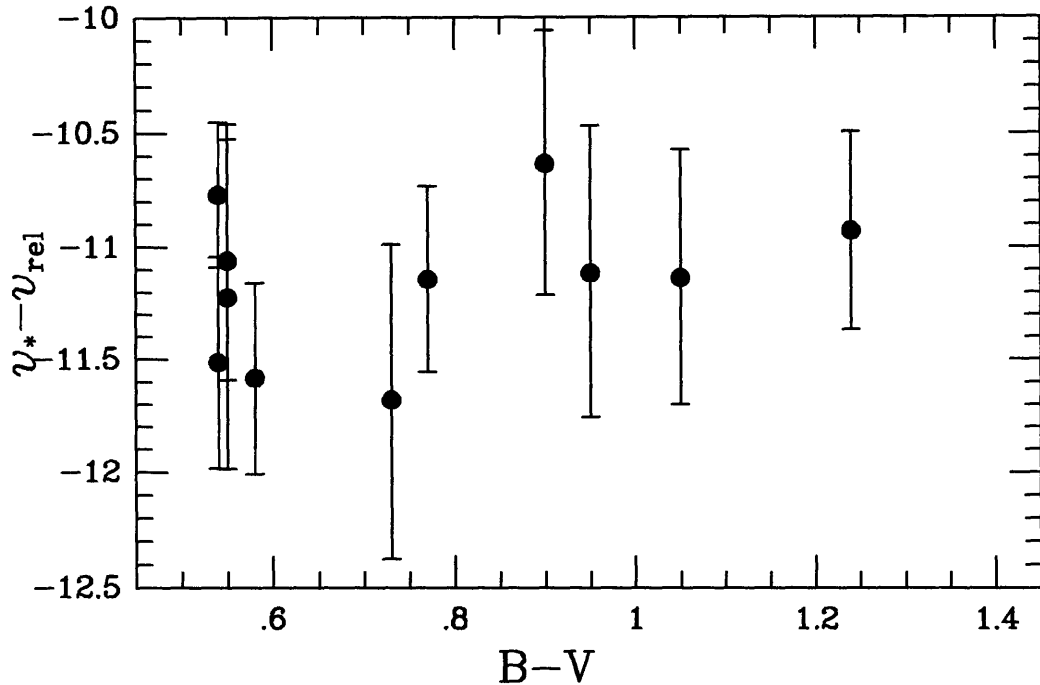
Figure 2-8: Velocity offsets between published CfA standard velocities and those measured here, plotted vs. $(B - V)$ color.

and several other sets of published velocities. Table 2.3 shows the zero-point values (v_0) and rms scatters of our measurements computed from several different velocity measures: Fletcher et al. 1982, hereafter VIC; Scarfe, Batten, and Fletcher 1990, hereafter DAO90; Fehrenbach and Duflot 1980, hereafter Haute; McClure 1987; Barnes, Moffett, and Slovak 1986; Mayor and Maurice 1985 (updated at the 1987 Baltimore IAU meeting), hereafter CORAVEL. We used every star reported in common when calculating zero-points and scatters; however, only two of the measures included all of our standards. The CfA, CORAVEL, and DAO90 velocities (though the last has only 6 stars in common) all show quite good agreement with our observations, with some variation in zero-point. In a private communication, R. P. Stefanik reported that further asteroid measurements made with CORAVEL indicate the previously reported velocities should be adjusted by 0.4 km s^{-1}. After adding in this correction, our computed zero-points for CfA and CORAVEL agree to within the measurement error.

Latham and Stefanik point out that $v_{\text{CfA}} - v_{\text{CORAVEL}}$ shows a significant trend

with $B - V$ color of almost 1 km s^{-1} over 0.8 magnitude. Figure 2-8 shows little or no trend in $v - v_{CfA}$ vs. $B - V$, though our $B - V$ range is more limited. A similar plot using CORAVEL velocities also shows no significant trend, indicating we may have split the difference. Figure 2-5c shows a velocity profile of HD8779, which is at the extreme of our reference stars with $B - V = 1.3$.

The computed radial velocities shown in Figure 2-6 vary from order to order, but in a somewhat regular fashion: a pattern in radial velocity vs. order is apparent, with a dip near order 55 rising back up and leveling off near order 63. One possible explanation is that different orders are dominated by lines formed at different depths. Abt (1978) found differences of up to 10 km s^{-1} between velocities measured with weak to moderate lines and strong lines in X Cygni, and Evans (1984) found differences of up to 5 km s^{-1} between lines formed lower in the stellar atmosphere and those formed higher. These differences are attributed to different pulsational amplitudes at different levels. However, our velocity measurements are not adequate to investigate this as we have limited sampling of different phases. It is also possible that the pattern represents a residual difference between the calibration fit and the influence of low-level fixed pattern noise from the detector.

One of our radial velocity standard stars turned out to have a radial velocity profile similar to those of the Cepheids. Figure 2-6 shows a typical profile for HD204867 (β Aqr), a type Ib supergiant. It appears that either this profile shape is due to properties of a supergiant atmosphere, or the atmosphere of 204867 is unstable. The proximity of this star to the instability strip suggests that it may be showing early (or late) signs of pulsation. In addition, we see a difference of ~ 3 km s^{-1} between the mean velocities of the first and second runs. Such variability is not uncommon in supergiants: Harris (1985a) found that half of the type Ib supergiants he measured showed variability at the 1 to 2 km s^{-1} level. HD204867 was excluded from the zero-point calculation of §III due to potential variability, and as a velocity determined for this star appears to be dependent on which lines are used in the measurement. HD114762 was also excluded as it is now known to have a companion (Latham *et al.* 1989).

The question arises, then, of how to assign a velocity for the Cepheids. Ideally,
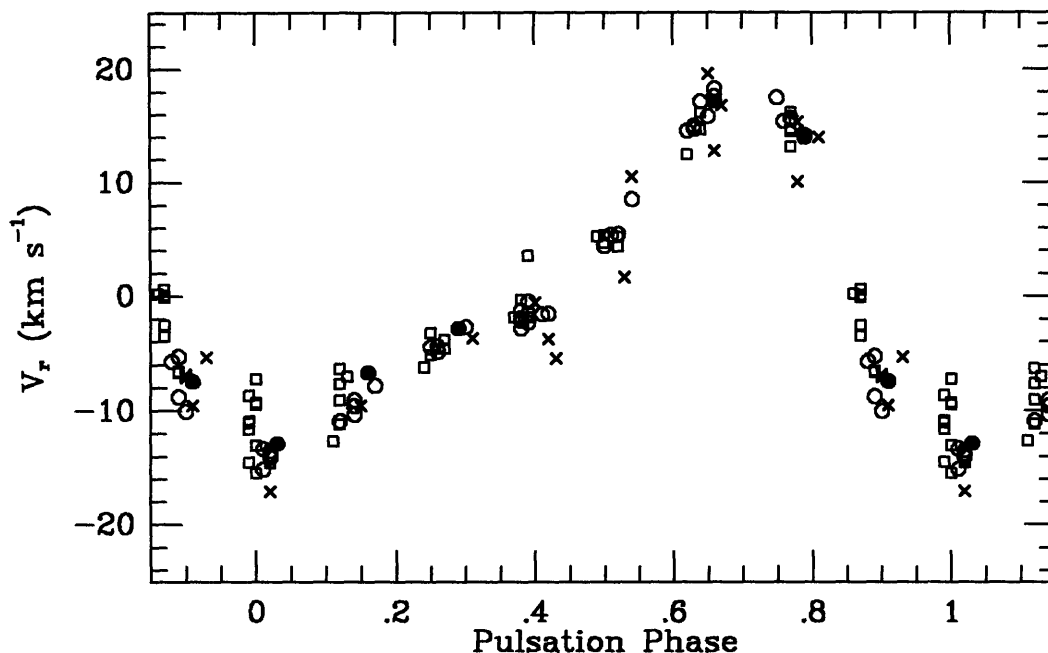
Figure 2-9: Radial velocity measurements of DL Cas, with orbital and γ velocity removed using elements derived by Harris *et al.* (1987). Crosses are measurements from Barnes, Moffett, and Slovak (1988); squares are from Mermilliod, Mayor, and Burki (1987); open circles from Harris *et al.* (1987); filled circles are from this paper. Errors are ~ 4.0 km s^{-1} for Barnes, Moffett, and Slovak (1988), and on the order of the size of the plot symbol for the others.

one would like to select a set of wavelength regions that contain lines with constant depth in the atmosphere, so that one could accurately trace the pulsation amplitude. However, it is beyond the scope of this paper to determine which parts of the spectrum would be best suited for determining a radial velocity for these stars. Since for our purposes we are more concerned with eventually obtaining accurate γ velocities, a slight change in depth over a period is less important, as it would tend to average out over a cycle. Therefore, for simplicity, we chose to fit a straight line to the velocity profile and extrapolate back to order 49, in the same manner as the reference stars. This tends to average out orders dominated by strong and weak lines, though a significant change in the shape of the profile may cause a deviation in the projected velocity. This solution should also be adequate to compensate for most of the effect of a fixed-pattern noise.

33

Figure 2-9 shows a plot of our DL Cas velocities compared with those of Harris *et al.* (1987), Mermilliod, Mayor, and Burki (1987), and Barnes, Moffett, and Slovak (1988). Orbital radial velocity (including a γ velocity of -38.1 km s^{-1}) was removed using orbital elements from Harris *et al.* (1987), and pulsation phase was computed using $P = 8.000610$ and $JD(V_{max}) = 2437043.910$, also from Harris *et al.* (1987). The agreement is quite good, with perhaps a 1–2 km s^{-1} difference between Harris *et al.* and us in the most negative velocities. As our velocities were taken at an orbital phase not well represented in the Harris *et al.* measurements, and the orbital parameters have associated uncertainties, the significance of this difference is unclear. The scatter of the Mermilliod, Mayor, and Burki (1987) velocities near zero pulsational phase is notable—there is a trend for the later measurements to be closer to those of Harris *et al.*, while measurements made at phases 0.2–0.8 do not change substantially over the same period.

2.3 Radial Velocities of Southern Hemisphere Cepheids

2.3.1 Observations

The radial velocity measurements consist of 277 observations of 47 Galactic Cepheids visible from the southern hemisphere. The Cepheids were selected from those for which $240° < \ell < 330°$, $|b| < 5°$, and for which there were few existing radial velocity measurements. Also included were several Cepheids that are possible members of clusters or associations: RU Sct, V367 Sct, CS Vel, CV Mon, QZ Nor, and V340 Nor (CC, Turner 1985). Velocities were also obtained for a few Cepheids observed for §2.2 and visible from the southern hemisphere. Southern hemisphere radial velocity standards from Maurice *et al.* (1984) were observed for use as reference templates and for calibration of the zero point.

Observations were divided into two runs separated by several weeks to allow good period coverage for both short and long period Cepheids. Spectra were obtained with the echelle spectrograph on the DuPont 2.5 m telescope at Las Campanas by P. Schechter during March and May of 1987. The instrument operates with the 2D-

34

Frutti photon counting detector which provides low signal-to-noise spectra at high resolution (Shectman, Price, & Thompson 1985). The multi-order spectra are read out from the detector as a two-dimensional image. The spectrograph configuration is fixed, giving a resolution of $R \sim 30000$ with a 1.5 arcsecond slit, projecting to about 3 detector pixels FWHM. The broad wavelength coverage of the instrument required spacing the orders closely together, limiting the entrance slit height to 4 arcseconds or ~ 8 pixels. To reduce the amount of data storage required for the observations, the format was reduced from the full 1520×1024 pixels to a central 1520×512 subraster, giving a wavelength coverage of 4200–7200 Å. In doing this we sacrificed the atmospheric absorption bands; in retrospect, it might have been better to include them to help remove the frame-to-frame drift of the instrument (as was done with the northern Cepheids, §2.2).

Since the entrance slit was only 4 arcseconds high in the spatial direction, we could not see far enough away from a star centered on the slit to obtain a good sample of the sky. Therefore, each star was observed twice, once at each end of the slit. On nights with poorer seeing, however, putting the star near the edge of the slit blocked a significant amount of the starlight from the spectrograph. On these nights the strategy was changed to observing the star centered on the slit, followed by observing a patch of sky nearby. In both cases wavelength reference arcs from a Th-Ar hollow cathode tube were taken immediately after each star observation for calibration.

2.3.2 Data Reduction

Reduction of the spectra to obtain radial velocities closely followed the procedure described in §2.2. Calibration arc lines from the Th-Ar spectra were identified and used to make a two-dimensional wavelength solution for each stellar spectrum. This solution was used to rebin the flattened spectrum to a logarithmic wavelength scale. A one-dimensional spectrum was then created by summing pixels containing the star and subtracting an appropriate amount of sky, either from the same exposure away from the star or from a separate nearby sky exposure.

Velocities were obtained by measuring redshifts relative to template spectra of HD
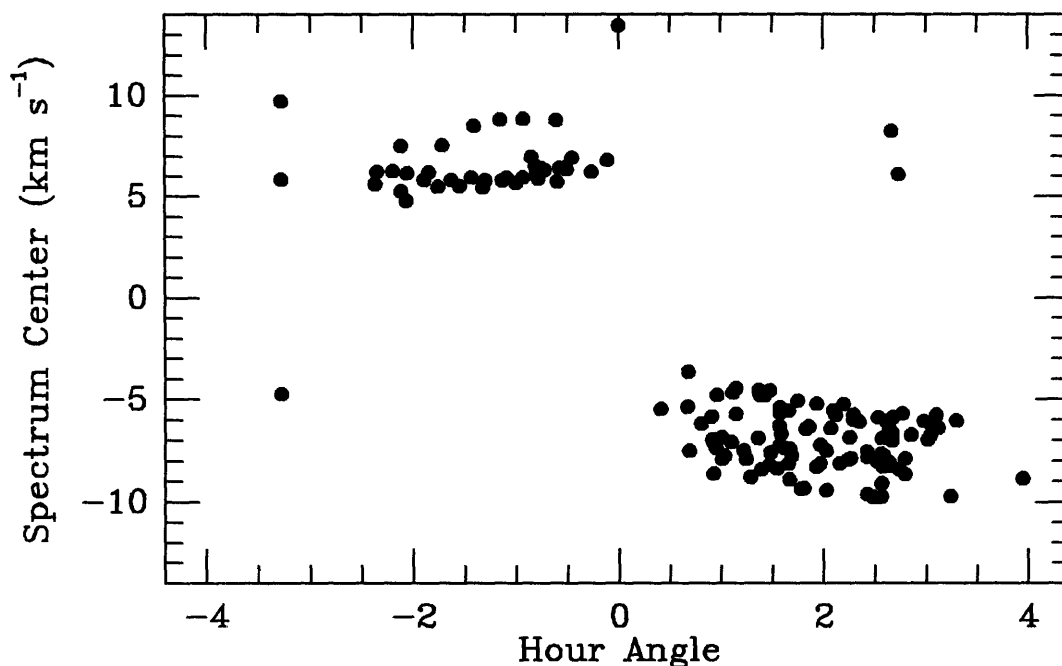
Figure 2-10: The position of the spectrum center, given in units of km s⁻1 about an arbitrary point, plotted vs. hour angle of the telescope. Note the abrupt change about the meridian.

111417 (MK spectral type K2IV). Redshifts were measured independently for each echelle order, and converted to heliocentric velocities using a correction for the earth's motion (Stumpff 1980). In contrast to the procedure used in §2.2, the velocity was determined from a weighted mean of the velocities in orders 60–80 (wavelengths 4250–5750 Å) rather than using a linear fit to the velocities and then making a correction based on the telluric absorption lines. The spectrograph showed less drift between observations than did the Palomar 60-inch echelle, though an additional correction from telluric lines would have been helpful (see §2.3.3 below). A large shift in the detector, corresponding to about 15 km s^{-1} was seen when the telescope crossed the meridian (see Figure 2-10). This was commonly referred to as the "Boksenberg flop" (it has since been corrected), and was due to a window in the image tube shifting when the orientation of gravity with respect to the instrument changed at the meridian. Our calibration was not affected by this shift, as during our runs the telescope did not cross the meridian between a star observation and its corresponding calibration
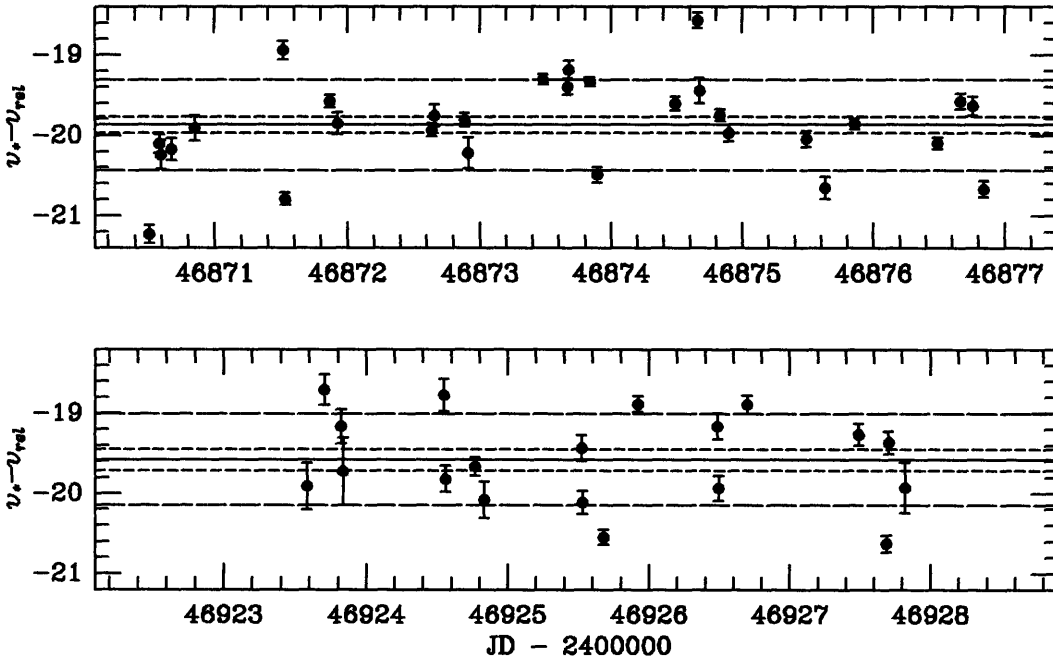
Figure 2-11: Reference template velocities, computed with respect to CORAVEL velocities, for each standard star observation vs. Julian date. The CORAVEL velocity of the standard is represented as v_*, and v_{rel} is the measured velocity of the standard relative to the template. The upper frame contains observations from the first run, the lower frame from the second; a different templates was used for each run. The solid, long-, and short-dashed lines correspond to the mean, σ, and error of the mean, respectively.

frame.

The velocity zero point was determined using CORAVEL faint southern velocity standards from Maurice *et al.* (1984). Two template spectra of HD 111417 were chosen, one from each run. An effective velocity for each template was computed as follows: the relative velocity of each standard star spectrum taken during a run, v_{rel}, was measured with respect to the template for that run (taking into account the heliocentric correction). The difference between the published CORAVEL velocity for the star, v_*, and this relative velocity gives a measurement of the absolute velocity of the template spectrum on the CORAVEL zero point. Figure 2-11 shows these measurements plotted vs. Julian date; no significant trend is evident. Taking the mean of the points results in an effective absolute velocity of each template spectrum, which was found to be -19.87 ± 0.10 km s^{-1} in the first run, and -19.58 ± 0.13 km s^{-1} in the

37

Table 2.4: Southern Standard Radial Velocities

Star	V_r	ε_f	ε_V	n
HD 39194	13.90	0.30	0.42	4
HD 48381	40.49	0.26	0.05	5
HD 83443	28.81	0.17	0.16	12
HD 83516	43.84	0.21	0.17	8
HD 101266	22.18	0.17	0.30	12
HD 111417	-19.14	0.18	0.20	10
HD 176047	-42.29	0.19	0.16	9
HD 193231	-30.02	0.32	0.07	4
HD 196983	-9.13	0.34	0.28	3
CPD -43° 2527	19.78	0.22	0.31	7

second. The effective template velocity was used to determine the absolute velocities by adding the template velocity to each velocity measured relative to the template spectrum.

The velocities were further adjusted to align the zero point with the northern hemisphere Cepheids of §2.2. The zero point of §2.2 is based on CfA velocities measured by Latham and Stefanik (private communication). It was shown in §2.2 that this zero point was 0.42 km s^{-1} higher than the CORAVEL zero point for the same northern hemisphere standards. Therefore the velocities were adjusted by 0.42 km s^{-1} under the assumption that the CORAVEL zero point is the same in both hemispheres.

2.3.3 Radial Velocities

Table 2.4 shows the radial velocity for each standard star, averaged over our measurements. Two error estimates are given: ε_f is the formal error from the measurement of the redshift (as in §2.2.3), and ε_v is the error in the average velocity from the scatter ($\sigma/\sqrt{n}$). For the standards, the order-to-order scatter is typically the same size as the formal error, about 0.2–0.8 km s^{-1}. However, the scatter in the velocities between different observations of the same star is larger, around 0.8 km s^{-1}. We attribute this discrepancy to the accuracy of the wavelength calibration. This accuracy depends on several factors, including the small number of lines available for calibration ($\approx$ 70) and the amount of drift in the detector between the star and calibration spectra. We

estimate the additional velocity uncertainty due to the calibration to be 0.56 km s^{-1}, based on the difference between the formal and measured errors in the standards. This uncertainty can be combined with the formal error to obtain an error estimate for a single velocity measurement.

The standard velocities are generally in good agreement with CORAVEL velocities. We find no significant trend in the difference between our velocities and CORAVEL with $B - V$ color, though we cannot exclude the existence of a trend. The range in $B - V$ colors of our standards is 0.7–1.4, so if the trend is similar to that seen by D. W. Latham (private communication) it is not likely we would detect it. The velocity for HD 101266 has a discrepancy with respect to CORAVEL of -1.8 km s^{-1}, significantly larger than the other standard stars. This would tend to support the suggestion by Maurice *et al.* (1984) that the radial velocity of this star is variable. For this reason HD 101266 was excluded from the determination of the zero point.

Table 2.5 lists the radial velocity measurements for the Cepheids. The error is shown in the σ column, computed by combining the error *external* to the measurement (i.e. the error attributed to the wavelength calibration above, 0.56 km s^{-1}) to the error *internal* to the individual measurement. The internal error was chosen as the larger of two error estimates: the first, the formal error from the Fourier quotient technique (Sargent *et al.* 1977); the second, the scatter of the velocities measured in different orders. Occasionally an order either did not converge or converged to a nonsense value; these orders were eliminated from the average and not used in computing the scatter. It was gratifying to see that the formal error and the scatter between orders agreed well even in the Cepheids, typically to 20% with no significant offset. The interal error was typically around 0.6 km s^{-1}, although it was occasionally 2 km s^{-1} or larger in spectra with very poor signal-to-noise ratios.

2.4 Gamma Velocities

Radial velocities with a precision of 1 km s^{-1} require a spectrograph with a resolving power of about 30000, and though velocities can be computed from low signal-to-

Table 2.5: Southern Cepheid Radial Velocities

JD -2400000	V_r km s^{-1}	σ	JD -2400000	V_r km s^{-1}	σ	JD -2400000	V_r km s^{-1}	σ
CQ Car			46874.594	94.34	0.63	FM Car		
46870.613	27.38	1.18	46875.711	99.97	0.60	46872.773	34.06	0.73
46871.738	36.33	1.15	46876.586	103.78	0.61	46873.727	36.45	0.74
46872.691	15.27	2.11	46923.613	113.26	0.73	46874.699	45.04	0.82
46873.555	5.42	0.96	46925.563	83.06	0.69	46875.785	58.04	0.69
46874.563	13.84	0.95				46876.695	55.38	0.78
46875.680	26.15	1.03	FF Car			46923.672	23.20	2.45
46876.566	32.33	1.07	46870.723	-5.22	0.74	46924.492	25.38	0.81
46927.473	9.09	2.31	46873.594	8.26	0.69	46925.609	30.25	0.86
			46874.602	10.28	0.76	46926.602	35.96	0.85
CR Car			46875.723	-0.79	0.86	46927.582	37.76	0.85
46870.625	36.53	0.59	46876.598	-6.44	0.70			
46871.750	42.80	0.63	46926.547	-13.69	0.86	GT Car		
46872.703	34.57	0.67	46927.543	-32.59	0.97	46870.793	12.19	0.64
46873.563	20.19	0.63				46871.773	16.05	1.19
46874.574	16.08	0.64	FI Car			46872.762	18.04	0.70
46875.691	18.93	0.63	46870.770	-5.00	0.63	46873.629	19.77	0.63
46876.543	18.62	0.63	46871.617	0.27	0.64	46876.684	13.90	0.65
46926.523	13.49	0.65	46872.750	6.77	0.61	46925.594	17.54	3.09
46927.523	21.13	0.62	46873.715	13.13	0.60	46926.594	19.49	2.19
			46874.625	20.98	0.60	46927.570	18.35	0.82
CS Car			46875.754	28.01	0.61			
46870.633	28.16	0.86	46876.617	32.16	0.62	HS Car		
46871.762	18.22	0.88	46923.637	-9.37	0.69	46870.707	21.81	0.78
46872.715	-3.35	0.86				46872.684	-3.87	0.63
46873.574	1.22	0.68	FK Car			46873.543	5.90	0.60
46874.582	7.46	0.66	46870.781	37.28	0.74	46874.555	15.86	0.63
46875.703	15.55	1.05	46871.633	41.62	0.61	46875.668	24.84	0.74
46876.578	19.76	0.65	46873.707	48.80	0.66			
46924.449	19.99	0.63	46875.766	54.96	0.79	II Car		
46925.555	1.25	1.25	46876.629	54.75	0.80	46870.746	48.19	2.46
46926.535	-0.74	0.87	46924.469	43.13	1.03	46873.617	45.59	1.35
46927.535	5.30	0.90	46925.574	44.88	0.85	46875.742	34.41	1.36
			46926.570	30.05	1.17	46924.461	41.22	1.24
CT Car						46926.563	41.83	1.44
46870.645	90.97	0.69						
46872.727	84.44	0.71						
46873.582	88.11	0.61						

Table 2.5—*Continued*

JD -2400000	V$_r$ km s^{-1}	σ	JD -2400000	V$_r$ km s^{-1}	σ	JD -2400000	V$_r$ km s^{-1}	σ
IO Car			46876.809	-15.93	0.68	46876.727	-21.41	0.64
46923.648	19.45	0.75	46925.691	-35.94	0.69	46926.641	-15.39	0.67
46924.480	21.77	0.64	46926.688	-28.49	0.68	46927.617	-10.81	0.83
46925.582	24.90	0.62	46927.664	-20.78	0.67			
46926.582	27.60	0.63				**TY Cru**		
46927.563	28.55	0.63	**QY Cen**			46871.797	3.57	0.93
			46870.891	-84.23	0.67	46872.824	-9.20	0.75
IZ Cen			46871.902	-78.85	0.62	46874.801	-16.30	0.71
46872.781	-19.67	0.67	46873.871	-69.15	0.59	46875.836	-5.42	0.71
46873.742	-13.68	0.88	46874.887	-64.90	0.60			
46874.711	-3.62	0.88	46875.891	-59.21	0.58	**VV Cru**		
46875.797	-22.09	0.76	46876.828	-54.94	0.59	46874.852	-15.54	0.63
46876.707	-33.22	0.74	46925.699	-77.28	0.68	46876.777	-50.14	0.63
46924.504	-29.95	1.03				46924.641	-41.44	0.66
			V641 Cen			46926.664	-43.63	0.75
MY Cen			46870.902	-40.73	0.93	46927.629	-36.61	0.65
46874.863	-8.15	0.61	46871.914	-40.47	0.98			
46876.820	-30.45	0.69	46873.883	-43.46	1.05	**VX Cru**		
46923.715	-2.70	0.77	46875.902	-42.86	0.87	46870.824	-27.01	0.59
46925.668	-27.00	0.81	46924.582	-34.89	0.71	46871.859	-19.16	0.60
46927.652	-0.11	0.78	46925.715	-35.03	0.69	46872.832	-12.90	0.61
			46926.723	-35.36	0.69	46873.832	-10.18	0.65
MZ Cen						46874.809	-12.04	0.68
46870.867	-12.48	0.62	**V782 Cen**			46875.848	-25.63	0.62
46871.879	-29.14	0.63	46870.805	45.83	1.12	46876.750	-33.10	0.64
46872.855	-35.18	0.62	46872.805	45.30	1.34	46926.676	-39.60	0.76
46873.852	-37.38	0.65	46873.754	35.13	1.91	46927.641	-39.85	0.68
46874.820	-44.01	0.62	46874.730	27.31	0.92			
46875.883	-45.56	0.62	46875.816	26.61	1.07	**AD Cru**		
46876.797	-38.27	0.60	46876.715	25.00	1.00	46874.844	-29.11	0.66
			46927.605	41.15	1.09	46876.770	-45.62	0.63
OO Cen						46923.695	-30.42	0.66
46870.879	-55.36	0.67	**SV Cru**			46924.629	-22.74	0.63
46871.891	-53.61	0.65	46872.867	4.10	0.66	46925.660	-15.49	0.66
46872.875	-47.04	0.64	46874.789	-30.66	0.77	46926.652	-51.02	0.68
46873.863	-39.47	0.63	46875.828	-27.59	0.68			
46874.875	-30.86	0.60						
46875.871	-22.62	0.61						

Table 2.5—*Continued*

JD -2400000	V_r km s^{-1}	σ	JD -2400000	V_r km s^{-1}	σ	JD -2400000	V_r km s^{-1}	σ
CV Mon			QZ Nor			CK Sct		
46870.527	38.80	0.64	46923.770	-31.26	0.68	46924.871	-1.39	0.62
46871.563	2.60	0.67	46924.699	-43.54	0.66	46925.809	8.15	0.61
46873.520	16.59	0.61	46925.852	-43.17	0.62			
46874.527	26.41	0.65	46926.797	-33.92	0.63	CM Sct		
46875.527	35.77	0.62	46927.777	-32.46	0.64	46924.910	23.79	0.69
46876.531	13.66	0.67				46925.902	32.60	0.62
46926.449	8.47	0.65	V340 Nor					
			46923.781	-43.12	0.81	CN Sct		
RS Nor			46924.707	-44.99	0.81	46924.922	11.14	0.90
46923.758	-57.00	0.75	46925.863	-45.80	0.65	46925.910	10.29	0.71
46924.688	-51.36	0.64	46926.809	-46.08	0.65			
46925.844	-42.63	0.61	46927.801	-47.73	0.71	V367 Sct		
46926.750	-35.64	0.60				46924.809	-6.84	0.71
46927.766	-26.07	0.61	HW Pup			46925.781	-2.52	0.65
			46870.664	115.93	0.68	46927.895	-21.85	1.82
SY Nor			46871.574	112.42	0.66			
46924.664	-28.08	0.61	46873.637	103.10	0.70	VY Sgr		
46925.824	-19.12	0.60	46874.645	96.31	0.69	46924.750	16.72	0.65
46926.734	-11.23	0.60	46875.602	100.86	0.63	46925.742	24.08	0.60
46927.746	-2.47	0.63	46876.641	107.52	0.62	46927.840	31.15	0.78
			46926.461	103.25	0.93			
TW Nor						AV Sgr		
46924.676	-46.89	0.69	X Sct			46924.738	41.75	0.65
46925.832	-62.31	0.67	46924.789	-7.70	0.87	46925.734	45.07	0.68
46926.742	-63.13	0.65	46925.762	3.57	0.69	46927.734	19.30	0.68
46927.758	-65.42	0.76	46927.863	28.57	0.79			
						V773 Sgr		
GU Nor			RU Sct			46924.730	4.51	1.43
46923.789	-30.97	0.64	46923.813	-13.40	0.63	46925.723	16.08	3.01
46924.719	-15.87	0.63	46924.895	-7.91	0.65	46926.844	-16.12	1.08
46925.871	-24.36	0.64	46925.883	-3.86	0.61	46927.723	-17.73	0.79
46926.816	-36.19	0.66						
46927.809	-21.29	0.63	TY Sct			V1954 Sgr		
			46924.902	25.28	0.63	46924.758	28.79	0.72
			46925.891	18.16	0.67	46925.754	-0.79	0.66
						46927.852	10.94	0.64

noise spectra, exposure times can be quite long for faint ($V\simeq14$ mag) Cepheids. Since rotation curve modeling requires only the center of mass (γ) velocity and not other properties of the velocity curve, we would like a simple method of finding a good γ velocity with relatively few observations. Some information such as the period and phase can be determined from photometry, which is much less expensive in photons. For most of the known Galactic Cepheids this has already been done: the Cepheids observed in §2.2 and §2.3 all have published epochs and periods (e.g. Kholopov *et al.* 1988).

The γ velocities of Cepheids are typically obtained by determining a function $V_r(t)$ from the data, and assigning γ as the velocity offset of this function. One method for finding $V_r(t)$ is to draw a curve through the velocity points by hand, then setting the γ velocity to the line which has equal areas above and below the curve. Though this method can work well (e.g., Moffett & Barnes 1987), it is somewhat subjective and it is hard to assign an error to the γ velocity. Other methods fit analytical curves to the data, such as a Fourier series or the "asymmetric cosine" method used by Imbert *et al.* (1989). While these methods in principle can model Cepheid velocity curves well, they require many free parameters to fit the velocity curves. The asymmetric cosine method requires determining nine parameters to adequately model Cepheids with a Hertzsprung bump (prominent in Cepheids with periods near 10 days), and the Fourier method can require even more. The Fourier technique is also especially sensitive to period undersampling or velocity errors.

2.4.1 Velocity Curve Fitting

Kovács, Kisvarsányi, and Buchler (1990) have examined Fourier decompositions of over 50 type I Cepheid velocity curves. Their analysis showed that the Fourier parameters of most Cepheids follow a continuous progression with period. Thus by knowing the period of a Cepheid, one can construct its approximate velocity curve using the Fourier coefficients. This curve can be fit to period-folded velocities with only two undetermined parameters, the γ velocity and the phase, which can be determined with only a few velocity points. The error in determining the two parameters comes

from both the errors of the individual the velocity measurements and the mismatch of the generated curve to the true velocity curve.

Kovács *et al.* (1990) fit Cepheid velocities to a Fourier expansion of the form

$$V_r(t) = A_0 + \sum_{k=1}^{M} A_k \sin\left[k\omega(t - t_0) + \phi_k\right],\qquad(2.1)$$

where t_0 is the epoch, A_0 is the γ velocity, and M is the order of the fit. They define $R_{k1} = A_k/A_1$ and $\phi_{k1} = \phi_k - k\phi_1$ to express the values of the coefficients. The shape of the velocity curve is determined primarily by the terms with $k \leq 2$, as R_{31} is typically less than 0.15 (i.e., A_3 is less than 3 km s^{-1}) and successive R_{k1} are small. Figure 2-12 shows the Kovács *et al.* (1990) data for the parameters A_1, R_{21}, and ϕ_{21} of the Cepheids in their sample. Superposed on the points in Figure 2-12 are low-order polynomial fits to the data. Since the behavior of these parameters changes significantly near a period of 10 days, we used separate polynomials for $P < 10$ days and $P > 10$ days. There is a scarcity of points at periods greater than about 15 days, which creates a large uncertainty in the fit at long periods. For a lack of more data we extended the fit line at a constant value for periods longer than 30 days.

For a given Cepheid we use its photometric period to determine the Fourier coefficients using the fit polynomials. The coefficients are used to generate a velocity curve, which is fit to the velocity data to determine A_0 ($\equiv \gamma$) and t_0. Results for the Cepheids from §2.2 and §2.3 are given in Table 2.6. Observations of Cepheids in common between the two were combined in a single fit. Also given in the table are reduced χ^2 values of the fits, given the reported errors. At first glance the χ^2 values may seem large, but they do not take into account the uncertainty in the Fourier coefficients used to generate the curve, nor that the low-order coefficients do not completely model the actual Cepheid velocity curve. Figure 2-13 shows typical curve fits to the velocity measurements of several Cepheids with good period coverage.

To more accurately determine the errors in the γ velocities, we have performed a Monte Carlo test of the fitting procedure. The spread of the Fourier parameters around the fit lines were assumed to be: $\sigma = 2.0$ and 4.0 km s^{-1} for A_1; 0.08 and 0.13

44
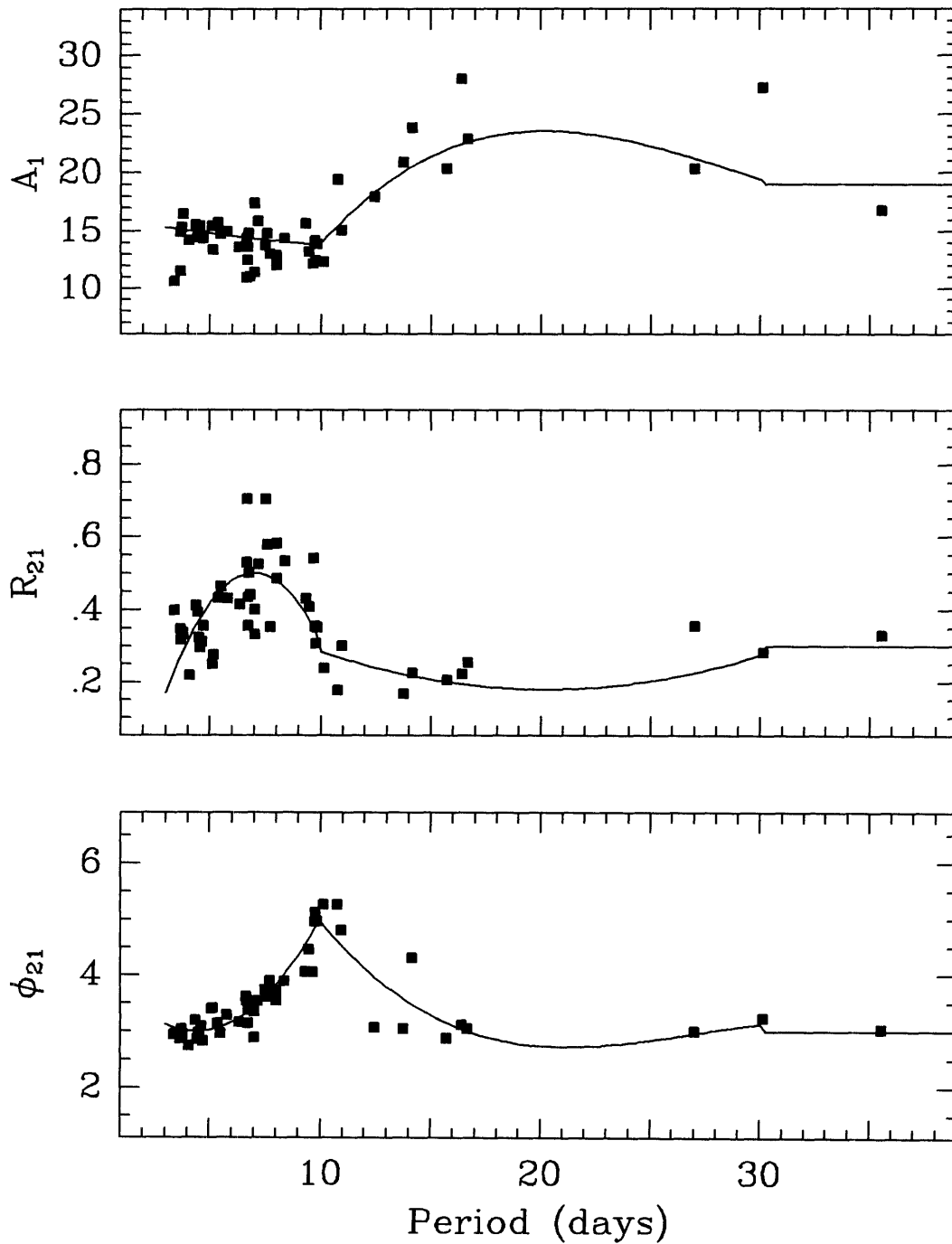
Figure 2-12: Data for three Fourier parameters from Kovács *et al.* (1990) with polynomial fits. Separate second-order polynomials are used for $P < 10d$ and $10d < P < 30d$, and a constant for $P > 30d$.

Table 2.6: Gamma Velocities

Cepheid	γ	σ_{fit}	σ_{MC}	χ^2_{fit}	Cepheid	γ	σ_{fit}	σ_{MC}	χ^2_{fit}
Aql V600	3.14	0.54	0.60	5.1	Cyg V402	−12.70	0.98	0.59	10.9
Car CQ	20.64	1.15	0.48	1.9	Cyg V438	−10.17:	1.77	0.66	32.9
Car CR	24.97	0.85	0.82	7.0	Cyg V459	−20.68	0.29	0.82	0.7
Car CS	10.83	1.30	0.46	13.0	Cyg V495	−11.01	1.61	0.70	37.9
Car CT	111.02:	1.38	4.04	15.7	Cyg V532	−16.20	0.18	0.82	0.2
Car FF	−14.47:	1.21	2.95	5.1	Cyg V1726	−15.32	0.21	0.57	0.4
Car FI	7.89:	0.98	2.68	1.7	Mon CV	18.90	1.21	0.97	10.0
Car FK	29.85:	0.96	3.77	5.3	Nor RS	−40.51	1.42	0.79	6.7
Car FM	39.66	0.51	0.47	1.5	Nor SY	−23.11:	1.09	5.45	0.3
Car GT	11.67:	0.27	3.05	0.1	Nor TW	−53.25:	1.54	3.84	3.7
Car HS	7.62	0.70	0.96	2.2	Nor GU	−24.51	0.79	0.66	3.2
Car II	28.10:	1.52	5.0?	2.3	Nor QZ	−38.60	0.74	0.67	2.6
Car IO	39.30:	1.62	5.86	8.2	Per UY	−44.96	0.68	0.85	2.1
Cas CF	−76.87	0.59	0.56	3.9	Per VX	−35.15	1.43	0.88	18.5
Cas CG	−79.26	0.64	0.49	3.1	Pup HW	116.21:	1.71	3.68	3.2
Cen IZ	−18.91	1.22	0.78	6.1	Sct X	11.09	0.64	0.41	4.7
Cen MY	−15.23	1.06	1.62	3.5	Sct RU	−4.85	0.69	1.39	9.7
Cen MZ	−30.57	1.63	1.97	13.3	Sct TY	25.48	0.47	1.09	3.5
Cen OO	−41.46:	1.37	3.35	2.9	Sct UZ	38.76	0.69	1.16	8.0
Cen QY	−77.25:	1.56	5.90	0.6	Sct CK	−0.36	0.89	0.56	13.3
Cep CP	−41.82:	0.44	2.16	1.5	Sct CM	39.47	0.47	0.40	3.5
Cep CR	−31.30	1.47	0.35	21.1	Sct EV	16.74	0.25	0.37	0.5
Cru SV	−15.37	0.81	0.56	3.0	Sct V367	−7.68:	2.11	0.52	66.8
Cru TY	−11.19	1.36	0.88	5.6	Sge GY	15.57:	0.22	2.5?	0.73
Cru VV	−35.07	1.62	1.30	12.0	Vel AB	28.07	1.50	0.45	9.2
Cru VX	−28.32	0.99	1.60	9.4	Vel CS	26.81	1.43	0.66	10.8
Cru AD	−34.51	1.73	0.79	17.8	Vel DD	26.02:	2.41	3.09	19.5
Cyg GH	−11.11	1.05	0.56	13.2	Vel EZ	96.38:	0.63	5.0?	0.8
Cyg V386	−5.63	1.30	0.66	15.8	Vul DG	2.57:	1.24	2.44	17.1
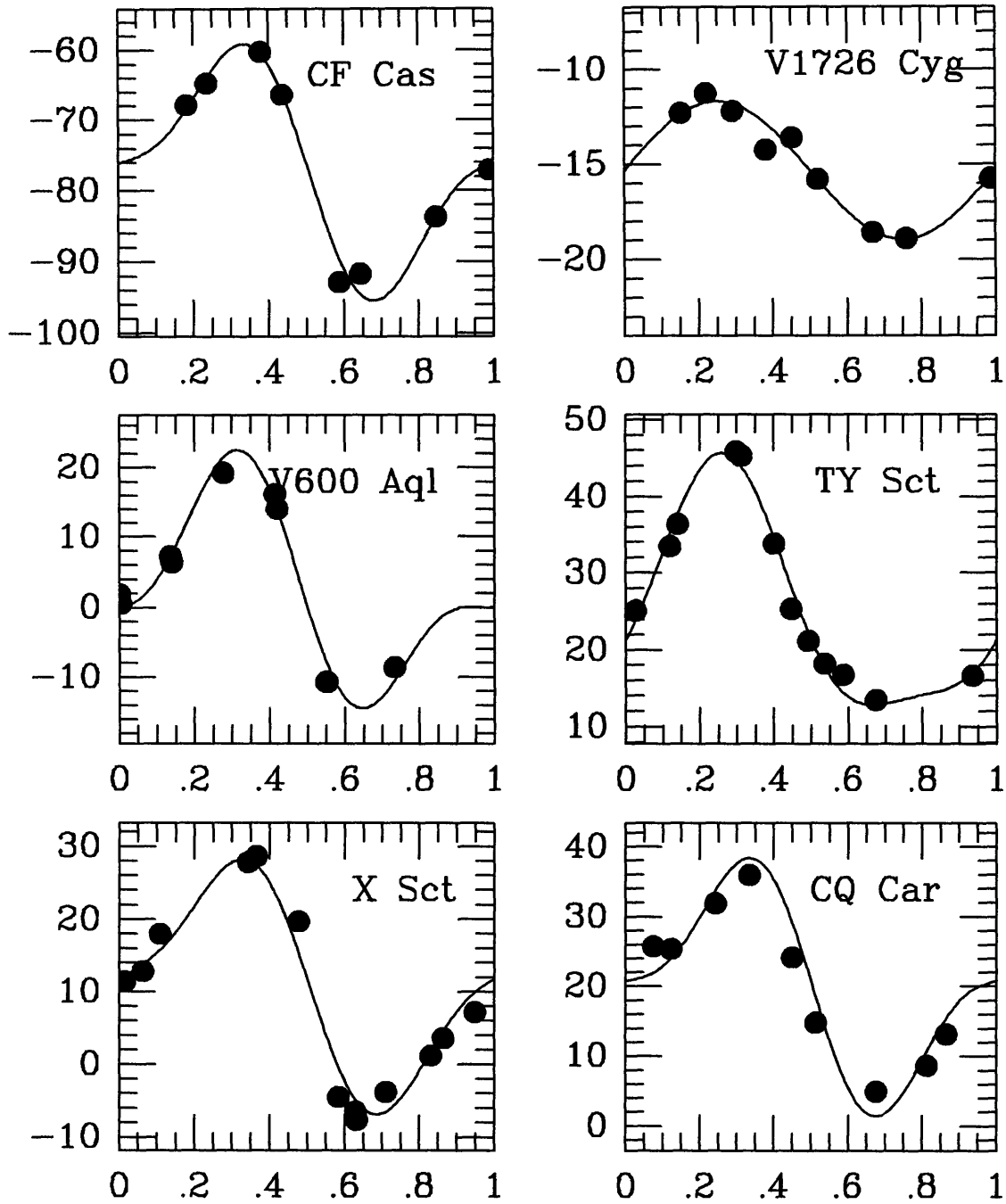
Figure 2-13: Velocity data and best-fit curves for well-sampled Cepheids. The abscissa shows the phase, and the ordinate radial velocity in km s⁻¹.
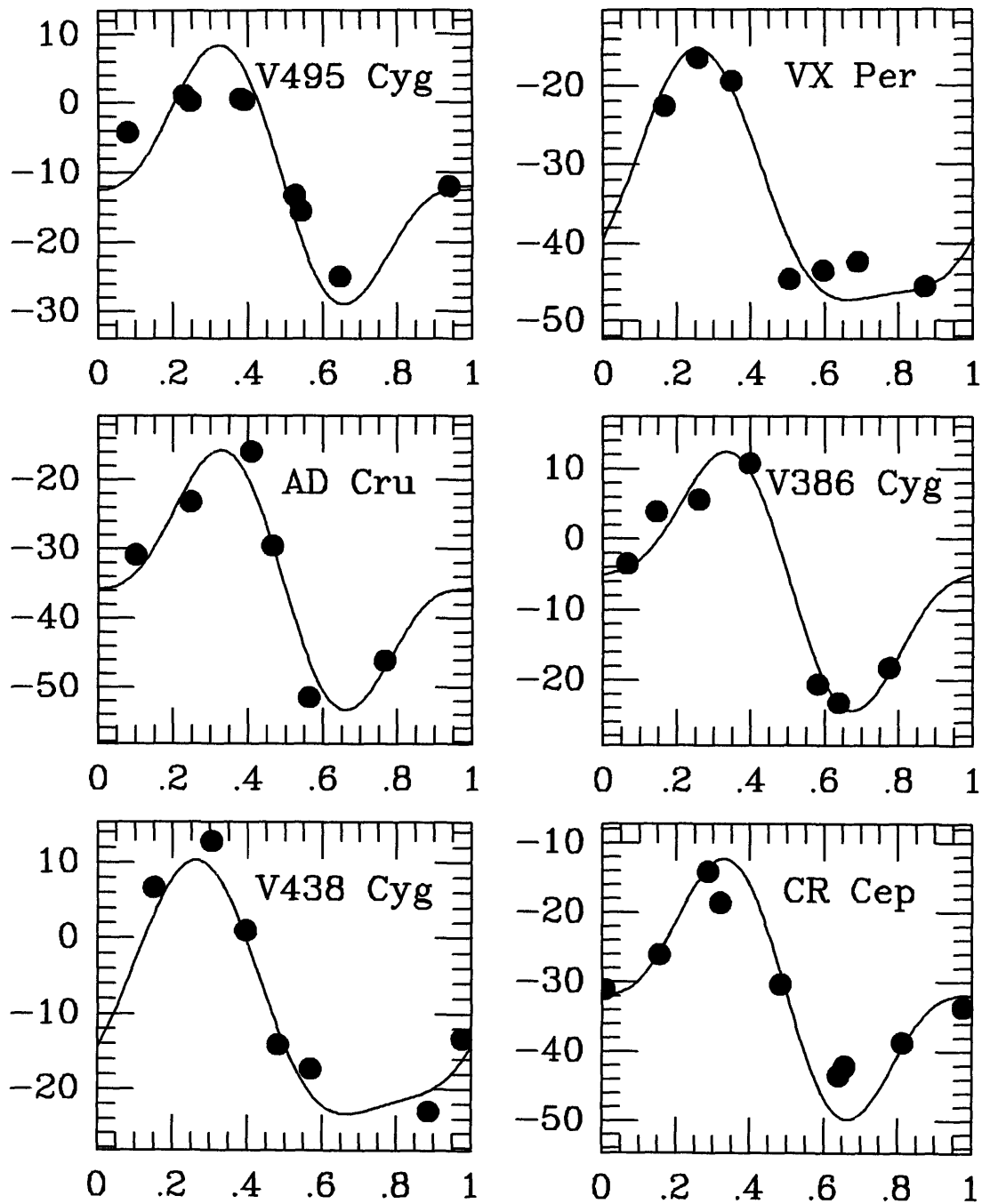
Figure 2-14: Cepheid data and velocity curves for which the χ^2 of the fit is greater than 20 and the Monte Carlo error in γ is less than 1 km s^{-1}.
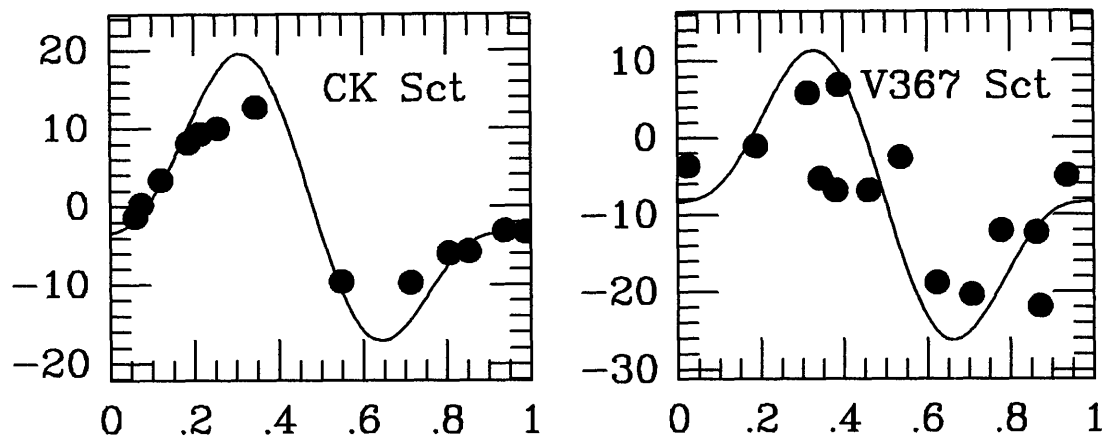
Figure 2-14: Continued

for R_{21}; and 0.6 and 0.7 radians for ϕ_{21}. The two values for each parameter represent the fits for $P < 10$ d and $P > 10$ d, respectively. For each Cepheid, 1000 velocity curves were generated with random Fourier coefficients, Gaussian about the values determined from the period, and uniform random phase. The curves were "observed" at the same intervals as the true observations with 1.0 km s^{-1} noise and fit using the same procedure as the actual data. The spread of the gamma velocities so determined is given in the σ_{MC} column of Table 2.6. These results show that for Cepheids with good phase coverage, γ velocities can be determined to better than 1 km s^{-1} with only 6 or 7 observations.

The error in the γ velocities was heavily dependent on the extent of the phase coverage, as expected. No systematic errors were uncovered in the Monte Carlo analysis; however, with incomplete phase coverage the distribution errors tended to be significantly non-Gaussian, even distinctly bimodal in extreme cases. This is because of the ambiguity in the phase of the fitted curve when the phase coverage is incomplete: the data may fit equally well to various parts of the velocity curve. One way to avoid this could be to use phase information from the light curves to fix an approximate phase to the pulsation velocity. This does not completely solve the problem, though, because even with the phase fixed the γ velocity determined is increasingly sensitive to uncertainty in A_1 as the phase coverage becomes more incomplete. The error analysis also assumes that the periods used for folding the Cepheid velocities are correct.

49

One way to perform a check would be to compare the epochs given for each Cepheid with the epochs we measure in the velocities. A comparison of the epochs given in Moffett and Barnes (1985), for the Cepheids in common, with the epochs of our fit velocity curves (assuming minimum velocity is at the same epoch as maximum light) shows good agreement. Fortunately, even for a Cepheid with its period determined to only 1 percent, errors in the phase will be small since our two runs were less than 60 days apart—the only significant effect on fitting the velocity curve would be if the period were not known well enough to obtain the *phase* of the folded velocities, which is not the case for the Cepheids considered here.

Some Cepheids have velocity curves very dissimilar to the ones we generate. Three of our Cepheids are "s" Cepheids: EV Sct, V532 Cyg, and V1726 Cyg. The s-Cepheids are anomalous in that they have low amplitude, sinusoidal light and velocity curves. To find γ velocities for these three, we fixed R_{21} at zero and allowed the three parameters A_0, t_0, and A_1 to vary, which is simply fitting a sine wave to the velocities. The curve fit to V1726 Cyg is shown in Figure 2-13. The Cepheid V367 Sct is a double-mode pulsator; its velocity measurements are shown in Figure 2-14 along with the generated velocity curve fit to the points. We found γ velocities using both the fundamental mode period, 6.2933 d, and the first overtone period, 4.3837 d (Mermilliod *et al.* 1987). In both cases the γ velocity is poorly constrained— the data do not fit the generated velocity curves well, and we do not know how to generate appropriate Fourier coefficients for a double-mode pulsator. Other Cepheid velocity curves having a large χ^2 are shown in Figure 2-14. Though the curve shape is somewhat different from the true velocities, the Monte Carlo analysis suggests that the errors in the γ velocities are less than 1 km s^{-1}. However, the actual data do not necessarily constrain γ as well in the fit, therefore the error should be taken to be the larger of σ_{fit} and σ_{MC}.

We cannot generate appropriate Fourier coefficients for GY Sge and II Car because of their long periods of 51 and 64 days. As an approximation we used coefficients similar to the longest period Cepheids for which we have data. Both also have poor phase coverage, adding additional uncertainty to the γ velocities we determine. Our
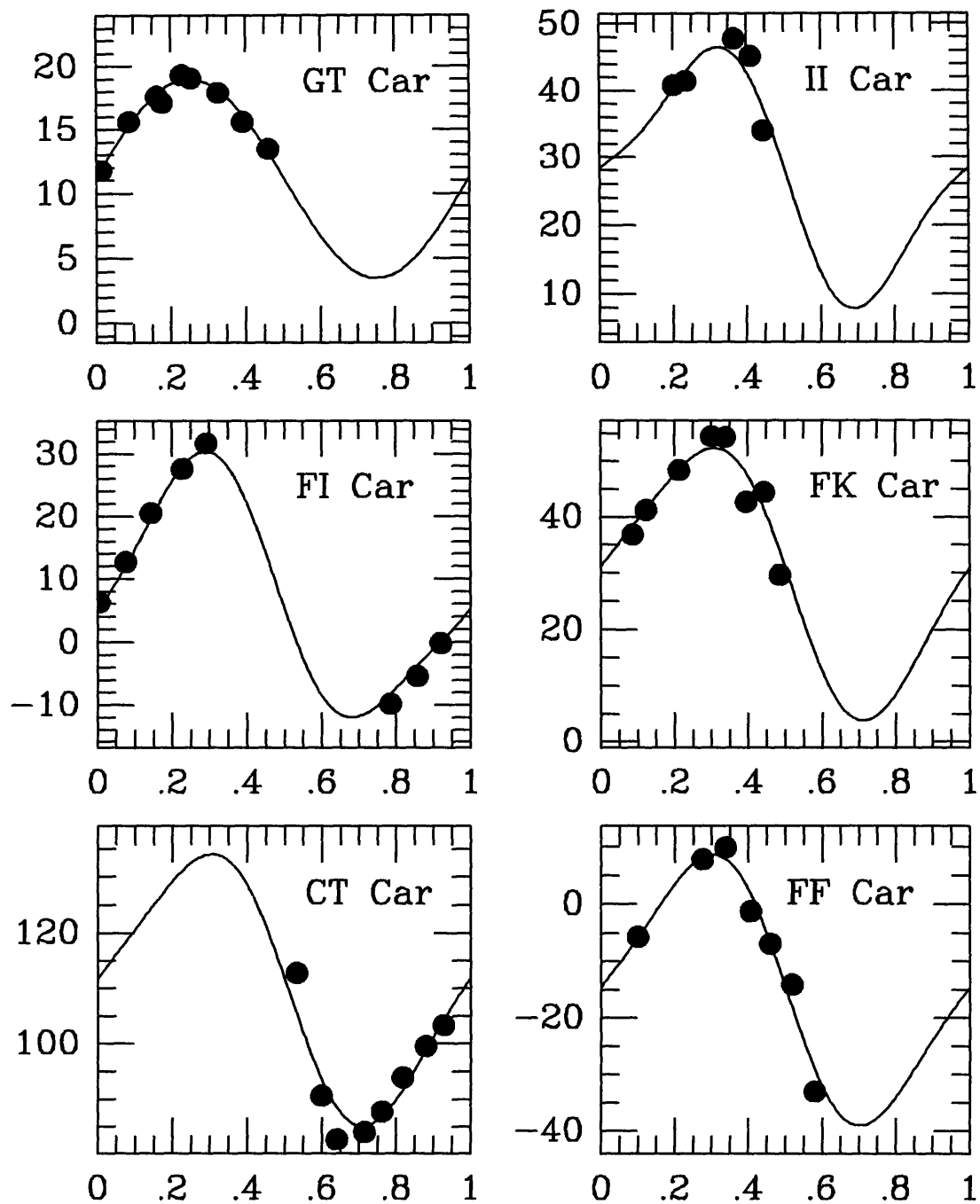
Figure 2-15: Velocity data and curves for Cepheids with poor phase coverage. Monte Carlo error estimates for these Cepheids are all greater than 2 km s^{-1}.
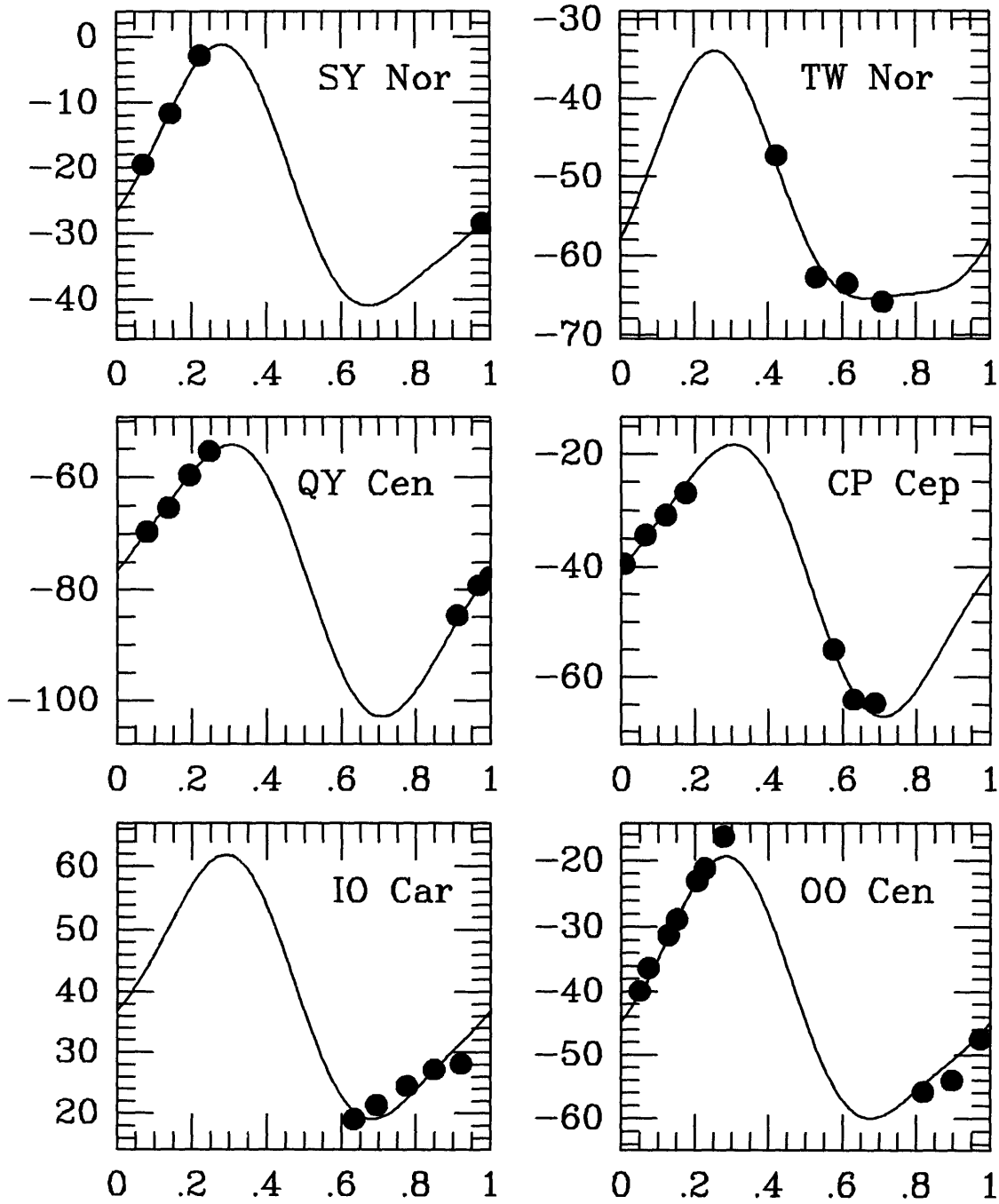
Figure 2-15: Continued
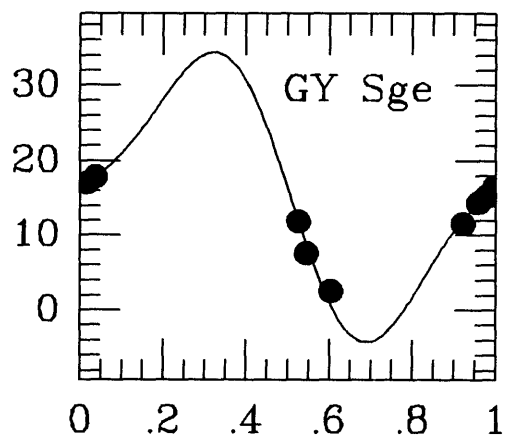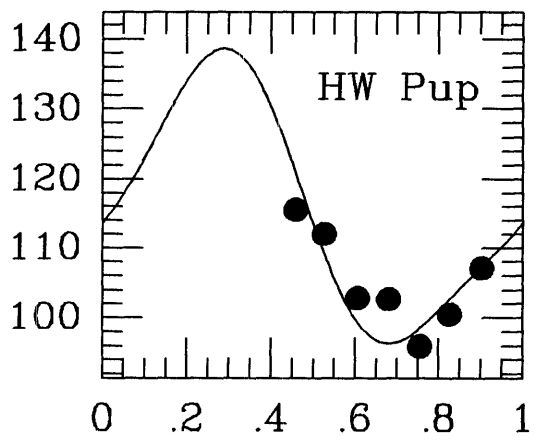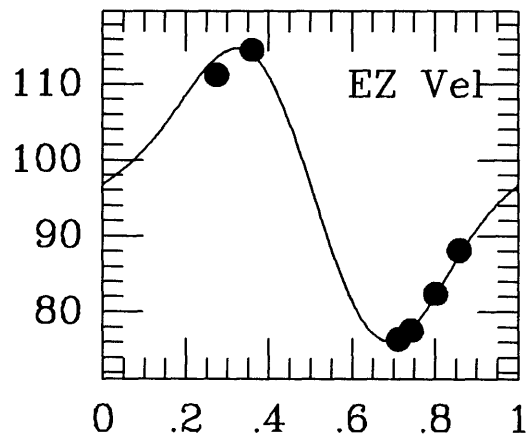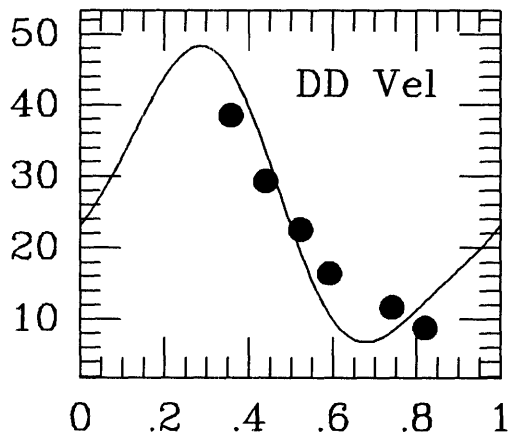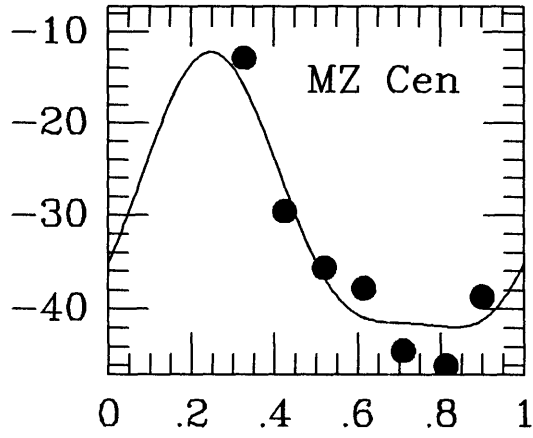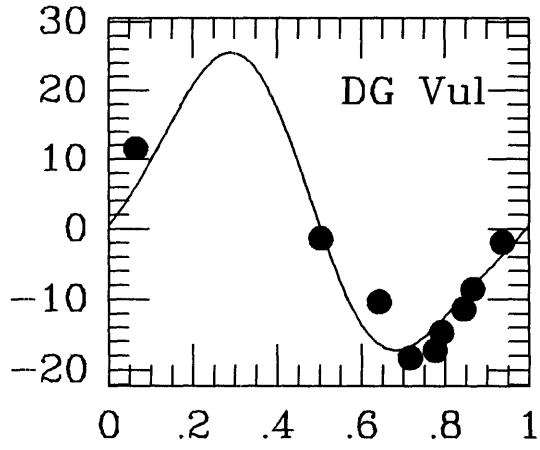
Figure 2-15: Continued
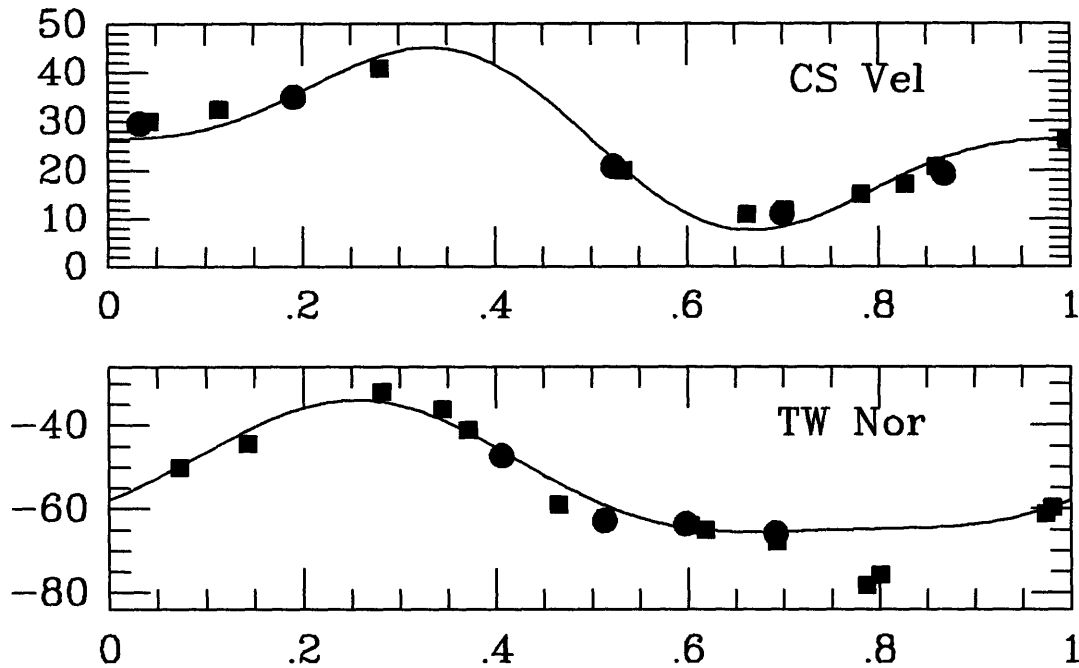
Figure 2-16: Comparison of velocities for two Cepheids. Data from Mermilliod *et al.* (1987) are plotted as squares, and our velocities as circles. The curves plotted were fitted using the circles only.

velocities and fit curves for these two Cepheids are shown in Figure 2-15, along with other Cepheids having poor phase coverage.

2.4.2 Discussion

We can compare our radial velocity measurements from §2.3 and our γ velocities from §2.4.1 to those from other sources where data exist. Figure 2-16 shows radial velocities of CS Vel and TW Nor from Mermilliod, Mayor, & Burki (1987) plotted together with velocities from §2.3. The Mermilliod *et al.* (1987) velocities were measured with CORAVEL, so for comparison the same zero point correction made to our velocities has been applied to theirs in Figure 2-16. The velocity curves, fit using only our data, are shown with the velocities in Figure 2-16. The additional CS Vel data agree well with our fit curve, though the curve amplitude is somewhat too high. The curve generated for TW Nor, however, does not reproduce the dip near phase 0.8 shown by the Mermilliod *et al.* data. This is a result of the truncation of the Fourier series—

Table 2.7: Gamma Velocity Comparison

Cepheid	γ	σ_γ	γ_s	σ_s	Source
V386 Cyg	-5.6	1.3	-5.1	1.0	MB
TW Nor	-53.3	3.8	-56.1	0.2	MMB
VX Per	-35.2	1.4	-35.3	1.0	MB
EV Sct	16.7	0.4	17.9	0.2	MMB
V367 Sct	-7.7	2.1	-8.0	0.4	MMB
CS Vel	26.8	1.1	26.4	0.2	MMB

Table 2.8: Gamma Velocities from MMB Data

Cepheid	γ	σ_γ	γ_{MMB}	σ_{MMB}
EV Sct	17.5	0.3	17.5	0.3
CS Vel	26.9	0.8	26.0	0.2
U Sgr	2.4	0.3	2.6	0.1
S Nor	6.2	0.4	5.9	0.1
TW Nor	-56.1	1.3	-56.6	0.2
V340 Nor	-39.9	0.2	-40.1	0.1

TW Nor is one of the few Cepheids which has $R_{31} > R_{21}$ in Kovács *et al.* (1990). Fitting our generated velocity curve to the combined data set gives a γ velocity of -55.2 ± 0.9 km s^{-1}, while allowing all of our parameters (t_0, γ, A_1, R_{21}, and ϕ_{21}) to vary gives a γ velocity of -55.1 ± 0.8 km s^{-1}. These values are consistent with the value of -56.1 ± 0.2 found by Mermilliod *et al.* and with the value we determine from our data (to within the quoted Monte Carlo error), indicating that γ is not especially sensitive to the curve mismatch.

Table 2.7 shows a comparison of γ velocities from Moffet and Barnes (1987, MB) and Mermilliod *et al.* (1987, MMB) with §2.3 velocities. MMB velocities were adjusted to our adopted zero point relative to CORAVEL. The only significantly different velocities are those of EV Sct; using a combination of MMB and §2.3 velocities in the fit gives a γ velocity of 17.4 km s^{-1}. Coker *et al.* (1989) report a γ velocity for VX Per of -35.4 ± 0.1, consistent with our value of -35.2 ± 1.4. We have also used the method of §2.4.1 on the MMB velocity data as a comparison of the different methods of determining γ. Results are given in Table 2.8, where γ is determined with the §2.4.1 method, σ_γ is the formal error of the fit, and γ_{MMB} and σ_{MMB} are taken from

Mermilliod *et al.* (Table 2.8 velocities have not been adjusted to our zero point). The γ velocities computed with the different methods show fairly good agreement, in each case to within the reported error. Note, however, that our uncertainties tend to be larger than those of Mermilliod *et al.*.

The new γ velocities were merged with the data from Caldwell & Coulson (1987) and used in a rotation curve model (see §2.6). Reddenings from Fernie (1990) were used when available, though a substantial fraction of the Cepheids in this paper lacked them: of the 58 Cepheids with new velocities, only 31 had available reddenings. Velocities for 13 of these were previously reported in Caldwell & Coulson and used in their model. Several have discrepancies of more than 10 km s^{-1}: DL Cas, SY Nor, UY Per, TY Sct, UZ Sct, and V367 Sct. The difference between the DL Cas velocities is likely due to its binary orbit. V367 Sct is a double-mode pulsator not well modelled by our constructed velocity curve, but the difference seems too large to account for in this manner. SY Nor has poor period coverage and a large Monte Carlo error estimate, which could account for the velocity discrepancy. Differences in the other three may be due to the lack of sufficient velocities available to Caldwell & Coulson for computing a γ velocity.

Results from the model were encouraging: uncertainties in several of the model parameters have been significantly reduced. In the Caldwell & Coulson (1987) model, the error in the determination of the distance to the Galactic center was 9%, and MCMS velocities reduced this to 8%. With the addition of the new γ velocities from this paper (those with reddenings only), the uncertainty decreased to 7% (see §2.6). If good color excesses were available for the remaining Cepheids with new velocities, we estimate the uncertainty could be reduced to as low as 5%. Other additional observations can help push down the uncertainty in the model parameters. New Cepheids at large distances from the Sun in the directions $\ell = 60°$ and $\ell = 300°$ have good leverage in determining R_0. Infrared photometry may decrease the uncertainties in distances to the Cepheids—infrared magnitudes are less affected by obscuration, and the infrared period-luminosity relations have smaller scatter and are less sensitive to metallicity (Hindsley & Bell 1990).

With only a few velocity measurements well distributed in phase, good γ velocities can be determined by fitting an expected velocity curve to the data. Much of the error in this approach arises from the uncertainty in the Fourier coefficients used to generate the velocity curve. Fourier coefficients for additional well sampled long-period Cepheids are needed. Further accurate radial velocities will allow better determination of the Fourier coefficients, reducing the scatter and allowing the use of higher order coefficients to generate the fit curve. One might also reduce the scatter by using properties of the light curve, obtainable from relatively inexpensive photometry, to constrain the selected Fourier parameters. This method will still be limited by intrinsic variations between different Cepheids; if a large number of velocity measurements are available for a particular Cepheid, other methods are better suited to determining the γ velocity. However, for faint Cepheids (especially those in other galaxies) that require extremely long exposures to obtain velocities, fitting a small number of velocities to an expected curve should prove effective.

2.5 Radial Velocities of Newly Discovered Cepheids

Caldwell, Keane, and Schechter (1991) conducted a search for distant Milky Way Cepheids near $\ell = 300°$ in an area covering 9.4 square degrees. From over 2000 identified variable stars, 37 were chosen as promising Cepheid candidates. To help confirm these candidates as Cepheids, and to obtain radial velocities for the Cepheids for use in kinematic models, we obtained spectra for many of the candidates in February 1991 at Las Campanas.

To help select the most promising candidates for frequent observation, we made use of preliminary data from multi-band followup photometry conducted using the Swope telescope at Las Campanas and the 1m telescope at the South African Astronomical Observatory (see Avruch 1991). We were able to make use of the I-band data from both the new observations and the original survey data, as well as new V-band observations that provide color information at different pulsational phases. Since Cepheids have a characteristic color change over the course of pulsation (see

Chapter 3), we ranked the candidates for observation based on the slope of dV/dI as well as the appearance of the I-band light curve.

2.5.1 Observations and Data Reduction

Spectra of the candidates were taken with the Modular Spectrograph on the DuPont 2.5m telescope at Las Campanas during the nights of 25 February through 2 March 1991. We used the spectrograph in a cross-dispersed mode with a 150 ℓ/mm immersion grating and a 300 ℓ/mm grism cross-disperser, projected onto a TI 800×800 CCD. We initially started with a 58 ℓ/mm immersion grating; however, the total throughput was too low to complete our observations each night. We placed shims under the primary disperser to place orders 14–25 onto the CCD, providing coverage from 5000–8700 Å. We used a 1.0 arcsec slit throughout the run, which projected to 2.2 pixels on the detector at 8400 Å giving an effective resolution of 60 km s^{-1}. Calibration frames were taken after each stellar spectrum using He-Ne and Fe-Ar lamps.

The data reduction was conducted using a slightly modified version of the software described in §2.2. Each spectrum was flattened using an incandescent lamp exposure, and strong cosmic ray events were removed. Calibration lines from the associated lamp exposures were identified and centroided using a modified version of DoPHOT (Mateo and Schechter 1989), and fit across orders with a fifth-order 2-dimensional Legendre polynomial. The high-order coefficients were fixed using a long lamp exposure that yielded over 300 identified lines, and the 4 lowest-order coefficients were fit to each calibration frame, which typically had 100 available lines. Each stellar spectrum was rebinned in log-λ according to the calibration, and each order was separately extracted and sky-subtracted.

During the course of the reduction, we noticed that the spectrum was shifting between two positions on the chip throughout the observing run. The shift was aligned in the direction of the cross-dispersion, and it is possible that the grism was not well secured, flopping between two positions. Figure 2-17 shows the position of the spectrum on the chip as a function of telescope hour angle, from which it is clear
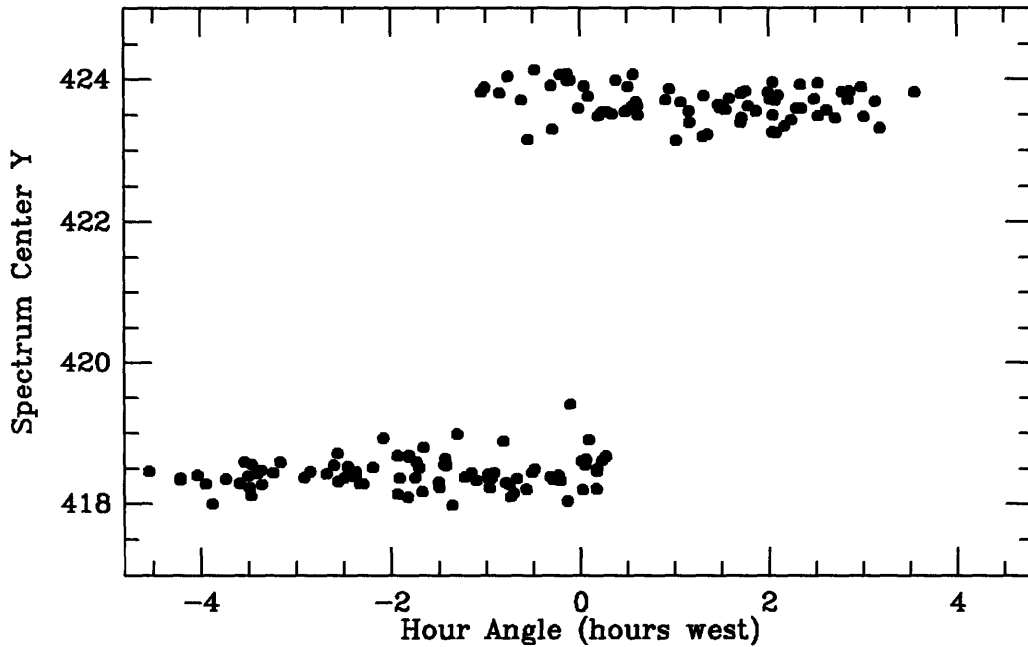
Figure 2-17: The pixel location of the center of the spectrum, along the cross-dispersed direction, plotted as a function of telescope hour angle. A significant shift is seen near the meridian (with some hysteresis), possibly caused by motion of the grism.

that the flop occurs near the meridian. To account for the shift in the data reduction, each spectrum and its associated calibration spectrum was classified into a "high" or "low" group. Separate flats and high-order wavelength calibrations were made for each group and the associated frames were reduced within its group. Three frames that encountered a shift during an exposure were discarded.

A velocity for each spectrum was calculated relative to a high signal-to-noise spectrum of HD 83443 using the Fourier quotient technique of Sargent *et al.* (1977). Several of the Cepheid candidates were too heavily reddened to provide an adequate signal for radial velocities using the blue orders, so we decided to use the Ca triplet (8498, 8542, 8662 Å) in order 14 to measure the individual velocities. Several CORAVEL faint southern radial velocity standards (Maurice *et al.* 1984) were observed throughout the run, and were used to calibrate the effective velocity of the template spectrum. The individual measurements of the standards (given as the corresponding template velocity, as in §2.2) are shown in Figure 2-18. The open and filled points correspond to
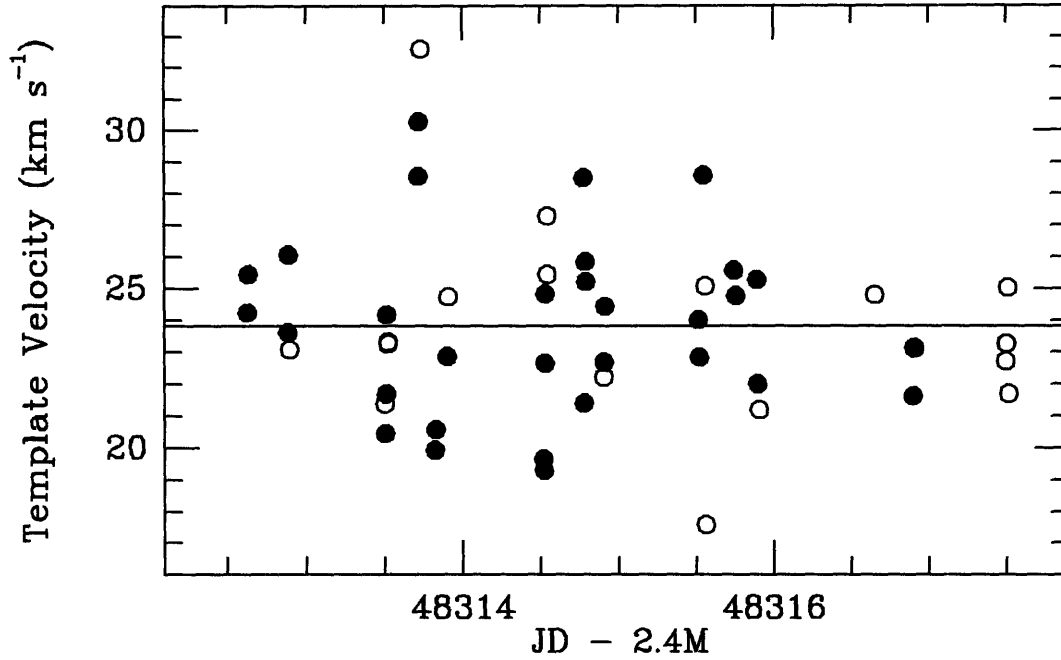
Figure 2-18: Velocities of the template calculated from spectra of radial velocity standards. The open and filled points correspond to velocities measured from the two different locations of the spectrum on the chip; the error of each measurement is typically 2.7 km s^{-1}. The solid line shows the adopted mean velocity for the template.

Table 2.9: Radial Velocity Standards, Feb 91

Star	V_r	ε_f	ε_V	n
HD 24331	26.6	1.7	1.3	3
HD 39194	16.4	1.7	0.8	4
HD 48381	40.1	1.5	0.5	4
HD 83443	27.4	1.2	0.7	6
HD 83516	43.3	1.2	1.5	7
HD 101266	21.5	1.3	1.5	6
HD 111417	-18.9	1.2	0.8	7
HD 176047	-41.5	1.3	0.6	5
CPD -43° 2527	19.3	1.3	1.2	5
HD 74000	205.5	4.6	1.6	4
HD 140283	-171.2	3.2	3.6	3

the low and high position measurements. The means of the velocities from the two groups are not significantly different, which confirms that the two groups of spectra are calibrated to the same zero point. Table 2.9 shows the mean measured velocities for each radial velocity standard, along with velocities for two metal-weak subdwarfs observed during the run. Each velocity has been adjusted upward by 0.4 km s^{-1} to bring these velocities to the same zero point as that of §2.2 and §2.3. Also as in these two sections, two error estimates are given: ε_f is the formal error in the velocity from the Fourier quotient, and ε_V gives the standard error of the mean of the individual measurements. The number of individual measurements in for each star is shown in the last column.

The individual radial velocities for the stars confirmed as Cepheids are given in Table 2.10. The other variables did not have spectra consistent with that of a Cepheid, and most did not have significant Ca triplet absorption lines and thus did not yield radial velocities. One star thought to be a Cepheid from its light curve (11582-6204), but suspect due to its near-infrared photometry (Schechter et al. 1992), is confirmed to be something other than a Cepheid based on its spectrum.

2.5.2 Gamma Velocities

Gamma velocities were computed for each of the Cepheids according to the method of §2.4.1. As before, the shape of the velocity curve is fixed by the photometrically determined period of the Cepheid; periods used for these stars were found by Avruch (1991). The γ velocity and phase are then fit using a χ^2 minimization procedure. The radial velocities for each star and the curves fit to the points are shown in Figure 2-19. Fit γ velocities, formal fit errors, Monte Carlo simulation errors, and reduced χ^2 values for eight Cepheids are given in Table 2.11.

Table 2.10: Cepheid Radial Velocities, Feb 91

JD -2400000	V_r km s^{-1}	σ	JD -2400000	V_r km s^{-1}	σ
11447-6153			12003-6213		
48312.748	23.8	4.0	48312.730	-3.9	4.1
48313.649	31.0	3.6	48313.754	-12.3	3.8
48314.661	42.8	3.2	48314.770	-3.5	3.4
48315.651	52.0	4.3	48315.728	11.8	4.1
48316.726	11.3	5.3	48316.806	24.5	3.4
48317.612	13.9	5.2	48317.709	20.0	4.6
11465-6209			13190-6235		
48312.679	-12.4	5.7	48312.794	-35.4	3.8
48313.581	-13.9	4.6	48313.812	-22.6	4.0
48314.598	-2.7	3.0	48314.820	-14.2	3.1
48315.606	-15.4	4.4	48315.817	-8.5	4.3
48316.676	-18.5	4.0	48316.877	-24.5	4.3
48317.577	-0.4	3.5	48317.770	-45.4	4.7
11492-6257			13240-6245		
48312.847	10.2	7.3	48313.765	-7.5	3.7
48313.682	-6.1	4.3	48314.831	-9.4	3.8
48314.742	4.8	5.6	48315.880	-26.6	5.0
48315.712	20.0	6.6	48316.830	-32.2	5.7
48316.757	-6.7	5.2			
48317.676	-3.1	4.6			
11521-6200			13323-6224		
48312.693	31.4	4.4	48313.782	-39.7	4.8
48313.596	4.4	3.9	48314.851	-54.9	4.9
48314.695	12.6	3.6	48315.869	-53.3	4.5
48315.620	14.1	4.9	48316.847	-41.9	3.7
48316.701	19.9	3.1	48317.799	-37.2	4.5
48317.638	26.0	3.9			
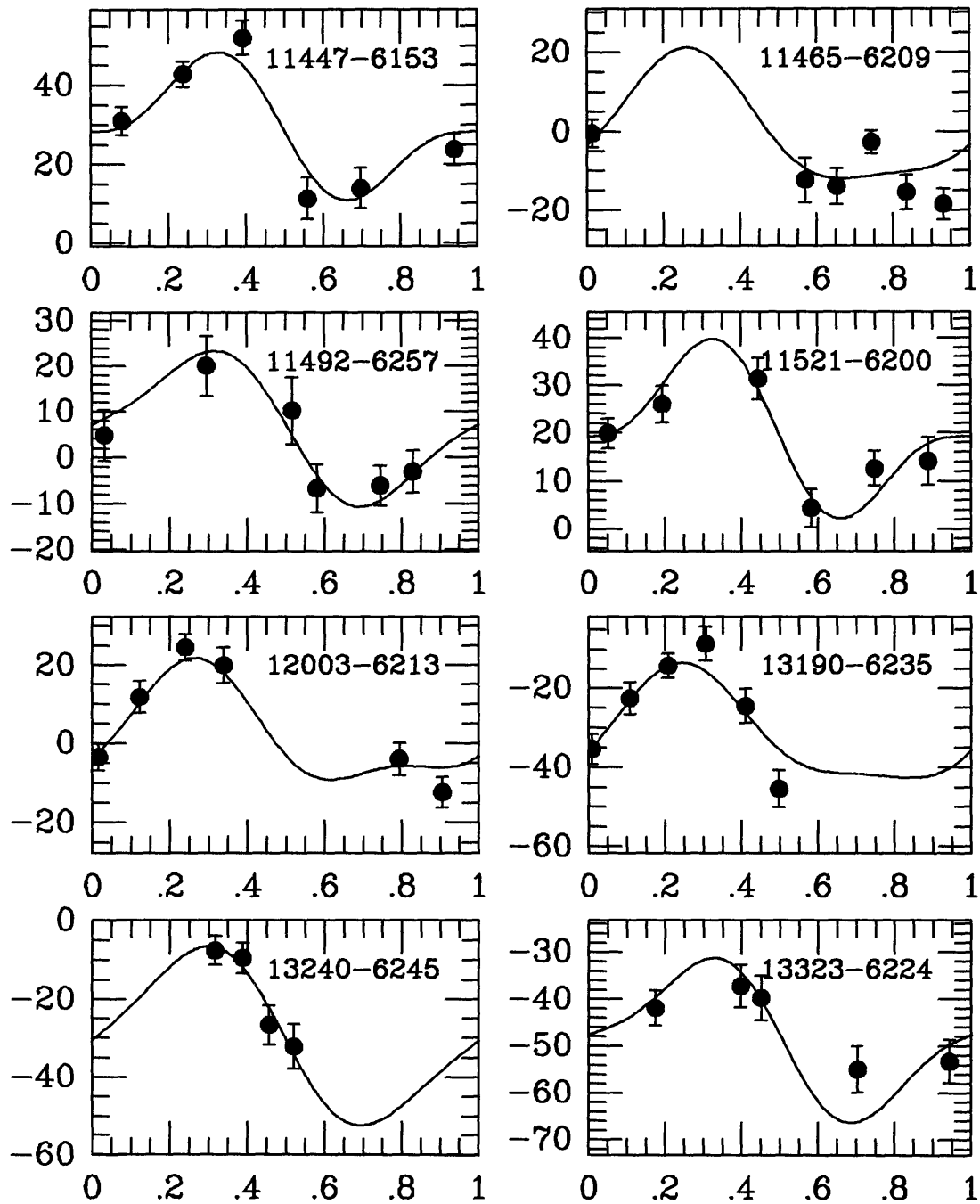
Figure 2-19: Radial velocity curves for the newly discovered Cepheids, along with CKS designations. The curve shape was determined from the period, and its position in phase and γ velocity were fit to the radial velocities shown.

Table 2.11: Gamma Velocities of New Cepheids

Cepheid	γ	σ_{fit}	σ_{MC}	χ^2_ν	Period[a]
11447-6153	29.1	2.0	1.9	1.5	6.4282
11465-6209	0.9:	4.0	3.8	4.4	11.0984
11492-6257	6.7	1.6	2.5	0.5	3.6798
11521-6200	20.4	1.7	1.7	1.2	6.6039
12003-6213	2.3	1.8	2.2	1.1	9.1266
13190-6235	-31.7	2.2	3.2	1.9	10.1576
13240-6245	-29.9:	3.3	8.6	0.6	15.0598
13323-6224	-48.3	3.0	2.1	2.2	4.2424

[a] Avruch (1991).

2.6 Rotation Models

The models we use to derive parameters of Galactic rotation, in particular the distance to the Galactic center, R_0, are based on a linear, axisymmetric rotation curve in a manner similar to Caldwell & Coulson (1987, hereafter CC). Figure 2-20 shows a geometric picture of a star with rotation speed Θ at a distance D from the Sun, which rotates with speed Θ_0. The star lies at a distance R from the center of the galaxy. For our models we assume that the height above the disk, $|z| = D|\sin b|$, is sufficiently small that the potential is dominated by the disk, and therefore a thin-disk model adequately represents the orbits (i.e. the primarily rotational orbits of the stars are decoupled from their vertical motion). For the Cepheid population, this is essentially guaranteed as they are confined to the disk with a scale heght of 70 pc (Kraft & Schmidt 1963). The radial velocity of a star as measured from the Sun, corrected to the local standard of rest and neglecting random motion, is then (cf. Mihalas & Binney 1981, eq. 8-1)

$$v_r^* = -\Theta_0 \sin \ell \cos b + \Theta \sin \alpha \cos b.$$

Defining $d \equiv D/R_0$ and $r \equiv R/R_0$, the law of sines gives

$$v_r^* = \left(\frac{\Theta}{r} - \Theta_0\right) \sin \ell \cos b.$$

64

If we make the approximation that the rotation curve is linear, i.e. that

$$\Theta(R) \approx \Theta_0 + (R - R_0)\left(\frac{d\Theta}{dR}\right)_{R_0} = \Theta_0 + (r - 1)\left(\frac{d\Theta}{dr}\right)_{r=1},$$

then the radial velocity is given by

$$v_r^* = \left(1 - \frac{1}{r}\right)\left[\left(\frac{d\Theta}{dr}\right)_{r=1} - \Theta_0\right]\sin\ell\cos b. \qquad (2.2)$$

Using the definition of Oort's A constant,

$$A \equiv \frac{1}{2}\left[\frac{\Theta_0}{R_0} - \left(\frac{d\Theta}{dR}\right)_{R_0}\right],$$

equation 2.2 can be rewritten as

$$v_r^* = -2AR_0\left(1 - \frac{1}{r}\right)\sin\ell\cos b. \qquad (2.3)$$

The transformation of the heliocentric distance d (in units of R_0) to the Galactocentric distance r is given by

$$r^2 = 1 + d^2 - 2d\cos\ell. \qquad (2.4)$$

Additional parameters were included in the model to reflect the Sun's peculiar motion with respect to the LSR (u_0, v_0, w_0), and to compensate for a possible zero-point offset (δv_r). The form of the model equation for a measured heliocentric radial velocity is then

$$\begin{aligned}
v_r = \ & -2AR_0\left(1 - \frac{1}{r}\right)\sin\ell\cos b \\
& + u_0\cos\ell\cos b \\
& - v_0\sin\ell\cos b \\
& - w_0\sin b - \delta v_r.
\end{aligned} \qquad (2.5)$$

Note that the sign of u_0 follows a Galactic radial convention and is opposite that used by CC.

Distances to the Cepheids were computed primarily via the period-luminosity relation in the V-band (PL-V), which can be parameterized

$$5 \log_{10} d = m - m_0 - \alpha(\log P - 1) \,. \tag{2.6}$$

Here m_0 corresponds to the unreddened apparent magnitude of a Cepheid with a 10-day period at a distance of R_0, and α is the slope of the adopted period-luminosity relation. The measured period and unreddened apparent magnitude for a particular Cepheid are given by P and m, respectively. The stars were dereddened as in CC, using the prescription for R_V derived from Olson (1975) and Turner (1976):

$$R_V \equiv A_V/E(B - V) = 3.07 + 0.28(B - V)_0 + 0.04E(B - V) \,,$$

whereby

$$m = \langle V \rangle - R_V \times E(B - V) \,.$$

This extinction correction is also used by Laney & Stobie (1993), and has a slightly higher value for the effective R_V than the reddening laws of Savage & Mathis (1979) and Rieke & Lebofsky (1985) (though the last two do not give an explicit dependence on intrinsic color). The dependence of R_V on the intrinsic color is caused by the shift in effective wavelength of the filters when measuring stars of different spectral class (Olson 1975). Extinction corrections for infrared photometry are handled separately and are described below.

We chose to avoid period-luminosity-color (PLC) relations and terms accounting for metallicity for two reasons. First, the PL-V relation is thought to be only weakly sensitive to metallicity, both in zero-point and slope (Iben & Renzini 1984, Freedman & Madore 1990; but see also Caldwell & Coulson 1986), and significantly less sensitive to metallicity than the PLC relation (Stothers 1988). Second, there is a problem when the PLC relation is used to derive distances to Cepheids dereddened using color excesses. By making a correction based on color, one must make some implicit assumption about the intrinsic color of the star; any difference between this

assumption and the actual color (perhaps due to metallicity) is amplified in the derived unreddened magnitude. This process can significantly increase the sensitivity of PLC distances to metallicity. The uncertainties in the reddening corrections themselves tend to be significantly larger than the effect of metallicity on the PL-V relation over a wide range of metal abundance (Stothers 1988); given this and the uncertainty in the slope of the PLC color term (Fernie & McGonegal 1983, Caldwell & Coulson 1986), we chose to use only PL relations (PL-V, plus the PL-K relation for some of the models below) with no explicit correction for a radial metallicity gradient.

2.6.1 Models and Data Sets

The data were fit to the models using a non-linear χ^2 minimization program. The model has parameters $2AR_0$, m_0, α, u_0, v_0, w_0, and δv_r; α was fixed according to the PL relation adopted and w_0 was fixed at 7 km s^{-1} (Delhaye 1965) as it is neither constrained by the data nor does it significantly affect the model, since b is small for most of the sample. The rest of the parameters were determined by fitting the measured radial velocities for each Cepheid to model velocities generated from the other measured quantities (ℓ, b, $\langle V \rangle$, P, and $E(B-V)$) via equation 2.5. Each measured velocity was weighted as in CC using the estimated radial velocity dispersion added in quadrature to the effective velocity error introduced by the distance measurement:

$$\sigma_i^2 = \sigma_v^2 + \sigma_d^2 (\partial v_r / \partial d)^2 . \tag{2.7}$$

The dispersion in the radial velocities is a combination of measurement error and the intrinsic velocity dispersion of the stars in the disk (the latter dominating), and was taken to be $\sigma_v = 11$ km s^{-1}. The error in distance from all sources (measurement, extinction correction, and PL dispersion), σ_d, was assumed to be 0.2 mag.

The model parameters were fit using several sets of data. We started with the data used by CC for their models, kindly provided in machine-readable form by J. Caldwell; this set contains 184 stars. A second data set was generated by incorporating reddenings by Fernie (1990, hereafter F90), updating velocities and adding

Table 2.12: Cepheid Data

Cepheid		ℓ	b	$v_r{}^{a,b}$	$\log P$	$\langle V \rangle^a$	E(B-V)^{a,c}
AQL	ETA	40.93	-13.07	-14.0	0.8559	3.897	0.140
AQL	U	52.32	-03.00	+9.0	0.8466	6.448	0.390
AQL	SZ	35.60	-02.34	+10.5	1.2342	8.603	0.658
AQL	TT	36.00	-03.13	+3.6	1.1385	7.131	0.505
AQL	FF	49.20	+06.37	-20.9	0.6504	5.372	0.202
AQL	FM	44.34	+00.90	-7.0	0.7863	8.271	0.633
AQL	FN	38.54	-03.11	+6.6	0.9769	8.382	0.509
AQL	V336	34.19	-02.13	+11.5	0.8636	9.861	0.636
AQL	V496	28.20	-07.12	+7.0	0.8330	7.720	0.403
AQL	V600	43.89	-02.62	3.1	0.8597	10.037	0.861
ARA	V340	335.19	-03.74	-83.4	1.3181	10.230	0.596
AUR	RT	183.14	+08.90	+18.8	0.5715	5.447	0.023
AUR	RX	165.77	-01.29	-23.3	1.0654	7.670	0.281
AUR	SY	164.74	+02.13	-3.5	1.0062	9.074	0.455
AUR	YZ	167.28	+00.93	-20.5	1.2599	10.378	0.583
CAM	RW	144.85	+03.79	-26.5	1.2152	8.690	0.664
CAM	RX	145.89	+04.70	-36.2	0.8983	7.682	0.563
CAM	TV	145.02	+06.14	-64.0	0.7239	11.707	0.626
CAR	L	283.20	-07.00	+1.9	1.5507	3.723	0.208
CAR	U	289.06	+00.05	+1.7	1.5889	6.281	0.323
CAR	V	275.25	-12.28	+13.1	0.8259	7.362	0.163
CAR	Y	285.68	-00.33	-14.1	0.5611	8.102	0.150
CAR	UX	284.78	+00.16	+7.0	0.5661	8.316	0.095
CAR	VY	286.55	+01.22	+2.0	1.2767	7.460	0.263
CAR	WZ	289.29	-01.18	-14.7	1.3620	9.255	0.409
CAR	XX	291.28	-04.88	-10.8	1.1962	9.331	0.363
CAR	XY	291.42	-03.86	-5.5	1.0947	9.294	0.424
CAR	XZ	290.29	-00.76	+1.6	1.2214	8.595	0.383
CAR	YZ	285.58	-01.39	+1.0	1.2592	8.712	0.414
CAR	AQ	285.77	-03.30	+2.1	0.9899	8.852	0.161
CAR	CN	283.56	-01.29	+9.0	0.6931	10.676	0.399
CAR	CR	285.67	-00.37	+25.0	0.9895	11.578	0.504
CAR	ER	290.08	+01.48	-20.1	0.8875	6.813	0.094
CAR	FI	287.78	+00.70	+7.9	1.1289	11.647	0.736
CAR	FO	290.53	-02.09	+3.8	1.0152	10.777	0.463
CAR	FR	291.09	+00.57	-7.3	1.0301	9.669	0.354
CAR	GI	290.26	+02.55	-20.6	0.6467	8.320	0.152
CAR	GZ	284.74	-01.95	-8.5	0.6190	10.239	0.443
CAR	IT	291.47	-01.11	-14.9	0.8773	8.092	0.186

Table 2.12—*Continued*

Cepheid		ℓ	b	v_r	$\log P$	$\langle V \rangle$	E(B-V)
CAS	RW	129.03	-04.58	-71.3	1.1700	9.238	0.432
CAS	RY	115.28	-03.25	-70.5	1.0841	9.944	0.656
CAS	SU	133.47	+08.51	-4.3	0.2899	5.970	0.240
CAS	SW	109.67	-01.61	-38.0	0.7357	9.705	0.477
CAS	SZ	134.83	-01.18	-41.0	1.1347	9.852	0.829
CAS	VV	130.36	-02.13	-50.5	0.7929	10.741	0.540
CAS	VW	124.63	-01.08	-58.5	0.7777	10.716	0.461
CAS	XY	122.75	-02.76	-42.0	0.6534	9.980	0.430
CAS	CF	116.58	-01.00	-76.9	0.6880	11.136	0.546
CAS	DD	116.77	+00.48	-69.5	0.9917	9.877	0.501
CAS	DL	120.26	-02.55	-38.1	0.9031	8.968	0.528
CAS	V636	127.50	+01.09	-24.9	0.9231	7.186	0.786
CEN	V	316.44	+03.31	-24.0	0.7399	6.816	0.273
CEN	TX	315.17	-00.60	-52.0	1.2328	10.530	1.075
CEN	UZ	294.95	-00.91	-11.9	0.5230	8.760	0.244
CEN	VW	307.56	-01.56	-30.8	1.1771	10.242	0.461
CEN	XX	309.46	+04.64	-18.0	1.0396	7.818	0.264
CEN	AZ	292.79	-00.20	-11.5	0.5066	8.635	0.128
CEN	BB	296.38	-00.72	-15.8	0.6018	10.146	0.370
CEN	BK	295.96	-01.04	-26.3	0.5016	10.063	0.371
CEN	KK	294.18	+02.71	-3.4	1.0857	11.500	0.649
CEN	KN	307.75	-02.10	-39.7	1.5320	9.855	0.963
CEN	MZ	305.37	-01.55	-30.6	1.0151	11.527	0.735
CEN	OO	306.88	-00.55	-41.5	1.1100	12.020	0.931
CEN	QY	311.90	+00.20	-77.3	1.2492	11.792	1.082
CEN	V339	313.48	-00.53	-22.2	0.9762	8.710	0.427
CEN	V378	306.11	+00.33	-16.5	0.8105	8.464	0.383
CEN	V381	310.84	+04.38	-31.8	0.7058	7.668	0.186
CEN	V419	292.06	+04.27	-15.2	0.7410	8.181	0.160
CEP	DELT	105.19	+00.53	-16.2	0.7297	3.954	0.075
CEP	CR	107.63	+00.33	-31.3	0.7947	9.654	0.745
CMA	RW	232.04	-03.82	+50.0	0.7581	11.146	0.529
CMA	RY	226.01	+00.27	+32.9	0.6701	8.110	0.227
CMA	SS	239.23	-04.21	+73.1	1.0919	9.939	0.556
CMA	TV	227.21	-02.37	+39.0	0.6693	10.561	0.562
CMA	TW	229.12	+00.12	+69.7	0.8448	9.561	0.348
CRU	R	299.63	+01.07	-16.5	0.7653	6.793	0.137
CRU	S	303.31	+04.44	-8.5	0.6712	6.563	0.142
CRU	T	299.44	+00.39	-10.0	0.8282	6.587	0.182

Table 2.12—*Continued*

Cepheid		ℓ	b	v_r	log P	$\langle V \rangle$	E(B-V)
CRU	X	302.28	+03.75	-25.0	0.7938	8.384	0.273
CRU	SU	299.21	-00.64	-28.0	1.1089	9.782	1.008
CRU	SV	296.82	-00.40	-15.4	0.8454	12.130	0.836
CRU	VX	300.88	+01.58	-28.3	1.0868	11.933	0.964
CRU	AD	298.45	+00.45	-34.5	0.8061	11.039	0.668
CRU	AG	301.67	+03.06	-8.5	0.5840	8.131	0.184
CRU	BG	300.42	+03.35	-20.3	0.5241	5.462	0.022
CYG	X	76.87	-04.26	+10.5	1.2145	6.390	0.303
CYG	SU	64.76	+02.51	-21.2	0.5850	6.862	0.069
CYG	SZ	84.44	+03.98	-12.1	1.1793	9.432	0.644
CYG	TX	84.35	-02.30	-17.4	1.1676	9.517	1.193
CYG	VX	82.17	-03.49	-18.0	1.3039	10.006	0.812
CYG	VY	82.89	-04.62	-11.9	0.8953	9.592	0.646
CYG	VZ	91.52	-08.51	-18.5	0.6870	8.958	0.269
CYG	BZ	84.80	+01.38	-13.2	1.0061	10.223	0.934
CYG	CD	71.07	+01.43	-11.6	1.2323	8.952	0.531
CYG	DT	76.54	-10.78	-1.6	0.3978	5.774	0.000
CYG	MW	70.92	-00.63	-16.4	0.7749	9.489	0.666
CYG	V386	85.52	-04.89	-5.6	0.7208	9.634	0.877
CYG	V402	74.14	+02.27	-12.7	0.6400	9.873	0.394
CYG	V459	90.46	+00.69	-20.7	0.8604	10.601	0.790
CYG	V532	88.95	-03.04	-15.3	0.5164	9.087	0.503
CYG	V1334	83.62	-07.95	-5.2	0.5228	5.885	-.105
DOR	BETA	271.74	-32.76	+6.1	0.9931	3.754	0.045
GEM	ZETA	195.74	+11.89	+6.0	1.0065	3.918	0.019
GEM	W	197.42	+03.37	-0.1	0.8984	6.948	0.277
GEM	RZ	187.72	-00.10	+13.9	0.7427	10.005	0.554
GEM	AA	184.59	+02.69	+9.5	1.0532	9.720	0.335
GEM	AD	193.27	+07.62	+45.0	0.5784	9.855	0.140
LAC	V	101.11	-05.34	-25.4	0.6975	8.936	0.337
LAC	X	92.02	-12.74	-28.9	0.7360	8.407	0.345
LAC	Y	101.24	-01.51	-22.0	0.6359	9.147	0.194
LAC	Z	105.76	-01.63	-35.0	1.0369	8.415	0.407
LAC	RR	105.64	-02.01	-39.1	0.8073	8.848	0.341
LAC	BG	92.97	-09.26	-18.6	0.7269	8.883	0.319
LUP	GH	324.95	+03.34	-16.1	0.9675	7.633	0.363
MON	T	203.63	-02.56	+28.8	1.4317	6.123	0.239
MON	SV	203.74	-03.68	+27.1	1.1828	8.252	0.262
MON	TX	214.14	-00.78	+51.0	0.9396	10.961	0.508

Table 2.12—*Continued*

Cepheid		ℓ	b	v_r	log P	$\langle V \rangle$	E(B-V)
MON	TZ	214.01	+01.28	+34.0	0.8709	10.763	0.433
MON	XX	215.52	-01.12	+64.5	0.7369	11.899	0.579
MON	AC	221.76	-01.86	+40.5	0.9039	10.037	0.503
MON	CV	208.56	-01.80	+18.9	0.7307	10.300	0.697
MUS	R	302.10	-06.54	+00.0	0.8756	6.317	0.113
MUS	S	299.64	-07.52	-2.5	0.9850	6.137	0.147
MUS	RT	296.53	-05.26	-5.5	0.4894	9.001	0.295
MUS	UU	296.82	-03.23	-17.0	1.0658	9.783	0.418
NOR	S	327.75	-05.39	+2.3	0.9892	6.414	0.189
NOR	U	325.64	-00.16	-21.8	1.1019	9.229	0.900
NOR	RS	329.08	-01.18	-40.5	0.7923	10.000	0.793
NOR	SY	327.50	-00.67	-23.1	1.1019	9.497	0.802
NOR	TW	330.36	+00.31	-53.3	1.0328	11.670	1.341
NOR	GU	330.54	-01.73	-24.5	0.5382	10.406	0.654
NOR	QZ	329.44	-02.12	-38.6	0.7300	8.866	0.249
NOR	V340	329.72	-02.27	-40.0	1.0526	8.370	0.320
OPH	Y	20.60	+10.13	-6.6	1.2337	6.150	0.672
OPH	BF	9.94	+07.09	-28.7	0.6094	7.360	0.222
ORI	RS	196.57	+00.34	+40.5	0.8789	8.412	0.382
PER	SV	162.59	-01.52	-0.5	1.0465	8.978	0.438
PER	SX	158.87	-06.36	+5.5	0.6325	11.151	0.466
PER	UX	133.58	-03.10	-41.5	0.6595	11.602	0.516
PER	UY	135.94	-01.42	-45.0	0.7296	11.346	0.902
PER	VX	132.80	-02.96	-35.2	1.0370	9.301	0.518
PER	VY	135.07	-01.68	-39.5	0.7429	11.257	0.925
PER	AS	154.14	-00.88	-25.5	0.6966	9.726	0.694
PER	AW	166.61	-05.40	+9.5	0.8105	7.486	0.522
PER	V440	135.87	-05.17	-26.1	0.8791	6.247	0.266
PUP	X	236.14	-00.78	+65.3	1.4143	8.460	0.472
PUP	RS	252.42	-00.19	+22.1	1.6172	7.010	0.488
PUP	VW	235.36	-00.62	+24.0	0.6320	11.382	0.490
PUP	VX	237.01	-01.31	+8.8	0.4787	8.315	0.165
PUP	VZ	243.42	-03.32	+63.3	1.3650	9.631	0.496
PUP	WW	237.38	+00.97	+87.0	0.7417	10.553	0.382
PUP	WX	241.50	-01.37	+54.6	0.9512	9.063	0.317
PUP	WY	241.78	+02.70	+44.0	0.7202	10.599	0.252
PUP	WZ	241.77	+03.33	+64.0	0.7013	10.328	0.201
PUP	AD	241.93	-00.04	+67.5	1.1333	9.877	0.340
PUP	AP	255.50	-05.72	+15.9	0.7062	7.427	0.189

Table 2.12—*Continued*

Cepheid		ℓ	b	v_r	log P	$\langle V \rangle$	E(B-V)
PUP	AQ	246.15	+00.10	+58.1	1.4777	8.669	0.545
PUP	AT	254.32	-01.61	+25.0	0.8240	8.003	0.172
PUP	BN	247.89	+01.06	+62.3	1.1358	9.889	0.448
PUP	HW	244.77	+00.78	+116.2	1.1288	12.051	0.733
PUP	LS	246.38	+00.13	+77.4	1.1506	10.447	0.489
PUP	MY	261.31	-12.86	+12.7	0.7555	5.666	0.049
SCO	RV	350.41	+05.68	-12.7	0.7826	6.973	0.328
SCO	RY	356.49	-03.41	-17.7	1.3079	8.016	0.799
SCO	KQ	340.39	-00.74	-22.1	1.4578	9.810	0.928
SCO	V482	354.36	+00.18	+13.8	0.6559	7.961	0.338
SCO	V500	359.02	-01.35	-7.4	0.9693	8.729	0.598
SCO	V636	343.51	-05.21	+6.9	0.8323	6.645	0.207
SCT	X	18.99	-01.56	+11.1	0.6230	10.015	0.595
SCT	Y	23.96	-00.85	+17.8	1.0146	9.629	0.825
SCT	Z	26.78	-00.76	+37.2	1.1106	9.599	0.550
SCT	RU	28.19	+00.24	-4.9	1.2945	9.485	0.978
SCT	SS	25.17	-01.80	-9.0	0.5648	8.179	0.309
SCT	TY	28.05	+00.12	+25.5	1.0435	10.791	1.018
SCT	UZ	19.16	-01.49	+38.8	1.1686	11.303	1.083
SCT	CK	26.30	-00.46	-0.4	0.8701	10.602	0.787
SCT	CM	27.16	-00.44	+39.5	0.5930	11.107	0.745
SCT	EV	23.97	-00.46	+16.7	0.4901	10.136	0.646
SCT	V367	21.63	-00.83	-7.7	0.7989	11.550	1.272
SGE	S	55.16	-06.11	-6.3	0.9234	5.623	0.123
SGE	GY	54.94	-00.56	15.6	1.7081	10.230	1.140
SGR	U	13.70	-04.45	+4.2	0.8290	6.692	0.393
SGR	W	1.57	-03.97	-25.2	0.8805	4.670	0.104
SGR	X	1.16	+00.22	-10.1	0.8459	4.561	0.188
SGR	Y	12.79	-02.13	-1.4	0.7614	5.745	0.190
SGR	VY	10.13	-01.07	-6.0	1.1322	11.529	1.293
SGR	WZ	12.11	-01.31	-15.7	1.3394	8.023	0.491
SGR	XX	14.98	-01.87	+2.0	0.8078	8.852	0.531
SGR	YZ	17.75	-07.11	+18.5	0.9802	7.347	0.292
SGR	AP	8.11	-02.43	-15.0	0.7040	6.910	0.173
SGR	AV	7.53	-00.58	+20.0	1.1878	11.540	1.281
SGR	AY	13.25	-02.39	-26.5	0.8175	10.526	0.908
SGR	BB	14.66	-09.00	+4.6	0.8220	6.926	0.273
SGR	V350	13.75	-07.95	-0.7	0.7122	7.344	0.294
TAU	SZ	179.48	-18.75	-3.8	0.4981	6.530	0.261

Table 2.12—*Continued*

Cepheid		ℓ	b	v_r	$\log P$	$\langle V \rangle$	E(B-V)
TRA	R	316.97	-07.75	-13.5	0.5301	6.640	0.097
TRA	S	322.13	-08.22	+4.0	0.8010	6.405	0.088
TRA	U	323.23	-08.03	-13.1	0.4097	7.940	0.049
UMI	ALPH	123.28	+26.46	-20.0	0.5990	1.973	-.033
VEL	T	265.54	-03.78	+6.3	0.6668	8.032	0.260
VEL	V	276.57	-04.19	-26.9	0.6407	7.596	0.186
VEL	RY	282.57	+01.48	-10.4	1.4493	8.372	0.593
VEL	RZ	262.88	-01.91	+24.1	1.3096	7.089	0.357
VEL	SV	286.00	+02.37	+3.5	1.1491	8.566	0.403
VEL	SW	266.19	-03.00	+22.9	1.3700	8.121	0.375
VEL	SX	265.49	-02.18	+30.9	0.9800	8.263	0.250
VEL	XX	284.80	+02.00	+15.0	0.8441	10.671	0.563
VEL	AH	262.44	-06.96	+22.0	0.6260	5.708	0.050
VEL	AP	262.98	-01.37	+26.3	0.4952	10.053	0.482
VEL	AX	263.33	-07.70	+22.1	0.4138	8.219	0.186
VEL	BG	271.86	-02.56	+7.9	0.8403	7.648	0.438
VEL	DD	271.51	-01.38	+26.0	1.1204	12.474	0.988
VEL	DR	273.22	+01.33	+20.6	1.0492	9.521	0.689
VEL	EZ	274.93	-01.94	+96.4	1.5383	12.440	1.216
VUL	S	63.44	+00.83	-2.0	1.8299	8.960	0.884
VUL	T	72.13	-10.15	-1.6	0.6469	5.753	0.041
VUL	U	56.07	-00.28	-12.5	0.9026	7.128	0.648
VUL	X	63.85	-01.28	-16.1	0.8007	8.848	0.836
VUL	SV	63.94	+00.33	-0.3	1.6532	7.243	0.615

[a] Caldwell & Coulson (1987) and references therein

[b] §2.4; Moffett & Barnes (1987)

[c] Fernie (1990)

additional Cepheids with radial velocities from §2.4, and including revised velocities of Moffett & Barnes (1987). The updated set consists of 214 stars; in addition to the stars excluded by CC we exclude CT Car (not used in the CC model, but has a γ velocity from §2.4), as it is suspected to be a W Virginis star (Pop. II Cepheid) based on its apparent height above the Galactic plane (Harris 1985b). The updated data set is shown in Table 2.12. The Cepheids discovered in the CKS survey were added to form a third set for the models, using γ velocities measured in §2.5 and JHK photometry of Schechter et al. (1992).

The values of $\overline{K}$ reported by Schechter et al. (1992) are a straight average of their individual measurements; if the measured points are not well-spaced in phase, such an average can be biased with respect to the true $\langle K \rangle$. Though we expect this difference to be small given the pulsation amplitude at K, to obtain a slightly more accurate average we fitted a sine function to the K points using periods computed in V by Avruch (1991). The amplitude was scaled from the V light curve amplitude, estimated from data of LeDell (1993), using the relation of Welch et al. (1984): $\mathrm{Amp}(K) = (0.30 \pm 0.03) \times \mathrm{Amp}(V)$. The results of this procedure, along with formal errors assuming $\sigma_K = 0.02$ mag for each observation, are given in Table 2.13. We tried adding higher-order terms to the light curves from the Fourier decompositions of Laney & Stobie (1993), but this had no significant effect on the computed $\langle K \rangle$ magnitudes. The star 13240–6245 had a high covariance ($r \simeq 0.6$) between $\langle K \rangle$ and the epoch, largely due to poor phase coverage.

Also shown in Table 2.13 are the amplitudes (peak-to-peak) of the V-band light curves, epochs of maximum light in both V and K, and improved period estimates. The K-band epochs were determined from the fit curve, and the improved periods are selected from values listed by Avruch (1991) (he gives several due to the possibility of aliasing) that are most consistent with the K data. We find that the V maximum light lags that in K by ~ 0.27 cycles, in rough agreement with Welch et al. (1984). We also note that the star 13323–6224 is peculiar in that it has a significantly smaller amplitude than expected given its period. Overall, we obtain a tight formal error on the $\langle K \rangle$ magnitudes; in particular, the uncertainties are smaller than the scatter

Table 2.13: Calculated Parameters for New Cepheids

Cepheid	Amp(V)	$\langle K \rangle$	$\sigma_{\langle K \rangle}$	$JD^a_{V_{max}}$	$JD^a_{K_{max}}$	Period
11447-6153	0.65	10.092	0.013	7962.97	8337.43	6.4282
11465-6209	0.88	8.558	0.014	7968.7	8337.84	11.0984
11492-6257	0.62	10.649	0.009	7959.80	8336.00	3.6529
11521-6200	0.63	9.645	0.014	7958.40	8335.16	6.5763
12003-6213	0.72	9.125	0.012	7958.67	8339.86	9.0131
13190-6235	0.82	8.739	0.015	7958.76	8342.12	10.3001
13240-6245	1.21	7.618	0.022	7966.94	8337.60	15.2158
13323-6224	0.46	7.910	0.012	7961.75	8336.63	4.2424

^{a} Modulo 2,440,000; $\sigma \simeq 0.025\times$ period.

in the PL-K relation and hence sufficient for our purposes. (It is interesting to note that only two of the average magnitudes are significantly different from the straight means computed by Schechter *et al.* [1992].) It was not necessary to phase and fit the $(H - K)$ colors, since they do not change appreciably over the pulsation cycle.

2.6.2 Cepheid Calibration

The two parameters m_0 and α in equation 2.6 determine the distances to each Cepheid in terms of R_0. The slope parameter α has been measured in many studies, using both Magellanic Cloud and Galactic cluster Cepheids (Fernie & McGonegal 1983, Caldwell & Coulson 1986, CC, Madore & Freedman 1991, Laney & Stobie 1994). Most tend to agree to within the quoted errors, and lie in the range -2.9 to -2.8 (with the notable exception of CC at -3.1). Some studies exclude the occasional Cepheid due to some peculiar feature or other, but this does not significantly affect the final results. There does appear to be a difference in computed slope of the PL relation, however, depending on the period range of Cepheids used in the fit. While studies using open clusters to calibrate the PL relation contain data over a wide range of period, many exclude the longest period Cepheids from the fit as they tend to be somewhat brighter than an extrapolation of the PL relation of short-period Cepheids would indicate (e.g. Fernie & McGonegal 1983). Freedman *et al.* 1993 derive a separate calibration of the PL relation based only on Cepheids with $1.0 < \log P < 1.8$ to match most closely

the range of periods in the M81 Cepheids. They find a PL-V slope of -3.35 ± 0.22, significantly steeper than found in other studies referenced here. Another possible explanation for the discrepancy is the intriguing suggestion by Böhm-Vitense (1994) that most Cepheids with periods shorter than 9 days are overtone pulsators. If the short and long period Cepheids form two offset, steeper PL relations, then a slope measured from combining the two would be shallower than that measured from either set independently. More work needs to be done to help verify the existence of the separate PL relations, particularly in the near-infrared where the intrinsic scatter about the PL relation is smaller. A quick examination of the PL-K data of Laney & Stobie (1994) shows little evidence for short-period overtone pulsators, while not necessarily ruling them out. Gieren, Barnes, & Moffett (1989) find evidence against this hypothesis based on the continuity of BW radii across a wide range of periods. Even if her suggestion is correct, as long as the range of periods of the calibrators is similar to the overall population used for distances, the derived slope and zero-point will still provide an accurate calibration (though perhaps with larger scatter). Considering that our Cepheid sample has a median $\log P \approx 0.9$, we can comfortably use the shallower slopes derived from Cepheids of similar period with a commensurate zero point.

The zero point of the Cepheid PL relation puts m_0 on an absolute distance scale. Different studies yield different Cepheid PL calibrations primarily due to differences in assumed extinction, metallicity or correction for metallicity, and the sample of stars used. Currently the most accurate methods for Galactic PL calibrations are those using Cepheids in clusters and associations (Turner 1985; Fernie & McGonegal 1983), and those using the visual surface brightness (Baade-Wesselink) method (Gieren 1989). The cluster calibrations are based on fitting main sequences for clusters containing Cepheids to either the Hyades or Pleiades, and the surface brightness method attempts to measure the radius of a Cepheid based upon accurate photometry and radial velocity measurements. A convenient comparison of Cepheid calibrations can be made by applying the calibrations to LMC Cepheids, and comparing the derived LMC distance moduli. The SMC is somewhat less suited to this purpose as it

is thought to be significantly extended along the line of sight. Feast & Walker (1987) give a comprehensive review of Cepheid calibrations up to that time, and conclude that for a Pleiades modulus of 5.57, the LMC lies at a true distance modulus of 18.47 ± 0.15. This estimate is based on the same extinction law used here. More recently, using updated V-band data, CC determine an LMC modulus of 18.45, and Laney & Stobie (1994) find an LMC modulus of 18.50 ± 0.07, both assuming the same Pleiades modulus and extinction law. The Baade-Wesselink calibrations yield distance moduli larger by 0.15 mag on average (Gieren & Fouqué 1993), and give a distance modulus for the LMC of 18.71 ± 0.10 mag. While significantly different, there appear to be systematic errors present that make the distance moduli too large: the four calibrators they discard as being significantly discrepant all have distance moduli too large by > 0.6 mag (possibly due to the presence of companions?), and the remaining distribution is asymmetric. We therefore prefer to adopt the cluster calibrations. To provide for a convenient reference point we follow the custom of normalizing our distances to an assumed modulus of the LMC, in our case 18.50, and adopt the normalized V-band calibration of

$$M_V = -4.10 - 2.87(\log P - 1). \tag{2.8}$$

The internal uncertainty in the zero point (exclusive of any systematic error in the LMC distance) is estimated to be $\simeq 0.07$ mag.

To incorporate the near-infrared data on the newly-discovered Cepheids, we use the period-luminosity relation in the K-band with an appropriate calibration and extinction law. The calibration zero point must give distances commensurate with those derived from V-band data, and thus we again normalize the zero-point to an LMC modulus of 18.50. After making this correction, the PL-K calibration of Welch et al. (1987) gives $M_K = -5.66 - 3.37(\log P - 1)$, with the K magnitudes on the same system (Elias et al. 1982) as the Schechter et al. (1992) photometry. Madore & Freedman (1991) give a self-consistent calibration based on a sample of 25 LMC Cepheids, each with photometry in both V and K, finding $M_K = -5.70 - 3.42(\log P -$

1), identical to within quoted errors. The Madore & Freedman PL-V calibration is also consistent with our adopted M_V. Laney & Stobie (1994) give a calibration of the PL-K relation in a slightly different photometric system; after converting to the Elias et al. (1982) system using the transformation of Laney & Stobie (1993b) and correcting to an LMC modulus of 18.50, we find

$$M_K = -5.70(\pm 0.04) - 3.40(\pm 0.05)(\log P - 1).$$ (2.9)

The scatter of the individual stars about the period-luminosity relation is significantly smaller in K than V, 0.16 mag rms vs. 0.25 mag rms, and hence the internal error associated with the zero point is correspondingly smaller at 0.04 mag. Since the quoted uncertainties in the Laney & Stobie (1994) calibration are the smallest of those quoted above, and that the relation is almost identical to the others, we adopt equation 2.9 for our models.

It is important to note, however, that there is a small discrepancy between the LMC moduli derived from V and K data when using Galactic cluster calibrations. Measurements of LMC distance modulus in the K band from the above references typically yield a value of 18.55–18.60, some 0.05–0.10 higher than the V calibration. This discrepancy could be due to a number of factors, including a difference in mean metallicity between Galactic and LMC Cepheids. Another possible source of systematic error arises from the correction for extinction: this is substantially larger for the Galactic calibrators, which have a mean E(B–V) of 0.65 (Feast & Walker 1987), than the LMC Cepheids, which have an E(B–V) of about 0.14 mag. Thus an error in the adopted value of R_V of even 0.1 (not unreasonable) would produce an apparent distance offset between the two of 0.05 mag. Since the difference here is only slightly greater than 1 σ, no useful limits can be placed on R (or $A_V - A_K$). However, we discuss below some implications of the kinematic distance scale using the newly discovered Cepheids on the adopted reddening law.

We used the $E(H - K)$ color excesses of Schechter et al. (1992) to compute the extinction in K, $A_K \equiv K - K_0$, for the newly discovered Cepheids. These

Table 2.14: CC Cepheids: Model Parameters and Covariances

		$2AR_0$ km s^{-1}	m_0 mag	u_0 km s^{-1}	v_0 km s^{-1}	δv_r km s^{-1}	R_0 kpc
Model A1 CC Data	$n = 184$	225 ±19	10.40 ±0.19	-8.6 ±1.5	12.8 ±1.3	3.2 ±1.0	7.94 ±0.72
	$2AR_0$	1.00	0.88	0.22	0.27	−0.09	
	m_0		1.00	0.17	0.31	−0.14	
	u_0			1.00	0.06	0.24	
	v_0				1.00	0.18	
Model A2 New v_r	$n = 184$	236 ±19	10.40 ±0.17	-7.0 ±1.4	13.2 ±1.2	3.1 ±0.9	
Model A3 New E_{B-V}	$n = 184$	227 ±19	10.30 ±0.17	-8.2 ±1.4	12.6 ±1.2	3.3 ±0.9	
Model A4 Both New	$n = 184$	240 ±19	10.32 ±0.17	-6.5 ±1.4	12.7 ±1.2	3.3 ±0.9	7.66 ±0.60
	$2AR_0$	1.00	0.88	0.22	0.27	−0.10	
	m_0		1.00	0.16	0.32	−0.15	
	u_0			1.00	0.06	0.24	
	v_0				1.00	0.17	

were derived assuming an intrinsic color locus in the H–K/P plane: $(H - K)_0 = 0.068 + 0.024(\log P - 1)$ (their equation 1). We adopted the same extinction law used by Schechter *et al.* for the total-to-selective extinction, that given by Cohen *et al.* (1981): $A_K = 1.39E(H - K)$. This can be compared with coefficients found in other sources: 1.7 (McGonegal *et al.* 1983, CIT system), 1.5 (Clayton, Cardelli & Mathis 1989, Johnson system), 1.8 (Rieke & Lebofsky 1984), and 1.6 (Laney & Stobie 1994, Carter system). The CKS Cepheids have an average $E(H - K)$ of 0.27; if we were to simply replace our reddening law with the average of the $A_K/E(H - K)$ values listed ($= 1.6$), the result would be an increase in mean distance modulus by 0.06 mag for the stars in the sample. Of course, this would not be strictly correct, as the values are based on magnitudes of different systems; we use the Cohen *et al.* (1981) value keeping in mind a possible systematic offset.

2.6.3 Model Results

For convenient reference each model run was given a designation consisting of a letter and a number. The letter differentiates a model, with a particular set of intrinsic parameters (i.e. α, R_V, axisymmetry, etc.), while the number differentiates between different sets of data used to fit the adjustable parameters. Errors shown in the tables listing model parameters are internal errors (those due to scatter about the adjustable parameters), and covariances between model parameters are expressed as correlation coefficients of the projected data (Bevington 1969):

$$r_{ij} = \frac{s_{ij}^2}{s_{ii}s_{jj}}$$

where the s_{ij}^2 are elements of the covariance matrix.

The first models were fit using the same set of Cepheids as Caldwell & Coulson (1987) used for their models. The model designated "A" is axisymmetric, with the adopted PL-V relation and corrections for extinction as discussed above. The results are given in Table 2.14. The first run, designated Model A1, was used primarily as a check on our modeling software—it uses the same data (magnitudes, velocities, and reddenings) used by CC. Though some of the details of the model itself are different, we closely reproduce the results of CC after taking into account the different zero-point calibration (CC used an effective LMC modulus of 18.45 mag). Model A4 was run on the same Cepheids, but with updated reddenings and velocities as described above. Note that while m_0 decreases by about 0.5σ, $2AR_0$ increases by 0.8σ between models A1 and A4. This is *opposite* the sense one would expect given the model covariances, and therefore the new data provides a significant change to the model data. To highlight this, we note that Oort's A constant effectively increases from 14.2 km s^{-1} kpc^{-1} to 15.7 km s^{-1} kpc^{-1} when the new data are used.

To help determine where this effect originates, we divided the changes into two separate data sets: one containing only updated velocities (67 stars having new velocities), and one containing only updated values of E(B–V) (stars changed). The best-fit parameters are shown in Table 2.14 as Models A2 and A3, respectively, and it is apparent that the new velocities tend to increase $2AR_0$, while the new reddenings

Table 2.15: Model Parameters and Covariances, V-Band Cepheids

		$2AR_0$ km s^{-1}	m_0 mag	u_0 km s^{-1}	v_0 km s^{-1}	δv_r km s^{-1}	R_0 kpc
Model A5	$n = 213$	242	10.25	-7.3	12.9	3.3	7.41
All V		±15	±0.14	±1.3	±1.1	±0.8	±0.50
	$2AR_0$	1.00	0.87	0.16	0.28	-0.17	
	m_0		1.00	0.14	0.35	-0.19	
	u_0			1.00	0.00	0.20	
	v_0				1.00	0.08	
Model A6	$n = 213$	244	10.27	-7.4	13.0	3.3	7.49
Clust Red		±16	±0.14	±1.3	±1.1	±0.8	±0.50
Model A7	$n = 213$	243	10.35	-7.6	13.5	3.2	7.76
CC Red		±16	±0.15	±1.3	±1.1	±0.9	±0.54
Model A8	$n = 213$	247	10.41	-7.6	13.3	3.3	7.97
F90 on CC		±16	±0.14	±1.3	±1.1	±0.8	±0.54

tend to decrease m_0. Comparisons of the old and new velocities are shown in Figure 2-21; reddenings are similarly compared in Figure 2-22. A clear trend is evident in the latter plot, such that the redder stars tend to have higher values of E(B–V) on F90's scale than that of CC. A linear fit to the data gives

$$E_{B-V}(\text{CC}) - E_{B-V}(\text{F90}) = 0.032(\pm0.006) - 0.107(\pm0.013) \times E_{B-V}(\text{F90}), \quad (2.10)$$

with a 0.05 mag scatter about the fit. This trend is responsible for changing R_0 by some 5%, and shows that systematic errors can be significant; this is discussed further below. We excluded Fernie's value for the reddening of GZ Car (by far the most deviant point in Figure 2-22), as it is unlikely that a Cepheid at its apparent modulus would have as little extinction as he indicates; we have used the CC value instead.

Model parameters fit to the entire set of Cepheids with available V-band photometry are given in Table 2.15. Model A5 is a fit of the A model to the full data set of Table 2.12, which has $E(B - V)$ reddenings from F90 on his photometric scale. Model A6 uses the same set of stars, but uses F90's "cluster" reddening scale. F90

81

Table 2.16: Model Parameters and Covariances, New Cepheids

		$2AR_0$ km s^{-1}	m_0 mag	u_0 km s^{-1}	v_0 km s^{-1}	δv_r km s^{-1}	R_0 kpc
Model B1	$n = 221$	248	10.32	-7.3	13.0	3.3	7.66
V&IR,F90		±12	±0.10	±1.3	±1.1	±0.8	±0.36
	$2AR_0$	1.00	0.80	0.17	0.24	−0.17	
	m_0		1.00	0.14	0.34	−0.20	
	u_0			1.00	0.00	0.21	
	v_0				1.00	0.10	
Model B2	$n = 221$	242	10.37	-7.6	13.1	3.4	7.83
F90 on CC		±12	±0.10	±1.3	±1.1	±0.8	±0.37
Model B3	$n = 218$	243	10.37	-6.7	12.9	3.7	7.82
Trimmed		±11	±0.10	±1.2	±1.0	±0.8	

compared his derived reddenings of cluster Cepheids to the E(B–V) values used by Feast & Walker (1987) to calibrate the Cepheid PL relation, and computed a linear correction to put his photometric reddenings on the same scale as was used for the PL calibration. The idea is that if one uses the same reddenings for the calibrators and for distance determination, any zero-point error will cancel. Based on his Figure 1, F90 concludes that though on casual inspection some trend is apparent in the difference between Feast & Walker's (1987) reddenings and his own, it is statistically insignificant, and the transformation between the two systems can be made by using only a small term proportional to pulsation period.

Model A7 is similar to model A5, except that original CC reddenings were used when available. Note once again the increase in m_0, here by 0.1 mag. Combining reddenings from Fernie and CC is somewhat less than satisfactory, however, since the extinctions will not be on a homogeneous scale. We therefore tried to generate a set of reddenings for all stars on a uniform scale, but consistent with the reddening scale of CC. We assumed that the linear fit of equation 2.10 would suffice to adequately transform the F90 reddenings to the CC system. Model A8 shows the fit parameters using reddenings generated in this manner; m_0 has increased by 0.16 over that from the unmodified Fernie reddenings.

Table 2.16 shows derived model parameters for the V-band data combined with K-band data for the newly-discovered Cepheids. These models have been designated with "B" as they additionally require the use of the PL-K relation, equation 2.9. Models B1 and B2 use F90 photometric reddenings and F90 reddenings on the CC scale, respectively. Model B3 is identical to B2 except for the elimination of the three most deviant points (see §2.6.4) below.

The positions of the Cepheids in the plane of the Milky Way are shown in Figure 2-23. Different symbols are used to show which Cepheids were added to these models through new reddenings (Fernie 1990), new radial velocities (§2.4), and the newly-discovered Cepheids. The squares indicate the Cepheids used by CC in their models and used in our models A1–A4. The data shown with circles (open and filled) are additional Cepheids used for Models A5–A8, and stars plot the CKS Cepheids added for the B models. Note that while many new distant Cepheids have been added to the models, there still remains a substantial asymmetry between the number of Cepheids at $\ell < 180°$ and $\ell > 180°$. Velocity residuals from model B2, scaled by σ according to equation 2.7, are shown in Figures 2-24 and 2-25, the latter with the positive and negative residuals plotted separately for clarity. The size of each plotted point is linearly proportional to χ_{B2}.

2.6.4 Discussion

The addition of new radial velocities and reddenings for previously known Cepheids to the models significantly decreases the internal error on model parameters, particularly R_0 for which the error decreases from 10% to 7%. Three of the model parameters, u_0, v_0, and δv_r, change only slightly between Models A1 and A5, as expected. These three parameters do not depend directly on the distance to the stars, and thus the new stars should only provide a statistical reduction in uncertainty for these parameters. Most of the change in u_0 can be attributed to improved radial velocities for the CC stars alone and not the addition of new stars per se: Model A2, using the same stars as CC but with new radial velocities, exhibits most of the change in u_0, and three of the four Cepheids with large negative velocity changes are within $\sim 30°$ of $\ell = 0°$

(SY Nor, TY Sct, UZ Sct; see Figure 2-21), and hence significantly affect the radial component u_0.

The addition of the known distant Cepheids to models A5–A9 not only significantly reduces the uncertainty in m_0, but also highlights the difference in m_0 caused by the use of different reddening systems. The comparison between the CC and F90 reddenings shown in Figure 2-22 shows a clear systematic difference between the two. Since the CC reddenings are based on the Dean et $al.$ (1978) prescription for computing $E(B - V)$ from BVI_C photometry, we conclude that the trend seen in Figure 1 of F90 between his reddenings and those of Feast & Walker (1987) is likely to be real, and is the same as the trend we find in Figure 2-22. The slope of 0.1 on the trend is actually quite large: since A_V is the same for each star independent of how $E(B-V)$ is measured, the slope corresponds to an effective change in R_V of 0.3. This is significantly larger than the overall uncertainty in R_V is believed to be (Turner 1976; Feast & Walker 1987, Laney & Stobie 1994 and references therein), and illustrates the importance of using R_V values consistent with the particular $E(B-V)$ system in question. This is not critical for low to moderate reddenings, such as present in the Magellanic clouds or typical open clusters, but as we have seen becomes significant for stars with $E(B-V) > 1$.

The reddening zero point is typically calibrated to agree for some sample of open clusters containing Cepheids; this is to make the reddenings commensurate with the Cepheid calibration, though the latter depends primarily on $R_{Cep} - R_{OB}$ rather than R_{Cep} directly. (By R_{Cep} and R_{OB} I mean the values of R appropriate for a Cepheid color and for a typical color used to perform the main-sequence fit to the cluster.) However, neglecting a scale difference assumes that a physical $E(B - V)$ is being measured; in practice color excesses are typically measured using multiwavelength photometry such as Strömgren or BVI_C (F90; Dean et $al.$ 1978). The F90 reddenings are based on theoretical colors from model atmospheres, but the relations to observed colors are only accurate for moderate reddenings (Fernie 1987). In addition, once the reddenings start to become relatively large, $E(B - V) > 1$, calibration of observed magnitudes to standard photometric systems becomes increasingly uncertain. Thus

84

one is not necessarily measuring $E(B - V)$, but rather a linear approximation valid for moderate extinction. Interestingly, Fernie (1987) compares his reddenings to those of other studies, including Dean *et al.* (1978), and finds that a few have significant scale differences. But the Dean *et al.* scale he finds is 1.18, compared to 0.89 that we find for CC—in the opposite sense! This could be due to the comparison including only moderate reddenings, with the associated uncertainties, or that CC reddenings may not be on the same scale as those of Dean *et al.* (1978).

We therefore conclude that for purposes of measuring R_0 and other large-scale Galactic rotation parameters, distances derived from V-band data are inadequate. For increasingly distant Cepheids with high extinction, distances accurate to better than 15% are not possible due to several reasons: (1) uncertainties in R and $E(B-V)$ that are acceptably small for nearby Cepheids become increasingly significant; (2) Determinations of color excess are sensitive to the standard system calibration (Fernie 1987) which becomes increasingly uncertain for more heavily reddened Cepheids; and (3) Some newly discovered Cepheids have sufficiently high extinction that standard methods of measuring color excess are impossible, including BVI_C (see Chapter 3 for examples).

Fortunately the near-infrared data are much less sensitive to extinction, and the errors in correcting for extinction are correspondingly smaller. Models B1 and B2 incorporate the CKS Cepheid data and show a substantial dcrease in the internal uncertainty of m_0, from 0.14 to 0.10 mag. This implies an internal precision of less than 5%, yielding one of the most precise measurements of R_0 to date. The overall accuracy of the measurement will still depend on the overall systematic errors, which are discussed below. The uncertainty for $2AR_0$ in the B models is slightly lower as well, and the remaining velocity parameters are essentially unchanged. Though we tend to prefer the B2 data (and hence the CC reddenings/R values) since they agree more closely with the K-band distance scale, we have no other good reason to eliminate one or the other. We therefore adopt as our best estimate of R_0 the average of the B1 and B2 model values: $7.75^{+0.37}_{-0.35}$ kpc.

Model C1 shows the results of fitting the two parameters m_0 and $2AR_0$ to the

Table 2.17: Model Data, Distant Cepheids

		$2AR_0$ km s^{-1}	m_0 mag	u_0 km s^{-1}	v_0 km s^{-1}	δv_r km s^{-1}	R_0 kpc
Model C1	$n = 8$	220	10.36	-7.6	13.1	3.4	7.78
New Cephs		±33	±0.13	—	—	—	±0.46
	$2AR_0$	0.11					
Model C2	$n = 7$	184	10.40	-7.6	13.1	3.4	7.93
7 New		±19	±0.078	—	—	—	±0.29
	$2AR_0$	0.03					
Model C3	$n = 9$	215	10.48	-7.6	13.1	3.4	8.25
Dist V		±17	±0.19	—	—	—	±0.75
	$2AR_0$	0.17					

K-band data of newly-discovered Cepheids, keeping u_0, v_0, and δv_r fixed. The value of m_0 has been converted to a V magnitude for the sake of comparison. Model C2 excludes the star 13323–6224, which lies at a smaller distance than the rest of the stars (0.3 R_0) and provides most of the remaining covariance between m_0 and $2AR_0$. The distances are in good agreement with the full model values, and are independent of the choice of $2AR_0$. Neither model adequately constrains $2AR_0$, of course, and the low scatter in model C2 is probably accidental. For Model C3 we have chosen a sample of distant Cepheids from the V-band data that lie in the same general direction as the newly-discovered Cepheids and have $d > 0.5R_0$: CR Car, FI Car, FO Car, SV Cru, VX Cru, MZ Cen, OO Cen, VW Cen, & QY Cen. The results show considerably larger scatter than the K data, as expected, and larger covariance, but are roughly consistent with distances from the full models B1 and B2 as well as C1 and C2. We see from these simple models that almost *all* of the precision in m_0 can be obtained using just the CKS Cepheids alone, given the Sun's peculiar velocity with respect to the Cepheid population as a whole.

Since χ^2 minimization is not a particularly robust estimator, the presence of a few strong outliers can significantly skew the derived parameters away from their "best" values. To test the sensitivity of our models to potential outliers, we started by removing the most deviant star from the model, and re-fitting the model parameters.

This process was repeated until there were no stars with $|\chi| > 2.5$; only three stars, WW Pup, AY Sgr, and SX Per, had to be removed to meet this condition. It is gratifying to note that this is close to the number one would expect given a Gaussian distribution (~ 2.2). The parameters of this trimmed model, B3, are given in Table 2.16. They are almost identical to the parameters derived from the full set (B2), and thus we conclude that the model is not overly strained by outliers.

Due to the distribution of stars, however, a significant amount of weight to the determination of $2AR_0$ rests on a only few stars. Figure 2-26 shows $-v_r^*/(\sin \ell \cos b)$ plotted vs. $1 - r^{-1}$, which projects the rotation curve to a straight line with slope $2AR_0$ running through (0,0) (cf. equation 2.3). Some of the most deviant points include CK Sct, RU Sct, and V367 Sct ($r < 1$) and SX Per, TV Cam, and TZ Mon ($r > 1$). The point to the far left is V340 Ara, and has comparatively more weight on $2AR_0$ by virtue of its small distance from the Galactic center (i.e. a larger lever arm for the slope). Excluding this star does not significantly change the model parameters, however, as it lies close enough to the $2AR_0$ line in this model (B2). This alleviates some concern that it might be unduly influencing the fit. To better determine the slope and constrain $2AR_0$, however, it would be useful to have Cepheids at $0.5 < r < 0.7$ to fill in the gap. Fortunately this is a region where tangent-point measurements from HI gas can help to constrain the rotation curve.

The residuals plotted in Figures 2-24 and 2-25 suggest a few spatial patterns in the residuals. For instance, there are isolated regions of positive residuals in patches toward $\ell = 90°$ and $\ell = 220°$ that have no corresponding negative residuals. Similarly there appear to be regions of primarily negative residuals toward $\ell = 60°$ and $\ell = 130°$. There are several possibilities that might explain such systematic deviations, unfortunately none of which we can adequately distinguish between given the data. One possibility is that they are due to unaccounted systematic offsets between data from different sources, which can tend to cluster given telescope scheduling or the hemisphere, etc. Most of these regions could be brought to the average with velocity shifts of $\approx$ 5–10 km s^{-1}, though that kind of offset seems unlikely given the precision of most modern radial velocity measurements. A second possibility is that real streaming

motions are responsible for producing the offsets, possibly associated with spiral arms. A third possibility is that the extinction law may have systematic differences along different lines of sight, perhaps after intersecting with regions containing clouds having differing compositions of dust. These individual are significant in that they provide evidence that an axisymmetric model isn't correct to higher orders; however, the mean deviations are relatively small on the scale of rotation ($< 0.15\Theta$) and thus are not inconsistent with the simple models we have used.

One significant improvement in the B models presented here is a reduction in the covariance between $2AR_0$ and m_0. This is illustrated by the two contour plots shown in Figure 2-27, showing the log probability of exceeding χ^2 for the model as a function of $2AR_0$ and m_0. The reason for the decoupling is that $1 - r^{-1}$ is small for almost all of the CKS Cepheids (i.e. they are close to the solar circle), thus by equation 2.5 only a small fraction of $2AR_0$ is present in the radial velocity. Most of the covariance between R_0 and $2AR_0$ is provided by the nearby Cepheids with a large rotational component reflected in radial velocities. The Cepheids near the solar circle, in particular the new CKS Cepheids at large distance, provide a significant additional constraint on m_0, serving to help decouple the two parameters. Indeed, the results of Model C1 imply that the distance to the Galactic center is determined to roughly 6% using only 8 stars, independent of the value of $2AR_0$. This enters into the combined model with some weight, but since there are a large number of nearby stars the differential shear still has significant leverage on R_0 (though here as a function of $2AR_0$). The fact that the models where R_0 has a significant covariance with $2AR_0$ yields a very similar m_0 to the C1 and C3 models lends additional confidence that we are measuring accurate values for both parameters, given the constraints of the model.
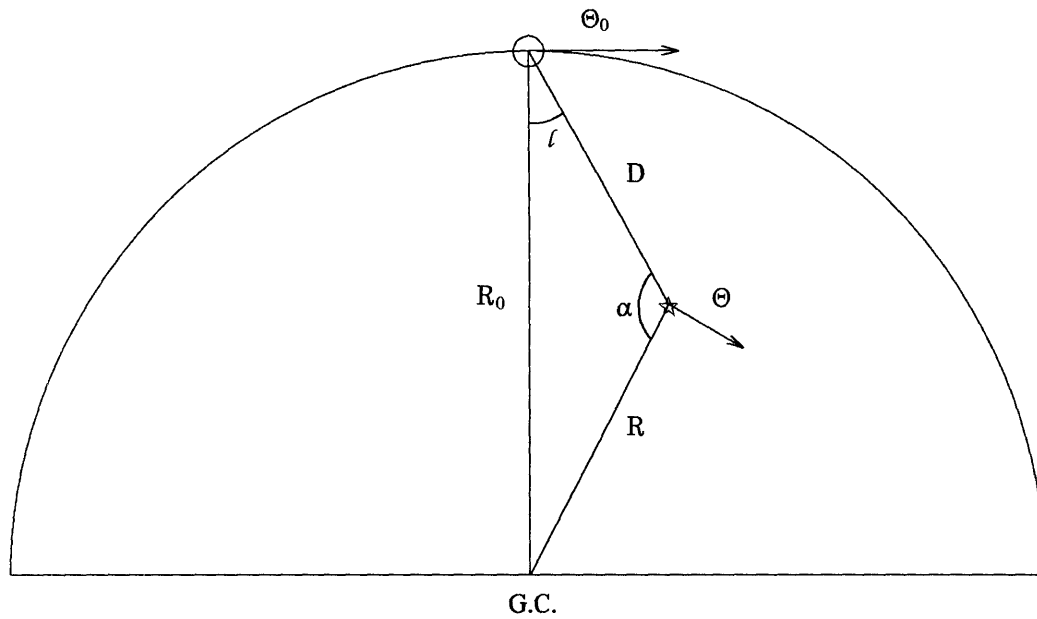
Figure 2-20: A schematic of Milky Way rotation, with labels indicating quantities discussed in the text. The sun is indicated by a circle near the top of the figure, and a fiducial Cepheid is indicated by a star. The Galactic center is labeled as GC.
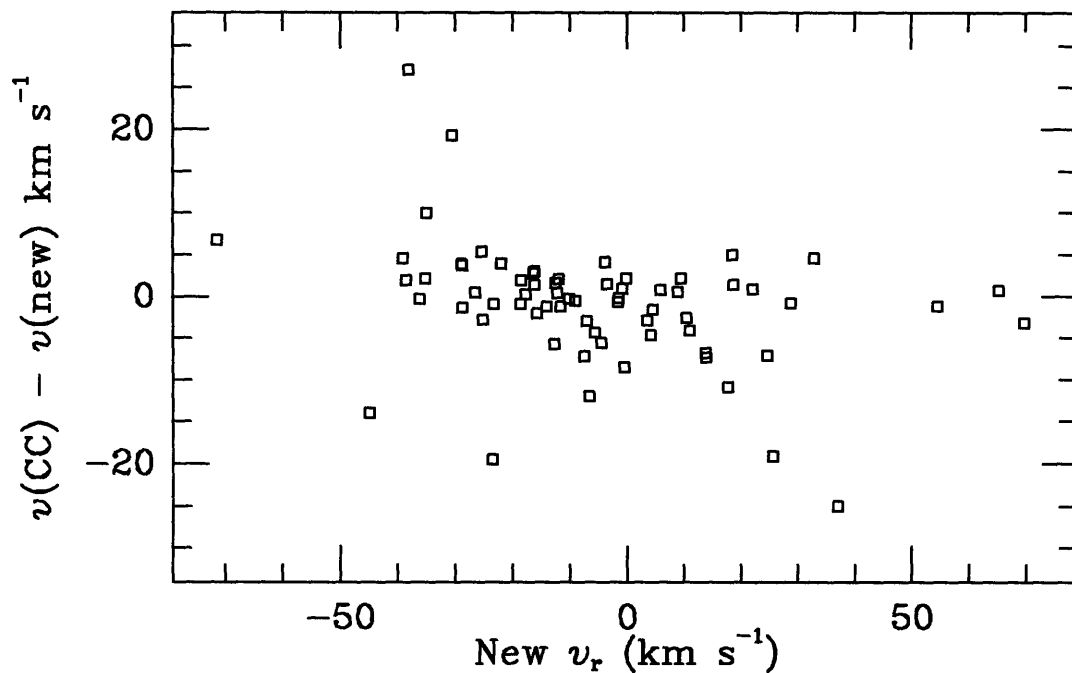
Figure 2-21: A comparison of the radial velocities from Caldwell & Coulson (1987) and new values as described in the text. The six most deviant points are, from left to right, UY Per, DL Cas, MZ Cen, SY Nor, TY Sct, and UZ Sct.
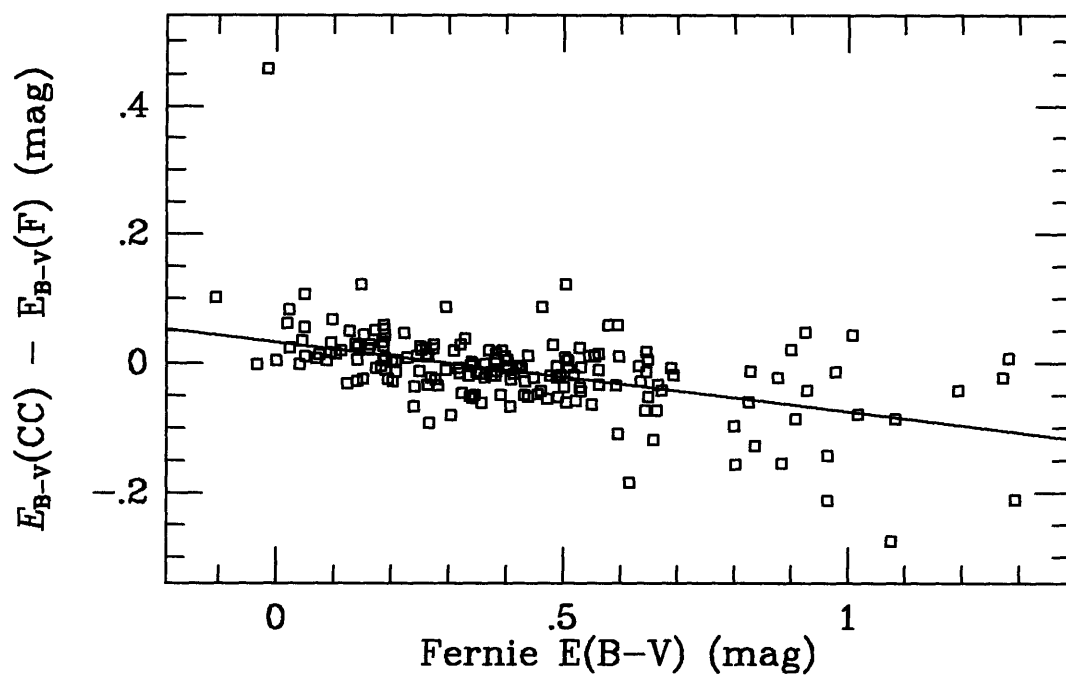
Figure 2-22: A comparison of the reddenings from Caldwell & Coulson (1987) and values from Fernie (1990). A linear fit is shown; the most deviant point, GZ Car, was excluded from the fit.
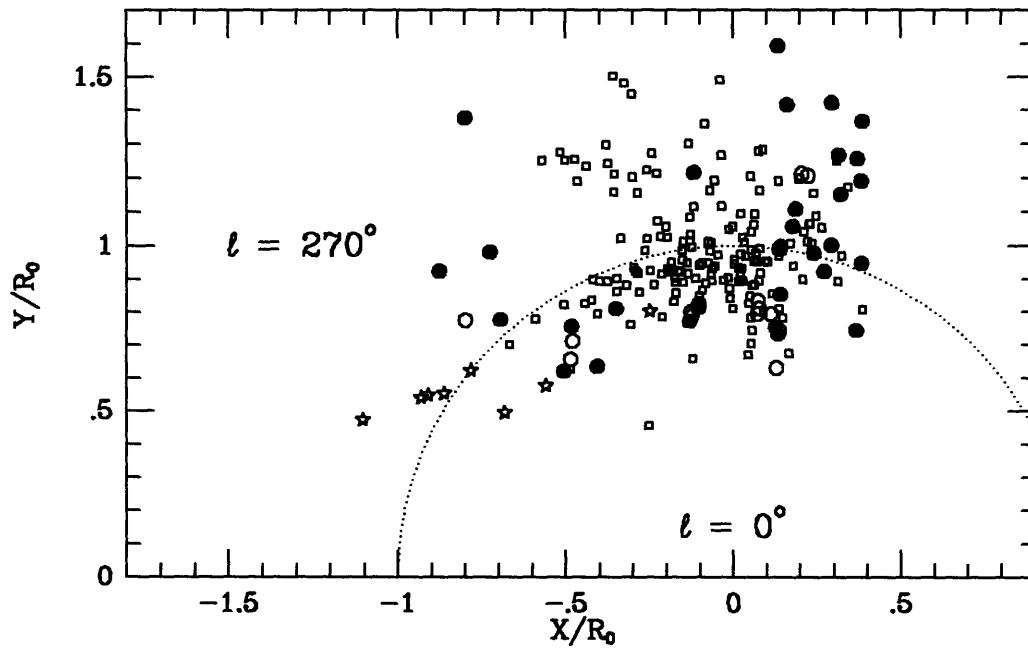
Figure 2-23: Locations of Milky Way Cepheids used in the rotation curve models. Squares indicate Cepheids modeled by CC. Open circles indicate additional Cepheids with new reddenings, filled circles Cepheids with new radial velocities from §2.4, and stars indicate Cepheids newly discovered by CKS. Cartesian coordinates are shown in units of R_0 with the Galactic center at (0,0) and the Sun at (0,1). The solar circle ($r = 1$) is shown with a dotted line.
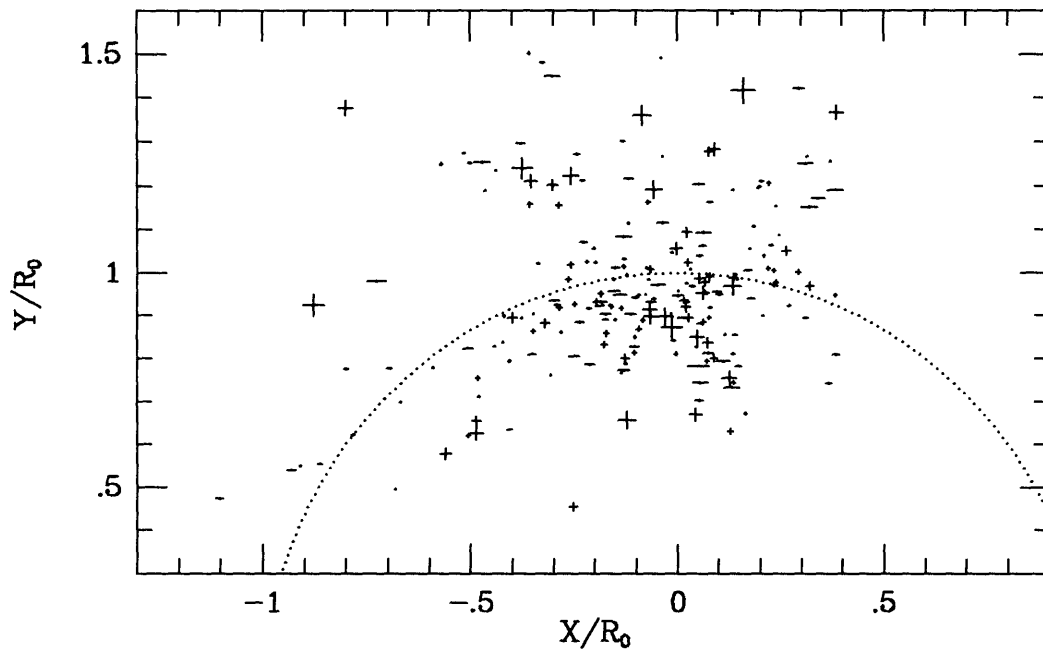
Figure 2-24: Weighted velocity residuals from the B2 model. The magnitude of the residual determines the size of the point, with the largest points having $\chi \simeq 3.0$; the sign (in the sense of v_r–Model) is indicated by the corresponding point shape. Coordinates are the same as in Figure 2-23.
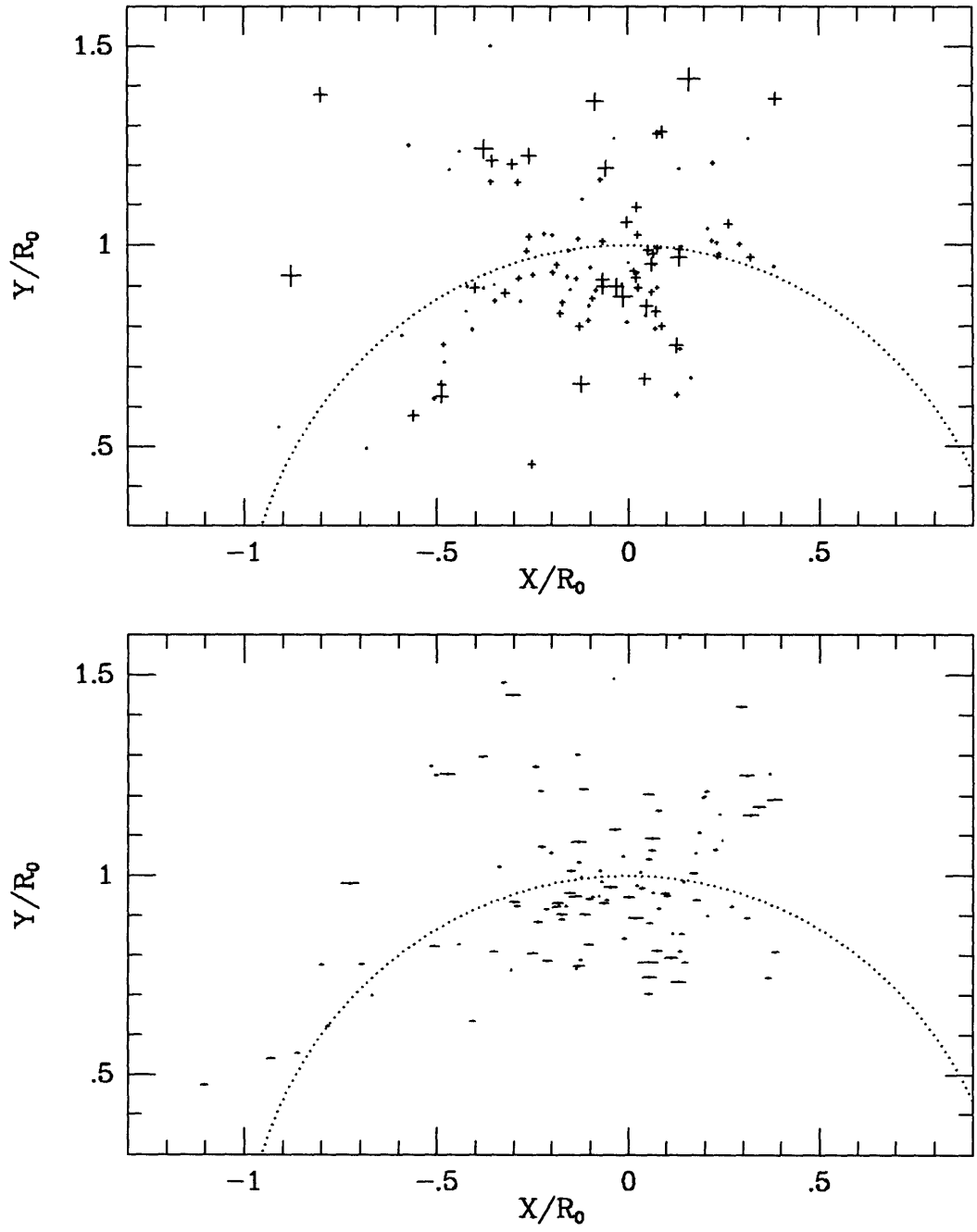
Figure 2-25: Figure 2-24 with positive and negative residuals plotted separately.
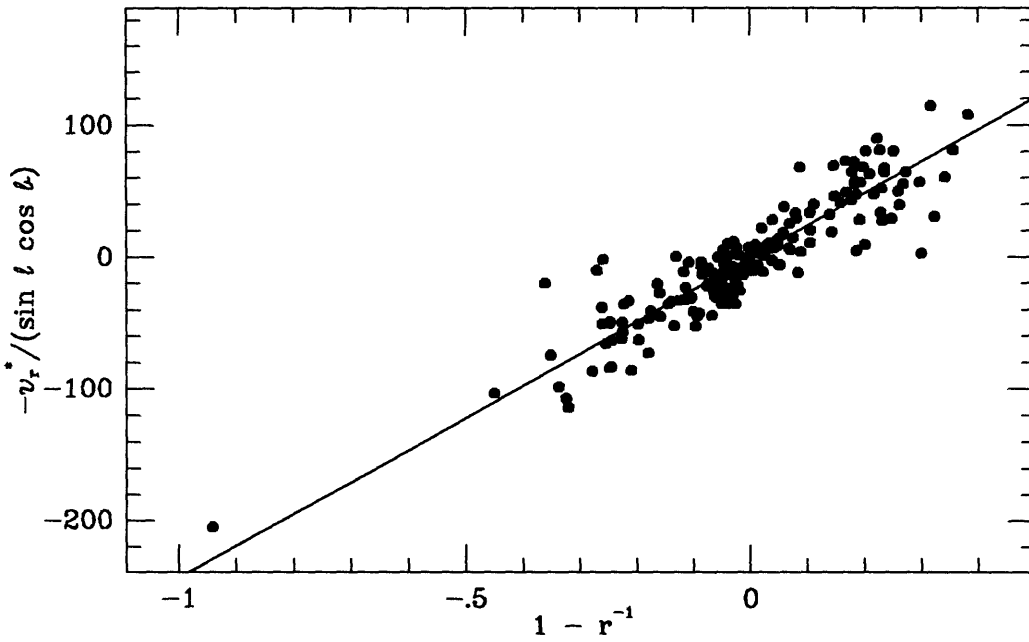
Figure 2-26: Radial velocities (with respect to the LSR) and distances of Cepheids in the sample, scaled so that $2AR_0$ is the slope of a line in the model. The line corresponds to the fit value of $2AR_0 = 242$ km s^{-1} from Model B2. Stars within 20° of the Galactic center and anticenter are not shown, as they have large errors in the ordinate.
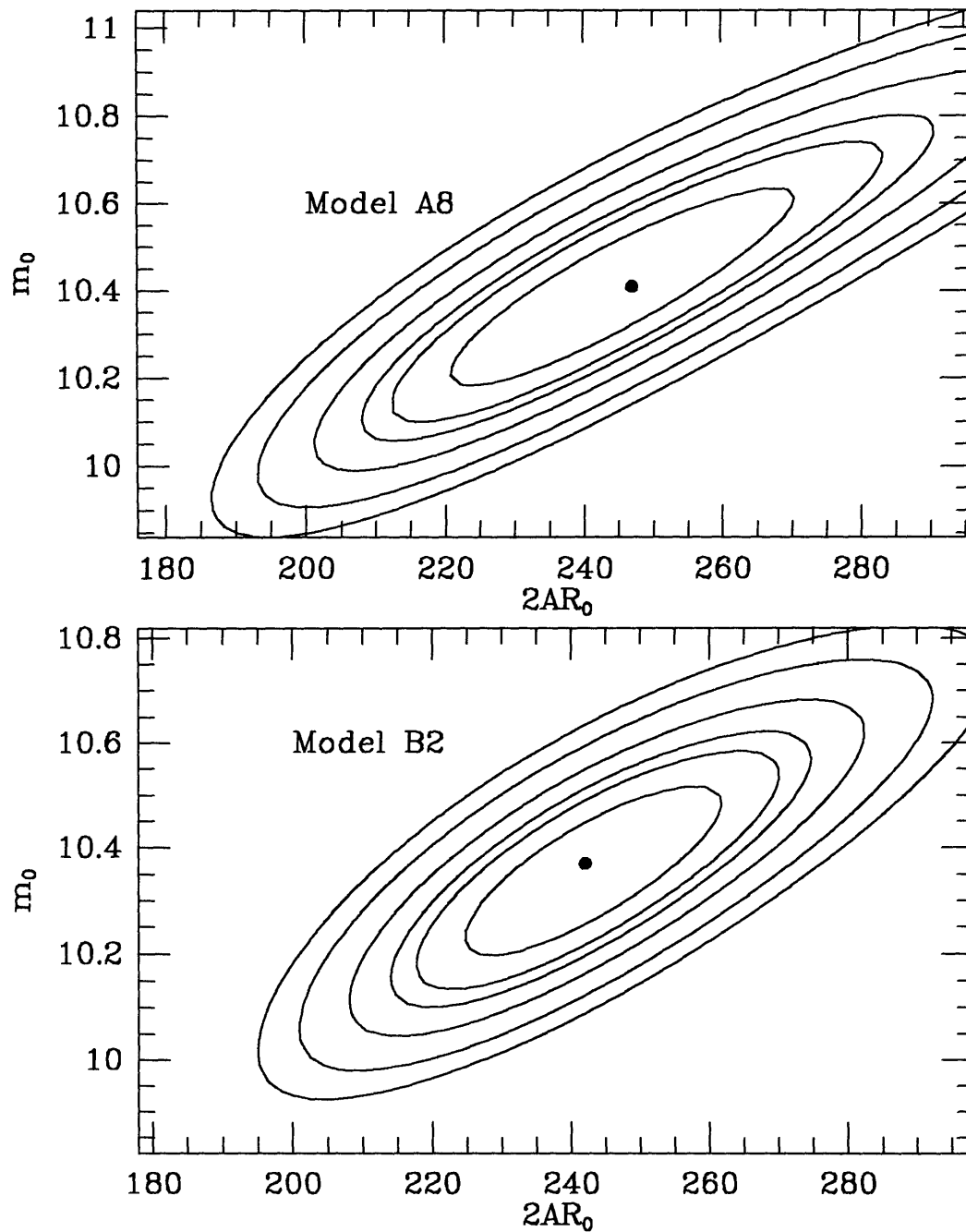
Figure 2-27: Constant $\delta\chi^2$ contours for two models projected in the $2AR_0$, m_0 plane. Contours shown are (from inside to outside) 1-σ, 90%, 2-σ, 99%, 99.9%, and 99.99%. The top panel is a model using all Cepheids with V-band data, including those with new radial velocity measurements. The bottom panel is a model that also includes CKS Cepheids, where distances were determined from K-band data.

2.6.4.1 Ellipticity

All of the models presented so far have been based on the assumption that the Milky Way rotation is axisymmetric. While many constraints can be placed on deviations from axisymmetry, Kuijken & Tremaine (1994, hereafter KT) point out that if the Sun lies near a symmetry axis of some non-axisymmetric distortion, it is difficult to detect using traditional means. More generally, if one treats the case of a constant elliptical ($m = 2$) distortion to the rotation curve by using two orthogonal components, one symmetric and one antisymmetric about the Sun-center line with individual ellipticities, the antisymmetric component can be constrained using several different types of observations (Kuijken & Tremaine 1991; Chapter 4). The symmetric component, however, is not as well constrained by current observations, and KT point out that even a relatively small symmetric ellipticity component can change derived Galactic rotation parameters by a large amount.

To judge the size of this effect for our data, we have fit the data used for Model B2 to the "standard" model of KT. This assumes a flat rotation curve, ellipticity constant with radius, and no antisymmetric ellipticity component. The last assumption might be checked from our data directly, but given the lopsided distribution of the currently known Cepheids fairly little information would be obtained. (Chapter 3 presents some new distant Cepheids toward $\ell = 60°$; with the addition of radial velocities, they should provide a strong constraint on this component.) The predicted mean radial velocities of the model are given by (KT, equation 24c)

$$v_r^* = v_c \left(\frac{1}{r} - 1\right) \sin \ell \cos b + c_\Psi v_c \left[\sin \ell + \sin(\phi - \ell)\right] \cos b, \qquad (2.11)$$

where v_c is the circular velocity, c_Ψ is the ellipticity of the symmetric component, and ϕ is the angle of the star measured from the Sun-center line in the direction of Galactic rotation ($= 180° - \ell - \alpha$) in Figure 2-20. Rewriting this in terms of parameters we use above, we have

$$v_r = v_c \left(\frac{1}{r} - 1\right) \sin \ell \cos b +$$

96
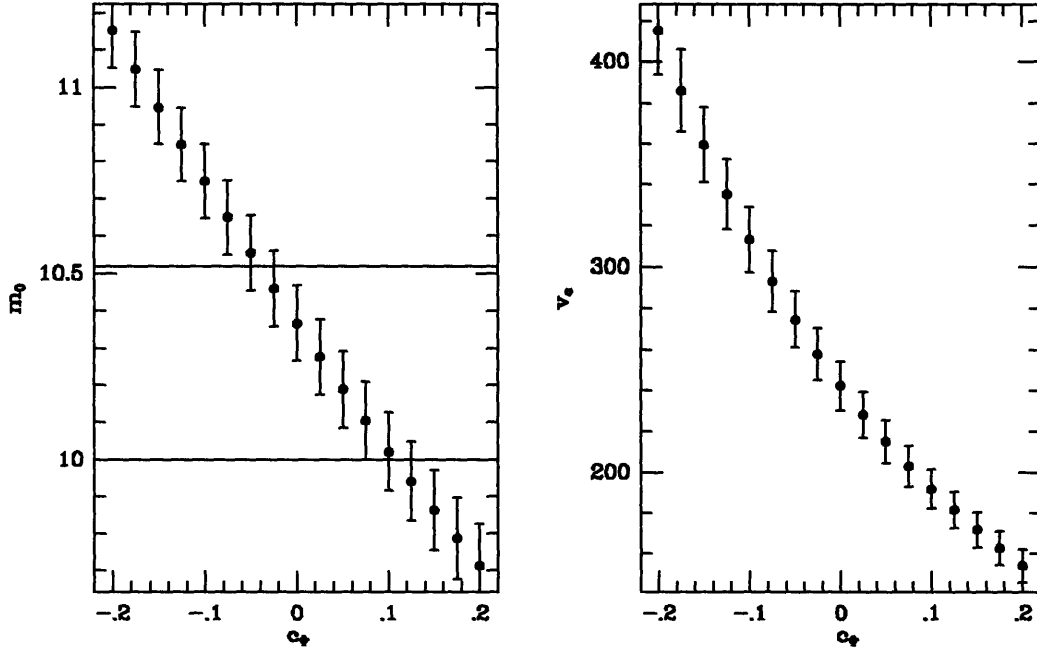
Figure 2-28: A plot of the best-fit model parameters as a function of ellipticity (symmetric component only). The left panel shows m_0, the right panel circular velocity. A flat rotation curve and constant ellipticity are assumed. The two horizontal lines represent 1-σ errors on other, non-kinematic distance measurements (Reid 1993).

$$+\frac{c_\Psi}{r}(2d\cos\ell - 1)\sin\ell$$

$$+ u_0 \cos\ell\cos b$$

$$- v_0 \sin\ell\cos b$$

$$- w_0 \sin b - \delta v_r\,. \tag{2.12}$$

As expected, if we fit for all six parameters (including c_Ψ) we find a covariance between $2AR_0$, m_0, and c_Ψ of ≈ 0.95—much too large to give any reasonable constraint on the parameters together.

We can, however, fix the ellipticity c_Ψ in the models, and solve for the other model parameters to see how ellipticity affects the model solutions. Figure 2-28 shows plots of m_0 and $2AR_0$ derived from our Model B2 data fit to equation 2.12. Also shown are upper and lower limits from a combination of non-kinematic GC distance estimates (Reid 1993). From this we can deduce a weak constraint on ellipticity: $-0.08 < c_\Psi < 0.14$. Alternatively, one can assume a value for the circular speed
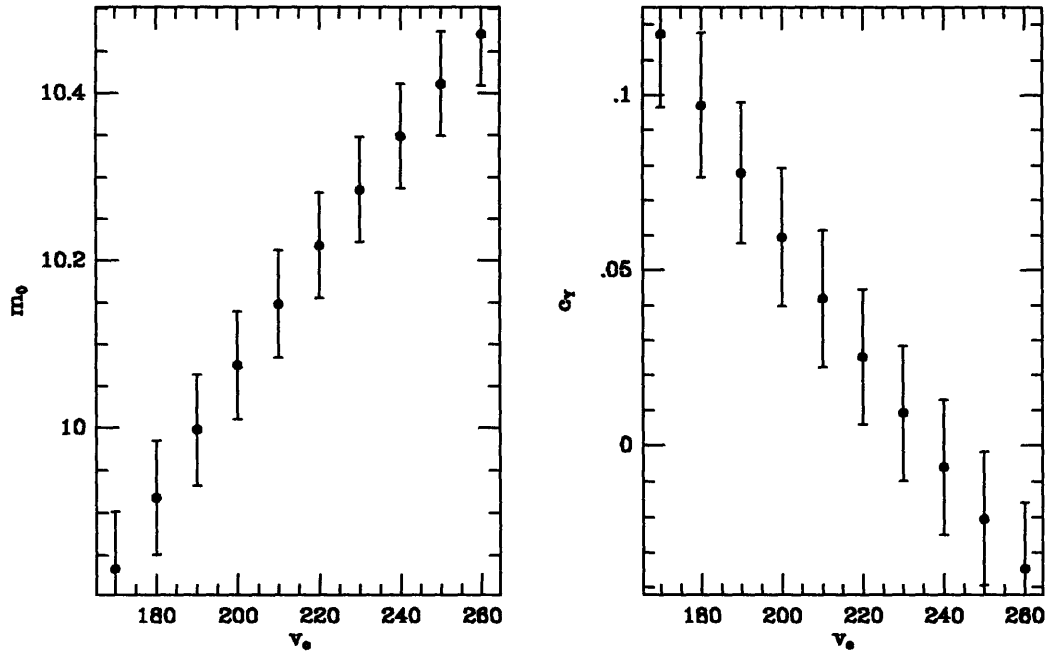
Figure 2-29: A plot of ellipticity and m_0 using v_c as the independent parameter.

and fit for the ellipticity and distance to the Galactic center; Figure 2-29 shows the resulting fits and statistical errors for these parameters. The IAU value for Θ_0 of 220 km s^{-1} implies $R_0 = 7.31 \pm 0.22$ kpc, $c_\Psi = 0.025 \pm 0.019$, and $A = 15.1 \pm 0.5$. These are statistical errors, of course, and assume an exact value of v_c; the covariance between v_c and m_0 makes the true uncertainties significantly larger.

2.6.4.2 Systematic Errors

To summarize systematic errors discussed above, we combine them into categories of calibration, metallicity, extinction, and model constraints. We estimate the uncertainty in the calibration of the V and K absolute magnitudes to a specific LMC modulus is about 0.10 mag in V and 0.05 mag in K (§2.6.2; since the K magnitudes have significant weight in our distance estimates, we take the overall uncertainty to be 0.08 mag. Since we have given our distance calibration in terms of a particular distance modulus of the LMC, our distances can be directly scaled to whatever value of LMC modulus one may choose. Nevertheless, we list separately an estimate of 0.1 mag error in LMC modulus (which is in turm mostly due to uncertainty in the Pleiades modulus) for comparison of these distances to others independent of the

LMC distance. It should be re-emphasized here that though an LMC distance of 18.50 is used as a convenient reference point, it is not arbitrary, and is in fact consistent with current estimates based on the cluster distance scale. As argued above, the changes in the PL relation due to metallicity differences between stars in the LMC and the Milky Way should be negligible considering other uncertainties. Systematic offsets due to uncertainties in the extinction laws are ≈ 0.06 mag for K, and an uncertainty in R_V of 0.15 translates to an uncertainty of ≈ 0.15 mag in V, leading to an estimated R_0 error of 0.11 mag in the present sample. We do not derive a formal uncertainty on the ellipticity, however we believe that at most $-0.08 < c_\Psi < 0.1$, corresponding to an uncertainty of 0.25 magnitude in R_0.

Taken together, this gives a combined systematic error (assuming each is statistically independent) of 0.14 mag, with an additional 0.1 for the LMC, and an additional 0.25 mag for possible ellipticity. The corresponding uncertainty associated with $2AR_0$, using the appropriate covariance, is 21 km s^{-1}, plus an additional 45 km s^{-1}for the weak limits on ellipticity.

2.7 Conclusions

With the goal of improving the estimates of the distance to the Galactic center, along with other parameters of Galactic rotation, we have measured new, accurate γ velocities for faint Milky Way Cepheids, most of which had no previous measurement in the literature. We also have measured radial velocities for the Cepheids discovered in the CKS survey, and reported new estimates of period, epoch, and $< K >$ for these stars. Adding this new data and other new measurements of reddening to the data compiled by CC, we have utilized axisymmetric models to determine, among other parameters, R_0 and $2AR_0$. Using a cluster distance scale comparable to a true distance modulus of 18.50 to the LMC, we find

$$R_0 = 7.75 \pm 0.37^{+0.52}_{-0.48} \text{ kpc}$$

$$2AR_0 = 245 \pm 12 \pm 21 \text{ km s}^{-1},$$

where the first error figure is due to internal error and the second to systematic error. We also find that, as noted by KT, an elliptical component to the rotation curve where the Sun lies near a major or minor axis is not constrained by our models, and can introduce a significant additional uncertainty to any kinematic models. The additional uncertainty associated with an elliptical distortion, if one exists, should be no more than $\approx$ 12% in R_0 and 45 km s^{-1} in $2AR_0$.

The uncertanties in estimates of R_0 using the Cepheid variables are currently dominated by systematic errors. The largest observational uncertainties currently lie in the correction for interstellar extinction; most of the leverage in determining R_0 comes from the most distant stars, which are also the most heavily reddened and therefore have larger uncertainties in dereddened magnitude. Obtaining near-infrared photometry for all of the Cepheids in the sample seems the most promising course for improving the accuracy of the distance measurements.

There also remain significant uncertainties in R_0 estimates from rotation curve modeling due to the possibile existence of non-axisymmetric components. This issue can be addressed by finding new tracers, Cepheids being particularly good candidates, in areas of the Galaxy that help to constriain the extent of any deviations from axisymmetry. We conduct one such project in Chapter 3, with the goal of finding distant Cepheids in the inner Galaxy that help to constrain the symmetry of the rotation curve. Beyond this survey, promising directions to look for extremely distant Cepheids are along $|\ell| \simeq 35°$—moderately distant Cepheids probe the inner rotation curve, and Cepheids at large distances can serve to constrain the ellipticity of the Galactic rotation curve. Due to the likelihood of extreme extinction in these directions, it will be necessary to conduct such surveys in the near-infrared.

2.8 References

Abt, H. A. 1978, PASP, **90**, 309

Avruch, I. M. 1991, M.S. Thesis, Massachusetts Institute of Technology.

Barnes, T. G., Moffett, T. J., & Slovak, M. H. 1986, PASP, **98**, 223

Barnes, T. G., Moffett, T. J., & Slovak, M. H. 1988, ApJS, **66**, 43

Bevington, P. R. 1969, *Data Reduction and Error Analysis for the Physical Sciences* (New York: McGraw-Hill)

Böhm-Vitense, E. 1994, AJ, **107**, 673

Caldwell, J. A. R. & Coulson, I. M. 1986, MNRAS, **218**, 223

Caldwell, J. A. R., & Coulson, I. M. 1987, AJ, **93**, 1090 (CC)

Caldwell, J. A. R., Keane, M. J., & Schechter, P. L. 1991, AJ, **101**, 1763 (CKS)

Carney, B. W., Storm, J., & Jones, R. V. 1992, ApJ, **386**, 663

Clayton, J. A., Cardelli, G. C., & Mathis, J. S. 1989, ApJ, **345**, 245

Cohen, J. G., Frogel, J. A., Persson, S. E., & Elias, J. H. 1981, ApJ, **249**, 481

Coker, R., Madore, B., Mould, J., Oke, J. B., Picard, A., Huchra, J., & Latham, D. 1989, PASP, **101**, 594

Dean, J. F., Warren, P. R., & Cousins, A. W. J. 1978, MNRAS, **183**, 569

Delhaye, J. 1965, in Galactic Structure, eds. A. Blaauw & M. Schmidt (Chicago: U. of Chicago), p. 61

Evans, N. R. 1984, ApJ, **281**, 760

Feast, M. W., & Walker, A. R. 1987, ARA&A, **25**, 345

Fehrenbach, C., & Duflot, M. 1980, A&AS, **39**, 31

Fernie, J. D. 1987, AJ, **94**, 1003

Fernie, J. D. 1990, ApJS, **72**, 153

Fernie, J. D., & McGonegal, R. 1983, ApJ, **275**, 732

Filippenko, A. V. 1982, PASP, **94**, 715

Fletcher, J. M., Harris, H. C., McClure, R. D., & Scarfe, C. D. 1982, PASP, **94**, 1017

Freedman, W. L., & Madore, B. F. 1990, ApJ, **365**, 186

Gieren, W. P., Barnes, T. G., & Moffett, T. J. 1989, ApJ, **342**, 467

101

Gieren, W. P., & Fouqué, P. 1993, AJ, **106**, 734

Harris, H. C. 1985a, in Stellar Radial Velocities, eds. A. G. D. Phillip & D. W. Latham (Schenectady, NY: L. Davis), p. 283

Harris, H. C. 1985b, AJ, **90**, 756

Harris, H. C., Welch, D. L., Kraft, R. P., & Schmidt, E. G. 1987, AJ, **94**, 403

Hensberge, H., & Verschueren, W. 1989, Messenger, **58**, 51

Hindsley, R., & Bell, R. A. 1986, PASP, **98**, 881

Hindsley, R. B., & Bell, R. A. 1990, ApJ, **348**, 673

Iben, I., & Renzini, A. 1984, Phys. Rept., **105**, 329

Imbert, M., Andersen, J., Ardeberg, A., Duquennoy, A., Lindgren, H., Maurice, E., Mayor, M., Mermilliod, J. C., Nordström, B., & Prévot, L. 1989, A&AS, **81**, 339

Joy, A. H. 1939, ApJ, **89**, 356

Kholopov, P. N., Samus, N. N., Frolov, M. S., Goranskij, V. P., Gorynya, N. A., Kireeva, N. N., Kukarkina, N. P., Kurochkin, N. E., Medvedeva, G. I., Perova, N. B., & Shugarov, S. Yu. 1988, General Catalogue of Variable Stars, 4th Ed. (Moscow: Nauka)

Kovács, G., Kisvarsányi, G., & Buchler, R. B. 1990, ApJ, **351**, 606

Kraft, R. P., & Schmidt, M. 1963, ApJ, **137**, 249

Kuijken, K., & Tremaine, S. 1991, in *Dynamics of Disk Galaxies*, ed. B. Sundelius (Göteburg: Göteburg Univ. Press), p. 71

Kuijken, K., & Tremaine, S. 1994, ApJ, **421**, 178 (KT)

Laney, C. D., & Stobie, R. S. 1986, MNRAS, **222**, 449

Laney, C. D., & Stobie, R. S. 1993a, MNRAS, **260**, 408

Laney, C. D., & Stobie, R. S. 1993b, MNRAS, **263**, 921

Laney, C. D., & Stobie, R. S. 1994, MNRAS, **266**, 441

Latham, D. W. 1990, private communication.

Latham, D. W., Mazeh, T., Stefanik, R. P., Mayor, M., & Burki, G. 1989, Nature, **339**, 38

Madore, B. F., & Freedman, W. L. 1991, PASP, **103**, 933

Mateo, M., & Schechter, P. L. 1989, in 1st ESO/ST-ECF Data Analysis Workshop,

eds. P. J. Grosbøl, F. Murtagh, & R. H. Warmels, p. 69

Maurice, E., Mayor, M., Andersen, J., Ardeberg, A., Benz, W., Lindgren, H., Imbert, M., Martin, N., Nordström, B., & Prévot, L. 1984, A&AS, **57**, 275

Mayor, M., & Maurice, E. 1985, in Stellar Radial Velocities, eds. A. G. D. Phillip & D. W. Latham, p. 299

McCarthy, J. K. 1988, Ph.D. Thesis, California Institute of Technology.

Mermilliod, J. C., Mayor, M., & Burki, G. 1987, A&AS, **70**, 389 (MMB)

Metzger, M. R., Caldwell, J. A. R., McCarthy, J. K,, & Schechter, P. L. 1991, ApJS, **76**, 803

Metzger, M. R., Caldwell, J. A. R., & Schechter, P. L. 1992, AJ, **103**, 529

Mihalas, D., & Binney, J. 1981, *Galactic Astronomy* (New York: Freeman)

Moffett, T. J., & Barnes, T. G. 1985, ApJS, **58**, 843

Moffett, T. J., & Barnes, T. G. 1987, PASP, **99**, 1206

Olson, B. I. 1975, PASP, **87**, 349

Reid, M. J. 1993, ARA&A, **31**, 345

Sargent, W. L. W., Schechter, P. L., Boksenberg, A., & Shortridge, K. 1977, ApJ, **212**, 326

Scarfe, C. D., Batten, A. H., & Fletcher, J. M. 1990, Publ. Dom. Astrophys. Obs., **28**, 21

Schechter, P. L., Avruch, I. M., Caldwell, J. A. R., & Keane, M. J. 1992, AJ, **104**, 1930

Shectman, S. A., Price, C., & Thompson, I.B. 1985, in Annual Report of the Director, Mount Wilson and Las Campanas Observatories, ed. G. W. Preston (Pasadena: MWLCO), p. 52.

Stefanik, R. P. 1990, private communication

Stothers, R. B. 1988, ApJ, **329**, 712

Stumpff, P. 1980, A&AS, **41**, 1

Turner, D. G. 1976, AJ, **81**, 1125

Turner, D. G. 1985, in Cepheids: Theory and Observations, ed. B. F. Madore (Cambridge: Cambridge), p. 209.

Welch, D. L., Wieland, F., McAlary, C. W., McGonegal, R., Madore, B. F., McLaren,

R. A., & Neugebauer, G. 1984, ApJS, **54**, 547

Chapter 3

A Survey for Distant Galactic Cepheids

3.1 Survey Design

As we saw in the last chapter, the distribution of known Cepheids in the Galactic disk is quite lopsided: a large fraction of the distant Cepheids, and hence most of the leverage in determining R_0 from kinematic models, lies in the region $270° < \ell < 360°$ (sometimes referred to as the "southern" Milky Way, due to the equatorial latitude of the Galactic plane in this area). Adding only eight well-placed Cepheids to the models significantly reduced the uncertainty in the measurement of R_0, and in fact almost all of the weight in the distance measurement rested on these new Cepheids. To confirm the distance measurement, one would like to obtain additional Cepheids with good R_0 leverage in some other area, as there is concern that some peculiarity in the properties of the small region containing the new Cepheids (such as a streaming motion, unusual dust properties, etc.) may systematically affect the estimate of R_0. One such source of uncertainty would be a large-scale deviation of the true rotation curve from axisymmetry (e.g. Blitz & Spergel 1991; Kuijken & Tremaine 1994), as most models assume circular rotation. In Chapter 2 we showed that the existing Cepheid sample is inadequate for measuring such deviations from axisymmetry, and we suggested a two-pronged strategy to extend the sample so that each of two ellipticity components could be measured directly. To address the issue of obtaining additional Cepheids to help reinforce our measurement of R_0, and to provide additional constraints on the rotation curve ellipticity, we conducted a survey

for Cepheids toward $\ell = 60°, b = 0°$.

The main goal of our survey was to find a number of Cepheids useful for improving the measurement of the distance to the Galactic center. The survey is similar in many respects to the one conducted in the southern hemisphere by Caldwell, Keane, and Schechter (1991, hereafter CKS), and the design of this survey is based in part on information from the CKS survey, in order to improve the efficiency by which Cepheids can be recovered. Wide-area surveys requiring accurate photometry of a large number of stars have only recently become possible due to the availability of large charge-coupled device cameras combined with inexpensive computers that can reduce the large amount of data collected. The new CCDs cover a large area of sky while providing enough spatial resolution to allow accurate photometry, even in the crowded fields associated with the Galactic plane. At the time the survey was proposed, one of the best facilities available was the KPNO 0.9m telescope/Tektronix 2048^2 CCD combination: this configuration can cover a square degree in seven pointings with 0.7 arcsecond sampling. We had initially started a survey during summer shutdown at the McGraw-Hill 1.3m telescope at MDM Observatory, but the only detector then available covered an area of sky 20 times smaller: each night on the KPNO 0.9m with the large CCD was the equivalent of 20 nights at MDM! Even with this high efficiency, however, only a limited area of the Galactic plane can be covered in a single observing run. We therefore took some care in the design of the survey to maximize the payoff in terms of Galactic structure study.

3.1.1 Area Selection

Our goal of finding Cepheids to make a precise measurement of R_0 requires us to look at great distance ($\gtrsim 0.5R_0$), as these stars will contribute the most leverage to R_0 (see Chapter 2). Cepheids that lie along the solar circle have the particular advantage of constraining R_0 independent of the rotational velocity. Given a fixed accuracy in measuring distances to the tracer, Schechter *et al.* (1992) find that for stars lying near the solar circle, the uncertainty in $d \log R_0$ caused by the intrinsic velocity dispersion of the tracer (~ 10 km s^{-1} in the disk for Cepheids) is minimized in the northern

106

Milky Way toward $\ell \sim 35°$. Unfortunately, extinction to these stars due to dust can be quite large: they lie at a distance of over $1.7R_0$, and the line of sight passes within $0.6R_0$ of the Galactic center. Further, measuring an asymmetry in the rotation curve is much simplified by having tracers symmetric about the Galactic center. We therefore chose to conduct the survey near $\ell = 60°$, reducing the total extinction and complementing the Caldwell, Keane, & Schechter (1991) survey toward $\ell = 300°$.

Limits on the survey latitude can be set based on the measured distribution of local Cepheids, which have a scale height of 70 pc (Kraft & Schmidt 1963). At a distance of R_0 (about 7.7 kpc, see Chapter 2) this corresponds to roughly $0°5$, thus to find Cepheids at a distance of R_0 we should concentrate to regions having $|b| < 0°5$. Indeed, of the Cepheids discovered in the CKS survey, all but one were within this latitude range. One might argue that since the extinction close to the plane is very high, we should avoid $b = 0°$ and look slightly away, improving the depth of our survey. We would point out, however, that the dust is unavoidable: the vertical scale height of Cepheids is similar to that of dust and gas, and so to reach distant Cepheids one must necessarily look through the dust as well. If one moves out of the plane, the integrated dust decreases, but the survey becomes less efficient as the Cepheid density drops.

The distribution of dust is not uniform, however, so one can gain an advantage by choosing lines of sight having relatively low extinction. CKS were fortunate to take advantage of one of the least heavily reddened lines of sight in the inner Galaxy; alas, there is no comparable region near $\ell = 60°$. We can nonetheless use existing survey data to provide an idea of which areas have lower extinction, and give these areas priority in our Cepheid survey. One method of estimating extinction is to compare the number of faint sources (or total source flux) in different regions. Since the stellar luminosity function $\Phi(M)$ is shallower than an $n = 3/2$ power law, the number of faint sources will increase dramatically as the extinction decreases. Surveys at optical wavelengths (e.g. the Palomar Observatory Sky Survey), however, provide little information on dust at a distance, as most of the sources seen will be closer than the Cepheids we seek. This is true particularly if the total extinction is large:
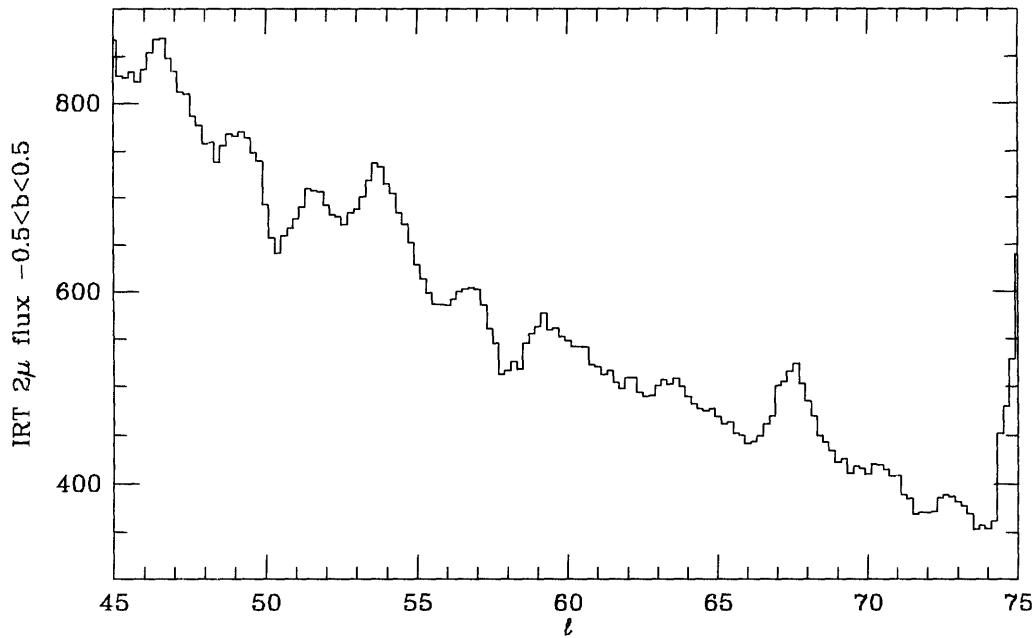
Figure 3-1: Spacelab IRT flux in the Galactic plane, integrated over one degree in latitude (raw data provided by S. Kent). The flux units are arbitrary. A general trend as a function of longitude can be seen along with smaller-scale variations. The effective resolution is about 1 degree; some peaks may be due to strong unresolved point sources. Note the strong peaks near $\ell = 68°$ and $\ell = 54°$, and the low brightness near $\ell = 58°$.

a Cepheid at a distance of R_0 with moderate extinction would have an apparent magnitude of $m_V \simeq 16$ mag, but we would not expect any significant contribution from other stars until ~ 5 magnitudes fainter, since Cepheids are at the extreme bright end of the luminosity function (Allen 1973). The optical surveys do have limited use for detecting nearby, dense clouds (light from any more distant objects must traverse these as well), but we are more interested in minimizing the total extinction over many kiloparsecs.

Near-infrared surface brightness maps are more useful in this regard. The extintion is significantly reduced at these wavelengths, and thus the surface brightness will have a greater contribution from stars at large distances. The surface brightness variations (after subtracting a smooth Galactic component, which varies with longitude) are thus more closely correlated to the extinction out to many kiloparsecs. To help select regions of interest, we examined data from the Spacelab IRT 2μm survey of the Galactic plane (Kent et al. 1992), which has an effective resolution of about 1 degree. Figure 3-1 shows a plot of flux integrated over $|b| < 0.^{\circ}5$ as a function of longitude. Most of the structure appears on scales larger than the effective resolution, relieving some concern about contamination from bright point sources.

Regions of potentially low extinction can also be mapped using data on molecular CO emission. The distributions of gas and dust in the Galaxy have been shown to be fairly well correlated (e.g. Hilditch, Hill, & Barnes 1976; Burstein & Heiles 1978, Heiles, Kulkarni, & Stark 1981); CO is a particularly good tracer of dust as both tend to survive under similar physical conditions. We examined data from the survey of Dame et al. (1987) to generate column densities of CO gas as a function of longitude in a 2-degree-wide band at the plane, shown in Figure 3-2. Another advantage of using gas is that the surveys effectively give column densities in individual narrow bands of velocity (1.3 km s^{-1} in the Dame et al. survey), allowing us to select the depth to which we measure the density. Since all of the gas on the near side of the solar circle has positive rotational velocity with respect to the LSR, and more distant gas has negitive velocity, by integrating only gas with positive velocity we produce a total CO column density out to the solar circle. This provides a better
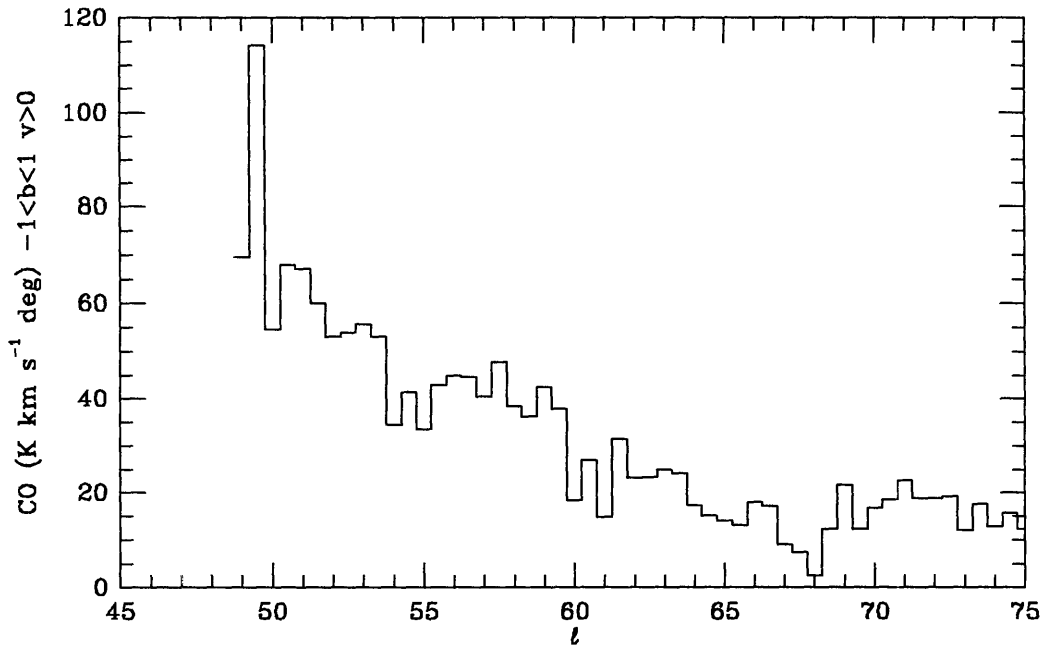
Figure 3-2: Galactic CO emission integrated over $|b| < 1°$, including only gas with positive LSR velocities. Note the similarity of the features between this map and the 2μ map, inverted, so that high 2μ corresponds to low CO emission, as would be expected if the features were caused by differential extinction.

indication of the total extinction between the Sun and the most interesting Cepheids. Several features can be seen in common between the near-infrared and CO maps: as an example, the strong 2μ emission near $\ell = 68°$ corresponds to a local minimum of CO column density, precisely what we would expect if this feature were caused by differential extinction.

Using a combination of these two data sets we assigned a relative priority to different areas along the Galactic plane in the vicinity of $\ell = 60°$, $b = 0°$. We divided this region of the plane into 98 regions of 1300 arcseconds square with borders aligned north-south. This is the size and orientation of the Tektronix CCD on the KPNO 0.9m telescope, allowing for a small overlap between regions (see §3.2). A list of the regions with numeric designations and coordinates is given in Table 3.1.

110

Table 3.1: Galactic Plane Regions, $50° < \ell < 70°$

Region ID	Edge $\ell°$	Center $\ell°$	Center $b°$	J2000 R.A	J2000 Dec
01	60.00	60.09	-0.16	19 44 41.6	+23 53 26
02	60.00	59.91	0.16	19 43 06.8	+23 53 26
03	60.42	60.51	-0.16	19 45 36.5	+24 15 06
04	60.42	60.33	0.16	19 44 01.4	+24 15 06
05	60.83	60.92	-0.16	19 46 31.7	+24 36 45
06	60.83	60.74	0.16	19 44 56.3	+24 36 45
07	61.25	61.34	-0.16	19 47 27.2	+24 58 23
08	61.25	61.16	0.16	19 45 51.6	+24 58 23
09	61.67	61.76	-0.16	19 48 23.0	+25 20 00
10	61.67	61.58	0.16	19 46 47.1	+25 20 00
11	62.08	62.18	-0.16	19 49 19.2	+25 41 36
12	62.08	61.99	0.16	19 47 43.0	+25 41 36
13	62.50	62.59	-0.16	19 50 15.7	+26 03 10
14	62.50	62.41	0.16	19 48 39.2	+26 03 10
15	62.92	63.01	-0.16	19 51 12.5	+26 24 42
16	62.92	62.83	0.16	19 49 35.8	+26 24 42
17	63.34	63.43	-0.16	19 52 09.8	+26 46 14
18	63.34	63.25	0.16	19 50 32.7	+26 46 14
19	63.75	63.84	-0.16	19 53 07.3	+27 07 44
20	63.75	63.66	0.16	19 51 30.0	+27 07 44
21	64.17	64.26	-0.16	19 54 05.3	+27 29 12
22	64.17	64.08	0.16	19 52 27.6	+27 29 12
23	64.59	64.68	-0.16	19 55 03.6	+27 50 39
24	64.59	64.50	0.16	19 53 25.6	+27 50 39
25	65.00	65.09	-0.16	19 56 02.3	+28 12 04
26	65.00	64.91	0.16	19 54 24.0	+28 12 04
27	65.42	65.51	-0.16	19 57 01.5	+28 33 28
28	65.42	65.33	0.16	19 55 22.8	+28 33 28
29	65.84	65.93	-0.16	19 58 01.0	+28 54 50
30	65.84	65.75	0.16	19 56 22.0	+28 54 50
31	66.25	66.34	-0.16	19 59 00.9	+29 16 11
32	66.25	66.16	0.16	19 57 21.5	+29 16 11
33	66.67	66.76	-0.16	20 00 01.3	+29 37 30
34	66.67	66.58	0.16	19 58 21.6	+29 37 30
35	67.09	67.18	-0.16	20 01 02.0	+29 58 47
36	67.09	67.00	0.16	19 59 22.0	+29 58 47
37	67.51	67.60	-0.16	20 02 03.2	+30 20 02
38	67.51	67.42	0.16	20 00 22.8	+30 20 02
39	67.92	68.01	-0.16	20 03 04.9	+30 41 16
40	67.92	67.83	0.16	20 01 24.1	+30 41 16
41	68.34	68.43	-0.16	20 04 07.0	+31 02 28
42	68.34	68.25	0.16	20 02 25.9	+31 02 28
43	68.76	68.85	-0.16	20 05 09.6	+31 23 38
44	68.76	68.67	0.16	20 03 28.1	+31 23 38
45	69.17	69.26	-0.16	20 06 12.7	+31 44 46
46	69.17	69.08	0.16	20 04 30.7	+31 44 46
47	69.59	69.68	-0.16	20 07 16.2	+32 05 52
48	69.59	69.50	0.16	20 05 33.9	+32 05 52
49	70.01	70.10	-0.16	20 08 20.2	+32 26 56
50	70.01	69.92	0.16	20 06 37.5	+32 26 56

111

Table 3.1—*Continued*

| Region | Edge | Center | | J2000 | |
ID	$\ell°$	$\ell°$	$b°$	R.A	Dec
51	59.58	59.67	-0.16	19 43 47.0	+23 31 44
52	59.58	59.49	0.16	19 42 12.5	+23 31 44
53	59.17	59.26	-0.16	19 42 52.8	+23 10 01
54	59.17	59.08	0.16	19 41 18.5	+23 10 01
55	58.75	58.84	-0.16	19 41 58.8	+22 48 17
56	58.75	58.66	0.16	19 40 24.8	+22 48 17
57	58.33	58.42	-0.16	19 41 05.1	+22 26 32
58	58.33	58.24	0.16	19 39 31.4	+22 26 32
59	57.92	58.01	-0.16	19 40 11.7	+22 04 46
60	57.92	57.82	0.16	19 38 38.2	+22 04 46
61	57.50	57.59	-0.16	19 39 18.6	+21 42 58
62	57.50	57.41	0.16	19 37 45.3	+21 42 58
63	57.08	57.17	-0.16	19 38 25.7	+21 21 10
64	57.08	56.99	0.16	19 36 52.7	+21 21 10
65	56.66	56.75	-0.16	19 37 33.2	+20 59 20
66	56.66	56.57	0.16	19 36 00.3	+20 59 20
67	56.25	56.34	-0.16	19 36 40.8	+20 37 30
68	56.25	56.16	0.16	19 35 08.2	+20 37 30
69	55.83	55.92	-0.16	19 35 48.7	+20 15 39
70	55.83	55.74	0.16	19 34 16.4	+20 15 39
71	55.41	55.50	-0.16	19 34 56.9	+19 53 46
72	55.41	55.32	0.16	19 33 24.7	+19 53 46
73	55.00	55.09	-0.16	19 34 05.3	+19 31 53
74	55.00	54.91	0.16	19 32 33.4	+19 31 53
75	54.58	54.67	-0.16	19 33 14.0	+19 09 59
76	54.58	54.49	0.16	19 31 42.2	+19 09 59
77	54.16	54.25	-0.16	19 32 22.8	+18 48 04
78	54.16	54.07	0.16	19 30 51.3	+18 48 04
79	53.75	53.84	-0.16	19 31 31.9	+18 26 08
80	53.75	53.66	0.16	19 30 00.6	+18 26 08
81	53.33	53.42	-0.16	19 30 41.2	+18 04 11
82	53.33	53.24	0.16	19 29 10.1	+18 04 11
83	52.91	53.00	-0.16	19 29 50.7	+17 42 13
84	52.91	52.82	0.16	19 28 19.8	+17 42 13
85	52.49	52.58	-0.16	19 29 00.5	+17 20 15
86	52.49	52.40	0.16	19 27 29.7	+17 20 15
87	52.08	52.17	-0.16	19 28 10.4	+16 58 16
88	52.08	51.99	0.16	19 26 39.8	+16 58 16
89	51.66	51.75	-0.16	19 27 20.5	+16 36 16
90	51.66	51.57	0.16	19 25 50.1	+16 36 16
91	51.24	51.33	-0.16	19 26 30.8	+16 14 15
92	51.24	51.15	0.16	19 25 00.6	+16 14 15
93	50.83	50.92	-0.16	19 25 41.4	+15 52 14
94	50.83	50.74	0.16	19 24 11.3	+15 52 14
95	50.41	50.50	-0.16	19 24 52.0	+15 30 12
96	50.41	50.32	0.16	19 23 22.1	+15 30 12
97	49.99	50.08	-0.16	19 24 02.9	+15 08 09
98	49.99	49.90	0.16	19 22 33.1	+15 08 09

3.1.2 Cepheid Detection

In addition to selecting areas with relatively low obscuration we can observe at a wavelength that is less affected by it. A longer-wavelength band such as I ($\sim$ 800 nm) suffers only about 60% of the extinction in *magnitudes* than does V ($\sim$ 530 nm), and less than half that of B ($\sim$ 420 nm) (see, e.g., Clayton, Cardelli, & Mathis 1989). While the situation improves even more at longer wavelengths, the existing detectors become significantly smaller: for surveys in the K-band (2.2 μm) the largest available detectors had sky dimensions 5 times smaller (and at poorer resolution) than the large optical CCDs, which would reduce the survey efficiency by a factor of over 20. Another competing factor to consider is the pulsation amplitude, which is significantly larger at blue wavelengths ($\sim$ 1.2 mag at B) than in I ($\sim$ 0.4 mag; Freedman & Madore 1991). Even so, the extra amplitude does not help us to find the less heavily reddened Cepheids where the photometric accuracy in I is more than sufficient to detect pulsation. For more heavily-reddened stars the flux in bluer bands drops dramatically, and requires very long exposures even to recover the objects. We therefore obtain the best detection sensitivity over a wide range of distance and extinction in the reddest bands we can use. For optical CCDs this is the I-band, and therefore we decided to observe in I for the primary survey, as did CKS in their survey.

The effects of extinction make dynamic range a particularly important issue. In the absense of extinction, the apparent brightness of a star at $0.1R_0$ and one at $1.0R_0$ differ by a factor of 100. However, it would not be unreasonable to encounter 5 magnitudes of extinction at I over $0.9R_0$ (7 kpc) in the inner galaxy, making the distant cousin appear 10,000 times fainter. The exposure times were therefore chosen to reach as faint as possible, while keeping nearby bright Cepheids that might lie in the survey regions undiscovered just under saturation. All but one of the Cepheids discovered in the CKS survey were fainter than 11th magnitude in I, typically with 2 or more magnitudes of extinction. To make our bright end cutoff, we tried to insure that we would recover a 10-day period Cepheid at a minimum distance of $0.3R_0$ under 2 magnitudes of extinction in I. Thus we set our exposures to a maximum time

that will place a star of I = 10.5 mag at the saturation limit, which was quoted as 240,000 photoelectrons pixel^{-1} for the Tektronix CCD. Cepheids much brighter than this would likely have been discovered previously, given the distribution of known Cepheid magnitudes (Kholopov *et al.* 1988); the faintest known Cepheid in our survey region, GX Sge, has $\langle V \rangle$ = 12.4 and $I \simeq 10.3$. Our faint magnitude limit is effectively determined by this exposure time and the brightness of the sky.

One significant difference between this survey and that of CKS was the decision to obtain data in the V band for each field at several epochs. This was motivated by the realization, during the follow-up to the CKS survey, that the characteristic pattern of color change of a Cepheid over its pulsation cycle is a useful way to distinguish Cepheids from other types of variable stars. In the CKS survey, stars were selected for follow-up photometry without the benefit of knowing the color change. If one were to have this information a priori, many variable stars could be eliminated before followup photometry was conducted, and a larger sample of promising candidates could therefore be examined. However, if V frames are observed throughout the survey, the total area covered would be cut in half (the V exposures would have to be at least as long as those in I). Our compromise was to observe V in each field for every three I observations, providing a reasonable chance of measuring a color change (which requires at least two points) while reducing sky coverage by only one quarter.

Another issue was the distribution of our individual observations over time. Identifying a Cepheid requires both detecting its variability at a sufficient confidence level and recognizing it as a Cepheid from the properties of its light curve (such as a fast rise/slow decline, color change, etc.) While better sampling provides more information on the light curve shape, CKS showed that 7 epochs of observations were sufficient to recognize a Cepheid, assuming coverage spaced over the entire cycle. Cepheids range in period roughly between 3 and 70 days, and the number distribution is heavily skewed towards shorter periods (Feast & Walker 1987). To obtain reasonable phase coverage of longer period Cepheids, the baseline (number of days between the first and last observation) should be as long as possible, and observations must be made frequently enough to sample the short-period Cepheids. In practice the

latter criterion is met without difficulty, as one can observe each field once per night or on every other night. The solution we chose was to observe each field once per night for four nights, pause for four nights, and observe again for four nights. This provides a baseline of 11 days, which should allow detection of Cepheids with up to 22 day periods (see §3.3), while providing adequate phase coverage for shorter-period Cepheids. It also provides a duration and schedule that the allocation committee might award on the 0.9m telescope. When we were scheduled observing time for the project, the time was broken into three nights on, two nights off, and five nights on, which lowered slightly our sensitivity to long-period Cepheids.

3.2 The Survey

3.2.1 Observations

Observations for the survey were taken with the 0.9m telescope at Kitt Peak National Observatory on the nights of June 9–11 and 13–18, 1992, using a Tektronix 2048^2 CCD. The detector scale was 0.69 arcseconds per pixel, giving a field of $\approx$ 23.5 arcminutes square (0.15 square degrees). The regions observed each night and the filters used are listed in Table 3.2. We were able to cover a total area of approximately 6 square degrees over a single night. The observing efficiency was limited primarily by the readout time of the chip and the rate at which the telescope could be moved between fields; a faster readout, automated repositioning, or possibly drift scanning would have improved observing efficiency. Figures 3-3 to 3-5 show star maps made using the HST Guide Star Catalog (Lasker *et al.* 1990, Russell *et al.* 1990), with surveyed regions outlined. Clouds prevented us from observing for part of night 6 (June 15) and all of night 9 (June 18). When telescope hardware problems occurred on two nights that limited the amount of usable observing time, first priority was given to acquiring the full set of I observations; for this reason no V observations were taken on night 2. Night 4 was fortuitous: we were given the last half of this night as additional time, the first half having been assigned as a "public observing night." After seeing some very nice images of the Ring Nebula and Jupiter through

Table 3.2: Observation Log

Region	Night							
	1	2	3	4	5	6	7	8
JD[a]	82	83	84	86	87	88	89	90
FWHM "	1.4	1.4	2.5	2.0	1.7	2.2	1.8	1.4
	Filters Observed							
01	VI	I	I	I	VI		I	VI
02	I	I	I	I	VI		VI	VI
03	VI	I	I	I	VI		I	VI
04	VI	I	I	I	VI		I	VI
05	VI	I	I	I	VI		I	VI
06	VI	I	I	I	VI		I	VI
07	VI	I	I	I	VI		I	VI
08	VI	I	I	I	VI		I	VI
15	I		VI	I	VI	I	I	VI
16	I	I	VI	I	I	VI	I	VI
17	I	I	VI	I	I	I	VI	I
18	I	I	VI	I	I	I	VI	VI
19	I	I	VI	I	I	VI	I	VI
20	I	I	VI	I	I	VI	I	I
21	I	I	VI	I	I	VI	I	I
22	I	I	VI	I	I	VI	I	I
23	I	I	VI	I	I	VI	I	I
24	I	I	VI	I	I	VI	I	I
35	I	I	I	VI	I	I	VI	I
36	I	I	I	VI	I	I	VI	I
37	I	I	I	VI	I	I	VI	I
38	I	I	I	VI	I	I	VI	I
51	VI	I	I	I	VI		I	VI
52	VI	I	I	I	VI		I	VI
53	VI	I	I	I	VI		I	VI
54	VI	I	I	I	VI		I	VI
55	VI	I	I	I	VI		I	VI
56	VI	I	I	I	VI		I	VI
61	I	I	I	VI	I		VI	I
62	I	I	I	VI	I		VI	I
63	I	I	I	VI	I		VI	I
64	I	I	I	VI	I		VI	I
65	I	I	I	VI	I		VI	I
66	I	I	I	VI	I		VI	I
75		I	I	I	I	I	VI	I
76		I	I	VI	I	I	VI	I
77			I	VI	I	I	VI	I
78			I	VI	VI	I	VI	I
81	I	I	I	VI	I	VI	I	VI
82	I	I	I	VI	I	VI	I	VI
83	I	I	I	VI	I	VI	I	VI
84	VI	I	I	VI	I	VI	I	VI

[a] Julian date minus 2,448,700

the eyepiece, and after the "public" had left, our field had just come up and we were able to complete a full set of observations in the remaining hours.

Exposure times were typically 40 s for I and 60 s for V, but were increased during periods of poor seeing to compensate for the effective increase in noise (and due to the reduced danger of saturating bright stars). The V filter used was a glass filter from the Kitt Peak "Harris" set, the I was a "Cousins" interference filter. Traces of the filter response curves are given by Schoening et al. (1991). Photometric standards of Landolt (1992) and Christian et al. (1985) were observed at the beginning and end of each night when possible. Images of both the twilight sky and an illuminated dome spot were taken each night in both filters to allow correction of the detector response to an even illumination level.

A significant problem with the images was the variation of the point spread function across the chip. The telescope focal plane was not flat with respect to the CCD, which caused the focus to vary from the center to the edge. The astigmatism (and, as apparent from the images, some coma) present in the optics produced out-of-focus images that were elongated in the NW-SE direction on one side of focus, and NE-SW on the other side. If the focus was properly adjusted at the center of the chip, the images at the corners were significantly distorted. Figure 3-6 shows the point spread function near the center and corner of the chip. Each plot is a composite of 10 stars, created by subpixelizing, interpolating, centroiding on the peak, and co-adding a region around each star. The contours shown are logarithmic at $\sqrt{2}$ intervals; the third contour from the center is the half-maximum. The image distortions are particularly troublesome as they constantly change: as the temperature varies through the night, the focus drifts and has to be re-adjusted. Between corrections, however, the PSF will shift shape as the focus shifts, with most areas typically becoming more elongated. Even if the focus could be tracked perfectly, the relative contribution of the astigmatism to the PSF shape is a function of the atmospheric seeing, which also varies throughout the observing run.

The PSF variation across the chip required some extra care in the data reduction, as described below. During the observing run, we attempted to reduce the problem
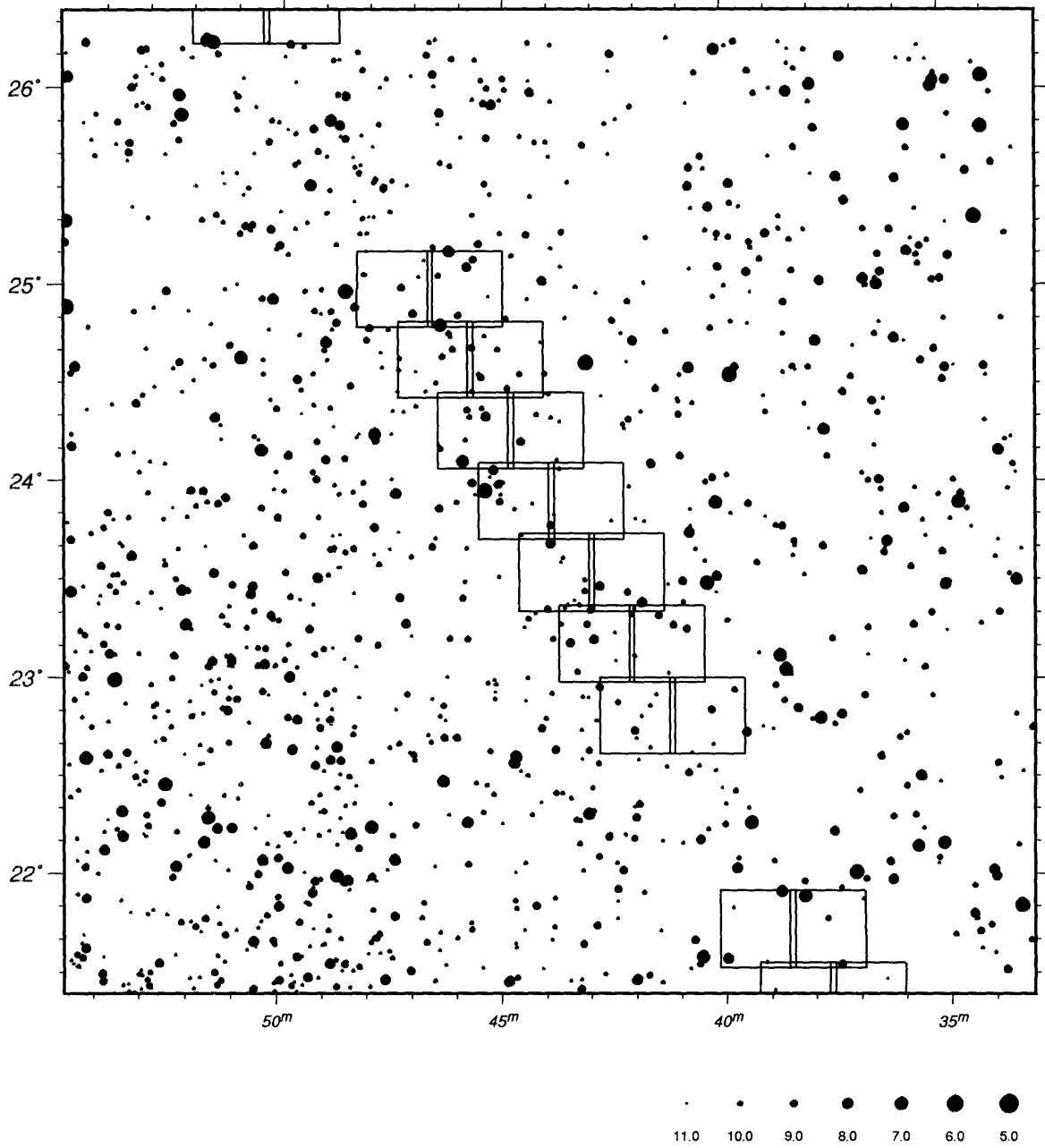
Figure 3-3: A chart made using data from the HST Guide Star Catalog, showing catalog stars brighter than V= 11 in a 5 degree square region centered on $\ell = 60°, b = 0°$. Regions observed in the Cepheid survey are outlined. The index in the lower right corner shows the point size scale for V magnitudes.
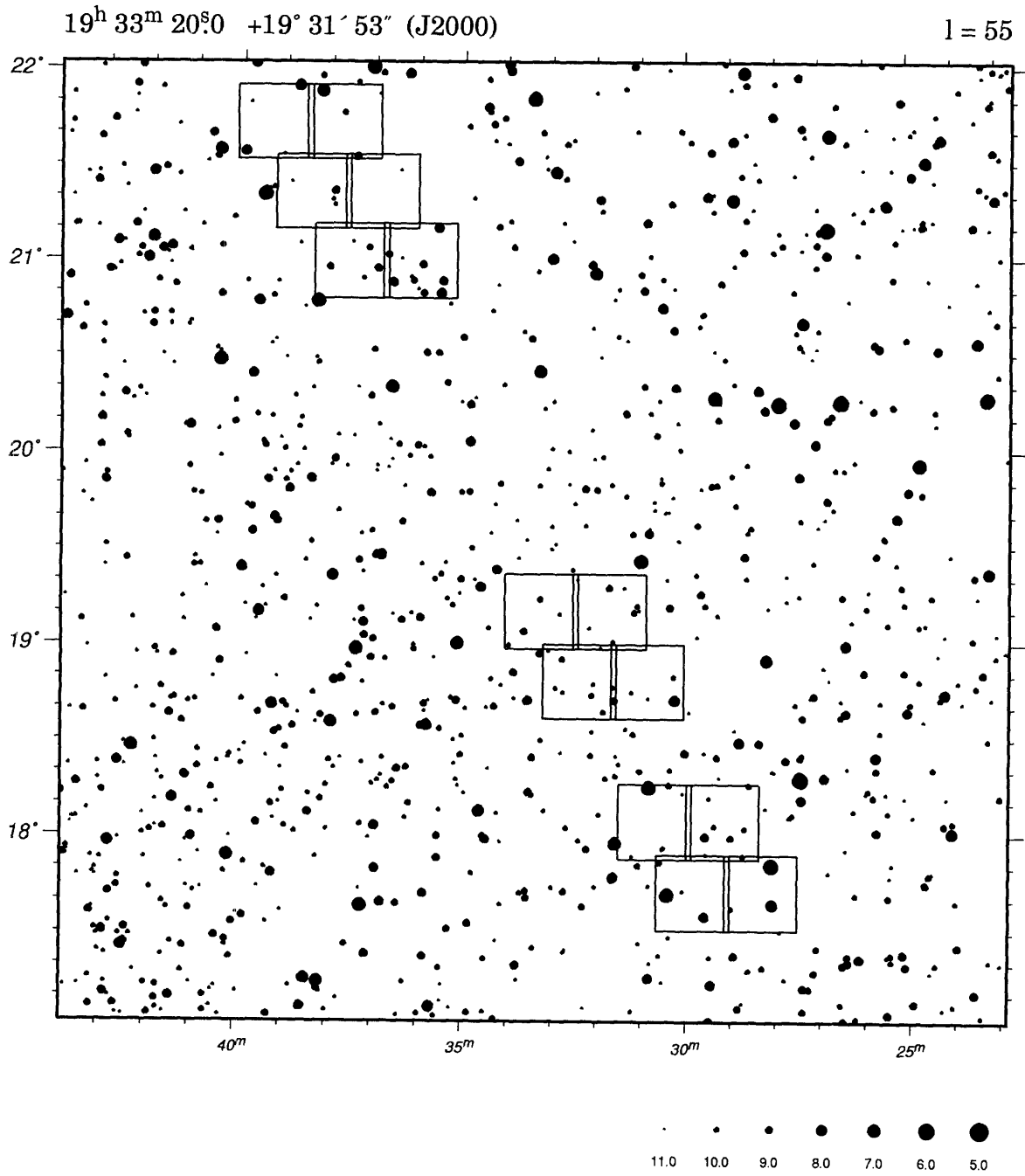
Figure 3-4: The region near $\ell = 55°$.

19^h 55^m 13^{s}0   +28° 12′ 04″ (J2000)   l = 65
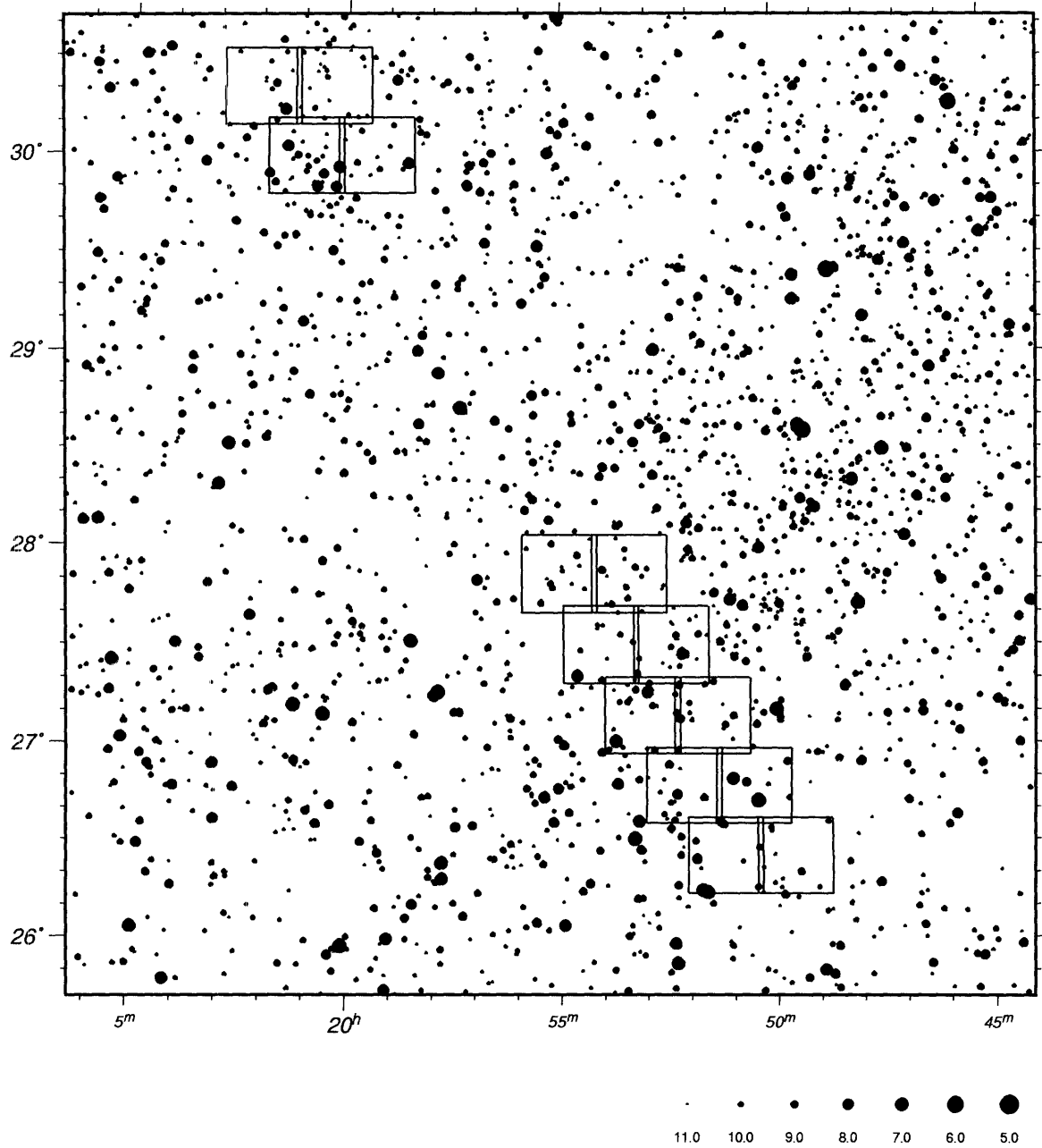
Figure 3-5: The region near $\ell = 65°$.
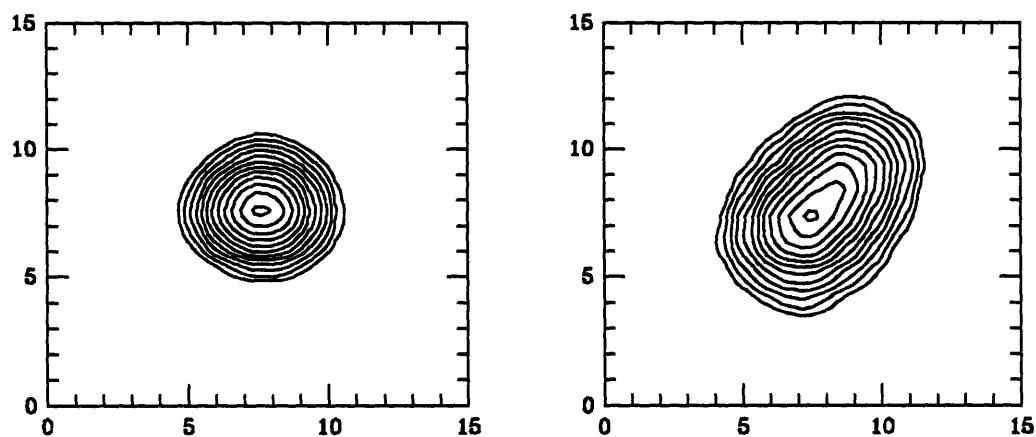
Figure 3-6: Stellar point-spread intensity functions at the center (left panel) and corner (right panel) of the CCD in a single exposure. The inside contour is chosen near the peak, and subsequent contours are spaced logarithmically by factors of $\sqrt{2}$. The image was taken in a period of relatively good seeing (1″5). Axes are shown in units of pixels; the boxy appearance is an artifact.

slightly by setting the focus at a compromise position, where images in a ring around the center were in focus, the center slightly outside focus, and the corners somewhat inside focus.

The field curvature problem has since been remedied at the 0.9m telescope: in the summer of 1993 a corrector lens was installed, giving the telescope a flat focal plane over a wide field.

3.2.2 Data Reduction

The bias from each image was computed from a serial overclock region and subtracted, then the images were corrected for variations in sensitivity using a composite twilight flat illumination exposure. A separate composite flat was constructed for each night, as they tend to differ slightly due to the movement of dust particles on the filters and dewar window. Composites were constructed from multiple exposures by scaling each image to a constant illumination level and averaging, eliminating stars and pixels deviating from mean value of more than 3σ from the final average. Some

121

systematic variation was evident between the individual flats, but it remained < 0.5% throughout. We compared the use of dome vs. twilight flats to correct the data, and found that the CCD illumination was quite different between the two. By comparing the flats to actual data images with high night sky levels or images of a globular cluster, M92, taken at many different positions on the chip, we found the twilight flats corrected the detector response quite well. The dome flats, however, did not properly remove the "dust rings" (a spec of dust well out of focus produces a ring of low light on the chip corresponding to the mirror shape), which were shifted in the flat images with respect to the data.

Stars were identified and measured in each of the images using a modified version of the photometry program DoPHOT (Schechter, Mateo, & Saha 1993). DoPHOT fits each star to an intensity profile of the form

$$I(x,y) = I_0 \left(1 + z^2 + \frac{\beta_4}{2} z^4 + \frac{\beta_6}{2} z^6 \right)^{-1}, \tag{3.1}$$

$$z^2 = \frac{1}{2} \left(\frac{x^2}{\sigma_x^2} + 2\sigma_{xy} xy + \frac{y^2}{\sigma_y^2} \right) ; \tag{3.2}$$

where the shape parameters β_4 and β_6 are held fixed, and the other shape parameters σ_x, σ_y, and σ_{xy} are allowed to vary when fitting the profile to individual bright stars. The standard DoPHOT algorithm computes an average shape for the stars in the image using the means of σ_x, σ_y, and σ_{xy}. This average shape is used in fitting each star to measure the flux, and typically provides a better flux estimate than if the shape parameters were allowed to vary independently.

This algorithm assumes that the PSF is constant; if the PSF varies across the chip, the average PSF will not fit any of the stars well, and will introduce additional photometric error. Worse yet, the PSF at the edge of the chip shown in Figure 3-6 is so elongated that it fits better to *two* average PSFs than one, and DoPHOT will happily split every star in the corner into two components. We therefore modified DoPHOT to allow the average shape of the point spread function to vary as a function of position on the chip, based on some earlier code by P. Schechter. Rather than taking

a straight average for the shape parameters, we fit a second order two-dimensional polynomial for each shape parameter as a function of position. The flux for each star was obtained by fitting a PSF using the shape parameters $\sigma_x(x_0, y_0)$, $\sigma_y(x_0, y_0)$, and $\sigma_{xy}(x_0, y_0)$ obtained from the 3 independent fit functions. The parameters β_4 and β_6 were fixed at 1.0 and 0.5, respectively.

The second order polynomial fit for the shape parameters turned out to be insufficient to match the PSF variation across the entire chip. However, by breaking up a single 2048^2 image into five 1124^2 tiles (four quadrants plus an overlapping center), we could adequately fit the PSF in each quadrant separately since the variation was roughly monotonic within a quadrant. After fitting for positions and fluxes for each star found, the catalogs of the individual quadrants were combined into a single catalog ("detiled"): the center tile was used as the reference, and each corner quadrant's overlapping stars were identified. A mean magnitude offset computed from the overlap stars was applied to each corner tile, to keep the instrumental magnitude system commensurate between tiles. This correction was small, typically 0.005 mag and not exceeding 0.013 mag.

3.2.3 Catalogs

To match stars between different observational epochs, the centroid positions of $\sim$ 200 bright stars per field were computed and cross-referenced between fields. A transformation consisting of an (x,y) offset and a linear 2x2 marix was computed from the coordinates, and the transformation was used to map the remaining stars to the reference template. The data of night 2 was used as the initial template, as it had the best average seeing. Two objects were considered a potential match if a box 3 pixels ($\sim$ 2") high, centered on the transformed position of the candidate object, included the reference object. If there were no other reference stars in the box, the match was considered good and the offsets in RA and Dec were recorded. If there was more than one reference star in the box, the closest star was considered the match and the object was flagged as possibly confused ("type b" confusion). If, however, a candidate would be matched to a reference star previously matched, both

the candidate and the prior match are labeled as confused ("type a" confusion), and the candidate closest to the reference object is considered the match. If a candidate object has no match on the reference frame, it is added to the reference catalog for subsequent use.

After the initial matches were made, a complete reference catalog was produced using the mean position for each object, and the matching procedure was repeated. The scatter in stellar positions between fields taken on different nights was typically 0.15 pixels rms, or $\sim$ 0.1 arcseconds, in each coordinate. The number of confused objects was a strong function of the field crowding, as expected: the least crowded fields, with $\sim$ 12,000 identified objects, typically had 20 confused objects; the most crowded fields had over 40,000 objects with roughly 300 confused.

In a survey searching for variability it is crucial to ensure that the observations at different epochs are on the same *relative* photometric system. We therefore used stars in the field at each epoch to determine a relative magnitude offset. Since the skies on night 2 were closest to being photometric, all epochs were transformed to the night 2 system. Of the stars matched to the reference frame, the brightest 5% and faintest 20% of the stars were eliminated, and the rest used to derive a mean magnitude offset. Stars deviating form this mean by more than 5σ were eliminated (such stars are likely variable), and a final mean offset was computed and applied to the field stars to bring them onto the reference photometric system. It turned out that a simple average was not sufficient to bring the two frames into good relative calibration, as the variation of the PSF produced errors $\geq$ 0.05 mag across the chip. Most of this effect was due to our having used a single correction to put DoPHOT fit magnitudes onto an aperture system, which is not strictly valid if the PSF shape varies across the chip. Another contribution comes from a systematic difference between the aperture magnitudes for the distorted and normal PSF. To correct for this, we fitted a second order two-dimensional polynomial to the (aperture – fit) magnitudes as a function of position for night 2, and used this to correct the magnitudes to full aperture. The relative calibration between night 2 and other nights was likewise computed from a two-dimensional polynomial. The data was thereby brought to a consistent system
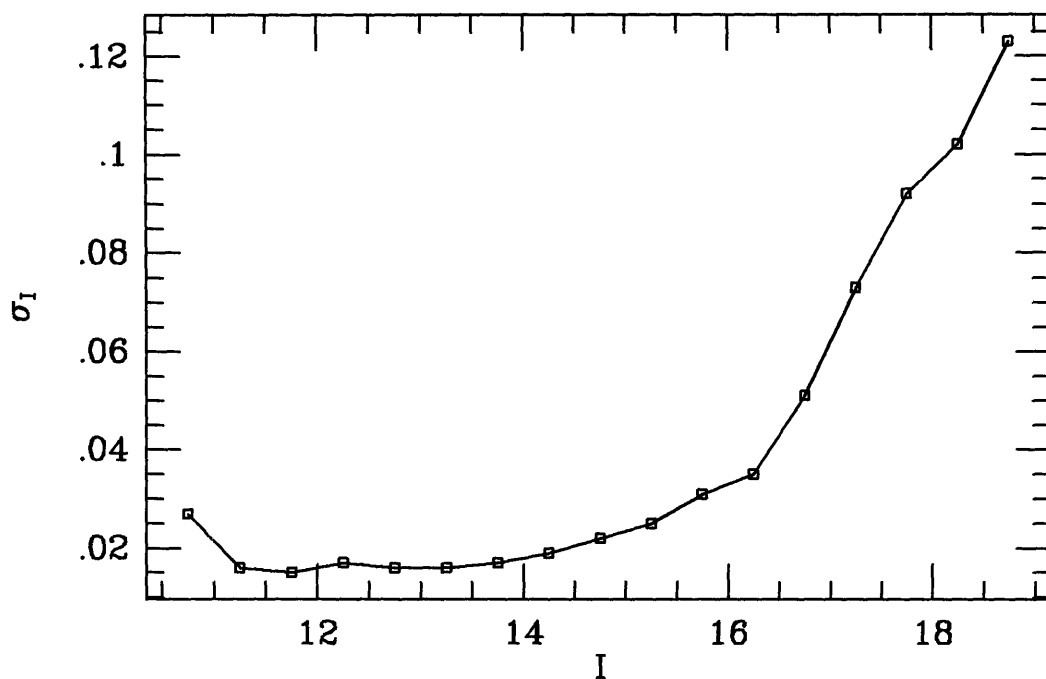
Figure 3-7: Measured dispersion in magnitudes for survey stars, plotted as a function of I magnitude.

that could be directly calibrated to standard magnitudes. The effectiveness of this can be seen both from the formal error in the fit to the offset, $\simeq 0.005$ magnitude, and by measuring $\chi_\nu^2 \simeq 1.0$ for the bright stars (the bright stars have small formal errors in apparent magnitude, and thus are a sensitive test for calibration errors). The locations of variable stars are also close to uniform, as shown below in Figure 3-10, though from the excess number of variables it is evident that the applied correction remained inaccurate in one corner.

Figure 3-7 shows the photometric errors as a function of I magnitude, computed from the scatter of non-variable stars over the course of the survey. Note that the error bottoms out near 0.016 mag, which is likely due to residuals from our polynomial fit calibration; for comparison, the formal error at $I = 11.5$ is 0.13 magnitude. Also note the rise in error brighter than $\ell = 11$–this is reflected in both the statistical dispersion and the formal error from DoPHOT, and is caused by charge levels nearing saturation on the detector in nights of good seeing. While we had initially designed the survey to avoid this effect down to $I = 10.5$, the detector nonlinearity extended down to

levels lower than the instrument specifications due to changes in the electronics to improve readout speed (R. Reed, private communication).

The night 2 instrumental I band magnitudes were converted to the standard system of Landolt (1992) using exposures of several fields at the beginning and end of night 2. Corrections were made for an absolute offset and an airmass term, but no color corrections were applied. Since many of the stars in our survey are too faint to be detected in the V band, and thus have no color information, we chose to keep the magnitudes homogeneous and forego a color correction. All magnitudes reported in this section are therefore on an "instrumental" magnitude system. The color corrections required to convert to a standard system are fairly small, at least over the color range $0 < (B - V) < 2.0$ (see §3.4).

Since V-band data for all regions were never taken on the same night, the offset to the standard magnitude system was done separately for each night. Light to moderate cirrus obscured our observations on several nights, and thus our absolute calibration is much less certain for V than for I. We can get an idea of how bad the cloud extinction is by looking at the I-band data taken shortly before or after a V image. With the exception of night 6, when the clouds increased steadily until it was no longer possible to observe, the total extinction from clouds in I was < 0.07 mag at all times. The absolute calibrations in V therefore should be accurate to ~ 0.10 mag. The photometry of §3.4 supports this assessment: for the fields that overlap the follow-up area, the absolute calibrations agree to better than 0.05 mag. We emphasize again that for the purposes of identifying Cepheids, the V photometry is important primarily to measure the color change, which is not dependent on an accurate absolute calibration.

Coordinates in equinox J2000 were determined by matching stars in the survey regions with stars in the *HST Guide Star Catalog* (Russel *et al.* 1990, hereafter GSC) in the same manner as we match the survey data. This produces a coordinate transformation from which we can calculate RA and Dec from the centroid position in pixel coordinates. Each region had between 19 and 182 GSC stars, enough to provide a solution good to the accuracy of the catalog (~ 1" quoted error, probably somewhat

higher near GSC plate edges).

As a side note, we initially tried the approach used by CKS to match survey objects, by first transforming to sky coordinates and performing the match based upon true sky distances. We found, however, that errors in star positions near the edges of the GSC survey plates introduced spurious errors into our coordinate transformation. We therefore chose to match in pixel coordinates, transforming to sky coordinates only at the end, and match objects in overlap regions using the same algorithm for *inter*-region matching as used above *intra*-region.

The complete survey catalog consists of 4,988,434 photometric measurements of 1,063,515 stars in an area of roughly 6.1 square degrees. Of these stars, 766,816 were detected on three or more nights, and are examined for variability in §3.3. Figure 3-8 shows the number distribution of catalog stars as a function of apparent magnitude. The distribution resembles a power law in number vs. flux, and the slope is intermediate between 3/2 and the intrinsic luminosity distribution of stars in the disk. The former case would approximate an environment with no dust, the latter one with extremely high extinction. We note that the completeness begins to fall off for stars of $I \gtrsim 17.5$ and those brighter than $I = 11$, assuming the validity of extrapolating the power law a small amount at each end.

Figure 3-9 shows color-magnitude diagrams of three survey regions covering the middle and two extremes of ℓ in our surveyed area. Though not all stars from each region have been plotted, to relieve crowding in the plot for region 38, the same fraction of stars is shown for each. Note the progression to redder colors and fewer identified stars with decreasing longitude: only 1,735 stars were identified in both V and I in region 84, while region 38 boasts almost 15,000. A comparison of the color-magnitude diagrams shows that most of the difference is due to extinction, which shifts a large number of main sequence stars below our flux limit.

3.3   Variable Stars and Cepheid Candidates
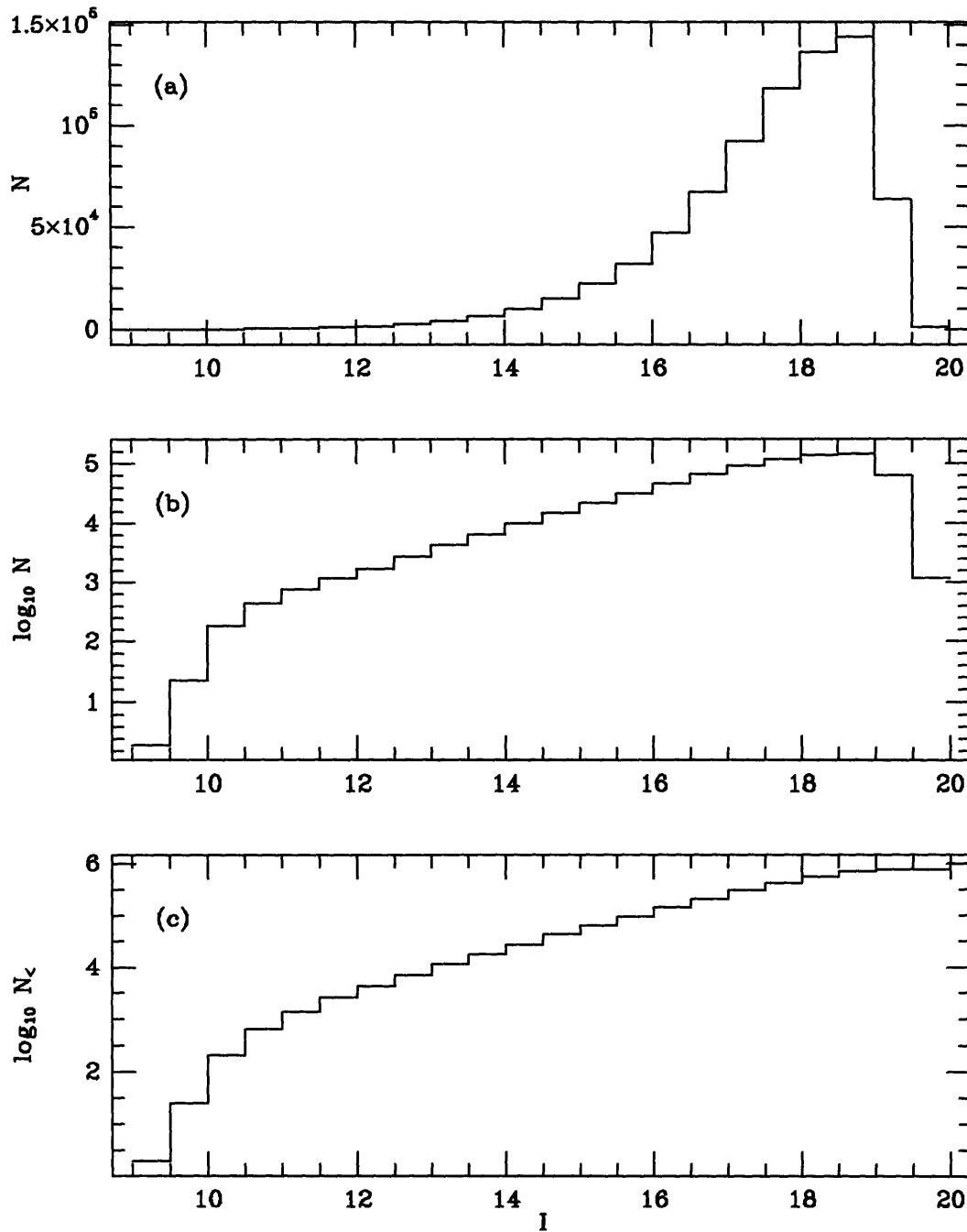
Figure 3-8: The magnitude distribution for stars in the survey, counted in 0.5 magnitude bins. (a) The linear count distribution as a function of apparent I magnitude. Only objects detected on multiple nights are included. (b) Same counts as (a) on a logarithmic scale. (c) The cumulative count distribution. The bright and faint magnitude cutoffs are evident; between the two the distribution follows roughly a power law in flux, though the exponent decreases slightly with fainter magnitude. $d \log N/dI \simeq 0.38$ at $I = 14$.
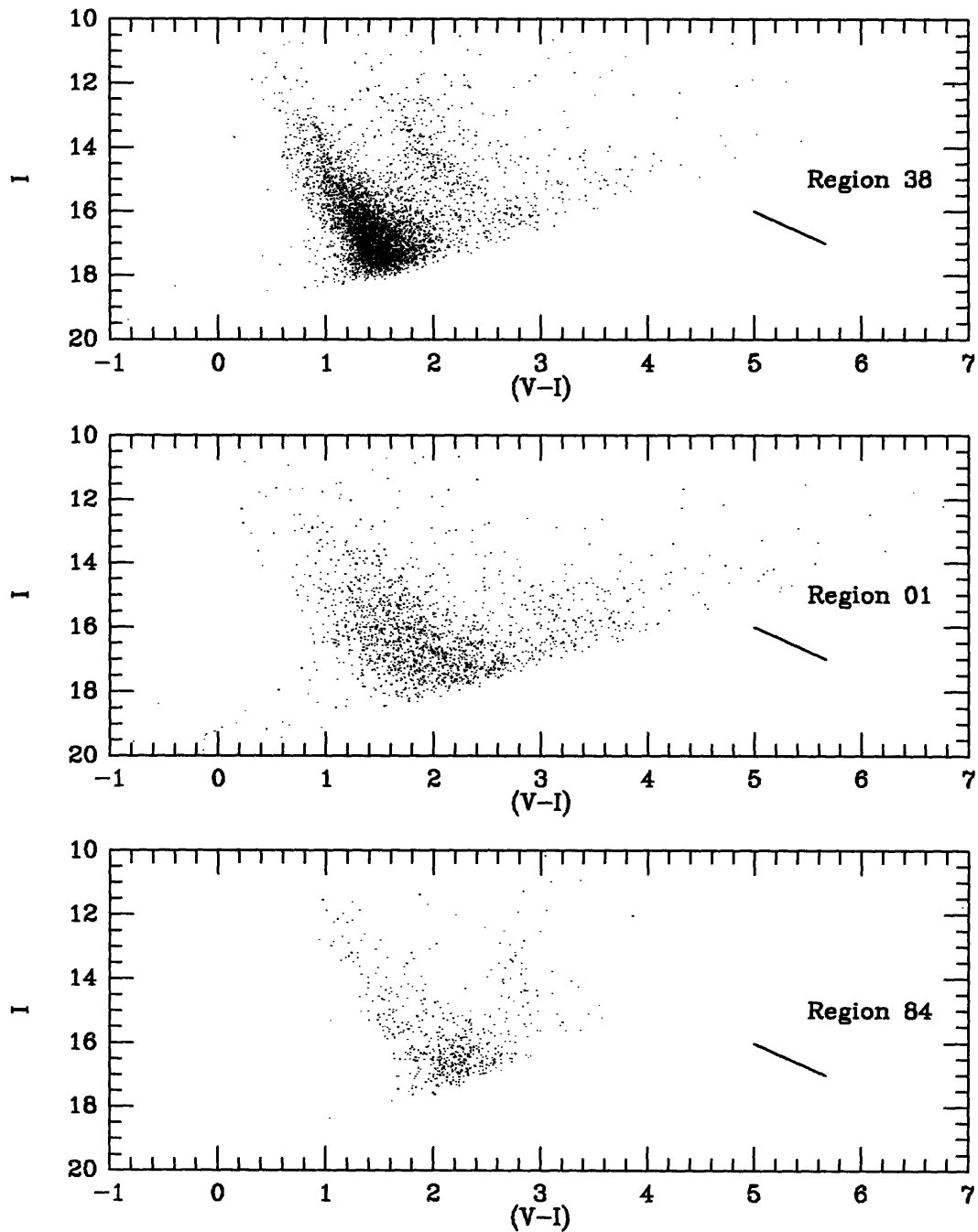
Figure 3-9: Color-magnitude diagrams for three survey regions: Region 38 at $\ell = 67.5°$, Region 1 at $\ell = 60°$, and Region 84 at $\ell = 52.9°$. To reduce crowding, one-thrid of the stars with (V–I) colors are plotted for each region. The line at the lower right of each plot shows the reddening vector for $A_V = 1$.
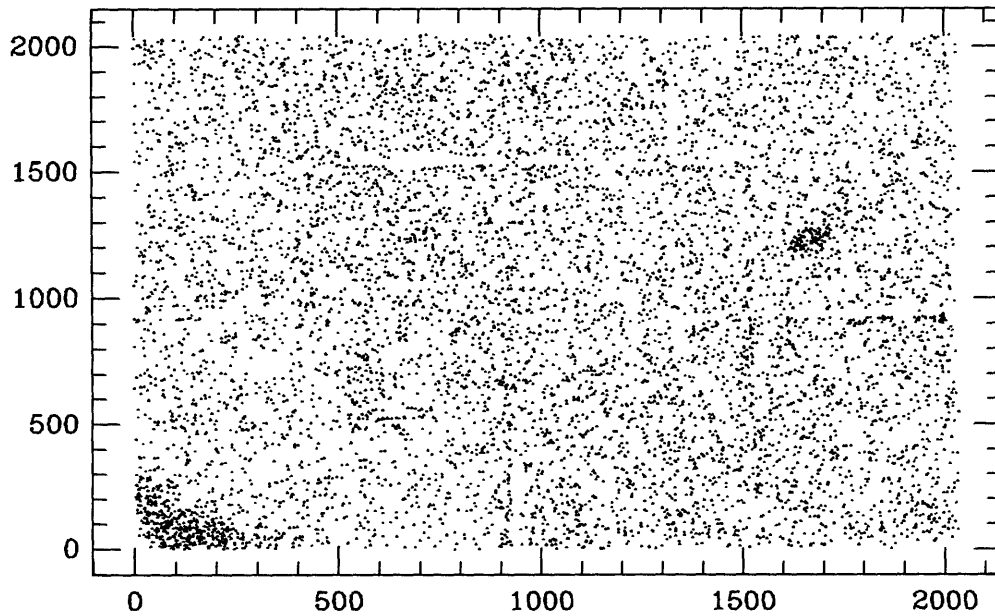
Figure 3-10: Pixel coordinates on the detector for the 7,821 survey stars flagged as variable. Two regions of significant excess can be seen, one in the corner where the point spread function was highly elongated, and the other near (1700,1200) where the detector may have been nonlinear. Some signs of the tiling procedure are also evident.
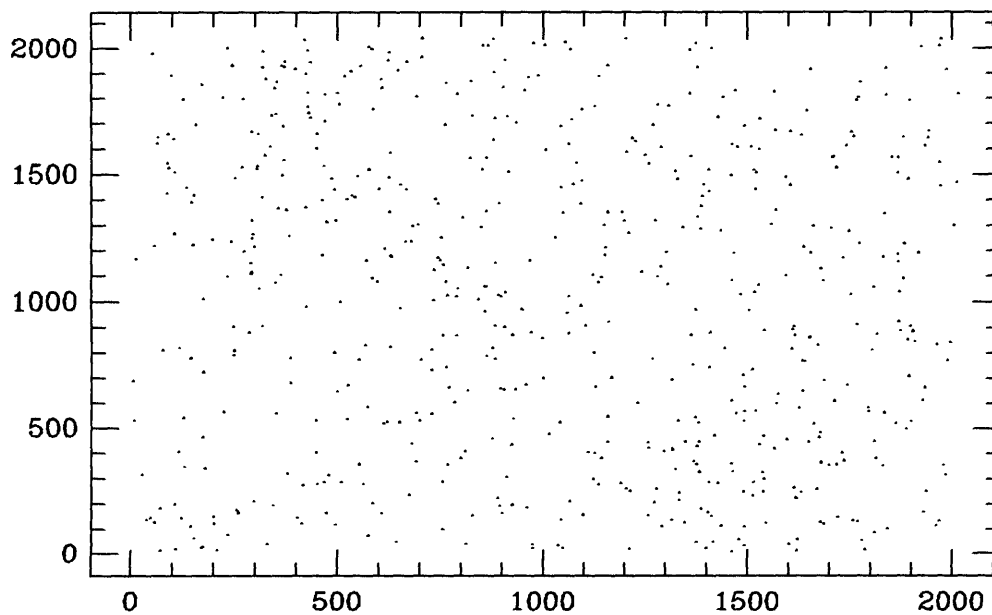
Figure 3-11: Detector pixel coordinates of 578 Cepheid candidates.

130

The catalog stars were tested for variability by using the formal errors from DoPHOT to determine a χ^2 value for each star, under the assumption that it does not vary. The criteria for flagging a star as variable were that it have at least 3 photometric measurements, and that the probability of exceeding χ^2 if it were not variable, $P(<\chi^2) < 10^{-4}$; this is similar to the algorithm used by CKS. Out of the roughly 765,000 stars in the catalog having three or more measurements, 7,821 were found to be variable. Some of these variable stars will be spurious: about 1% due to the χ^2 statistics alone. There are also a higher number of variables found among survey stars near one corner of the chip, most liekly due to our inability to completely compensate for the systematic offset in photometry. Figure 3-10 shows the location on the detector where each variable star appeared in the survey; in the absence of irregularities, the distribution should be uniform. Aside from the PSF troubles in the corner, there is a small patch with an anomalously large number of variables. This is near a location of low intrinsic response on the detector, which we can compensate for properly only if the detector maintains a linear response in that region. Slightly nonlinear response will lead to errors in the photometric calibration, and could produce the excess of spurious variables we see.

Further criteria were placed on the variable star catalog to extract a subset having a sufficiently high variability amplitude to potentially be a Cepheid. The typical amplitude of a Cepheid in I is about 0.4 magnitude peak-to-peak; if we approximate a Cepheid by a continuous sine function, we can calculate the RMS variability amplitude expected of a Cepheid as follows. For a full cycle we have

$$\sigma_I^2 = \frac{\int_0^{2\pi} \sin^2 x \, dx}{\int_0^{2\pi} dx} \frac{A^2}{4} = \frac{A^2}{8} \; ;$$

for a Cepheid observed over the first half of the cycle we find

$$\sigma_I^2 = \frac{\int_0^{\pi} \left(\sin x - \frac{2}{\pi}\right)^2}{\int_0^{\pi} dx} \frac{A^2}{4} = \frac{0.095 A^2}{4} .$$

A Cepheid will therefore have $\sigma_I \simeq 0.14$ mag observed over a full cycle and 0.06

Table 3.3: High Amplitude Variable Stars

Catalog ID	RA (J2000) Dec		$\langle I \rangle$	σ_I	χ^2_ν	$\langle V \rangle - \langle I \rangle$	Notes
01-00195	19 44 48.0	+23 54 18	15.20	0.084	59.6	1.88	
01-00427	19 44 24.8	+23 49 51	17.88	0.596	44.8		
01-00637	19 44 44.6	+23 53 35	16.20	0.206	31.2		1
01-00793	19 44 21.4	+23 47 42	16.03	0.087	28.3	1.78	
01-00966	19 45 00.3	+23 56 22	16.90	0.108	15.0	2.76	
01-01196	19 44 52.2	+23 52 04	16.84	0.233	24.3	2.95	
01-03774	19 45 13.3	+23 50 03	13.42	0.152	185.9	1.62	
01-05204	19 44 45.2	+23 44 40	17.69	0.559	34.6		
01-07279	19 44 33.4	+23 46 52	17.48	0.167	16.0		
01-08549	19 44 58.9	+23 59 47	12.40	0.123	203.7	3.35	1
01-08687	19 45 13.6	+23 59 35	14.09	0.076	43.1	1.44	
01-09100	19 45 25.3	+23 54 50	16.11	0.061	14.7	1.99	
01-09318	19 45 15.7	+24 00 51	16.42	0.080	16.5	2.19	
01-11655	19 44 08.9	+23 56 58	15.07	0.099	52.7	1.69	
01-11809	19 43 52.7	+24 04 34	16.07	0.124	17.6		
01-11982	19 44 23.6	+23 59 47	17.20	0.136	12.6		
01-12561	19 43 49.8	+23 56 50	16.09	0.634	373.2	2.03	
01-19057	19 43 59.8	+24 05 03	15.00	0.240	21.7		
02-00285	19 43 01.1	+23 47 31	15.40	0.149	75.9	1.96	
02-02092	19 42 42.7	+23 47 38	18.48	0.553	22.9		
02-02141	19 43 02.3	+23 45 16	13.63	0.249	667.7	1.08	
02-02434	19 43 09.5	+23 47 06	16.17	0.080	17.8	2.56	2
02-02442	19 43 41.1	+23 46 54	16.08	0.150	47.7	2.10	
02-02735	19 43 47.6	+23 54 22	17.44	0.218	19.4	2.39	
02-04392	19 42 26.5	+23 44 02	16.88	0.164	25.5	2.35	
02-05822	19 43 21.4	+24 02 06	15.21	0.066	32.6	1.75	
02-06335	19 43 22.3	+23 59 45	16.51	0.123	22.3	2.38	
02-06414	19 43 46.0	+23 54 56	16.51	0.187	64.4	2.44	
02-07921	19 42 33.4	+24 01 06	15.20	0.114	11.5	1.71	
03-00022	19 46 01.7	+24 14 22	12.62	0.442	2763.6	1.12	
03-00055	19 45 51.7	+24 09 11	12.96	0.094	22.8	2.81	
03-00092	19 45 36.7	+24 12 09	13.21	0.087	67.6	3.20	1
03-00360	19 45 27.6	+24 11 39	15.55	0.175	99.1	1.71	
03-00433	19 45 21.1	+24 20 06	15.43	0.100	13.5	1.65	
03-02298	19 45 42.8	+24 11 36	17.50	0.300	17.6	2.21	
03-02725	19 45 24.0	+24 19 34	17.88	0.752	25.8	1.16	
03-06544	19 46 11.5	+24 09 04	12.51	0.090	77.1	2.72	1
03-06552	19 46 04.0	+24 05 36	12.06	0.252	757.2	2.36	
03-12117	19 45 03.6	+24 04 16	15.25	0.147	47.0	2.70	2
03-12186	19 44 45.5	+24 12 58	15.64	0.090	15.9	1.58	
03-12425	19 45 07.2	+24 04 07	16.11	0.082	13.5	2.85	
03-13446	19 45 09.4	+24 09 24	17.94	0.201	16.3		
03-15534	19 45 36.9	+24 26 15	13.78	0.092	15.2		
03-15889	19 45 55.4	+24 24 48	16.39	0.292	61.0	2.99	
03-15979	19 45 40.3	+24 21 52	16.33	0.130	24.1	2.04	
03-15994	19 46 15.6	+24 21 27	15.58	0.119	47.1	2.08	
03-17215	19 46 11.6	+24 21 58	17.76	0.307	18.4	1.94	
04-00354	19 43 49.9	+24 13 30	15.47	0.164	138.1	2.76	
04-01038	19 44 17.4	+24 17 55	16.98	0.187	21.1	1.66	
04-01192	19 44 02.1	+24 15 32	17.06	0.264	25.8	2.50	

Table 3.3—*Continued*

Catalog ID	RA (J2000) Dec		$\langle I \rangle$	σ_I	χ^2_ν	$\langle V \rangle - \langle I \rangle$	Notes
04-13254	19 43 24.7	+24 07 21	12.14	0.189	333.0		2
04-13563	19 43 26.8	+24 05 16	14.88	0.135	70.8		
04-24229	19 43 53.6	+24 24 38	16.36	0.216	57.0		
05-00043	19 46 07.9	+24 38 38	12.86	0.123	64.7	1.40	
05-00130	19 46 26.2	+24 40 40	15.03	0.060	18.3	2.64	2
05-00483	19 46 28.3	+24 38 07	15.96	0.091	34.5	2.69	2
05-00490	19 46 35.0	+24 37 47	16.71	0.152	37.3	2.64	
05-00506	19 46 16.4	+24 36 38	16.29	0.231	107.5	2.75	
05-00518	19 46 19.4	+24 36 06	16.18	0.092	23.3	2.39	2
05-00750	19 46 14.7	+24 39 16	16.98	0.253	18.7	2.56	
05-00831	19 46 27.2	+24 37 03	17.02	0.196	30.2	3.00	
05-00857	19 46 22.9	+24 36 01	17.05	0.152	21.3	3.09	
05-00862	19 46 09.5	+24 35 46	17.12	0.220	44.5	2.65	
05-00863	19 46 17.9	+24 35 48	17.40	0.183	17.9	3.13	
05-00883	19 46 16.5	+24 35 15	16.94	0.140	16.3	2.98	
05-00891	19 46 17.6	+24 35 02	16.98	0.201	23.3	2.78	
05-00910	19 46 10.5	+24 34 17	17.15	0.272	64.3	2.60	2
05-01414	19 46 22.7	+24 37 07	17.57	0.162	12.1	2.90	
05-01442	19 46 21.9	+24 36 35	17.96	0.197	13.4		
05-01531	19 46 08.2	+24 34 50	17.41	0.256	34.6	2.73	
05-01532	19 46 28.4	+24 34 53	17.75	0.295	25.4		
05-01534	19 46 17.3	+24 34 50	17.44	0.227	17.2	2.62	
05-05246	19 47 00.1	+24 31 10	16.07	0.076	15.5	2.48	2
05-05714	19 46 48.5	+24 30 13	16.78	0.127	19.1	2.40	
05-05929	19 46 54.0	+24 27 15	16.78	0.175	56.1	2.38	
05-10709	19 46 21.5	+24 26 43	14.76	0.085	72.0	3.25	3
05-11145	19 45 57.6	+24 28 08	15.71	0.372	302.2	2.54	1
05-11674	19 46 01.8	+24 28 20	16.82	0.344	90.1	2.62	
05-17081	19 46 31.5	+24 42 30	16.02	0.146	58.7	2.55	2
05-17712	19 46 31.2	+24 47 48	16.63	0.091	12.1	1.81	
05-19221	19 46 36.7	+24 43 50	18.00	0.317	16.1		
06-00098	19 44 47.8	+24 38 49	13.74	0.060	24.1	2.97	
06-00194	19 44 42.0	+24 39 39	14.15	0.071	14.5	1.99	
06-01047	19 45 10.6	+24 42 20	16.71	0.106	13.9	2.61	
06-01546	19 45 09.6	+24 35 59	16.53	0.365	31.0	1.83	
06-01645	19 45 17.8	+24 34 37	16.99	0.373	23.1	1.99	
06-01715	19 45 04.9	+24 33 40	16.47	0.288	41.0	2.39	
06-02268	19 45 19.9	+24 39 52	17.56	0.228	25.4	1.97	
06-02717	19 44 49.5	+24 36 17	17.07	0.191	13.1	2.48	
06-03496	19 44 38.3	+24 41 43	18.25	0.156	16.2	2.37	
06-09107	19 45 37.0	+24 26 15	13.82	0.085	49.4		
06-09299	19 45 38.1	+24 34 43	15.18	0.147	61.9	2.72	
06-10063	19 45 27.3	+24 34 37	16.50	0.163	44.3	2.02	
06-10992	19 45 32.1	+24 33 39	17.26	0.398	66.5	2.80	
06-15908	19 44 16.6	+24 25 56	14.50	0.061	22.3	2.27	
06-17023	19 44 39.1	+24 27 25	16.51	0.196	48.5	2.47	
06-17680	19 44 35.7	+24 29 59	17.52	0.231	35.0	2.39	
06-22725	19 45 26.4	+24 39 29	15.91	0.102	42.1	2.43	
06-22995	19 45 07.7	+24 45 16	16.70	0.144	24.4	2.68	
06-23154	19 45 12.9	+24 43 20	16.55	0.154	21.8	2.03	

Table 3.3—*Continued*

Catalog ID	RA (J2000) Dec		$\langle I \rangle$	σ_I	χ^2_ν	$\langle V \rangle - \langle I \rangle$	Notes
06-23154	19 45 12.9	+24 43 20	16.55	0.154	21.8	2.03	
06-23881	19 45 17.2	+24 44 29	17.57	0.221	13.1	2.05	
06-25612	19 45 27.4	+24 42 20	17.88	0.325	26.8	2.32	
06-27930	19 44 18.2	+24 45 43	13.53	0.210	74.4	1.41	
06-28214	19 44 23.0	+24 39 11	15.35	0.121	57.8	1.99	
06-28287	19 44 48.4	+24 45 59	15.90	0.220	21.6	2.08	
06-28309	19 44 24.2	+24 44 59	15.85	0.152	39.3	1.82	
07-00415	19 47 06.1	+25 00 23	16.10	0.187	72.2	2.24	1
07-00559	19 47 44.5	+24 54 35	16.03	0.060	18.2	2.43	
07-01341	19 47 22.8	+25 02 06	17.31	0.129	14.5	2.33	
07-06650	19 47 38.5	+24 52 11	12.49	0.237	453.7	1.39	
07-06944	19 47 32.0	+24 49 33	15.24	0.164	62.8	1.49	
07-07501	19 47 39.2	+24 50 26	16.59	0.170	56.9	2.60	
07-07580	19 47 43.8	+24 49 01	16.59	0.129	29.7	2.73	
07-11383	19 46 46.9	+24 46 47	11.43	0.071	39.8	2.74	
07-11910	19 46 52.2	+24 49 53	16.41	0.197	69.5	2.03	
07-13247	19 47 00.5	+24 49 22	17.72	0.313	39.9	2.24	
07-16959	19 47 52.4	+24 59 44	13.45	0.229	872.1	1.28	1
07-18391	19 48 01.2	+25 08 15	17.30	0.243	26.0	2.49	
07-19159	19 48 10.6	+24 59 35	18.18	0.886	49.4		
08-00258	19 46 11.9	+25 00 33	15.28	0.134	94.6	3.82	1
08-00556	19 46 14.0	+24 58 08	15.86	0.097	41.1	1.93	
08-00732	19 46 13.1	+24 52 44	15.66	0.061	26.1	2.91	
08-00905	19 46 14.2	+25 01 45	16.79	0.111	19.9	2.46	
08-01219	19 45 39.9	+24 54 33	16.39	0.125	31.9	2.24	
08-01541	19 45 55.8	+25 02 15	17.04	0.173	41.8	2.28	
08-05329	19 45 55.8	+25 00 41	18.66	0.531	18.3		
08-09012	19 46 40.0	+24 48 00	17.05	0.151	18.0		
08-15718	19 45 15.7	+24 46 57	17.05	0.198	37.0	1.70	
08-21281	19 46 12.4	+25 09 49	14.06	0.078	29.0	1.47	
08-21347	19 45 54.0	+25 08 04	13.87	0.175	171.8	3.03	
08-21473	19 46 14.0	+25 07 04	15.97	0.108	48.3	2.29	2
08-21560	19 46 38.2	+25 00 26	15.48	0.119	80.7	1.81	
08-22483	19 45 47.7	+25 09 25	17.56	0.231	14.0		
08-26454	19 45 07.4	+25 04 25	14.57	0.222	51.6	1.79	
08-26487	19 45 23.7	+25 00 37	14.82	0.067	23.1	1.70	
08-26544	19 45 11.3	+25 07 45	15.80	0.200	44.3	1.42	
08-26741	19 45 02.0	+25 07 40	16.07	0.194	34.9	1.66	
15-00026	19 50 49.3	+26 19 45	12.85	0.113	16.6	3.80	1
15-01794	19 51 35.4	+26 25 22	17.97	0.423	26.0		
15-06776	19 51 38.9	+26 20 51	16.66	0.187	32.2	2.12	
15-10073	19 50 40.0	+26 25 04	15.99	0.126	24.5	1.77	
15-10585	19 50 28.5	+26 22 01	17.34	0.217	35.0	2.01	
15-18923	19 50 24.5	+26 30 03	15.16	0.136	24.1	1.53	
16-00177	19 49 20.5	+26 26 24	14.76	0.086	37.7	1.76	
16-06219	19 50 21.0	+26 13 29	10.55	0.190	16.8	1.10	
16-07440	19 49 46.2	+26 18 20	17.03	0.224	53.6	1.86	
16-07845	19 49 33.8	+26 13 18	16.95	0.137	28.7	2.29	
16-12052	19 48 57.2	+26 23 23	11.26	0.138	163.9	0.75	GU Vul
16-12081	19 48 59.1	+26 14 45	12.76	0.076	56.2	6.96	3

Table 3.3—*Continued*

Catalog ID	RA (J2000) Dec		$\langle I \rangle$	σ_I	χ^2_ν	$\langle V \rangle - \langle I \rangle$	Notes
16-12214	19 48 44.9	+26 22 17	14.98	0.209	244.7	2.82	
16-12281	19 49 18.5	+26 13 48	14.88	0.110	73.0	1.66	
16-12802	19 49 16.6	+26 14 01	15.86	0.358	14.9	2.23	
16-13366	19 49 14.3	+26 13 57	17.04	0.131	16.6	2.11	
16-13611	19 48 57.3	+26 22 21	18.03	0.215	11.4		
16-14121	19 49 22.8	+26 15 30	17.18	0.199	14.3	2.28	
16-15140	19 49 01.1	+26 16 56	18.33	0.176	14.2		
16-17136	19 50 08.6	+26 32 25	10.48	0.100	18.5		
16-17546	19 49 52.5	+26 34 23	16.31	0.118	29.0	1.94	
16-21257	19 49 07.5	+26 33 04	15.20	0.184	96.2	2.84	
16-21428	19 49 22.4	+26 32 00	16.74	0.122	23.7		
16-21518	19 48 49.0	+26 27 23	16.29	0.108	21.0	2.36	
16-21635	19 48 46.8	+26 34 02	16.22	0.142	39.1	1.82	
16-21841	19 48 50.6	+26 28 00	17.17	0.106	10.3	2.34	
16-22000	19 48 43.6	+26 34 38	17.25	0.280	15.7	1.76	
17-00483	19 52 00.8	+26 49 00	15.66	0.121	11.6	2.07	
17-00533	19 52 02.0	+26 47 34	15.99	0.299	228.7	1.65	
17-10448	19 51 39.0	+26 39 27	15.40	0.141	19.7	1.51	
17-10628	19 51 32.5	+26 35 44	15.66	0.128	53.6	1.74	
17-11369	19 51 24.9	+26 36 30	17.07	0.173	13.6	1.95	
17-14495	19 52 16.4	+26 54 42	12.65	0.062	33.3	0.94	
17-15211	19 52 53.0	+26 51 57	16.62	0.124	32.6	1.74	
17-15632	19 52 23.2	+26 54 05	16.72	0.205	18.2	1.86	
17-16490	19 52 57.2	+26 54 25	17.38	0.298	16.6		
18-00380	19 50 26.0	+26 51 44	16.09	0.184	100.8		1
18-00385	19 50 48.9	+26 51 43	16.00	0.140	12.2	3.62	
18-00435	19 50 24.5	+26 50 21	15.92	0.126	41.0	2.16	
18-01288	19 50 10.5	+26 51 56	17.49	0.135	12.9	1.89	
18-04940	19 50 08.7	+26 45 20	18.73	0.423	15.2		
18-05947	19 51 12.8	+26 44 32	15.31	0.147	133.6		1
18-06482	19 51 14.8	+26 46 05	16.90	0.107	15.2		1
18-06889	19 50 37.6	+26 36 13	16.79	0.119	24.5	3.63	2
18-10803	19 50 04.6	+26 46 23	14.84	0.134	80.7	1.60	
18-11202	19 50 03.2	+26 38 13	15.86	0.146	52.1	3.99	1
18-11615	19 49 47.2	+26 38 20	17.25	0.123	14.6	1.91	
18-13466	19 49 59.6	+26 35 49	18.34	0.319	23.7		
18-15147	19 51 01.3	+26 47 47	14.78	0.078	15.2	2.82	
18-16415	19 51 19.0	+26 56 43	17.53	0.313	45.8		
18-18876	19 50 57.6	+26 56 33	18.42	0.423	18.9		
18-20676	19 50 19.8	+26 57 26	16.70	0.099	13.9	2.99	
19-01752	19 52 46.1	+27 13 26	17.26	0.222	41.1	2.07	
19-14311	19 52 28.7	+27 07 14	13.56	0.183	299.5	1.26	
19-14765	19 52 31.4	+27 06 38	16.14	0.125	28.1	2.26	
19-14853	19 52 38.3	+27 02 47	16.43	0.163	42.6	2.43	
19-20390	19 53 24.8	+27 16 10	15.48	0.201	190.3	1.66	
19-21204	19 53 23.3	+27 15 22	17.05	0.211	31.1	2.35	
19-25767	19 52 35.4	+27 13 13	14.09	0.180	65.9	2.34	
19-26913	19 52 18.6	+27 09 53	17.39	0.212	19.3	2.08	
20-00839	19 51 32.5	+27 02 28	15.60	0.064	12.0	2.47	
20-07994	19 52 06.9	+27 00 35	16.02	0.140	45.8		

Table 3.3—*Continued*

Catalog ID	R.A (J2000) Dec		$\langle I \rangle$	σ_I	χ^2_ν	$\langle V \rangle - \langle I \rangle$	Notes
20-08240	19 51 55.0	+27 07 29	16.76	0.156	16.6		
20-08400	19 51 58.7	+27 02 45	16.40	0.094	20.3		2
20-08458	19 52 04.1	+27 01 31	16.35	0.177	28.0		
20-13230	19 50 53.7	+27 07 01	13.54	0.116	129.9	1.91	2
20-18473	19 51 59.5	+27 16 40	12.60	0.322	637.9	2.19	EW Vul
20-18890	19 51 58.5	+27 10 08	15.17	0.072	31.7	1.71	
20-19031	19 51 53.3	+27 16 48	16.65	0.220	71.6		
20-19531	19 51 54.6	+27 16 38	17.03	0.163	11.2		
20-19927	19 52 06.8	+27 09 03	16.79	0.121	11.2		
20-23924	19 50 47.2	+27 18 25	16.12	0.112	10.5		
20-23963	19 51 17.9	+27 17 37	15.90	0.117	18.2		
20-24387	19 50 41.4	+27 17 38	16.37	0.167	12.4		
21-00186	19 54 17.4	+27 27 56	13.83	0.080	34.0	3.15	1
21-00775	19 53 37.9	+27 24 52	16.53	0.294	21.6	1.46	
21-01393	19 54 22.5	+27 26 13	16.72	0.181	11.6		
21-07784	19 54 25.0	+27 21 10	14.80	0.455	158.6	2.42	
21-08141	19 54 27.3	+27 22 33	15.57	0.103	37.0	1.82	
21-08244	19 54 01.1	+27 19 18	15.64	0.112	21.4	2.12	
21-09370	19 54 30.3	+27 21 15	17.03	0.304	45.2	2.12	
21-13243	19 53 23.4	+27 26 39	15.95	0.082	23.5	1.80	
21-18223	19 54 22.8	+27 39 04	15.60	0.074	16.5	3.21	
21-18320	19 54 53.5	+27 32 12	15.49	0.196	129.9	1.59	
21-18396	19 54 41.9	+27 39 33	15.95	0.194	59.1	1.62	
21-18936	19 54 40.2	+27 36 46	16.24	0.109	12.8	2.43	
21-19697	19 54 15.6	+27 36 07	17.26	0.208	23.0	2.28	
21-23691	19 53 45.1	+27 38 12	16.30	0.141	20.3	1.60	
21-27530	19 53 47.3	+27 36 35	10.54	0.094	15.8	2.17	
22-00135	19 52 42.6	+27 26 10	13.19	0.061	19.0		2
22-00294	19 51 59.8	+27 34 42	15.34	0.473	531.9	2.83	
22-00982	19 52 02.4	+27 34 10	16.93	0.159	18.9		
22-01453	19 52 47.4	+27 26 20	16.47	0.183	40.2	1.74	
22-01905	19 52 17.5	+27 31 53	16.99	0.200	28.3	2.77	
22-06140	19 53 08.2	+27 25 35	14.42	0.078	71.2	1.48	
22-06242	19 53 15.6	+27 17 40	14.94	0.132	16.2	1.21	
22-06256	19 53 00.3	+27 28 37	15.47	0.160	139.2	1.42	
22-06348	19 52 36.9	+27 22 16	15.40	0.070	14.5	1.41	
22-07214	19 52 28.8	+27 21 15	16.25	0.136	23.1	1.77	
22-11806	19 52 07.0	+27 18 56	15.44	0.099	29.7	1.57	
22-11884	19 51 48.1	+27 28 08	16.00	0.283	34.5	2.01	
22-11970	19 51 52.6	+27 25 16	15.70	0.089	27.4		2
22-12029	19 51 50.7	+27 22 23	15.97	0.201	145.7	2.40	
22-15989	19 52 39.4	+27 39 43	16.16	0.099	22.1		2
22-16708	19 53 03.0	+27 33 19	17.16	0.142	18.2	2.05	
22-19809	19 52 01.7	+27 37 42	14.29	0.092	48.7	2.42	
22-20093	19 51 41.2	+27 40 33	15.48	0.112	12.7	1.60	
22-20307	19 52 14.5	+27 36 13	15.79	0.129	15.4	1.42	
22-20516	19 51 40.3	+27 40 06	16.41	0.263	24.5	1.47	
22-20525	19 52 02.2	+27 40 02	16.70	0.134	12.2	1.49	
22-20675	19 52 11.6	+27 37 37	17.09	0.119	13.5	1.52	
22-21032	19 51 47.7	+27 30 46	16.98	0.237	31.3	2.60	

Table 3.3—*Continued*

Catalog ID	RA (J2000) Dec		$\langle I \rangle$	σ_I	χ^2_ν	$\langle V \rangle - \langle I \rangle$	Notes
22-24908	19 51 52.8	+27 25 04	10.48	0.252	75.8		
23-00077	19 54 49.7	+27 52 24	13.24	0.097	54.6	2.67	2
23-00194	19 55 03.3	+27 45 44	14.10	0.253	372.0	1.51	
23-00931	19 54 46.5	+27 53 02	16.53	0.206	54.8	1.80	
23-06067	19 55 34.6	+27 42 21	11.65	0.115	134.3	0.66	KN Vul
23-06309	19 55 26.7	+27 43 02	15.45	0.138	30.1	1.77	
23-09616	19 55 28.5	+27 44 05	18.20	0.518	31.4		
23-10522	19 54 23.4	+27 41 39	15.64	0.190	140.9	1.52	
23-11603	19 54 23.9	+27 49 05	17.58	0.231	13.5	1.40	
23-15573	19 55 43.6	+27 58 27	16.44	0.121	28.1	2.71	
23-15801	19 55 44.1	+28 01 20	16.65	0.164	16.2		
23-20205	19 54 25.3	+28 01 50	14.68	0.121	26.4	2.02	
24-00362	19 53 33.5	+27 46 53	14.61	0.251	133.1	1.58	
24-00588	19 53 18.0	+27 50 41	15.22	0.176	17.0	1.36	
24-06513	19 54 08.6	+27 45 12	14.12	0.064	38.9		2
24-06712	19 53 43.4	+27 40 20	14.92	0.324	448.9	2.46	
24-07115	19 54 09.1	+27 49 59	16.16	0.110	17.7	2.11	
24-11308	19 52 50.8	+27 44 28	14.66	0.074	35.3	1.17	
24-11337	19 53 03.3	+27 40 48	14.41	0.117	114.8	1.68	
24-11606	19 52 40.4	+27 50 42	16.14	0.213	51.8	1.23	
24-16952	19 53 33.9	+27 59 33	14.99	0.069	38.7	1.34	
24-17086	19 53 54.0	+28 02 02	16.25	0.084	12.2	1.83	
24-17155	19 53 55.0	+27 59 56	16.04	0.190	45.8	1.79	
24-17641	19 53 46.8	+27 58 20	16.48	0.164	35.7	1.36	
24-18670	19 53 58.1	+27 52 56	16.93	0.137	27.5	1.42	
24-21087	19 52 36.9	+27 57 38	12.94	0.243	91.5	1.00	
24-23679	19 52 55.1	+27 59 04	17.88	0.361	38.7		
35-00355	20 01 05.8	+29 57 48	13.70	0.715	14.4	0.69	
35-06608	20 01 51.2	+29 47 28	13.56	0.060	15.1	0.91	
35-07618	20 01 24.1	+29 51 56	16.34	0.146	14.8	1.60	
35-09484	20 01 36.8	+29 55 44	17.58	0.274	15.4	1.89	
35-11140	20 01 30.8	+29 57 51	18.06	0.589	42.7		
35-13010	20 00 11.3	+29 52 35	14.48	0.261	16.2	1.28	
35-13082	20 00 44.3	+29 46 59	14.60	0.319	378.0	3.52	
35-18917	20 01 36.8	+30 03 32	13.93	0.145	248.8	4.06	1
35-19147	20 01 02.3	+30 08 01	14.82	0.187	12.1		
35-19448	20 01 48.5	+30 07 40	15.97	0.291	23.9	1.41	
35-19679	20 01 32.8	+30 01 41	15.87	0.068	12.9	2.62	2
35-20279	20 01 48.5	+30 02 55	17.08	0.283	31.9	2.09	
35-20946	20 01 50.9	+30 06 30	17.18	0.310	13.9	1.75	
35-25040	20 00 08.6	+30 08 51	14.98	0.111	18.7	1.29	
35-25970	20 00 07.2	+30 06 42	17.17	0.327	17.5		
36-00407	19 59 47.2	+30 04 04	15.34	0.250	394.3	0.92	
36-00855	19 59 28.0	+30 02 31	16.08	0.145	17.6	1.97	
36-00880	19 59 04.7	+30 02 06	15.77	0.106	24.7	1.64	
36-01261	19 59 40.1	+29 54 48	15.73	0.115	18.9	1.34	
36-01739	19 59 38.5	+30 00 36	16.52	0.163	30.7	1.54	
36-02011	19 59 13.3	+29 57 20	16.06	0.187	9.9	1.58	
36-03696	19 58 59.7	+29 54 57	17.21	0.195	18.4	2.01	
36-03868	19 59 23.5	+29 53 45	16.42	0.112	12.9	1.49	

Table 3.3—*Continued*

Catalog ID	RA (J2000) Dec		$\langle I \rangle$	σ_I	χ^2_ν	$\langle V \rangle - \langle I \rangle$	Notes
36-05483	19 58 59.7	+29 56 57	17.02	0.325	14.8		
36-09212	19 59 54.5	+29 48 37	13.59	0.077	37.1	5.66	3
36-09664	19 59 39.7	+29 47 23	14.92	0.147	138.3	1.26	
36-09813	20 00 11.1	+29 53 57	16.13	0.221	49.1	2.36	
36-10674	19 59 34.7	+29 50 11	16.92	0.180	22.1	1.60	
36-11218	19 59 53.3	+29 56 41	16.63	0.133	13.1	2.76	
36-14000	19 59 52.6	+29 59 50	17.98	0.863	97.9		
36-15390	19 58 42.0	+29 56 08	11.85	0.074	31.5	6.46	3
36-15475	19 58 40.9	+29 56 43	13.79	0.185	172.6	2.68	
36-15842	19 58 40.9	+29 52 53	15.55	0.196	51.8	1.54	
36-16031	19 58 40.6	+29 59 46	15.96	0.098	13.5	1.36	
36-16947	19 58 42.8	+29 52 58	16.47	0.118	16.6	1.94	
36-16989	19 58 43.9	+29 52 23	16.52	0.179	40.0	1.66	
36-17130	19 59 07.2	+29 51 03	15.81	0.315	12.6	2.36	
36-18278	19 59 13.3	+29 51 45	16.74	0.119	10.7	1.64	
36-22620	20 00 06.1	+30 04 55	15.38	0.106	14.1	1.15	2
36-24523	19 59 59.1	+30 09 04	17.42	0.253	14.5	1.24	
36-28705	19 58 56.9	+30 08 10	14.69	0.148	44.7	0.96	
36-29140	19 58 31.4	+30 10 12	15.45	0.162	12.7	1.10	
37-00124	20 01 43.8	+30 16 52	13.20	0.112	92.5	1.08	
37-00292	20 02 21.7	+30 25 56	15.65	0.138	70.1	2.11	
37-00575	20 01 55.2	+30 24 16	15.41	0.085	19.4	1.91	
37-01333	20 02 08.2	+30 19 14	16.72	0.427	106.2	1.72	
37-01334	20 02 15.5	+30 19 14	16.66	0.207	11.2	2.53	
37-01450	20 01 43.6	+30 17 34	16.37	0.067	11.2	1.80	
37-01862	20 01 35.0	+30 24 01	17.24	0.151	12.1	2.59	
37-07750	20 02 36.8	+30 18 56	14.27	0.178	58.0	1.14	
37-07882	20 02 46.9	+30 18 38	15.42	0.080	44.2	1.79	
37-08639	20 02 22.5	+30 14 14	16.85	0.284	26.1		
37-08729	20 02 41.0	+30 12 45	16.61	0.153	31.7	2.59	
37-09722	20 01 58.6	+30 10 45	17.33	0.306	34.3	1.85	
37-13395	20 01 32.8	+30 10 52	14.90	0.062	14.8	1.55	
37-18803	20 02 50.0	+30 24 19	15.01	0.178	21.7	1.34	
37-18943	20 02 13.9	+30 26 44	15.26	0.081	15.1	1.48	
37-19050	20 02 33.2	+30 31 13	15.74	0.170	13.5	1.74	
37-19223	20 02 36.3	+30 26 19	16.31	0.147	21.3	2.46	
37-19321	20 02 21.2	+30 31 37	17.43	0.411	40.3		
37-23358	20 01 17.3	+30 29 59	13.92	0.069	11.3	1.36	
37-24134	20 01 14.4	+30 30 24	16.01	0.135	11.5	1.66	
38-00413	20 00 20.0	+30 23 46	15.23	0.107	41.1	1.22	
38-01096	20 00 30.9	+30 16 42	15.41	0.080	13.7	1.26	
38-01882	20 00 00.6	+30 18 16	15.97	0.135	11.2	1.59	
38-02045	20 00 22.9	+30 16 18	16.16	0.280	19.1	1.35	
38-02105	20 00 41.1	+30 15 36	15.96	0.185	9.9	1.24	
38-03663	20 00 25.3	+30 15 55	17.20	0.225	9.9		
38-05062	20 00 08.9	+30 20 04	17.49	0.221	13.5	1.63	
38-05440	20 00 28.3	+30 18 15	17.18	0.328	20.4		
38-09264	20 00 50.7	+30 12 39	13.86	0.089	15.2	0.87	
38-09441	20 01 01.4	+30 11 17	13.91	0.146	164.5	4.01	1
38-10032	20 00 23.8	+30 13 13	15.76	0.258	63.1	1.63	

Table 3.3—*Continued*

Catalog ID	RA (J2000) Dec		$\langle I \rangle$	σ_I	χ^2_ν	$\langle V \rangle - \langle I \rangle$	Notes
38-10063	20 00 52.7	+30 12 43	16.39	0.127	10.7	1.78	
38-10433	20 01 03.2	+30 19 47	16.90	0.103	14.3	1.77	
38-10767	20 01 10.1	+30 13 24	17.33	0.321	15.3		
38-11218	20 00 39.8	+30 08 57	16.93	0.102	16.3		
38-12096	20 00 22.9	+30 12 24	16.74	0.214	32.8	1.38	
38-16121	19 59 42.8	+30 12 33	13.08	0.159	334.9	0.91	
38-16916	19 59 32.6	+30 17 08	16.35	0.121	9.9	1.53	
38-17172	19 59 50.3	+30 11 42	16.05	0.176	15.7		
38-17232	19 59 50.2	+30 10 48	15.80	0.195	18.1	1.31	
38-17604	19 59 35.0	+30 17 39	16.71	0.242	13.6	1.07	
38-17741	19 59 35.3	+30 15 24	16.93	0.144	14.6	1.23	
38-18325	20 00 12.9	+30 08 41	16.90	0.222	23.5	1.31	
38-18357	20 00 14.4	+30 08 23	16.61	0.234	26.2	2.20	
38-23132	20 00 52.4	+30 28 51	10.87	0.072	16.0	1.96	
38-23302	20 01 01.5	+30 31 44	14.42	0.124	55.1	2.76	1
38-23333	20 00 16.9	+30 29 39	14.50	0.096	49.9	2.97	
38-23426	20 00 50.5	+30 24 35	14.52	0.257	180.8	1.43	
38-23533	20 01 09.2	+30 29 59	15.05	0.187	116.2	1.60	
38-23680	20 01 09.3	+30 24 54	15.10	0.235	29.3	1.18	
38-24194	20 01 02.8	+30 22 36	15.87	0.149	9.9		
38-24279	20 00 39.6	+30 31 20	16.18	0.217	10.1	1.54	
38-29692	19 59 53.2	+30 24 20	11.90	0.084	39.8	0.74	V1023 Cyg
38-29859	19 59 35.5	+30 31 21	14.44	0.186	12.7	2.38	
38-29986	19 59 40.0	+30 22 38	14.97	0.229	53.5	1.30	
38-30954	19 59 58.6	+30 29 53	16.96	0.204	38.7	1.48	
38-31872	19 59 28.3	+30 30 06	16.96	0.207	16.1	1.69	
51-00059	19 44 05.3	+23 26 48	13.18	0.073	18.1	1.78	3
51-00328	19 43 27.6	+23 26 24	15.87	0.165	106.3	2.60	2
51-00530	19 43 32.1	+23 27 17	16.72	0.152	32.8	3.15	
51-03079	19 43 48.6	+23 20 19	16.57	0.091	14.0	2.41	2
51-04279	19 43 59.5	+23 24 48	18.40	0.493	23.3		
51-04725	19 43 07.5	+23 26 04	14.18	0.503	1462.6	1.59	
51-04729	19 43 10.2	+23 25 32	14.90	0.286	423.2	2.14	
51-04794	19 43 01.6	+23 26 29	15.79	0.126	54.9	1.82	
51-04843	19 43 24.0	+23 20 09	15.28	0.070	38.0	2.32	2
51-04902	19 42 58.3	+23 24 11	16.32	0.178	33.7	2.30	
51-04931	19 43 33.4	+23 21 48	16.11	0.135	49.2	3.76	2
51-05073	19 43 40.8	+23 23 21	16.41	0.112	27.2		3
51-05114	19 43 40.6	+23 20 46	16.66	0.115	14.9	3.00	
51-05129	19 43 38.5	+23 20 07	17.29	0.223	21.3	2.76	
51-05346	19 43 21.1	+23 21 29	17.51	0.282	27.0	2.58	
51-06491	19 44 11.4	+23 39 52	14.50	0.105	119.2	1.31	
51-09719	19 43 05.6	+23 36 38	13.61	0.087	37.9		3
51-09875	19 43 14.2	+23 41 28	15.73	0.164	57.5	1.65	
51-09898	19 43 03.1	+23 39 12	16.08	0.089	12.4	2.33	
52-01458	19 42 37.4	+23 26 38	17.47	0.219	22.0	2.60	
52-04808	19 42 59.5	+23 25 35	13.37	0.161	318.0	4.76	1
52-04812	19 42 22.0	+23 24 25	13.35	0.124	174.6	1.42	2
52-05099	19 42 58.3	+23 24 10	16.32	0.171	47.1	2.27	
52-05123	19 42 49.8	+23 22 36	16.01	0.088	14.4	2.02	

Table 3.3—*Continued*

Catalog ID	RA (J2000) Dec		$\langle I \rangle$	σ_I	χ^2_ν	$\langle V \rangle - \langle I \rangle$	Notes
52-05204	19 42 49.6	+23 29 14	17.12	0.289	27.1	2.95	
52-05277	19 42 58.2	+23 24 28	17.05	0.117	19.7	2.66	
52-05279	19 42 55.2	+23 24 25	16.67	0.201	37.3	3.03	
52-05732	19 42 10.1	+23 20 02	17.52	0.209	26.3	2.62	
52-07795	19 41 50.4	+23 22 59	16.72	0.247	124.1		
52-08080	19 41 45.6	+23 28 01	17.19	0.226	25.9	2.88	
52-10915	19 42 40.3	+23 38 04	15.43	0.139	73.8	1.73	
52-14193	19 41 33.0	+23 33 52	14.45	0.090	21.5	2.09	
53-00032	19 42 27.9	+23 05 15	12.87	0.106	14.3	2.25	1
53-00212	19 42 27.6	+23 05 11	15.55	0.152	16.8	2.31	
53-00249	19 42 41.1	+23 14 02	15.94	0.112	40.6	2.44	
53-00252	19 43 15.0	+23 13 57	16.30	0.132	38.8	3.03	
53-00371	19 43 07.3	+23 04 33	16.06	0.118	32.6		1
53-00423	19 43 13.4	+23 14 35	17.11	0.193	17.0	2.70	
53-00658	19 43 14.8	+23 15 30	18.17	0.488	19.3	2.27	
53-03085	19 43 32.9	+23 00 49	12.29	0.064	42.8	1.64	1
53-03220	19 43 34.8	+23 07 33	15.76	0.076	25.5	1.69	
53-03492	19 42 51.2	+23 03 13	16.66	0.243	12.1	3.30	
53-04937	19 42 16.7	+23 05 14	14.44	0.083	21.2	1.83	
53-05748	19 42 23.8	+23 07 53	17.02	0.324	15.3	3.17	
53-05808	19 42 24.4	+23 06 23	17.23	0.326	48.7	2.93	
53-08371	19 43 21.0	+23 19 03	15.38	0.116	84.0	2.59	
53-08381	19 42 57.0	+23 18 23	14.72	0.106	105.1	1.41	
53-08520	19 43 24.5	+23 20 13	16.04	0.156	81.7	2.14	2
53-08525	19 42 52.3	+23 19 58	16.00	0.067	17.2	2.25	
53-08544	19 43 23.6	+23 18 38	16.64	0.087	13.6	2.50	
53-08551	19 43 11.6	+23 18 21	16.57	0.106	30.2	2.67	
53-08598	19 43 22.8	+23 16 29	16.61	0.065	15.1	2.88	2
53-08735	19 43 17.0	+23 17 52	17.40	0.395	49.1	2.88	
53-08767	19 43 08.7	+23 17 21	17.35	0.137	13.9	2.89	
53-08790	19 43 06.0	+23 16 49	16.91	0.103	16.8	2.24	
53-08794	19 43 06.1	+23 16 45	17.22	0.145	15.7	2.34	
53-08830	19 43 32.0	+23 15 10	16.94	0.161	38.0	2.73	2
53-08831	19 43 30.1	+23 15 06	16.92	0.374	121.4	2.65	
53-08833	19 43 30.0	+23 14 56	17.27	0.152	16.6	2.65	
53-08834	19 43 18.9	+23 14 44	17.23	0.119	12.1	2.65	
53-08848	19 43 24.7	+23 13 42	16.75	0.108	23.2	3.22	
53-08877	19 43 23.1	+23 11 43	16.75	0.108	20.8	2.79	2
53-09075	19 43 24.2	+23 17 26	17.62	0.231	26.0	3.10	
53-09112	19 43 18.5	+23 16 48	17.49	0.212	31.1		
53-09146	19 43 11.2	+23 16 10	17.57	0.124	17.2	2.47	
53-09623	19 42 51.4	+23 16 22	17.95	0.409	23.6	2.58	
53-09690	19 43 33.4	+23 15 40	18.00	0.391	35.2		
53-09925	19 43 02.9	+23 19 47	18.54	0.441	16.9		
53-10178	19 43 05.0	+23 16 52	18.23	0.362	11.8		
53-11025	19 42 38.6	+23 17 25	17.35	0.174	18.9	3.10	2
53-11501	19 42 31.3	+23 15 51	17.68	0.264	28.6	2.77	
54-00084	19 41 18.8	+23 09 51	13.47	0.067	21.4		3
54-01618	19 41 42.0	+23 04 19	17.26	0.161	16.5	2.76	
54-02875	19 41 38.9	+23 15 12	18.69	0.715	34.4		

Table 3.3—*Continued*

Catalog ID	RA (J2000) Dec		$\langle I \rangle$	σ_I	χ^2_ν	$\langle V \rangle - \langle I \rangle$	Notes
54-04854	19 41 58.5	+23 03 41	15.63	0.162	101.1	2.58	
54-05032	19 41 26.2	+23 03 22	15.95	0.134	64.5	3.73	
54-12995	19 41 46.6	+23 14 57	17.39	0.215	32.5	2.91	1
54-13774	19 41 46.4	+23 11 39	17.74	0.209	17.9	2.86	
54-15020	19 40 47.7	+23 18 18	15.49	0.109	50.6	1.64	
54-15113	19 40 49.9	+23 20 09	16.20	0.149	40.8	1.73	
55-00246	19 42 09.7	+22 50 57	14.94	0.079	15.2	2.92	
55-00925	19 42 04.3	+22 45 56	16.54	0.078	15.9	2.97	
55-00938	19 41 44.3	+22 45 26	16.57	0.156	42.8	3.33	2
55-05432	19 42 28.3	+22 40 55	14.73	0.189	295.3	1.30	
55-05603	19 41 59.8	+22 36 36	16.16	0.158	85.6	1.42	
55-09503	19 41 24.8	+22 38 18	16.32	0.119	44.2	1.69	
55-12610	19 42 36.7	+22 55 33	10.74	0.111	18.7	0.64	
55-13691	19 42 02.5	+22 55 15	17.48	0.215	24.0	2.59	
56-00061	19 40 41.2	+22 48 48	13.84	0.073	9.9	1.44	
56-00263	19 40 06.1	+22 45 41	15.07	0.081	42.9	1.36	
56-08288	19 39 54.4	+22 36 28	15.37	0.110	53.8	2.64	
56-10655	19 40 38.8	+22 57 27	10.83	0.100	18.3	0.66	
56-11012	19 41 02.6	+22 59 00	16.39	0.105	10.0	1.77	
56-15109	19 39 45.2	+22 57 53	13.00	0.153	12.2	1.26	
56-15248	19 39 33.0	+22 53 40	15.60	0.257	112.9	1.41	
61-00177	19 39 23.5	+21 42 15	15.60	0.126	28.2	3.14	
61-00185	19 39 04.1	+21 41 07	15.61	0.128	16.3	2.56	
61-05291	19 38 38.8	+21 41 54	16.28	0.322	145.5		
61-05490	19 38 45.7	+21 37 18	16.72	0.140	34.0	2.85	
61-08902	19 38 49.0	+21 49 53	14.64	0.080	31.7	2.96	2
61-09480	19 38 44.3	+21 48 05	18.13	0.250	15.0		
62-00031	19 37 57.9	+21 46 45	14.72	0.226	509.2	2.80	
62-02623	19 38 19.5	+21 36 15	17.93	0.795	106.9		
62-04700	19 36 58.6	+21 37 12	17.70	0.904	99.5		
62-07871	19 37 36.1	+21 49 22	15.60	0.091	41.0	2.98	1
62-07920	19 37 20.0	+21 50 31	15.87	0.239	224.4		
62-07998	19 37 09.6	+21 52 22	16.42	0.160	39.9	2.71	
63-00075	19 38 23.3	+21 22 59	14.64	0.094	61.4	1.94	
63-01072	19 38 18.4	+21 16 53	17.17	0.153	21.7	2.38	
63-03172	19 38 07.3	+21 16 13	18.18	0.758	52.8		
63-06533	19 37 41.6	+21 16 44	16.57	0.182	75.2	2.30	
64-00009	19 36 44.2	+21 21 12	11.60	0.083	24.8	8.47	
64-00061	19 36 42.6	+21 20 49	14.34	0.099	77.1	2.19	
64-00129	19 36 38.1	+21 21 13	14.93	0.070	35.2	4.06	
64-00302	19 36 43.0	+21 17 25	15.47	0.211	179.5	2.43	2
64-06140	19 37 26.7	+21 21 18	18.42	0.811	34.2		
64-07553	19 36 21.3	+21 17 12	17.29	0.260	42.1		
64-09887	19 37 33.5	+21 23 19	15.98	0.066	27.4		
64-10050	19 36 48.2	+21 32 46	17.19	0.235	19.3		
65-00117	19 37 07.4	+21 02 04	14.13	0.212	323.2	1.51	2
65-00166	19 37 37.2	+21 04 44	15.12	0.084	51.1	1.86	
65-02674	19 37 40.8	+21 04 08	18.65	0.453	14.6		
65-03783	19 37 46.5	+20 56 12	18.51	0.738	32.5		
65-08324	19 36 55.0	+20 55 45	17.37	0.233	22.7		

Table 3.3—*Continued*

Catalog ID	R.A (J2000) Dec		$\langle I \rangle$	σ_I	χ^2_ν	$\langle V \rangle - \langle I \rangle$	Notes
65-11254	19 37 27.3	+21 08 52	16.27	0.259	126.5	2.10	
66-00044	19 36 04.5	+20 55 30	13.65	0.068	14.6	1.72	
66-00452	19 35 39.5	+20 59 47	16.19	0.147	43.9	2.49	
66-00801	19 35 59.6	+21 00 56	17.04	0.163	16.2		
66-03863	19 36 35.3	+20 49 40	12.96	0.120	157.7	4.32	1
66-03935	19 36 17.4	+20 48 06	14.59	0.135	173.3	1.95	
66-04471	19 36 07.1	+20 47 37	16.57	0.143	33.4	2.45	
66-06620	19 35 12.2	+20 51 51	15.35	0.073	38.1	2.39	
66-06867	19 35 35.3	+20 48 47	16.15	0.061	13.8	2.53	
66-07238	19 35 24.1	+21 00 18	17.53	0.173	17.6		1
66-08635	19 35 28.7	+20 49 08	17.81	1.004	134.4		
75-00568	19 32 56.4	+19 15 33	15.96	0.099	12.3	2.44	
75-07329	19 33 54.6	+19 10 44	16.19	0.119	11.5	4.07	
75-16726	19 33 41.9	+19 14 18	17.90	0.307	22.1		
75-19524	19 32 42.2	+19 20 11	12.79	0.075	14.6	2.16	
75-19710	19 33 06.5	+19 18 09	15.23	0.208	56.2	2.07	
75-19891	19 33 05.4	+19 19 06	15.94	0.119	15.1	2.21	
76-00518	19 31 52.9	+19 06 36	15.30	0.181	78.8	3.10	2
76-08902	19 31 54.7	+19 01 25	16.37	0.601	90.2	2.55	
76-12785	19 31 12.0	+19 01 19	11.06	0.183	337.3	2.53	1
76-12859	19 31 13.5	+19 05 33	14.17	0.063	33.7	3.62	2
76-12902	19 30 53.8	+18 58 50	14.09	0.071	24.3	2.60	2
76-12965	19 31 13.7	+19 04 02	14.47	0.146	101.8	1.59	
76-13269	19 31 15.5	+19 00 42	15.54	0.130	44.8		1,4
76-14470	19 31 34.1	+18 59 49	17.34	0.380	11.4	2.01	
76-22932	19 30 57.7	+19 12 40	14.81	0.274	151.0	2.56	
76-32830	19 31 10.5	+19 15 25	10.19	0.120	56.7	2.64	GX Sge
77-00326	19 32 06.8	+18 43 35	14.50	0.089	26.1	1.71	
77-08982	19 32 32.1	+18 57 26	16.29	0.315	60.9	2.23	
78-00246	19 30 29.1	+18 42 13	14.69	0.085	53.9	2.43	1
78-00686	19 30 42.1	+18 49 24	16.07	0.267	51.0	3.62	
78-01001	19 31 11.5	+18 53 20	17.22	0.178	14.4		
78-02471	19 31 23.5	+18 46 27	13.59	0.179	417.2	1.69	2
78-03092	19 30 47.8	+18 38 04	15.45	0.256	116.4	3.75	
78-04303	19 30 43.5	+18 38 36	14.99	0.121	108.4	3.82	
78-04318	19 30 25.6	+18 37 49	15.03	0.075	13.2	3.90	
78-05828	19 30 39.9	+18 39 53	17.57	0.461	23.9	2.82	
78-06093	19 30 57.3	+18 56 50	14.85	0.082	38.2	2.77	
78-06552	19 31 12.5	+18 56 35	15.93	0.104	12.9	2.90	
78-08001	19 30 05.2	+18 55 42	14.99	0.172	16.8	1.56	
78-08123	19 30 22.1	+18 56 07	15.29	0.172	76.2	3.80	1
81-03815	19 31 02.4	+17 57 28	15.77	0.099	34.2	2.05	
81-03994	19 31 03.7	+17 57 59	16.61	0.229	52.3	2.11	
81-04790	19 31 26.2	+18 01 04	18.20	0.458	34.9		
81-06268	19 29 55.8	+17 55 08	15.87	0.061	12.7	3.17	2
81-07564	19 30 55.6	+18 12 11	12.59	0.081	27.4	6.67	3
81-08167	19 30 43.1	+18 12 28	16.54	0.096	12.7	2.46	
81-10759	19 30 11.5	+18 13 55	13.99	0.151	102.5	1.23	2
81-10950	19 30 25.2	+18 14 41	16.68	0.170	34.4	2.82	2
82-00220	19 29 25.6	+17 59 09	15.69	0.084	19.2	2.42	

Table 3.3—*Continued*

Catalog ID	RA (J2000) Dec		$\langle I \rangle$	σ_I	χ^2_ν	$\langle V \rangle - \langle I \rangle$	Notes
82-00311	19 28 44.6	+18 06 57	16.85	0.126	28.0	2.61	
82-00607	19 29 02.7	+18 05 54	17.10	0.218	12.0	2.39	
82-00693	19 29 21.0	+18 02 13	16.81	0.286	39.6	2.76	1
82-01853	19 29 26.0	+18 05 52	18.40	0.440	23.6		
82-02322	19 29 50.0	+17 55 25	15.46	0.106	34.6	2.28	
82-02366	19 29 49.7	+17 58 59	15.80	0.103	16.7	3.77	2
82-02506	19 29 48.6	+17 58 00	17.07	0.199	22.4		2
82-03186	19 28 36.6	+17 53 27	16.02	0.129	73.3	2.40	1
82-03221	19 28 23.4	+17 56 58	15.76	0.172	109.9	2.64	
82-03227	19 29 01.1	+17 56 07	15.70	0.147	60.9	2.74	1
82-03288	19 28 32.4	+18 01 17	16.41	0.140	30.3	2.58	
82-03315	19 28 40.2	+17 56 46	16.73	0.120	16.0	3.01	
82-03514	19 28 47.8	+17 54 42	17.23	0.185	28.1		
82-03535	19 28 39.3	+17 52 57	17.69	0.302	39.1		
82-04489	19 29 29.7	+18 14 42	15.93	0.060	11.9	1.92	
83-00527	19 29 35.7	+17 46 19	17.17	0.200	38.6		
83-02288	19 29 55.0	+17 31 48	14.60	0.077	41.1	3.30	
83-02538	19 30 13.9	+17 39 03	16.95	0.100	12.4		
83-04195	19 29 38.7	+17 35 58	15.25	0.143	89.2	2.59	
83-04421	19 29 17.1	+17 31 45	17.66	0.556	24.3		
83-05829	19 29 44.6	+17 48 58	16.54	0.098	12.0	3.30	
83-05837	19 30 12.6	+17 48 36	16.74	0.228	61.9	3.17	
83-06056	19 29 54.3	+17 48 51	17.64	0.231	16.7		
84-00055	19 28 38.3	+17 40 56	14.98	0.240	213.4		2
84-00147	19 28 09.1	+17 35 47	15.32	0.158	103.3	2.26	
84-01800	19 28 37.7	+17 32 36	12.24	0.062	46.9	1.97	1
84-03741	19 27 46.4	+17 38 46	15.70	0.112	59.7	2.53	
84-05362	19 28 41.3	+17 48 20	15.81	0.095	25.8	2.48	
84-05396	19 28 59.8	+17 43 43	16.03	0.095	14.4		2
84-05414	19 28 30.8	+17 51 44	16.93	0.225	33.6		2

Notes:

1. Cepheid candidate selected for followup photometry.
2. Less promising Cepheid candidates based on visual inspection.
3. Long period variable.

mag over one half cycle. We therefore adopted a lower limit of 0.06 mag for the RMS variability in I, to catch the longest period Cepheids, and a further criterion of $P(< \chi^2) < 10^{-14}$ to eliminate spurious candidates. The final selection criterion is that the star must still qualify as a variable star $(P(< \chi^2) < 10^{-4})$ after any single point in the light curve is removed. Strong single-point eclipsers are thus eliminated from further consideration. The resulting catalog of high-amplitude variables contains 578 stars, and is presented in Table 3.3.

Unfortunately, the number of high-amplitude variables that are potentially Cepheids based upon the above criteria is too large to readily acquire additional photometry or spectra for each candidate. We therefore plotted light curves and color-magnitude diagrams for each variable star and selected candidates for followup based upon visual inspection. I selected approximately 40 stars that I thought were most promising, based upon several criteria. First, if a candidate's color change was inconsistent with a dV/dI slope of 1.5, it was set aside. This removed about 200 of the candidates, though a large fraction of the candidates do not have color information (see Table 3.3) so this criterion could not be used. The last eliminations I made were those stars showing light curves inconsistent with a Cepheid's, primarily if the amplitude was too high or the rise time was much slower than the decline. Light curves were also independently evaluated by P. Schechter, whose comments were read only after making my own evaluation (i.e. double-blind). In cases where there was disagreement as to the promise of a candidate, we tried to be inclusive. In the end, however, the number of candidates was cut to the number we could perform follow-up photometry on in a single observing run; others not included may still be proven to be Cepheids in the future.

Stars selected for follow-up photometry are indicated in Table 3.3. The "B" team candidates–a second set that looked promising but which we were unable to observe– are also indicated in the table, and are perhaps worthy of further photometry. Stars that were classified as high-amplitude variables and showed a monotonic increase or decrease in brightness are also noted in the table. Some of these stars may actually be long-period Cepheids, but direct follow-up photometry was not performed. In the

future we hope to obtain spectra for these stars to help classify them.

Most of the variable stars from the General Catalog of Variable Stars, 4th Edition (Kholopov *et al.* 1988, hereafter GCVS) in our survey area were recovered, including GU Vul (W UMa-type), EW Vul (RR Lyr), KN Vul (W UMa), V1023 Cyg (Algol), and GX Sge (δ Cep). A known Cepheid with $<I> = 10.2$, GX Sge was at the bright end of our survey limit and was barely recovered—on two nights with the best seeing, it had saturated the detector. We initially thought we had missed this star, but after further examination we found it 1 arcminute away from its reported position in the GCVS. We measure GX Sge at RA 19h 31m 10.5s, Dec $+19°$ 15' 25" (J2000), and provide a finding chart for future reference. Other GCVS stars recovered were found at the published locations to within quoted errors. The GCVS stars not recovered included V1022 Cyg, a semi-regular variable with a period of 60 days, which is slightly too bright at I to be recovered in the survey; GK Vul, a semi-regular with no listed period, possibly too long for the variability to be detected in this survey; and CQ Vul, a slow irregular variable.

3.4 Follow-up Photometry

Additional photometry of the top Cepheid candidates was obtained on the nights of May 28–June 7 1993 at the 1.3 m McGraw-Hill telescope of the Michigan-Dartmouth-MIT Observatory. Images were obtained in both V and I bands using a Tektronix 1024^2 CCD ("Charlotte"; see Metzger, Tonry, & Luppino 1993 for a general description of the MDM CCD systems). The CCD and filters used were similar to the ones used for the main survey: in both cases the CCD used was thinned with 24μ pixels, and the I filter was the same type of interference filter used a year earlier. The pixel size was 0".51, which meant that under the best seeing conditions (0".9) our images were slightly undersampled. Conditions were photometric on several nights, allowing us to improve the absolute calibration for the Cepheids over the original survey data. Twilight sky flat-field images were taken each night, and photometric standards of Landolt (1992) were taken frequently at multiple zenith angles to allow a correction

for atmospheric extinction.

Each frame was corrected for variations in detector response and throughput using composite twilight flats, one composite for each night. The composites were created using the standard method of averaging many images of the sky, excluding regions around stars that appear above the 0.5% level in the individual images. After removing the amplifier bias (zero-signal level) measured using an overclock region off the edge of the CCD, each image was divided by the normalized composite flat. Signal levels in the composite flats were kept above $150,000$ e$^-$ to reduce the amount of noise added to the images. We checked the consistency and linearity of the response by flattening other flats: from one night to another and over a range of exposure levels, the corrected response was constant to $< 0.3\%$, except for a striking difference between those taken before night 6 and those on or after. During the day before the 6th night, the dewar was allowed to warm up and then re-cooled to the 173 K operating temperature; we believe this was was responsible for the 0.6% RMS response difference between nights 5 and 6. This highlights the necessity of taking flat-field images each night, not only to correct for moving dust rings (cf. §3.2.2) but in case of other, unforseen changes in the instrument.

Instrumental magnitudes were measured using apertures $3\overset{''}{.}5$ in diameter, and corrected to an effective magnitude for a 10" aperture using isolated bright stars in the images (this correction would vary depending on the seeing). Instrumental magnitudes were measured for the standards in the same manner, and used to determine atmospheric extinction coefficients and color corrections to a standard magnitude system. The transformations are given by

$$I = m^i_{1e} + 23.253(10) - 0.121(20)[\sec z - 1.0] + 0.017(8)[V - I]$$

and

$$V = m^v_{1e} + 23.683(10) - 0.215(19)[\sec z - 1.0] - 0.014(7)[V - I],$$

where $m^b_{1e} = -2.5 \log_{10}(f^b)$, f^b is the corrected 10" flux in e$^-$ s^{-1}. Colors of standards used to compute these relations were in the range $-0.21 < (V - I) < 1.76$ and were

Table 3.4: New Cepheids

Star	Catalog ID	RA (J2000) Dec		$\langle I \rangle$	$\langle V \rangle - \langle I \rangle$	Period
19313+1901	76-13269	19 31 15.5	+19 00 42	15.54	4.3	4.1643
19430+2326	52-04808	19 42 59.5	+23 25 35	13.37	4.7	7.8888
19431+2305	53-00371	19 43 07.3	+23 04 33	16.06	> 6	5.6646
19456+2412	03-00092	19 45 36.7	+24 12 09	13.21	3.2	4.0758
19504+2652	18-00380	19 50 26.0	+26 51 44	16.09	5.2	5.8326
19508+2620	15-00026	19 50 49.3	+26 19 45	12.85	3.8	5.9497
19462+2409	03-06544	19 46 11.5	+24 09 04	12.51	3.0	3.8799
19462+2501	08-00258	19 46 11.9	+25 00 33	15.28	3.7	4.7842
19468+2447	07-11383	19 46 46.9	+24 46 47	11.43	2.7	4.9427
20010+3011	38-09441	20 01 01.4	+30 11 17	13.91	3.8	7.1395
19286+1733	84-01800	19 28 37.7	+17 32 36	12.24	1.9	4.1643

linear to within the errors. Most of our target stars are outside this range, therefore we have extrapolated this relation to all colors. Such an extrapolation is uncertain, however, and should be viewed with caution. Fortunately the color terms are small, and we expect that for $(V - I) < 3.5$ the uncertainty should be smaller than the typical photometric error for all but the brightest stars.

3.4.1 New Cepheids

Of the 31 stars observed, 10 are confirmed to be Cepheids, with one additional star likely to be a Cepheid but with unusual color change properties. Table 3.4 shows a summary of the data, and Figures 3-12–3-21 show I light curves and V vs. I color data for the newly-discovered Cepheids. Of the remaining stars, most had no identifiable periodicity when combined with the original survey data, down to a period of about 2 days; others appeared periodic but did not have the appropriate color change for a Cepheid ($dV/dI \gtrsim 1.3$; Madore & Freedman 1991, Avruch 1991). The candidate 19450+2400 exhibited clearly periodic behavior with a long period, and $dV/dI = 1.45$, but the light curve was too sinusoidal for a Cepheid of that period.

One candidate star (19508+2620) appeared to have a slope of color change too shallow to be a Cepheid; however, under closer examination of a V image taken in good seeing, we discovered a neighboring star close to the candidate that was roughly equal in brightness to the Cepheid at minimum light. The V photometry was contaminated with the light from this star, which caused the V amplitude to appear

147

shallower and thereby affected the slope of the color change. The companion star is not visible in I, nor does it affect the I light curve of the Cepheid since the Cepheid is much brighter in I ([V–I]= 3.8). Since this is an effect of roughly 0.4 magnitudes at V, the overall slope in V if this star were not present would be $\sim$ 1.6, in line with what we expect for a Cepheid. Since the I light curve is also clearly consistent with that of a Cepheid, we are confident that this star is properly classified as such. Another candidate, 19286+1733, also has a light curve similar to that of a Cepheid and dV/dI too shallow. We were unable to identify a contaminating star in this case, so we have left its classification as tentative pending spectroscopic observations.

Periods for the Cepheids were determined using the minimum string length method (Burke *et al.* 1970, Dworetsky 1983), in a similar way as was used for the southern hemisphere Cepheids by Avruch (1991). The observations were folded about a particular test period, and a string length is computed by summing distances between points consecutive in phase. A wide range of test periods were searched for each star, and the one having the minimum string length is taken to be the period. In practice this method is quite sensitive to photometric errors, and isn't well suited to occasional outliers. In cases where this is a problem, however, the minimum string length will usually correspond to some period that is clearly discordant, and single points can be deleted and re-fit. Avruch (1991) perfomed a Monte Carlo analysis of period errors associated with this method, but since we have two sets of observations taken one year apart, our error is dominated by that due to adding or deleting one full cycle between the two observing seasons. It is the one year baseline which gives most of the precision in determining the period: a change in period of roughly 1 part in 70 (1 cycle change over a year for a 5 day period) is not well constrained by data from one year alone, and thus our periods are accurate only to the 1 part in 70 level. To improve the measurement, we would need a third set of observations to remove the abmiguity, at which point periods should be obtainable to better than 1 part in 1000.
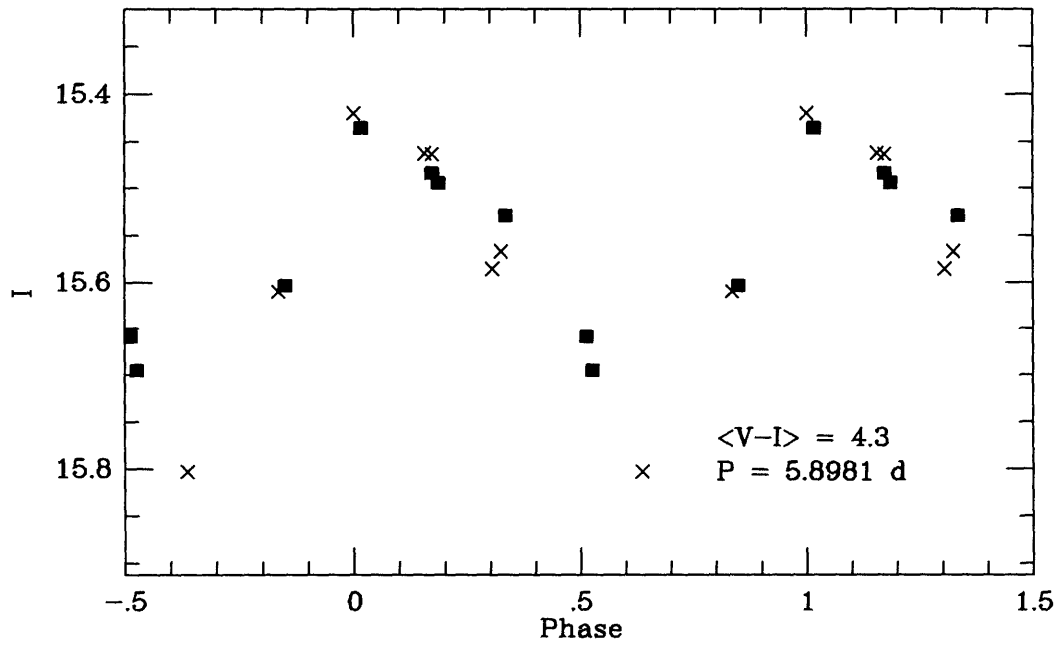
Figure 3-12: I light curve for the Cepheid 19313+1901. Crosses are data from the 1992 survey, squares from the 1993 followup.
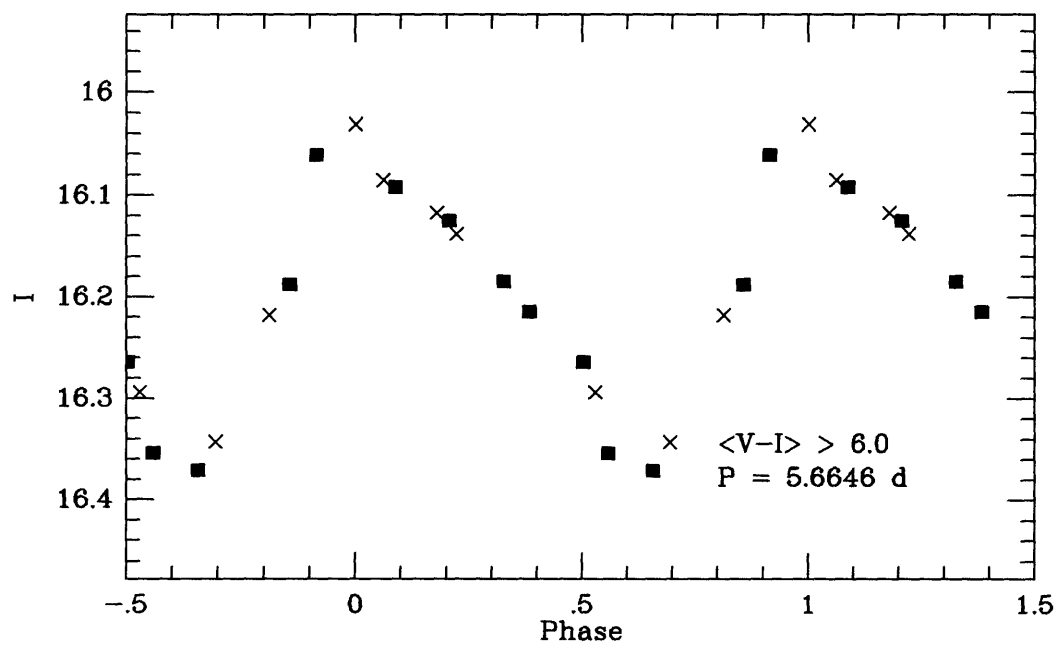

Figure 3-13: I light curve for the Cepheid 19431+2305.

Figure 3-14: I light curve and two-band plot for 19430+2326.

Figure 3-15: I light curve and two-band plot for 19462+2409.

151

Figure 3-16: I light curve and two-band plot for 19456+2412.
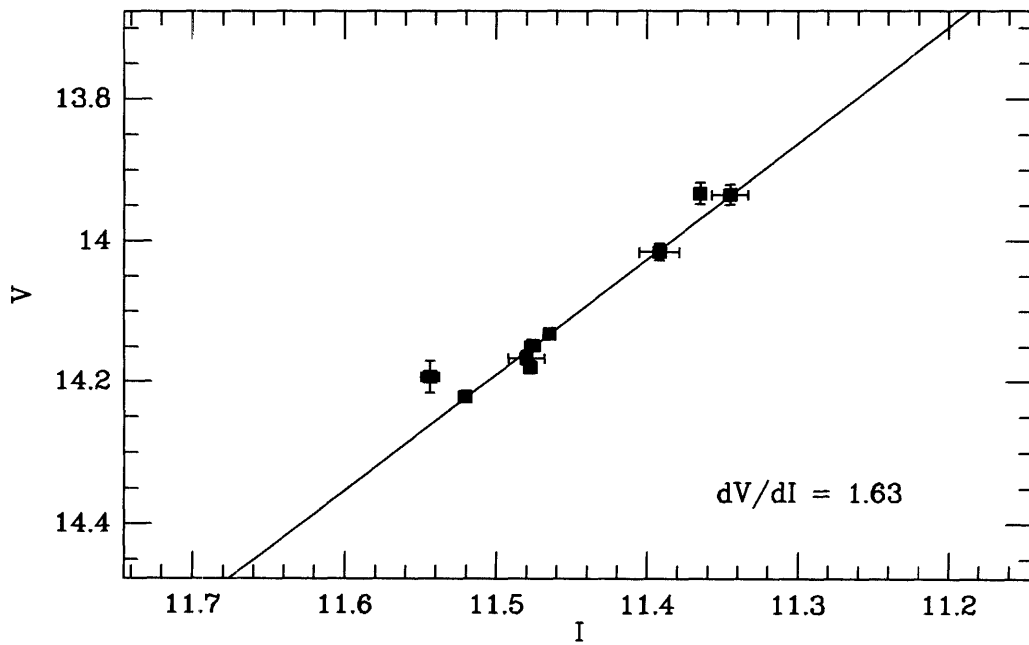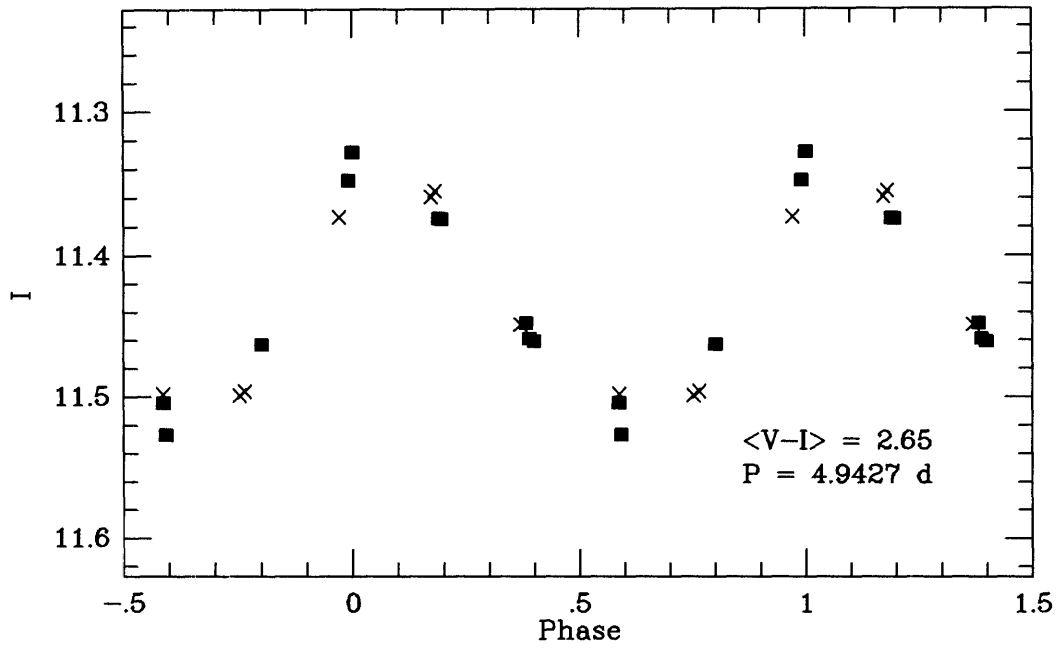
Figure 3-17: I light curve and two-band plot for 19468+2447.
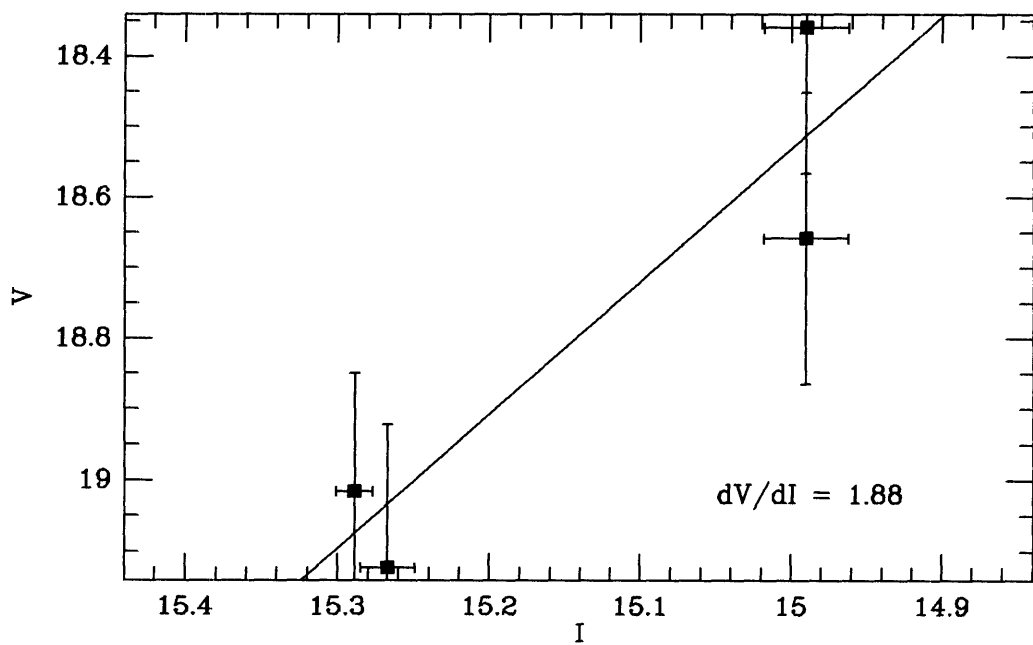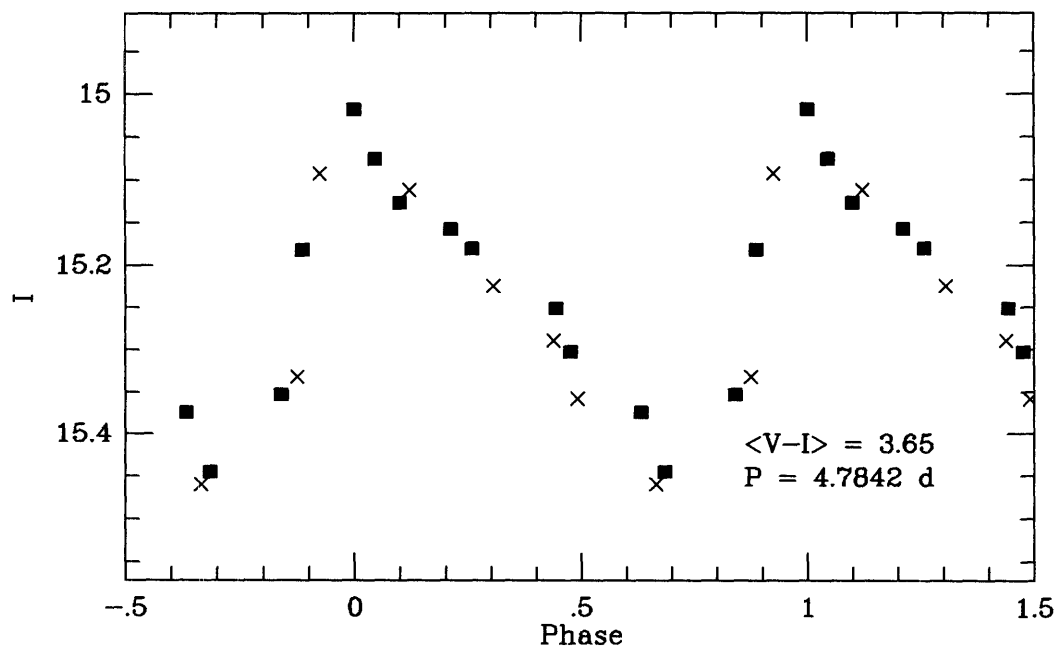
Figure 3-18: I light curve and two-band plot for 19462+2501.
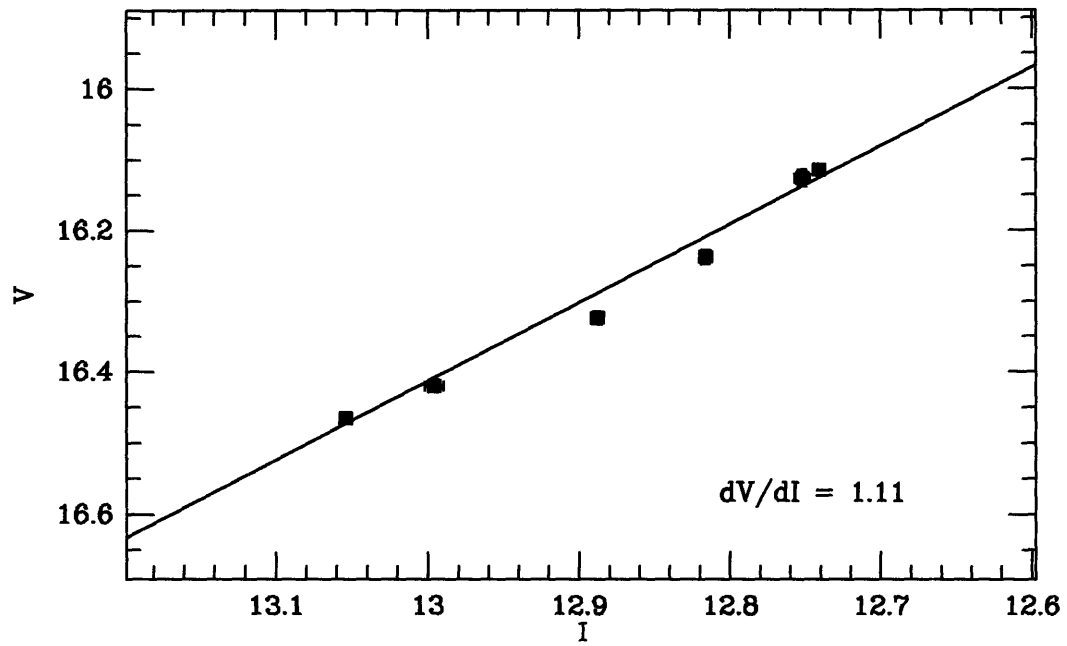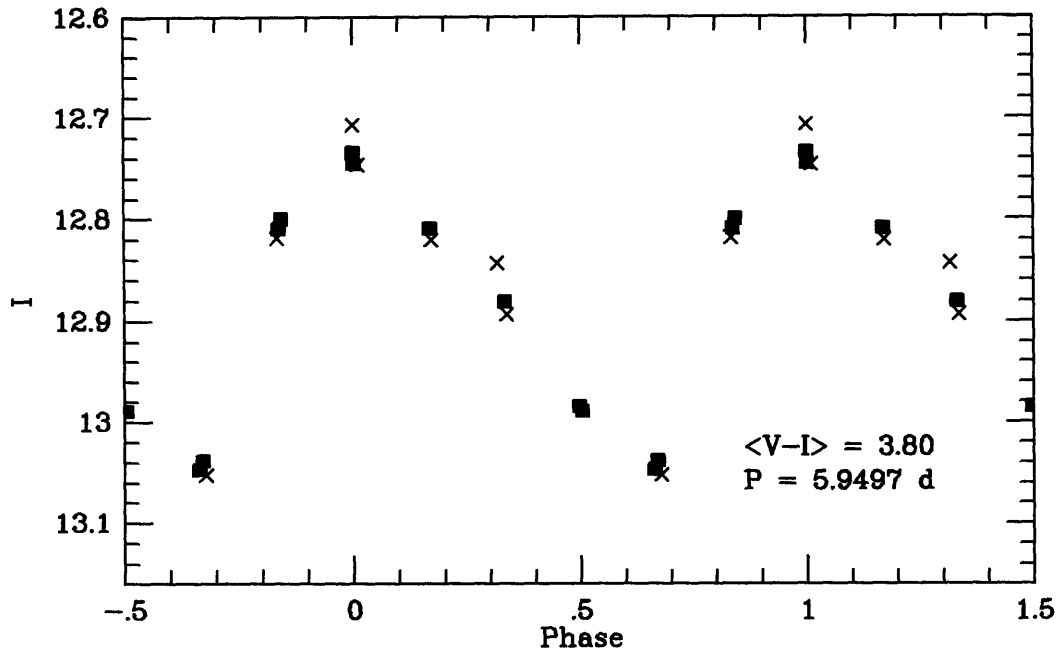
Figure 3-19: I light curve and two-band plot for 19508+2620.
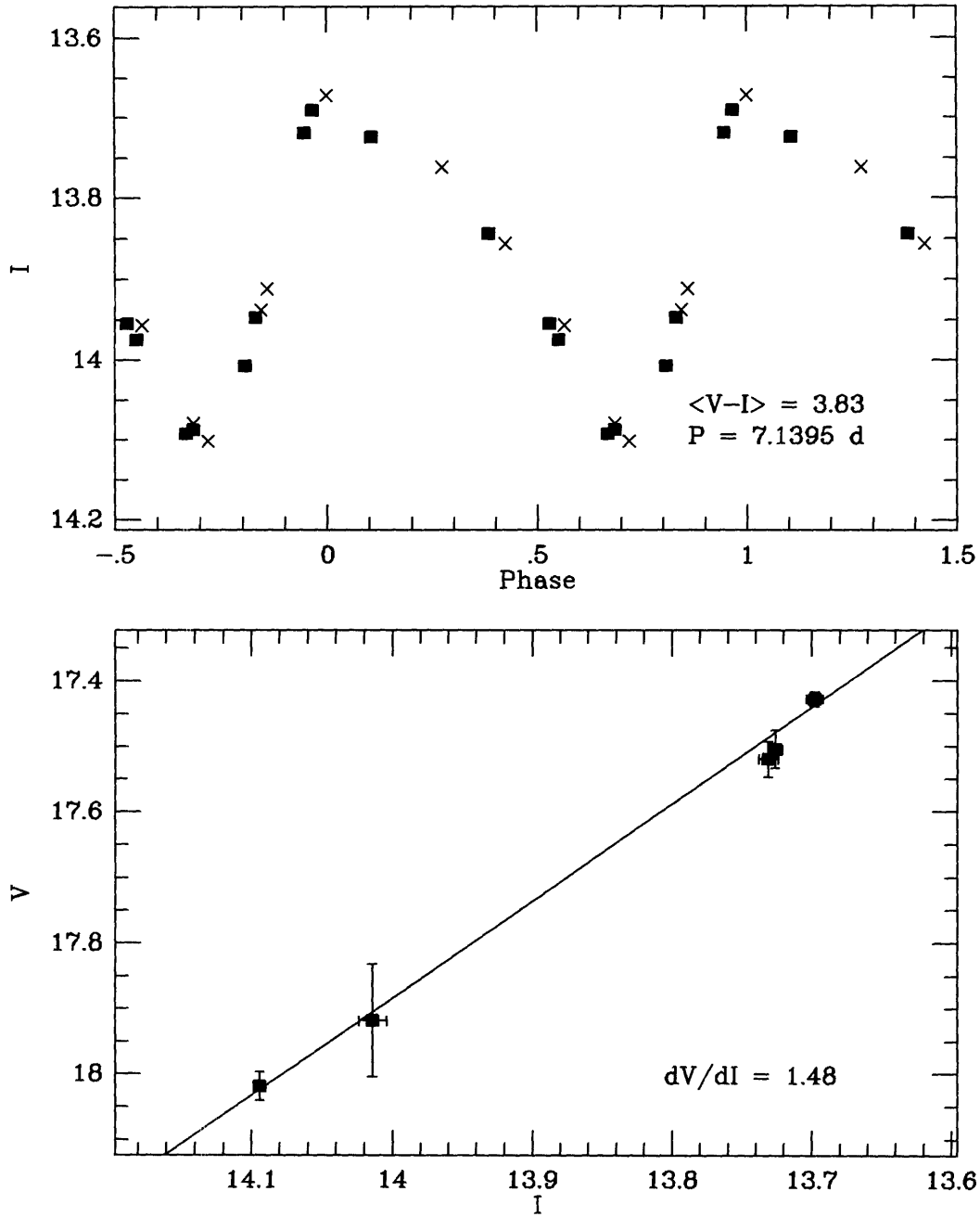
Figure 3-20: I light curve and two-band plot for 20010+3011.

$\langle$V–I$\rangle$ = 1.9
P = 4.1643 d

dV/dI = 1.22
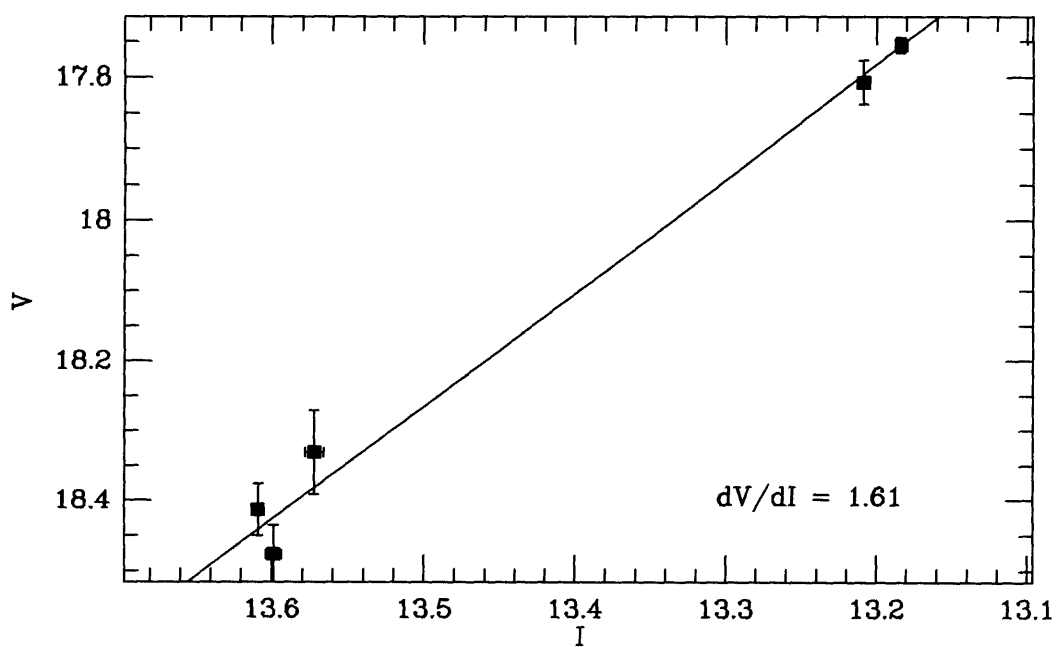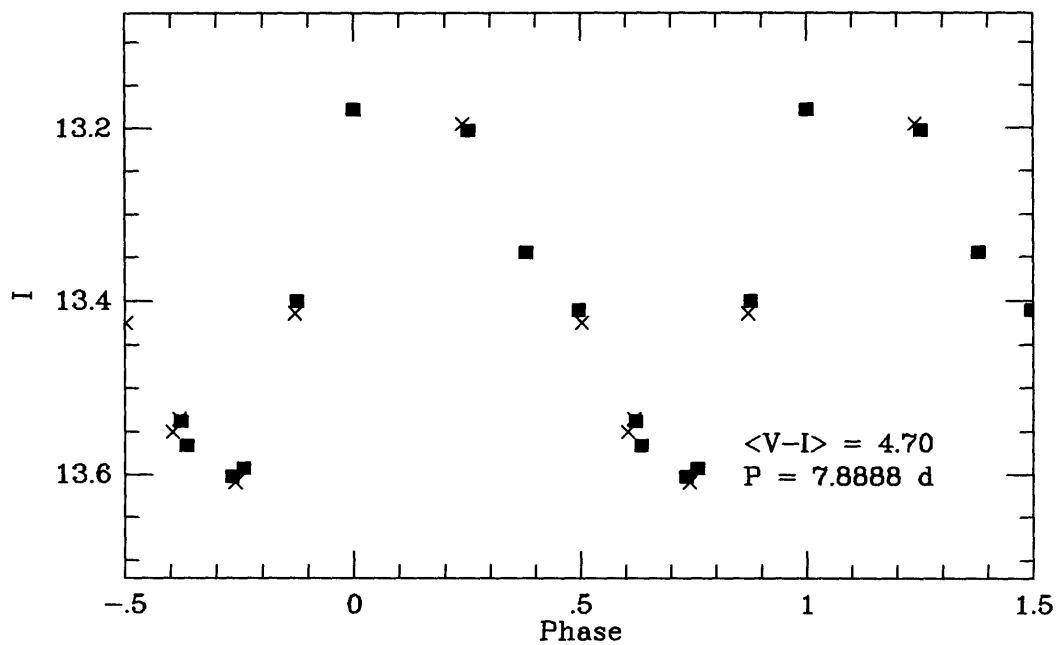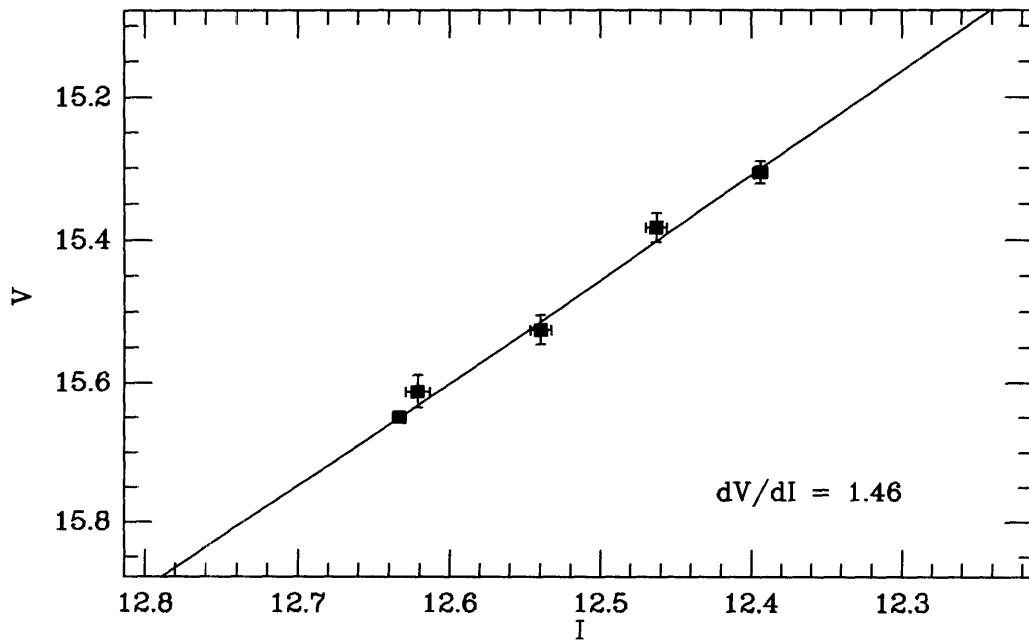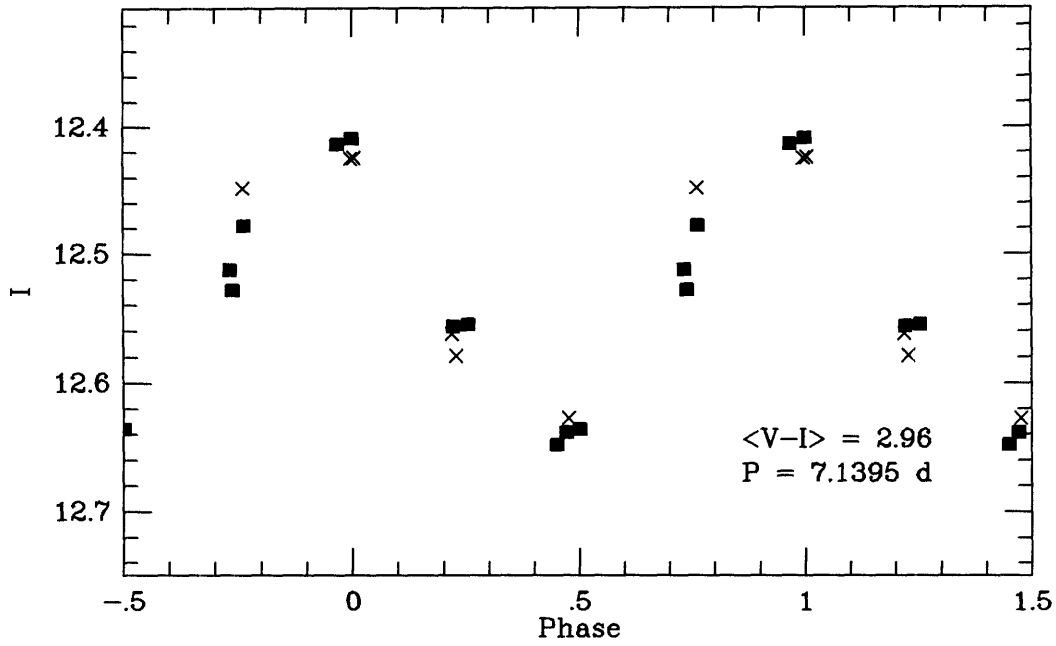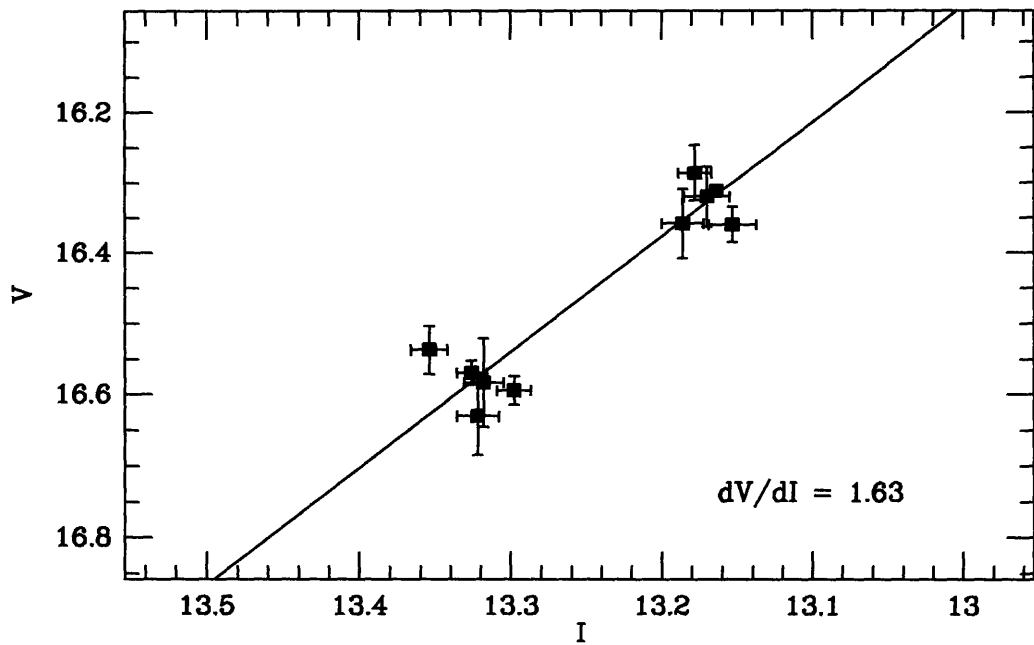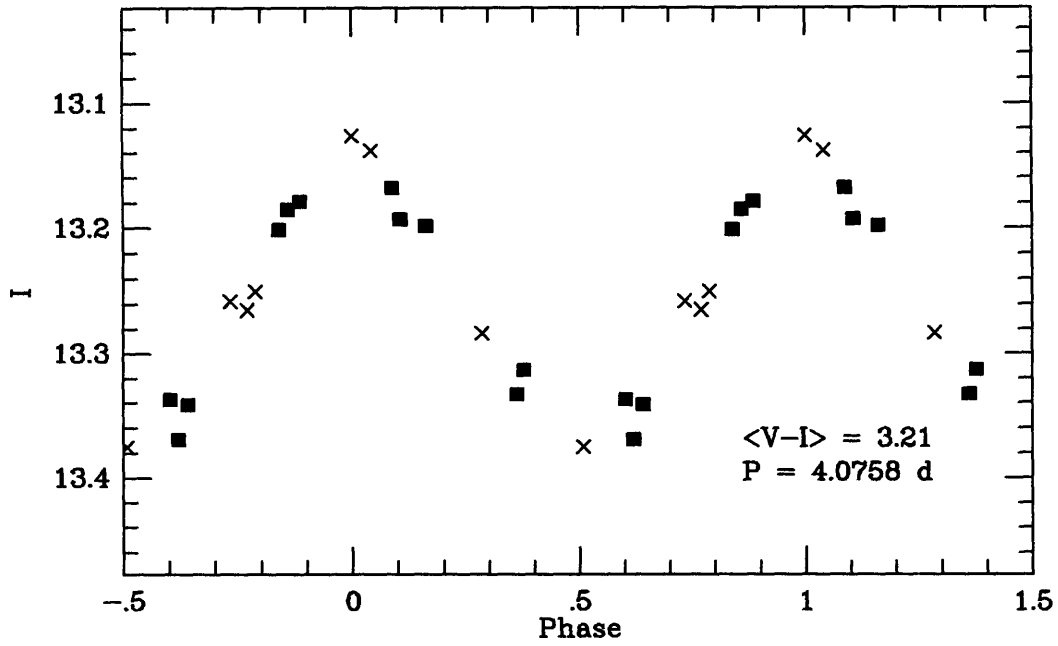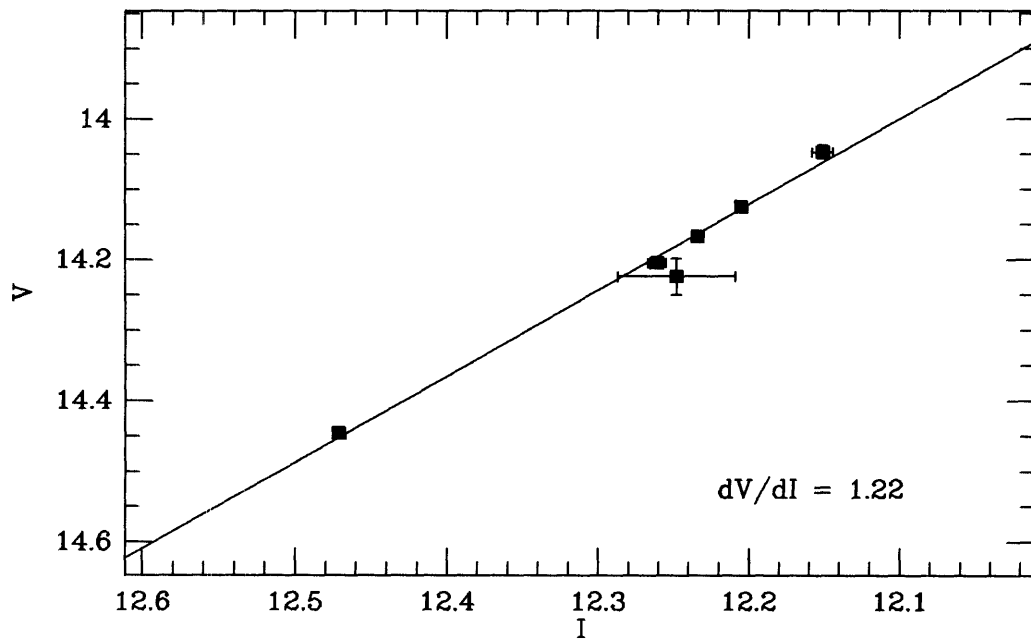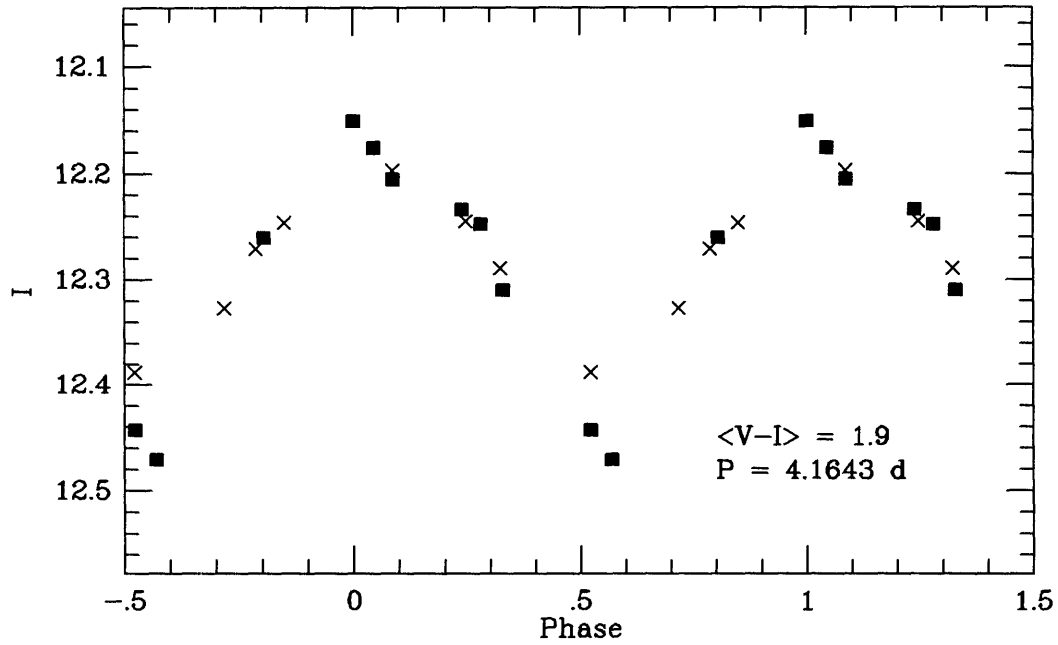
Figure 3-21: I light curve and two-band plot for 19286+1733.
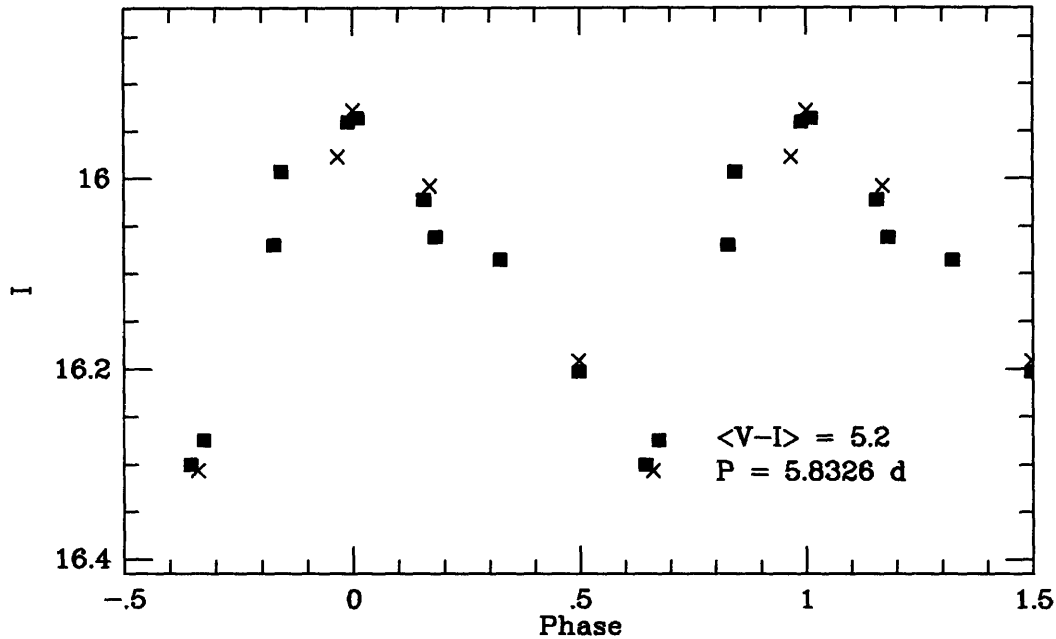
Figure 3-22: I light curve for the Cepheid 19504+2652.

3.5 Discussion and Impact

Out of a total of over 1 million stars in a six square degree area, we have discovered 10 new Cepheid variables with periods ranging from 4 to 8 days. As we expected, the extinction toward these stars is significantly higher than that toward the Cepheids discovered in the CKS survey. There may also be a bias against Cepheids outside the 4–8 day period range; such a bias may have arisen in the qualitative evaluation of the light curves from the survey, which clearly show the light curve shape for periods in this range. The lack of Cepheids with longer periods is of less concern, as they are both preferentially excluded due to our short baseline in the survey, and are much rarer than shorter period stars.

One of our Cepheids, 19431+2305, is the most heavily reddened Cepheid known. While we do not have an accurate color for this star, we can just barely detect it in a single long exposure obtained at the 2.4m Hiltner telescope, which would give it a color of approximately (V–I)= 6.3. Assuming an intrinsic color of roughly 0.65 (Madore & Freedman 1991), this implies a total extinction in V, A_V, of roughly

14 magnitudes, using an extinction law appropriate for Cousins I (see Chapter 2). This places the star at a distance modulus of approximately 12.2, or only 3 kpc! Of course, such an estimate is only approximate, as both the calibration of magnitudes to standard bands and the extinction law are not well determined for stars this heavily reddened. Clearly, however, we are running into a limit on the distance of Cepheids we can recover, and how accurately we can determine distances to them.

The approximate positions of the new Cepheids are shown in Figure 3-23, based on the distance scale adopted in Chapter 2. An intrinsic color of (V–I) = 0.65 was assumed, and an absolute magnitude calibration of $M_I = -3.06(\log P - 1) - 4.87)$ was used to determine distances (Madore & Freedman 1991). Apparent I magnitudes of the stars were de-reddened using the relation $A_I = 1.5E(V - I)$, following the reddining law of Cohen et $al.$ (1981). Most of the Cepheids are closer than R_0, though we apparently reached the solar circle at $\ell = 61.2$ and $\ell = 67.4$. The distances are uncertain primarily due to the uncertainty in dereddening the apparent magnitudes. We have also assumed that each star is a classical (Type I) Cepheid, though with the available data we are unable to distinguish them from W Vir stars (Type II Cepheids). The contamination from W Vir stars should be small, however, as they are Population II stars and the survey was confined to the disk.

Based on this preliminary analysis, we see that most of the new Cepheids lie in regions where none were previously known, and once radial velocities are measured for these stars, they will provide useful constraints on both R_0 and the ellipticity of the rotation curve. Using the relation given by Schechter et $al.$ 1992,

$$\frac{dv}{d\ln R_0} = v_o \sin \ell \left[\frac{d^2 - d\cos\ell}{[1 + d^2 - 2d\cos\ell]^{3/2}} \right],$$

we find that the most distant Cepheid should provide an estimate of R_0 of 12%, assuming an intrinsic velocity dispersion of 11 km s^{-1} in the disk. The total sample should yield an R_0 measurement with an uncertainty of 8% once radial velocities and accurate distances are measured. When combined with the full sample of known Galactic Cepheids, these stars can be used to directly test the symmetry of the rota-

159
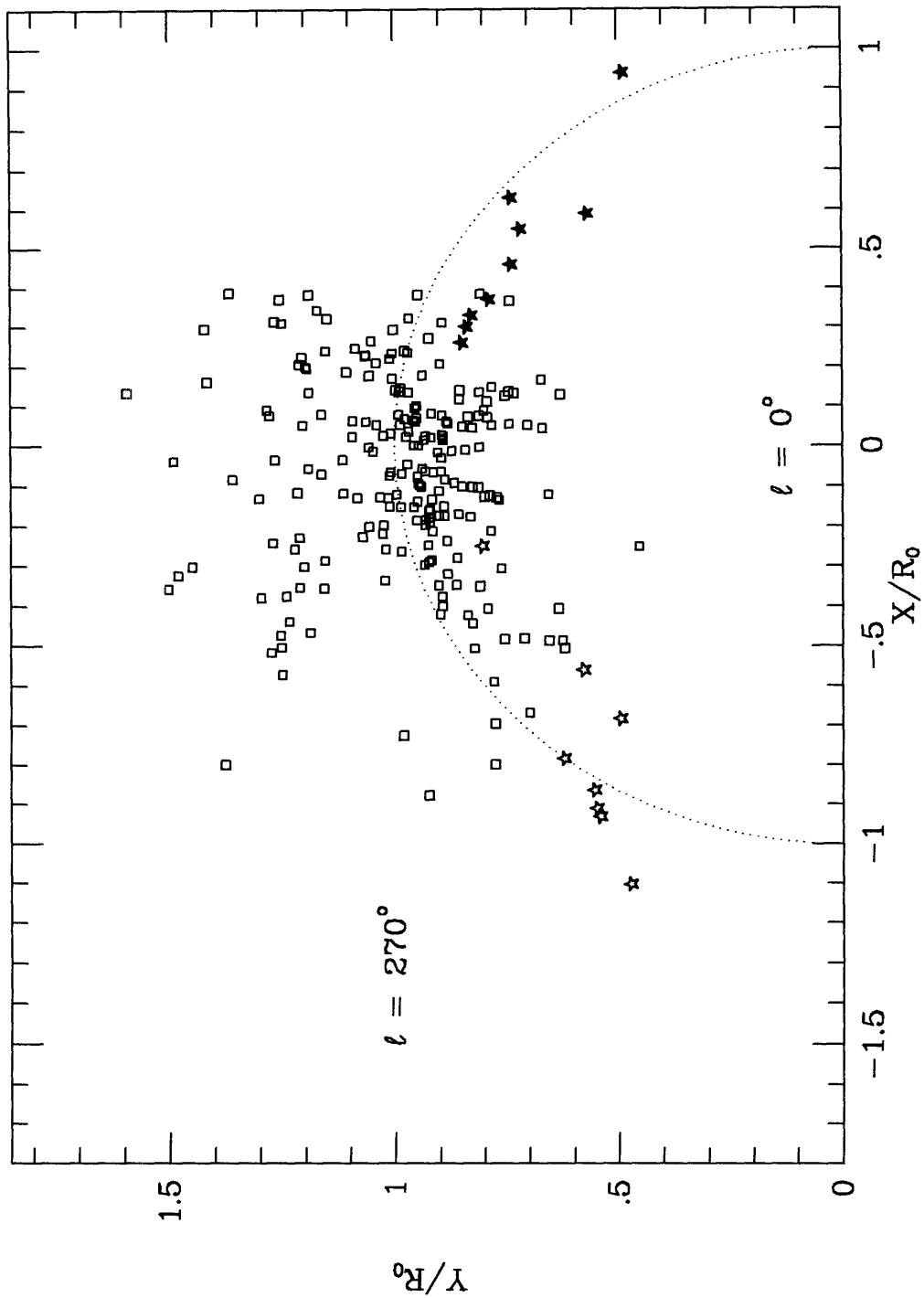
Figure 3-23: Positions of Cepheids in the Milky Way, plotted as in Figure 2-23. Newly discovered northern hemisphere Cepheids are shown as filled stars.

tion curve about the Galactic center to roughly 10%: current estimates from the new southern hemisphere Cepheids are about 5%, and the measured R_0 can be directly compared in the northern and southern hemispheres.

The high extinction found in the direction of these stars presents two problems. The immediate problem is to measure accurate distances to the newly discovered Cepheids, which can be best accomplished by obtaining photometry in the near-infrared K band. We have started an observational program to measure these stars, and have obtained data for these and many other accessible Cepheids nearby. As discussed in Chapter 2, the K-band is significantly less affected by extinction and presents a smaller scatter in the observed PL relation, both leading to more accurate distances than can be obtained optically. Radial velocity measurements are also made more difficult by the high extinction, but should be more straightforward from high-resolution infrared spectra.

It is also evident from the extinction encountered that future surveys for more distant Cepheids should be moved to the near infrared. A survey concentrating at K, with additional JH photometry to aid identification and provide reddening estimates, is probably the best strategy for ground-based surveys. At K wavelengths and longer, the amplitude of variation is roughly 0.3 magnitude, reflecting the change in surface area (Welch *et al.* 1984). Even under the equivalent of 30 magnitudes of extinction in V (approximately the extinction to the Galactic center), a 3-day period Cepheid at a distance of R_0 would have an apparent magnitude of $\sim$13.5 and can easily be measured with the required photometric accuracy for detecting variability. Crowding will become a significant problem, however, and therefore a substantial survey awaits the development of large-format infrared arrays that can simultaneously cover large areas with sufficient angular resolution.

3.6 References

Allen, C. W. 1973, *Astrophysical Quantities* (London: Athlone)

Blitz, L., & Spergel, D. N. 1991, ApJ, **370**, 205

Burstein, D., & Heiles, C. 1978, ApJ, **225**, 40

Caldwell, J. A. R., Keane, M. J., & Schechter, P. L. 1991, AJ, **101**, 1763 (CKS)

Christian, C. A., Adams, M., Barnes, J. V., Hayes, D. S., Siegel, M., Butcher, H., & Mould, J. R. 1985, PASP, **97**, 363

Clayton, J. A., Cardelli, G. C., & Mathis, J. S. 1989, ApJ, **345**, 245

Dame, T. M., Ungerechts, U., Cohen, R. S., de Geus, E. J., Grenier, I. A., May, J., Murphy, D. C., Nyman, L.-Å., & Thaddeus, P. 1987, ApJ, **322**, 706

Dworetsky, M. M. 1983, MNRAS, **203**, 917

Feast, M. W., & Walker, A. R. 1987, ARA&A, **25**, 345

Heiles, C., Kulkarni, S., & Stark, A. A. 1981, ApJ, **247**, 73

Hillditch, R. W., Hill, G., & Barnes, J. V. 1976, MNRAS, **176**, 175

Kent, S. M., Mink, D., Fazio, G., Koch, D., Melnick, G., Tardiff, A., & Maxson, C. 1992, ApJS, **78**, 403

Kholopov, P. N., Samus, N. N., Frolov, M. S., Goranskij, V. P., Gorynya, N. A., Kireeva, N. N., Kukarkina, N. P., Kurochkin, N. E., Medvedeva, G. I., Perova, N. B., & Shugarov, S. Yu. 1988, *General Catalogue of Variable Stars*, 4th Ed. (Moscow: Nauka) (GCVS)

Kraft, R. P., & Schmidt, M. 1963, ApJ, **137**, 249

Kuijken, K., & Tremaine, S. 1994, ApJ, **421**, 178

Landolt, A. U. 1992, AJ, **104**, 340

Lasker, B. M., Sturch, C. R., McLean, B. J., Russell, J. L., & Jenkner, H. 1990, AJ, **99**, 2019

Madore, B. F., & Freedman, W. L. 1991, PASP, **103**, 933

Metzger, M. R., Tonry, J. L., & Luppino, G. A. 1993, in Astronomical Data Analysis Software and Systems II, eds. R. J. Hanisch, R. J. V. Brissenden, & J. Barnes, Astronomical Society of the Pacific Conference Series Volume 52, p. 300.

Russell, J. L., Lasker, B. M., McLean, B. J., Sturch, C. R., & Jenkner, H. 1990, AJ, 99, 2059

Schechter, P. L., Avruch, I. M., Caldwell, J. A. R., & Keane, M. J. 1992, AJ, 104, 1930

Schechter, P. L., Mateo, M., & Saha, A. 1993, PASP, 105, 1342

Schoening, B., Massey, P., Armandroff, T., Jacoby, G., Neese, C., & Salzer, J. 1991, *Operation of the CCD Direct Imaging Camera for the 0.9 Meter Telescope*, Kitt Peak National Observatory manual.

Welch, D. L., Wieland, F., McAlary, C. W., McGonegal, R., Madore, B. F., McLaren, R. A., & Neugebauer, G. 1984, ApJS, 54, 547

Chapter 4

Radial Motion of the Local Standard of Rest

This chapter appeared in similar form as "Whither the LSR: Anticenter Carbon Star Velocities", *The Astrophysical Journal*, January 1, 1994 (Metzger & Schechter 1994).

4.1 Background

The typical model used to describe Galactic rotation is axisymmetric with rotation rate varying with radius. It has long been known from H I surveys (e.g. Weaver & Williams 1974, Kerr *et al.* 1986), however, that the H I gas in the Galactic disk exhibits motions which are inconsistent with a simple axisymmetric model. Recently, Blitz and Spergel (1991a, hereafter BS) proposed a model of the galaxy which accounts for two features evident in the H I maps: that the gas toward the Galactic anticenter has an apparent inward motion, and that the outer Galaxy gas appears asymmetric about $\ell = 180°$. They support their model by showing it to be consistent with CO measurements toward the Galactic center, H I column density, and the vertex deviation of the velocity ellipsoid in the solar neighborhood.

A feature of the BS model is an outward motion of the LSR due to a non-axisymmetric rotation curve, produced by a rotating triaxial spheroid in the inner galaxy. (This is distinct from the smaller scale bar at the Galactic center detected by Blitz & Spergel [1991b], Binney *et al.* [1991], Weinberg [1992], and others.) The

rotation curve ellipticity in the BS model decreases outward to about 2.5 R_0 from the Galactic center, where it becomes circular. Thus the gas toward the Galactic anticenter should appear to be moving inwards relative to the LSR, increasing in magnitude until $\approx 2.5R_0$ where we should see the full reflection of the radial component of the LSR motion. The outward motion of the LSR is 14 km s^{-1} in the BS model, accounting for the 14 km s^{-1} apparent inward motion of the anticenter gas.

If the LSR has such an outward motion, we would expect to see this motion reflected in stars as well. To detect it one would need a sample of tracer stars toward the anticenter at distances $\gtrsim$ 1.5 R_0 where the ellipticity of the rotation curve in the model is small. Extinction from dust in the disk is substantial, requiring a tracer that is intrinsically bright. The sample of stars also needs to be large enough to allow a good measurement of the mean velocity: the radial velocity dispersion in the galactic disk is $\approx$ 20 km s^{-1} at 1.5 R_0 (Lewis & Freeman 1989). Carbon stars are good candidates for such a tracer population. Though they are not the best of standard candles, they are relatively numerous and are very bright at infrared wavelengths ($M_K = -8.1$ mag), allowing them to be detected at large distances even through absorbing dust. They are also easy to identify on objective prism surveys from strong absorption bands in their spectra.

Fortunately a significant number of carbon stars have already been identified at the galactic anticenter. Fuenmayor (1981) found 216 carbon stars in a survey conducted in a region covering $\sim$ 200 square degrees at the Galactic anticenter, complete to $I = 11$ mag. K-band photometry of 211 of these stars was obtained by Jura, Joyce, and Kleinmann (1989), allowing distances of the stars to be determined. This shows that the Fuenmayor stars lie at distances of about 2–10 kpc from the Sun, or about 1.2–2.1 R_0 from the galactic center. In addition, Aaronson et al. (1990) measured velocities for 55 of these stars. A preliminary examination of these velocities revealed little evidence of LSR motion, but the sample was too small to draw a firm conclusion. We therefore decided to obtain velocities for the rest of the Fuenmayor stars to allow us to measure the outward motion of the LSR predicted by the BS model.

4.2 Observations

We obtained spectra for most of the 216 Fuenmayor carbon stars on the nights of 27–30 November 1990 using the Gold Camera on the 2.1 m telescope at Kitt Peak. We used an 831 line mm^{-1} grating in first order centered at 7950 Å, projected onto a Texas Instruments 800 by 800 CCD. This gave a wavelength coverage of $\approx$700 Å at 0.9 Å pixel^{-1}. The region around λ 8000 Å contains strong bands of CN absorption, which allow the redshift to be measured accurately. We were limited by the internal camera focus of the spectrograph to a resolution of about 3 pixels FWHM with a 1.2 arcsec slit. After binning the pixels by 3 in the spatial direction to reduce readout noise, the spatial resolution was about 2.5 pixel FWHM, which corresponded to 6 arcsec on the sky. Helium-Neon-Argon calibration arcs were taken after each stellar spectrum. Though clouds during our observing run prevented us from obtaining spectra for every catalog star, we managed to obtain usable spectra for 179 of the 216 Fuenmayor stars.

The spectra were reduced by rebinning the pixels of each spectrum according to a low-order polynomial fit made to the associated calibration frame. One axis of the resulting image corresponded to the normalized spatial direction, and the other to log wavelength. The spectra were then collapsed spatially along the star image and sky-subtracted using pixels away from the star on the same spectrum. The region of the spectrum near 7650 Å contains the telluric absorption A-band and was excluded. The redshift between each star spectrum and a reference spectrum of a bright carbon star was then calculated using the Fourier quotient technique of Sargent *et al.* (1977). Observed relative velocities were adjusted to the heliocentric frame.

Many additional carbon stars were observed to provide a zero-point calibration. These stars were selected from the carbon stars with velocities reported by Aaronson *et al.* (1990) that were visible during our run. The reference spectrum chosen for computing redshifts was one of a bright carbon star with $K = 3.9$ mag, number 82 in Stephenson's (1989) catalog, for which we obtained a spectrum with a high signal-to-noise ratio. Velocities were computed relative to this template for the program stars
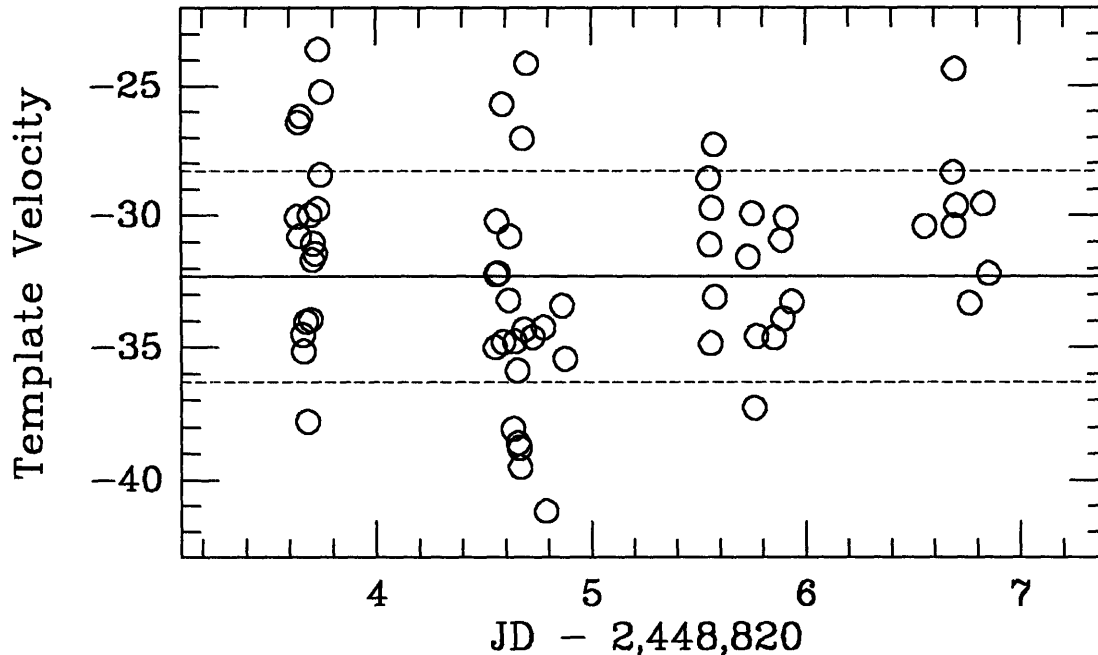
Figure 4-1: Individual measurements of the template velocity vs. Julian date of observation for 62 carbon stars. The solid line shows the mean, used as the velocity for the template, and the dashed lines correspond to 1-σ of the distribution.

and converted to absolute velocities based upon a derived velocity for the template. The template velocity was obtained by measuring a velocity of each of the zero-point calibration stars relative to the template. The difference between this velocity and the star's velocity as reported in Aaronson et al. (1990) gives a measurement of the template's velocity, aligned to their zero point. The measurements are then averaged to obtain the derived template velocity. A total of 62 stars were used to compute our reference template velocity, -32.30 ± 0.51 km s^{-1}. Individual velocities for the template are shown in Figure 4-1. From this we find a scatter between our velocities and those of Aaronson et al. of 4.0 km s^{-1} (1-σ).

Velocities for 179 anticenter carbon stars are shown in Table 4.1. The formal errors of the individual velocities from the Fourier quotient are $\simeq 2.0$ km s^{-1}, which does not include error contributed by the wavelength calibration. The scatter of the velocities used in computing the template velocity gives a good estimate of the total individual measurement error, aside from any overall systematic error. The scatter from Figure 4-1 is 4.0 km s^{-1}, and using the quoted error for the Aaronson et al.

Table 4.1: Radial Velocities of Fuenmayor Carbon Stars

Star[1]	JD[2]	v_r	v_m	Star[1]	JD[2]	v_r	v_m
1	3.930	−34.0	7.9	45	3.978	−12.9	0.4
2	3.934	8.7	−16.4	46	3.988	6.3	12.0
3	3.938	34.8	−16.3	47	3.983	−33.5	1.7
4	3.763	−1.8	−9.6	48	3.993	−27.1	−7.5
5	3.766	−10.4	−18.7	49	3.996	−3.3	4.9
6	3.771	7.5	−17.5	50	3.999	−19.5	−7.0
8	3.774	14.8	−16.4	51	4.711	20.9	−1.6
9	3.779	34.0	−14.1	52	4.005	−35.2	−8.7
10	3.784	49.7	−6.8	53	4.715	−2.7	−6.5
11	3.788	−6.6	−8.6	54	4.725	−5.3	2.1
12	3.791	−23.1	−12.7	55	4.738	8.3	−2.3
13	3.795	−1.2	−14.7	56	4.749	−9.0	−3.7
14	3.798	18.7	−4.9	57	4.766	0.8	−8.9
15	3.803	−20.0	−18.0	59	4.770	29.2	−5.7
16	3.806	−30.0	−15.8	60	4.776	6.1	0.0
17	3.811	7.4	14.9	61	4.788	−3.1	2.0
18	3.815	−25.1	−8.8	63	4.802	14.5	−0.7
19	3.823	6.8	11.1	64	4.793	4.3	3.4
20	3.819	27.7	−7.9	65	4.811	15.6	7.9
21	3.826	15.4	6.7	66	4.820	49.6	15.2
22	3.831	11.1	−2.9	67	4.815	30.4	6.4
23	3.835	30.2	−1.1	70	4.832	−39.3	6.8
24	3.841	42.3	10.7	71	4.807	20.0	2.1
26	3.846	−52.5	−18.9	72	4.835	16.8	7.5
27	3.850	0.2	−12.8	73	5.731	12.3	1.3
28	3.854	32.8	−6.0	75	5.751	11.5	6.1
30	3.857	31.3	−12.3	76	5.770	25.1	0.0
31	3.864	−4.8	−0.4	77	5.780	−6.5	11.8
32	3.874	−0.1	3.6	78	5.824	32.1	12.0
33	3.882	40.1	−7.8	79	5.776	44.4	1.8
34	3.895	5.6	−3.9	80	5.760	31.6	4.8
35	3.905	23.6	3.9	82	5.789	19.3	12.2
36	3.910	1.0	2.9	83	5.811	7.6	7.3
37	3.919	−18.1	−8.4	84	5.827	17.2	13.8
38	3.915	−8.7	0.1	86	5.806	10.4	3.0
39	3.925	5.2	−16.8	87	5.830	8.9	16.8
40	3.950	39.6	−9.5	88	5.814	27.2	12.0
41	3.951	−33.9	−14.8	89	5.839	−37.7	−2.8
42	3.966	19.8	−8.6	90	5.849	−5.7	1.2
43	3.958	35.0	8.4	91	5.864	−1.0	10.4
44	3.975	8.3	1.0	92	5.853	−36.8	−0.1

168

Table 4.1—*Continued*

Star[1]	JD[2]	v_r	v_m	Star[1]	JD[2]	v_r	v_m
93	5.874	45.4	17.7	150	7.004	34.0	8.9
94	5.868	9.9	9.5	151	4.997	46.1	23.1
95	5.883	12.7	2.1	153	5.001	22.5	21.1
96	5.887	−5.7	4.0	154	5.006	35.0	15.0
97	5.879	−4.6	19.6	155	5.919	33.1	25.2
98	5.896	−4.7	8.3	156	5.929	34.7	10.3
99	5.909	15.2	6.0	157	5.935	48.4	20.2
100	6.901	−21.3	12.0	158	5.953	61.3	22.9
101	2.902	−1.1	13.3	159	5.963	49.1	12.4
103	6.933	8.5	13.1	160	5.930	30.8	10.7
106	6.937	−0.9	17.4	161	5.944	73.7	19.6
108	6.765	39.0	9.8	162	5.965	6.1	15.3
109	6.880	31.5	5.0	163	5.956	31.5	26.3
110	6.967	23.3	8.1	164	5.982	−20.0	15.0
113	6.828	29.9	4.2	165	5.971	29.9	25.4
114	6.820	−8.5	1.6	166	5.976	8.0	31.1
115	7.010	−23.6	−1.0	167	5.996	11.2	24.5
116	6.853	−22.4	15.6	168	5.987	46.6	13.2
122	7.014	38.1	5.9	169	6.003	−15.8	25.8
123	4.842	26.4	8.9	170	6.011	−8.6	20.1
124	4.844	28.6	9.0	171	5.998	4.5	26.3
127	4.863	5.9	10.5	173	6.015	22.0	11.3
128	4.876	20.8	18.6	174	6.018	−2.4	8.3
129	4.894	23.6	21.3	176	6.810	72.4	28.9
130	4.872	25.1	11.1	179	6.771	46.6	11.8
131	4.885	7.9	20.1	180	6.022	3.3	15.2
132	4.908	54.0	8.8	183	6.774	10.7	14.2
133	4.912	−3.0	6.7	186	6.031	41.3	6.7
134	4.917	−0.3	4.7	187	6.833	40.8	26.0
135	4.919	14.0	6.2	188	6.838	19.0	23.7
136	4.924	16.0	4.4	189	6.844	0.9	25.8
137	4.899	14.7	21.4	190	6.848	16.1	23.8
138	4.934	8.1	11.5	191	6.860	8.8	22.7
139	4.926	12.3	8.1	192	6.864	89.8	22.9
140	4.938	−27.1	9.2	193	6.871	38.0	20.8
141	4.943	−16.4	19.1	194	6.887	52.4	39.9
142	4.950	32.6	17.2	195	6.874	19.9	22.0
143	4.944	20.2	20.0	196	6.894	39.3	27.7
144	4.976	48.5	10.7	197	6.950	47.6	30.5
145	4.982	−1.9	5.8	198	4.030	35.5	4.9
146	4.988	38.9	0.0	199	6.890	7.7	27.9

Table 4.1—*Continued*

Star[1]	JD[2]	v_r	v_m	Star[1]	JD[2]	v_r	v_m
200	4.024	49.8	39.1	209	6.929	12.2	17.5
201	6.959	42.1	23.9	210	6.999	44.8	37.3
202	6.962	26.3	23.9	211	6.914	26.1	38.5
203	6.954	26.1	28.8	212	6.993	40.8	40.4
204	6.971	52.4	38.6	213	6.975	75.4	38.6
205	6.924	81.0	38.7	214	5.032	9.5	5.6
206	6.983	−15.1	36.2	215	6.996	18.7	27.7
208	6.987	82.3	37.9				

[1] Designation from the catalog of Fuenmayor (1981).
[2] Julian date − 2,448,220.

(1990) velocities of 3.0 km s^{-1}, we can calculate an error for our individual velocities of approximately 2.6 km s^{-1}. Given the resolution of the detector of 34 km s^{-1} pixel^{-1}, however, we prefer a more conservative error estimate of 3.5 km s^{-1} according to our estimate of the wavelength calibration accuracy. Multiple observations of the same star on several occasions are consistent with this latter estimate. Table 4.2 shows velocities for non-Fuenmayor carbon stars measured during our run. Stars in Table 4.2 having velocities reported in Aaronson *et al.* (1990) were included in the computation of the zero point.

4.3 Analysis

The first step in the analysis was to determine crude distances to the carbon stars in the sample. Carbon stars have a fairly large intrinsic dispersion in absolute K manitude, roughly 0.6 mag (Schechter *et al.* 1991, Cohen *et al.* 1981), which corresponds to a 32% error in distance. Distance estimates are further complicated by interstellar absorption. In principle one might correct for the latter based upon color excesses. Complete photometry for our sample is available only in $I-$ and $K-$bands, however, which gives a single color. Jura *et al.* (1989) investigated a correction using this color for the Fuenmayor catalog stars. They found that the dispersion in $I - K$ vs. K was large, due in part to a wide variation of the intrinsic $I - K$ colors of carbon stars. For this reason, we instead chose to adopt an average extinction gradient.

The use of an extinction gradient leaves significant uncertainty in the unreddened magnitude estimates. Aside from problems with the uneven distribution of extinction in the disk, the extinction gradient in K is poorly known. Schechter et al. (1991) report a value corresponding to 0.03 K mag kpc^{-1} based on H I column densities, while Jura et al. (1989) use a much higher value of 0.15 mag kpc^{-1}. To further complicate matters, the Fuenmayor catalog stars were a magnitude-limited sample taken in the I band, so that stars with large reddenings were preferentially excluded from his catalog. However, Jura et al. (1989) find their high extinction gradient to be consistent with the Fuenmayor sample based in part on the stars' $I - K$ colors.

As a first attempt to check the extinction gradient in our sample, we computed infrared reddenings of the subset of Fuenmayor stars observed in JHK bands by Aaronson et al. (1990) using the zero-reddening locus adopted by Cohen et al. (1981). We find an extinction gradient of 0.1 K mag R_0^{-1}. This low value is not unexpected as the stars in the subset were selected for bright V magnitudes, further excluding more reddened stars.

We can also check an assumed extinction law by comparing the mean $(I - K)$ color of the Fuenmayor stars with the color we would predict a carbon star to have at the mean distance derived for the sample. Combining the I-band photometry of Costa (1990) with K-band photometry from Frogel (1992) for 62 carbon stars in the LMC, we find a mean $(I - K)$ color of 3.52. The intrinsic color is bluer by about 0.1 mag when corrected for LMC extinction, but Cohen et al. (1981) imply that the galactic carbon stars are about 0.1 mag redder in $(I - K)$ than the LMC carbon stars (see their figure 2). Assuming 0.03 K mag kpc^{-1}, we derive (see below) a mean sample distance of 5.4 kpc, corresponding to $A_K = 0.16$ mag. Using the adopted reddening law of Cohen et al. (1981) for the Cousins I band, this gives $E(I - K) = 0.92$. We therefore expect the mean color of a carbon star to be $\langle (I - K) \rangle = 4.44$, compared to 4.9 observed for the sample. This method converges to an extinction value of about 0.05 K mag kpc^{-1}.

We finally adopted the Schechter et al. (1991) value of 0.03 mag kpc^{-1}, to be consistent with their analysis. It is also consistent with the smooth number count
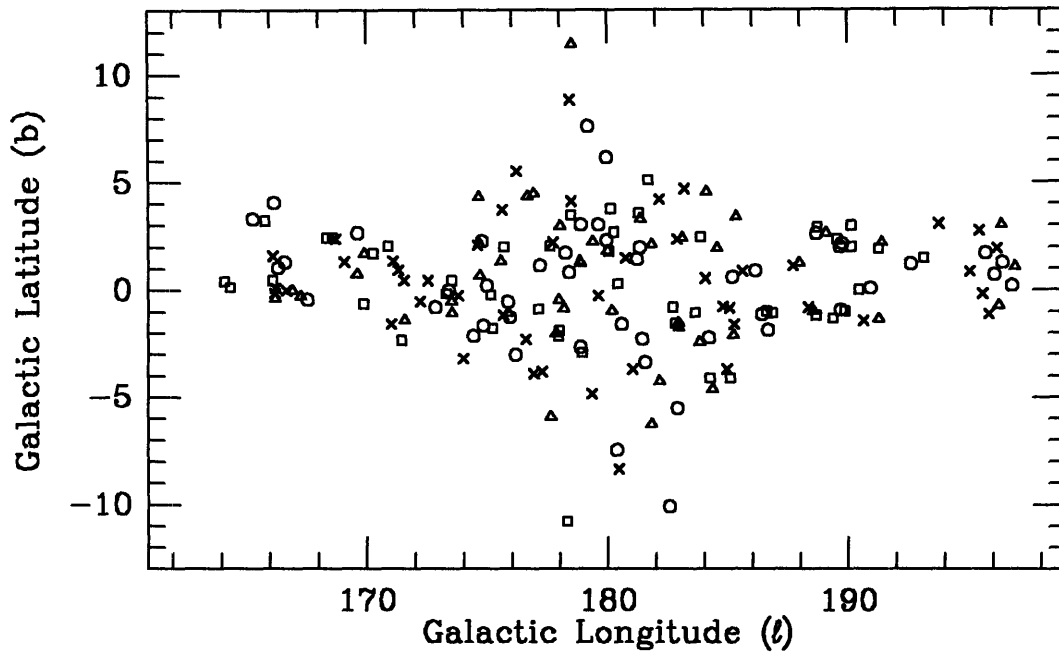
Figure 4-2: Positions of the Fuenmayor stars in Galactic latitude and longitude. Stars in the first through fourth quartiles in distance are shown by triangles, squares, circles, and crosses, respectively.
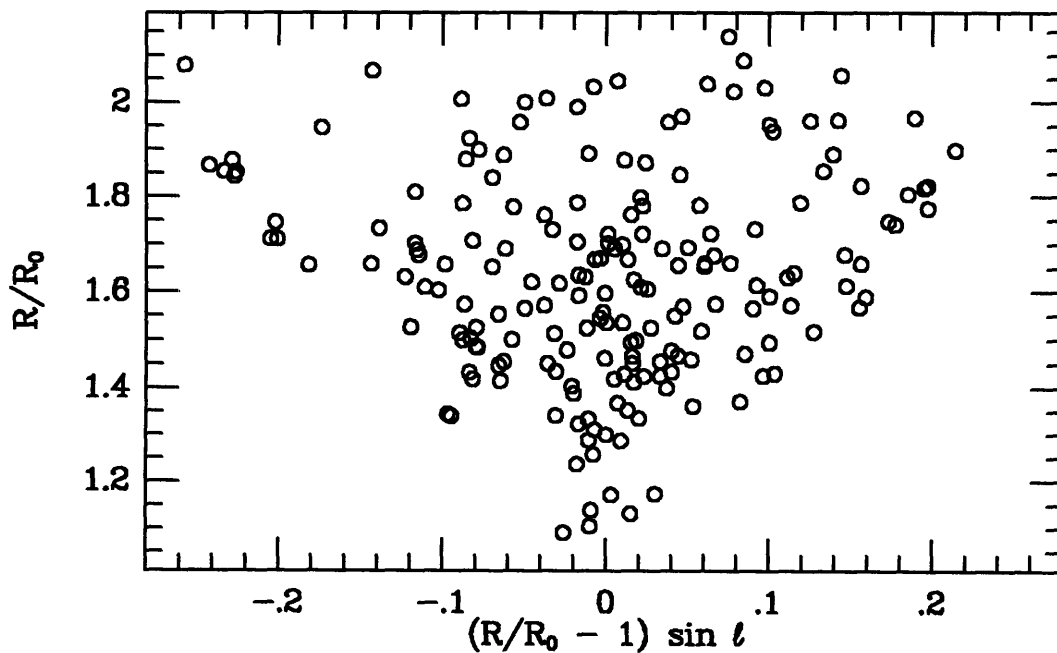
Figure 4-3: Positions of the Fuenmayor stars, projected onto the plane of the Galaxy. The coordinates are chosen so that the opening angle in longitude is expanded, so that the points can be more readily seen.

distribution we compute below to correct for Malmquist's effect. The difference between distances computed with this value and with 0.05 is less than 5 percent. The derived motions of the sample with respect to the LSR are fairly insensitive to errors of $\lesssim 0.8$ mag, as the stars are confined to within about 15° in galactic longitude of the anticenter. Therefore, the difference in adopted extinction would not affect our velocities, and changes the mean distances to the stars by only a small amount. Figures 4-2 and 4-3 show the location of the sample stars in galactic coordinates. The large difference between our estimated extinction and that found by Jura *et al.* (1989) is due to a discrepancy in assumed mean $(I - K)$ color. Jura *et al.* use a value of 2.71 reported by Claussen *et al.* (1987). We believe the source of the discrepancy stems from the use of different I bands: the Claussen *et al.* value is for the system of Johnson (1965), which has an I-band filter response that extends to longer wavelengths that the Cousins I (Bessel 1979). Our $(I - K)$ color is based on the Cousins I system, which is closer to the Kron system used by Fuenmayor (1981) for the carbon stars. The extreme red color of carbon stars makes them apparently brighter in the Johnson (1965) system, producing an $(I - K)$ color that is significantly bluer.

In deriving distances we applied a correction for Malmquist's effect, using a model disk with an exponential scale length of 4.4 kpc (Lewis & Freeman 1989) and a scale height of 200 pc (Claussen *et al.* 1987). The $K-$band luminosity function was assumed to be a Gaussian centered at $M_K = -8.1$ (Frogel *et al.* 1980) with $\sigma = 0.6$ mag (Schechter *et al.* 1987). A Fermi-Dirac function centered at $K = 7$ mag with an effective width of about 1 mag was used as an approximate selection function. Though the selection function is somewhat ad hoc, the resulting number count distribution function matches the observed distribution well. The correction was computed from the smooth distribution with $\Delta M = -\sigma^2 d\ln A/dm$ (Mihalas and Binney 1981), where ΔM is the correction to the carbon star mean absolute magnitude. It is less than ± 0.2 mag for most of the sample, but increases to 0.55 mag at $m_K = 7.3$. We calculated corrections based upon a wide variety of models and found that the derived mean velocity is insensitive to the model chosen. The most significant effect of using the various models is to change the mean distance to the stars, which affects the computed
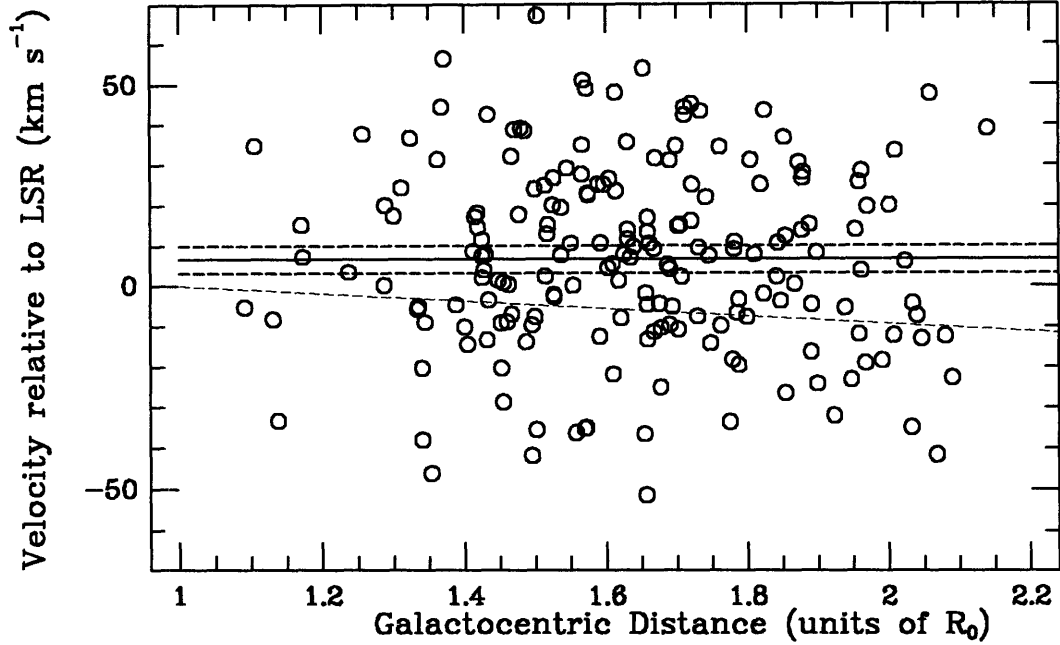
Figure 4-4: Velocities of the Fuenmayor carbon stars relative to the LSR after subtracting a flat, axisymmetric rotation curve model, plotted vs. computed distance. The solid line is the mean velocity of the sample, and the dashed lines are offset from this by 2 standard errors of the mean. The lower dashed line shows the mean predicted by the BS model.

median distance of each quartile of our sample (see below). The effect is largest in the most distant quartile, and widely varying models produce differences of $\simeq 0.2 R_0$ for this quartile.

Figure 4-4 shows the derived galactocentric distances of the carbon star sample, plotted vs. residual velocity from our rotation curve model. Galactocentric distance was computed assuming the unreddened K magnitude of an average carbon star at a distance of R_0, m_0, is 6.3 mag in a volume-limited sample. The residual velocity was computed by subtracting the velocity due to a flat, axisymmetric rotation curve with the standard values $\Theta_0 = 220$ km s^{-1} and $R_0 = 8.5$ kpc (Kerr and Lynden-Bell 1986). Also subtracted from this velocity is Sun's motion peculiar to the LSR, using a value of 16.5 km s^{-1} in the direction $\ell = 53°$, $b = 25°$ (Delhaye 1965). Each star's model velocity is shown in the V_m column of Table 4.1. The mean residual velocity for our entire sample is 6.6 ± 1.7 km s^{-1}, in the sense that the carbon stars and the LSR are moving apart. The lack of any significant trend with distance can be more
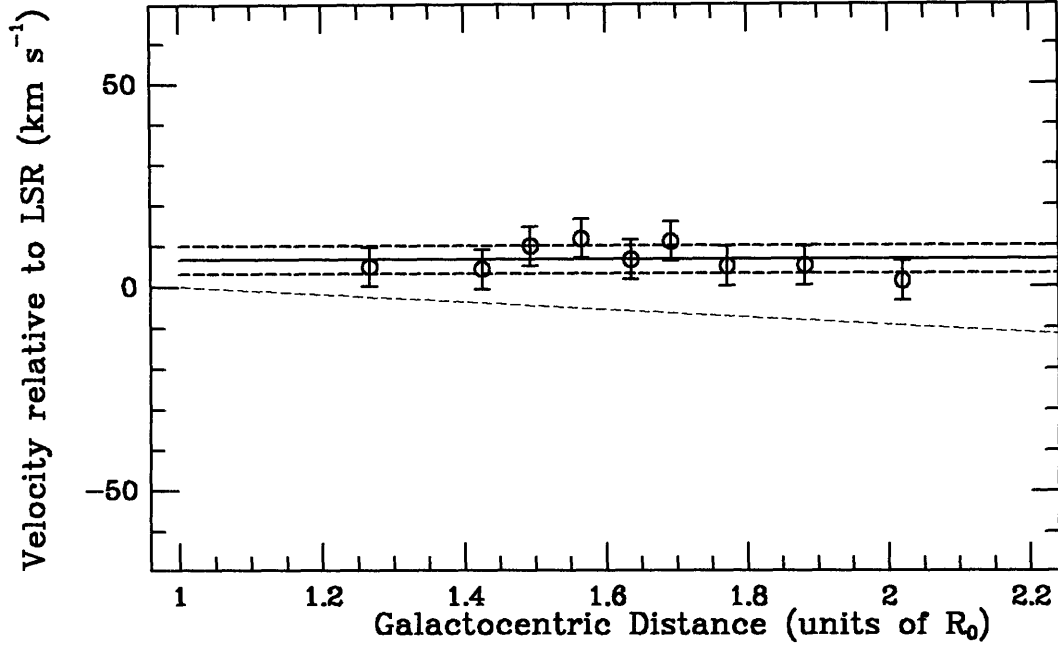
Figure 4-5: The same data as Figure 4-4, but the data have been binned into groups of 20 and averaged. The error bars on each point show the standard error of the mean, assuming the velocities to be normally distributed.

easily seen in Figure 4-5, where we have binned 20 velocities into each plotted point. Dividing the sample at $\ell = 180°$, we obtain mean velocities of 8.5 ± 2.3 km s^{-1} for $\ell < 180°$ and 4.7 ± 2.5 km s^{-1} for $\ell > 180°$.

Our estimate of the motion of the LSR is most sensitive to the radial component of the sun's peculiar motion, -9 km s^{-1}. Fortunately it is fairly well determined: many other estimates of this component agree with this value to within 1 km s^{-1} (Kuijken and Tremaine 1991). The distance errors to individual stars are estimated to be on the order of 50% (of the heliocentric distance, which in units of R_0 is $\simeq R - 1$), including the additional uncertainty in the extinction. The median galactocentric radius for the sample is 1.64 R_0. No significant trend in mean velocity with distance is evident, and the distance quartiles have mean velocities of 5.2 ± 3.3, 11.2 ± 3.6, 6.5 ± 3.3, and 3.6 ± 3.3 km s^{-1}, at median distances of 1.40, 1.55, 1.70, and 1.92 R_0 respectively.

We also were able to estimate the radial velocity dispersion, σ_R, using our sample. Since all but 13 of the stars have $|b| < 5°$, we take the observed velocity dispersion to

175

Table 4.2: Other Carbon Star Velocities

Star[1]	JD[2]	v_r	Star[1]	JD[2]	v_r
caa1	3.699	−29.1	cyb26	5.625	−31.8
caa2	3.693	−58.9	cyb36	5.647	−92.3
caa6	3.704	−58.5	cyb40	5.635	−83.8
caa14	3.709	−20.9	cyb69	3.634	−53.5
caa21	3.733	−92.7	cyb75	3.639	−34.5
caa24	3.718	−80.3	cyc26	5.552	−41.8
caa25	3.728	−55.9	cyc28	3.644	−48.5
caa36	3.746	−75.3	cyc38	5.548	−54.8
caa40	3.742	−74.9	cyc40	3.651	−15.9
caa41	4.698	−75.5	cyc41	5.557	−69.6
cab13	4.585	−31.9	maa19	4.663	−45.3
cab20	4.589	−94.1	maa20	4.668	−55.0
cab23	6.695	−122.4	maa21	4.678	−92.0
cab30	4.619	−54.1	maa22	4.688	−51.7
cad14	4.657	−24.5	ms2	3.686	−21.2
cad15	4.653	−20.6	ms64	4.576	−69.3
cep5	3.682	−115.7	ms92	4.579	−60.3
cep9	6.556	−65.1	ms120	4.624	−62.1
cya5	5.601	−71.4	ms128	4.627	−68.0
cya6	5.589	−28.1	ms145	4.633	−60.8
cya35	5.578	−47.9	ms159	4.643	−60.1
cya52	5.572	−2.8	nb246	6.552	−58.5
cyb18	5.619	−35.1			

[1] Designation of Aaronson et al. (1990).
[2] Julian date − 2,448,220.

be equal to σ_R. In the 4 distance quartiles described above, $\sigma_R = 22.5$, 24.8, 22.5, and 22.5 km s^{-1}, respectively, with an error of $\simeq$ 3 km s^{-1}. The velocity dispersion for the entire sample is 23.1 km s^{-1}. While we can measure the dispersion in quartiles or as a gradient with distance, the distance associated with each bin is uncertain due largely to the uncertainty in the average extinction gradient for our sample. In addition, if the velocity dispersion σ_R has a significant gradient, as measured by Lewis and Freeman (1989), the scatter due to differential reddening and the intrinsic luminosity function of carbon stars would tend to obscure the gradient.

4.4 Discussion

The mean velocity of the anticenter carbon stars is 6.6 ± 1.7 km s^{-1} away from the LSR, rather than 14 km s^{-1} toward the LSR as predicted by the BS model. The discrepancy is attributable to the apparent difference in the kinematics of the anticenter gas, upon which the BS model is based, and that of the carbon stars. Lewis and Freeman (1989) see a similar mean velocity in their K giant sample: 13.0 ± 4.2, 16.1 ± 4.6, and 5.7 ± 4.5 km s^{-1} at radii of 12.5, 14.8, and 17.7 kpc respectively. This is also in the sense that their sample is moving away from the LSR, and is roughly consistent with our carbon star velocities.

Another way to test the BS model is to look for asymmetry around $\ell = 180°$. The mean velocities of $\ell > 180°$ and $\ell < 180°$ sample subsets are consistent at the 1-σ level, and the difference between the two is in the opposite sense as one would expect from the BS model. The model only predicts a difference of ~ 2 km s^{-1}, however, so the test is inconclusive using our sample.

From the statistical error alone, the average velocity for the sample is non-zero at a 2-σ level. Can this be accounted for by a systematic error in measurement or analysis? One source of potential systematic error is our adoption of a zero point. We believe, however, that the Aaronson *et al.* zero point is good to better than 2 km s^{-1}, as their data were taken over a period of several years and corrections for varying zero point from year to year were smaller than this value. We investigated the possibility of systematic error from our choice of template by trying several other template spectra of varying signal level, noise level, and radial velocity. Though the noisier templates produced larger scatter in velocity, as expected, no systematic errors were found, and the mean velocity difference was < 0.5 km s^{-1} in each case.

Another source of systematic error may be that the optical radial velocity of the carbon star does not accurately measure its true center of mass velocity. Barnbaum (1992) found that a significant number of carbon stars in her sample had systematic differences between CO and optical velocities, in the sense that the optical velocities were redshifted relative to CO. She also found the presence of a systematic velocity

177

deviation was correlated with variability class and the ratio of flux at 12μ and 2μ. Jura *et al.* (1989) report 2μ fluxes from their K-band photometry and 12μ fluxes from IRAS point source identifications. Fifty of our carbon stars have $\log(12\mu/2\mu) > -0.4$, identifying them as having potential velocity offsets. This subset of stars has a mean residual velocity of 7.0 ± 3.2 km s^{-1}, and the remaining stars have a mean velocity of 6.5 ± 2.0 km s^{-1}. It is unclear why our sample does not show the effect seen by Barnbaum. Though we cannot rule out the possibility of an optical velocity offset, if present a correction would have to be larger by a factor of 2–3 than measured by Barnbaum to be consistent with the motion of the anticenter gas. Thus even in the presence of systematic errors we examined, we find a significant disagreement between the carbon stars and the anticenter gas, inconsistent with the BS model prediction.

Our measured dispersion agrees well with Lewis and Freeman's (1989) K giant sample. They measure $\sigma_R = 22.4 \pm 3.9$, 22.8 ± 3.3, and 12.7 ± 3.0 km s^{-1}, at galactocentric distances of 12.5, 14.8, and 17.7 kpc, respectively. The first two agree well with our measurement of $\sigma_R = 23$ km s^{-1}, though the third is significantly lower. Our most distant quartile corresponds to a median distance of 16.3 kpc, which while not as distant falls well within the distance error of Lewis and Freeman's 17.7 kpc bin. As discussed in §3, our 16.3 kpc bin may be contaminated from stars of higher velocity dispersion scattering into the more distant bin, making the dispersion anomalously large. Monte Carlo estimates of this suggest that from our sample the error should be no larger than 5 km s^{-1} or so, though a few outliers make a good statistical estimate difficult. Even so, it would seem to suggest that Lewis and Freeman's well-measured dispersion gradient in the K giants, extending from 0.6 kpc to 18 kpc, may not hold in the carbon stars out to $2R_0$.

4.5   References

Aaronson, M., Blanco, V. M., Cook, K. H., Olszewski, E. W., & Schechter, P. L. 1990, ApJS, **73**, 841

Barnbaum, C. 1992, ApJ, **385**, 694

Bessel, M. S. 1979, PASP, **91**, 589

Binney, J., Gerhard, O. E., Stark, A. A., Bally, J., and Uchida, K. I. 1991, MNRAS, **252**, 210

Blitz, L., and Spergel, D. N. 1991a, ApJ, **370**, 205 (BS)

Blitz, L., and Spergel, D. N. 1991b, ApJ, **379**, 631

Claussen, M. J., Kleinmann, S. G., Joyce, R. R., and Jura, M. 1987, ApJS, **204**, 242

Cohen, J. G., Frogel, J. A., Persson, S. E., and Elias, J. H. 1981, ApJ, **249**, 481

Costa, E. 1990, PASP, **102**, 789

Delhaye, J. 1965, in Galactic Structure, eds. A. Blaauw & M. Schmidt (Chicago: U. of Chicago), p. 61

Frogel, J. A. 1992, private communication

Frogel, J. A., Persson, S. E., and Cohen, J. G. 1980, ApJ, **239**, 495

Fuenmayor, F.J. 1981, *Rev. Mexicana Astron. Astrof.*, **6**, 83

Jura, M., Joyce, R. R., & Kleinmann, S. G. 1989, ApJ, **336**, 924

Johnson, H. L. 1965, ApJ, **141**, 923

Kerr, F. J., Bowers, P. F., Jackson, P. D., and Kerr, M. 1986, A&AS, **66**, 373

Kerr, F. J., & Lynden-Bell, D. 1986, MNRAS, **221**, 1023

Kuijken, K., and Tremaine, S. 1991, in *Dynamics of Disk Galaxies*, ed. B. Sundelius (Göteburg: Göteburg Univ. Press), p. 71

Lewis, J. R., & Freeman, K. C. 1989, AJ, **97**, 139

Mihalas, D., and Binney, J. 1981, *Galactic Astronomy* (New York: Freeman)

Sargent, W. L. W., Schechter, P. L., Boksenberg, A., and Shortridge, K. 1977, ApJ, **212**, 326

Schechter, P. L., Aaronson, M., Blanco, V. M., & Cook, K. H. 1987, in The Outer Galaxy, eds. L. Blitz & P. J. Lockman (Berlin: Springer), p. 31

Schechter, P. L., Aaronson, M., Blanco, V. M., & Cook, K. H. 1991, AJ, **101**, 1756

Stephenson, C. B. 1989, *Pub. Warner & Swasey Obs.*, **3**, No. 2

Weaver, H. F., and Williams, D. R. W. 1973, A&AS, **8**, 1

Weinberg, M. 1992, ApJ, **384**, 81

Chapter 5

Vertical Velocity Structure and the Local Disk Mass Density

5.1 Introduction

Up to this point, we have been concerned with the radial and azimuthal structure of the disk, treating it as two-dimensional and ignoring the vertical structure. In this chapter, we examine the vertical structure of the local kinematics, measuring radial velocities and line strengths for a sample of K dwarfs toward the south Galactic pole (SGP). This sample was selected from the larger sample of Schechter & Caldwell (1989) to be representative of the stellar population at different vertical heights. When combined with the photometry of the larger sample (Caldwell 1994), the velocity dispersion and density can be accurately measured as a function of height out of the Galactic plane. Under the assumption of dynamical equilibrium, one can then measure the acceleration perpendicular to the plane, $K(z)$, and determine the local mass density in the Galactic disk.

A population of collisionless tracer particles in dynamical equilibrium can be described by the Jeans equation:

$$\frac{\partial(\nu \overline{v_i v_j})}{\partial x_i} = -\nu \frac{\partial \Phi}{\partial x_j} - \frac{\partial(\nu \sigma_{ij}^2)}{\partial x_i}.$$

For a cool Galactic disk in cylindrical coordinates, if we stay close to the plane (close

enough to neglect effects of change in density with radius) where the vertical structure of the potential is dominated by the disk, the Jeans equation simplifies to

$$\frac{1}{\nu}\frac{\partial(\nu\sigma_z^2)}{\partial z} = -\frac{\partial\Phi}{\partial z}$$

(Binney & Tremaine 1987). This relates the vertical velocity dispersion $\sigma_z^2(z)$ and the density $\nu(z)$ to the acceleration perpendicular to the plane $K_z \equiv -\partial\Phi/\partial z$. Thus if we can simultaneously measure the density and velocity dispersion of a tracer in the Galactic disk, we can reconstruct the force law $K_z(z)$. When combined with the Poisson equation,

$$\frac{\partial^2\Phi}{\partial z^2} = 4\pi G\rho\,,$$

the force law can be used to infer the mass density.

The pioneering investigation of the acceleration perpendicular to the Galactic plane is due to Oort (1932), who used photometric and radial velocity data for stars of many different spectral classes to measure $K_z(z)$. By comparing the dynamical mass estimate with estimates of the local density from visible stars, Oort deduced that there was a significant amount of unseen matter in the disk near the sun. Another study of K giants by Hill (1960), and an analysis of this data by Oort (1960), both found a local disk mass density of 0.15 $M_\odot$ pc^{-3}. More recently, Bahcall (1984a, 1984b) performed detailed modeling of the F-star sample of Hill, Hilditch, & Barnes (1979) and the K giant samples of Hill (1960) and Upgren (1962), and deduced that half of the local matter in the disk could not be accounted for in an inventory of known mass components. The analysis by Kuijken & Gilmore 1989 (hereafter KG) of a sample of K dwarfs toward the south Galactic pole, however, indicated that the distribution was consistent with no missing mass. A recent study of an independently selected sample of SGP K giants by Bahcall, Flynn, & Gould (1992) heightened the controversy with the conclusion that their models are inconsistent with the no dark matter hypothesis at the 86% confidence level.

In this chapter we present new radial velocity measurements of a subset of the stars from the survey of Schechter & Caldwell (1987), which when combined with the

181

recent photometry for the sample by Caldwell (1994) should provide new estimates of the disk mass near the Sun. We give a rough first-cut at the analysis of the data, and suggest additional observations that should help to reduce the uncertainties in the local mass estimates.

5.1.1 K Dwarf Sample

The stars used in this study are from a survey by Schechter & Caldwell (1987) for K dwarfs over 20 square degrees around the South Galactic Pole (SGP). The survey was conducted using a drift-scanned CCD in both V and I bands, and is complete down to $\sim$ 18th magnitude in V. An auxiliary survey covering an additional 20 square degrees was conducted in a nearby field, primarily to increase the numbers of bright stars. Stars in the color range $0.97 < (V - I) < 1.13$, corresponding to K spectral type, were chosen for the work described below. A subset of this sample, uniformly spaced in half-magnitude intervals over the range $13 < V < 17$, was selected for radial velocity measurements. The idea behind selecting a uniform sample was to both to allow an accurate measurement of the velocity dispersion at intervals of height above the disk, and to use line strengths from the spectra to estimate the relative contamination of giant stars over the magnitude range. Once the velocity structure is found from this subset, it can be combined with density information from the full sample to provide a measurement of K_z.

5.2 Radial Velocities and Line Strengths of K Dwarfs

5.2.1 Observations

Spectra of K stars in the selected sample were observed by P. Schechter during two observing runs at the 2.5m DuPont telescope of Las Campanas Observatory in Chile. The first run took place on the nights of 4–15 September 1986, during which 265 sample K stars and 37 velocity reference stars were observed. The observations were not completed due to an instrument failure, and were continued the following season. On the second run, from 5–12 October 1987, an additional 44 stars were observed, and

28 stars from the 1986 run were re-observed. The spectra were taken using the echelle spectrograph/2D-Frutti detector combination (Shectman, Price, & Thompson 1985), which is the same instrument used to measure radial velocities of Cepheids in §2.3 and is described in more detail there. The configuration used was almost identical to that for the Cepheid observations, except that for the 1986 run an older camera was used. This camera suffered from significant abberations near the edges of the spectrogram, limiting the useful spectral range on each order to the central 600 pixels.

Wavelength calibration was achieved by taking reference arcs from a Th-Ar hollow cathode tube after each observation. Since the slit height was relatively small, measurements of the sky spectrum level for subtraction was accomplished by either observing the star once at each end of the slit (1986) or by observing an adjacent blank field (1987, when the seeing was considerably worse on average). The spectrograph slit was aligned with the parallactic angle for each observation to reduce light loss from atmospheric refraction (Filippenko 1982). Stars with known radial velocities, as measured by Griffin (1971), were observed throughout the run to provide a zero point for the relative velocities we measure. Several faint CORAVEL southern radial velocity standards were also measured during the 1987 run, to which we eventually fixed our zero point.

5.2.2 Data Reduction

The spectra were reduced following the procedure outlined in §2.3.2. Calibration lines were identified in a long exposure of the Th-Ar lamp, and 4th-order two-dimensional Legendre polynomial was fit to all lines across the orders, mapping wavelength to position on the detector. The low-order coefficients were then fit to the individual calibration spectra, and used to extract the individual orders as a function of slit position and $\log \lambda$. The spectra are then summed along the spatial direction and the sky is subtracted either from an nearby blank field or from the opposite half of the slit.

A high-signal template spectrum was chosen for each run, and radial velocities are measured for each observation relative to this template using the Fourier quotient
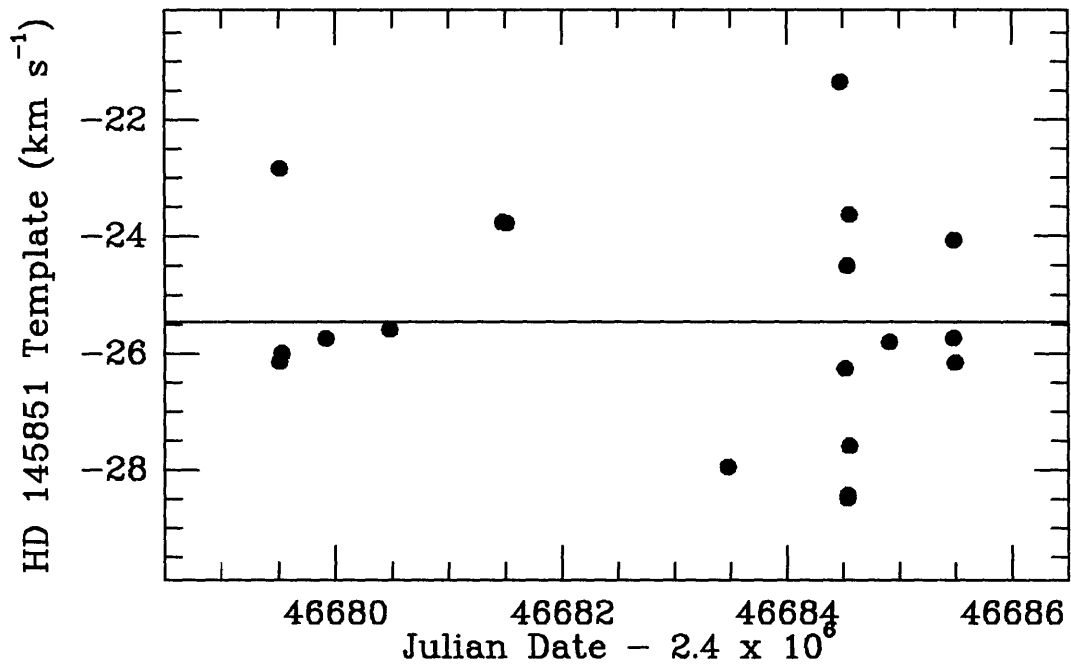
Figure 5-1: Radial velocity of the template spectrum for the 1986 run (HD 145851), measured using relative velocities to stars with known radial velocity from Griffin (1971). The mean of these measurements is used as the zero point for the radial velocities, and is shown plotted with a line. The dispersion about the mean is ~ 2 km s^{-1}, and results from a combination of our calibration error and the error of Griffin's velocities.
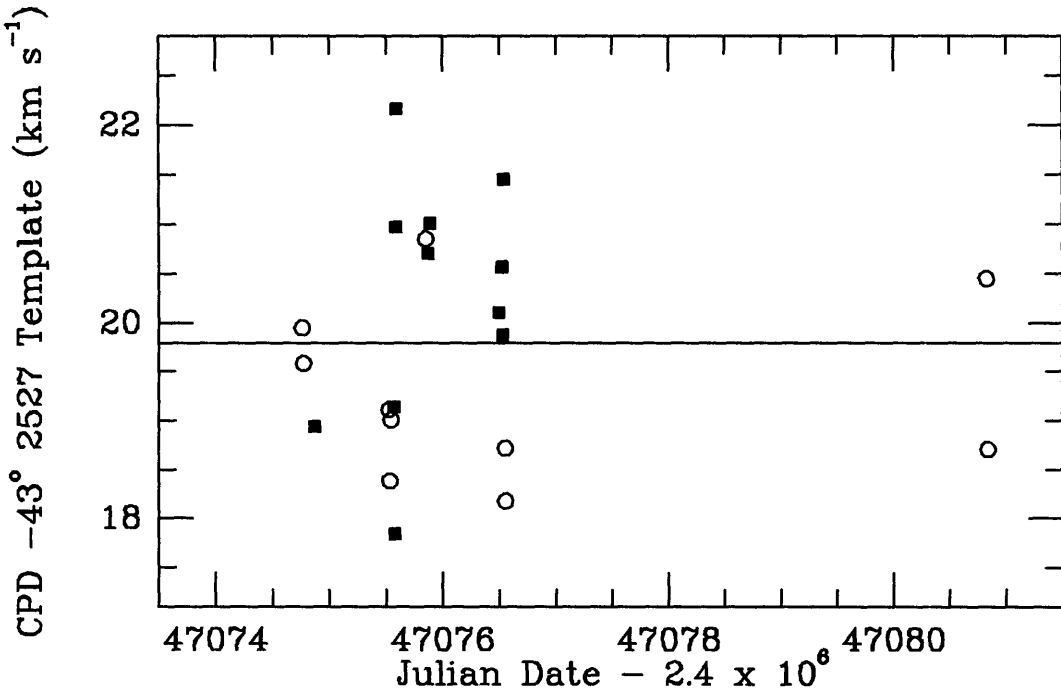
Figure 5-2: Radial velocity of the template spectrum for the 1987 run (CPD -43°
2527). Squares correspond to CORAVEL standards (ref), and circles stars measured
by Griffin (1971). The dispersion about the mean is ~ 1.0 km s^{-1}, due primarily to
error in the calibration of the spectrum using the Th-Ar lamps and a small difference
in zero point between CORAVEL and Griffin.

method of Sargent *et al.* (1977). The Fourier quotient also provides a relative line strength, γ, which we utilize below to separate the giant stars from the dwarfs and to eliminate stars of very low metallicity. For the 1986 run we chose a spectrum of HD 145851 (spectral type K2), a star measured by Griffin (1971), and for 1987 we chose the CORAVEL standard CPD $-43°$ 2527 (spectral type K1III). The velocity of each template (and thus the zero point for our radial velocities) is measured by using the relative velocities of stars with known velocity to generate an estimate of the template velocity. Figures 5-1 and 5-2 show the velocities for the template measured throughout our run; the 1986 data in Figure 5-1 were measured relative to stars from Griffin (1971); both Griffin and CORAVEL stars (Maurice *et al.* 1984) are shown in Figure 5-2 for the 1987 data. Two Griffin stars were eliminated from the measurement, as they lie significantly away from the average and are likely variable: HD 156731 and HD 167807 (the former was noted as being variable by Griffin). From the remaining data, the mean velocity for HD 145851 is found to be -25.46 ± 0.44 km s^{-1}, and for CPD $-43°$ 2527 we find -19.80 ± 0.26 km s^{-1}.

To successfully measure a velocity dispersion from the combined data, the velocities for each of the two data sets must have commensurate zero points. As an example, if two equal size sets of Gaussian distributed data are combined with means offset by x, the variance measured from the combined data will exceed the true variance by $x^2/4$. As a check on the velocity zero point, we can use 9 stars of Griffin measured in both 1986 and 1987 to estimate a mean velocity offset. If we use the template velocities above to set the zero point, however, we find an offset of 1.53 ± 0.20 km s^{-1}—much larger than the error on the template velocities would indicate. It turns out that the difference derives from the use of different stars from Griffin (1971) in 1986 and 1987 for computing the template velocity; if we limit it to just the 5 stars in common between the two years, the offset disappears, albeit with a larger zero point error of 0.7 km s^{-1}. In addition, the zero point computed from the Griffin stars in 1986 differs from the 1987 CORAVEL zero point by over 2 km s^{-1}.

We might expect a loss of accuracy in computing a zero point from the Griffin stars. Since they have only a few measured velocities each, some of the stars may be

Table 5.1: Radial Velocities of Standard Stars—1986 Data.

Star	v_r	σ_v	Star	v_r	σ_v
HD 26151	-6.26	0.58	HD 167807	8.13	0.57
HD 42637	-13.85	0.59	HD 170052	-35.41	0.56
HD 42759	55.51	0.60	HD 178126	10.05	0.61
HD 142709	34.80	0.62	HD 184860	63.78	0.59
HD 144904	-7.13	0.56	HD 191514	-15.65	0.56
HD 144936	12.86	0.57	HD 192246	-38.13	0.58
HD 145515	-26.70	0.56	HD 192562	-20.10	0.57
HD 145851	-27.08	0.53	HD 192961	32.72	0.69
HD 146643	-42.76	0.64	HD 196794	-52.50	0.59
HD 146800	1.38	0.62	HD 201139	-23.48	0.42
HD 147006	17.15	0.68	HD 201195	11.29	0.59
HD 149606	-3.78	0.59	HD 202304	0.45	0.95
HD 154363	31.84	0.68	HD 203066	-24.79	0.88
HD 154590	-25.82	0.59	HD 203850	-45.85	0.63
HD 155526	-14.15	0.73	HD 207491	-10.13	0.60
HD 155842	-20.53	0.59	HD 209742	-25.17	0.59
HD 156731	5.46	0.58	HD 212038	-1.83	0.62
HD 157199	-14.01	0.56	HD 213042	5.24	0.58
HD 161848	-94.63	0.60			

variable. We therefore chose to fix the zero point of the 1987 data to the CORAVEL standards (as for the Chapter 2 southern velocities), which are well-measured over many years and have individual velocity errors of ~ 0.1 km s^{-1}. We then set the zero point of the 1986 data using the 9 bright reference stars in common, thus insuring that the relative zero point would be identical. It is interesting to note that the dispersion between the 1986 and 1987 velocities for these stars, 0.6 km s^{-1}, is significantly smaller than that between our velocities and Griffin's. This could be due to the larger errors in Griffin's individual velocities (1.5 km s^{-1}), or some long-term variability not detected in our measurements over a 1-year interval. Finally, we added 0.4 km s^{-1} to the CORAVEL zero point to bring the velocities to the IAU system (see §2.2.3). The zero-point uncertainty for the 87 data is then 0.3 km s^{-1}, from the measured dispersion of the CORAVEL standards, and 0.35 km s^{-1} for the 86 data, after adding the offset uncertainty between the two years in quadrature.

The radial velocities measured for the standard stars are given in Tables 5.1 and

Table 5.2: Radial Velocities of Standard Stars—1987 Data.

Star	v_r	σ_v	Star	v_r	σ_v
HD 14680	52.45	0.67	HD 196794	-53.14	0.65
HD 17155	34.55	0.80	HD 196983	-7.99	0.66
HD 21209	-9.30	0.66	HD 200410	-47.47	0.65
HD 24331	22.95	1.05	HD 201139	-23.84	0.66
HD 25061	47.26	0.71	HD 201195	11.76	0.74
HD 26794	56.86	0.65	HD 202168	-7.78	0.65
HD 31560	6.77	0.75	HD 202169	8.52	0.64
HD 33661	11.96	0.66	HD 203066	-23.95	0.65
HD 34033	42.32	0.66	HD 207144	-10.51	0.69
HD 39194	14.32	0.82	HD 209742	-25.00	0.70
HD 42637	-13.50	0.69	HD 211031	10.34	0.65
HD 45046	-11.51	0.67	HD 211904	14.59	0.69
HD 176047	-41.95	0.65	HD 218566	-36.26	0.64
HD 178126	9.40	0.65	HD 218693	-9.93	0.65
HD 191514	-15.11	0.64	HD 219509	68.28	0.67
HD 192961	31.97	0.73	CPD −43°2527	19.70	0.62
HD 193231	-30.09	0.72			

5.2. The radial velocity is shown as v_r (in km s^{-1}), with associated errors σ_v. Each radial velocity shown is a weighted mean of individual velocities measured separately for each order used (orders 61–70 for 1986 stars and 60–75 for 1987). Any order that had a velocity more than 5σ deviant from the mean or did not converge was discarded. The error is calculated using the formal error from the Fourier quotient, plus an additional term to account for the error in the wavelength calibration. This was estimated by comparing the measured dispersion about a mean for the CORAVEL standards with their formal uncertainties; we find that for both seasons an additional 0.6 km s^{-1} must be added in quadrature to bring the two error estimates into agreement.

5.2.3 Analysis

Table 5.3 gives the radial velocities measured for the program objects, along with estimated uncertainties for each. The primary region stars are designated by "cs", and the additional bright stars observed in an adjacent field are designated "aux".

Table 5.3: Radial Velocities and Line Strengths of SGP K Stars

Star	Date[1]	v_r	σ_v	γ	ε_γ	Star	Date[1]	v_r	σ_v	γ	ε_γ
aux42	6680.566	-18.54	1.16	0.44	0.03	aux2963	6681.585	-16.12	0.88	0.65	0.02
aux46	6684.569	-9.23	0.86	0.80	0.03	aux2963	7075.794	-15.19	0.78	0.50	0.03
aux74	6682.583	29.86	0.86	0.74	0.03	aux3008	6684.595	46.16	0.93	0.70	0.04
aux109	6684.593	0.04	0.86	0.70	0.03	aux3197	6682.527	-39.79	0.97	0.58	0.03
aux109	7075.805	-1.47	0.74	0.55	0.03	aux3225	6679.572	18.19	0.86	0.61	0.02
aux130	6680.552	-3.62	1.15	0.64	0.05	aux3225	7075.712	17.95	0.74	0.47	0.02
aux169	6684.577	-5.72	1.26	0.68	0.04	aux3421	6683.577	-9.42	0.87	0.66	0.04
aux176	6684.586	32.11	1.09	0.68	0.04	aux3421	7075.731	-9.15	0.73	0.61	0.02
aux185	6684.603	32.20	1.40	0.38	0.04	aux3432	6682.591	-21.59	0.85	0.75	0.03
aux706	6680.559	3.43	0.93	0.65	0.03	aux3432	7074.532	-20.26	0.76	0.65	0.02
aux706	7075.771	3.77	0.81	0.46	0.04	aux3442	6684.560	37.10	0.96	0.65	0.03
aux718	6684.582	-6.91	1.25	0.56	0.03	aux3443	6681.577	-3.58	1.26	0.65	0.04
aux803	6684.603	-2.58	0.93	0.68	0.03	aux3443	7076.570	-4.70	0.86	0.65	0.04
aux803	7074.552	-3.86	0.72	0.59	0.02	cs99	6684.731	23.41	0.97	0.78	0.05
aux804	6684.586	-5.57	1.00	0.72	0.04	cs163	6678.634	10.76	1.69	0.65	0.06
aux818	6684.563	15.32	1.03	0.69	0.04	cs166	6684.708	20.67	1.18	0.76	0.05
aux851	6684.575	37.51	1.66	0.40	0.04	cs170	6681.894	2.49	1.44	0.69	0.06
aux1438	6680.573	11.03	0.80	0.66	0.03	cs197	6681.757	17.65	1.47	0.65	0.06
aux1438	7075.740	10.61	0.77	0.51	0.02	cs213	6678.670	-0.69	1.31	0.67	0.05
aux1471	6681.569	80.39	2.33	0.22	0.03	cs232	6680.692	-35.71	1.48	0.65	0.05
aux1471	7075.786	82.17	2.72	0.21	0.02	cs264	6682.887	-0.01	1.60	0.65	0.06
aux1472	6680.582	-8.83	0.92	0.61	0.03	cs268	6682.820	26.37	1.60	0.78	0.05
aux1472	7075.751	-9.77	0.75	0.56	0.02	cs269	6679.761	13.56	2.03	0.46	0.05
aux1475	6684.573	-25.82	6.35	0.16	0.02	cs312	6680.774	-44.03	2.52	0.51	0.07
aux1481	6684.569	-3.58	0.87	0.77	0.03	cs339	6678.815	7.12	1.82	0.66	0.07
aux1490	6684.578	20.17	0.82	0.79	0.03	cs845	6678.603	-16.77	0.96	0.72	0.03
aux1491	6684.586	27.30	0.98	0.73	0.05	cs878	6684.775	-34.34	1.10	0.71	0.04
aux1501	6680.590	30.59	1.01	0.60	0.03	cs898	6684.751	29.15	1.01	0.70	0.03
aux1501	7075.761	29.57	0.81	0.49	0.02	cs909	6684.681	12.69	1.14	0.67	0.04
aux1531	6682.577	12.63	1.14	0.60	0.04	cs932	6683.623	-11.73	1.49	0.62	0.04
aux1560	6684.588	10.86	0.93	0.70	0.04	cs932	6684.654	-7.41	1.20	0.65	0.06
aux1567	6683.595	-67.54	1.32	0.43	0.03	cs1029	6682.762	-23.00	1.65	0.54	0.05
aux1641	6679.579	59.46	1.12	0.51	0.03	cs1051	6680.756	32.80	1.92	0.74	0.06
aux2203	6684.578	-8.60	1.12	0.67	0.03	cs1071	6679.777	0.55	1.84	0.54	0.06
aux2227	6684.586	-42.47	0.76	0.74	0.02	cs1536	7080.572	33.21	0.94	0.56	0.02
aux2227	7075.816	-46.92	0.73	0.53	0.01	cs1550	6684.635	31.93	1.18	0.66	0.04
aux2235	6684.595	29.95	0.92	0.71	0.04	cs1586	6681.648	42.02	1.32	0.63	0.04
aux2235	7074.557	31.05	0.73	0.56	0.02	cs1598	6677.746	32.23	1.18	0.61	0.04
aux2236	6684.604	-12.24	0.90	0.69	0.03	cs1598	6678.611	32.95	1.79	0.65	0.06
aux2236	7075.826	-11.02	0.94	0.52	0.02	cs1605	6684.622	4.56	3.46	0.31	0.04
aux2241	6683.586	61.46	1.29	0.37	0.03	cs1631	6683.764	8.76	1.63	0.63	0.04
aux2241	7075.720	39.59	1.17	0.29	0.02	cs1631	6684.760	3.48	3.79	0.59	0.05
aux2260	6684.559	-18.95	1.58	0.42	0.03	cs1688	6683.877	-117.88	2.83	0.30	0.05
aux2260	7081.499	-18.21	2.17	0.44	0.03	cs1691	6678.658	-9.06	1.42	0.54	0.05
aux2265	6684.568	14.25	1.13	0.58	0.04	cs2111	6683.612	-13.94	1.08	0.57	0.03
aux2297	6684.597	56.71	1.11	0.53	0.04	cs2111	7074.635	-7.76	0.75	0.49	0.02
aux2300	6683.602	15.30	0.91	0.77	0.03	cs2140	7074.653	-22.40	0.77	0.55	0.02
aux2940	6679.564	-20.70	0.92	0.60	0.03	cs2147	7074.816	16.32	0.79	0.66	0.02
aux2940	7075.688	-14.93	0.75	0.52	0.02	cs2156	6684.855	12.70	1.17	0.73	0.04

Table 5.3—*Continued*

Star	Date[1]	v_r	σ_v	γ	ε_γ	Star	Date[1]	v_r	σ_v	γ	ε_γ
cs2206	6684.779	71.08	1.18	0.57	0.04	cs5915	7074.856	-1.87	0.74	0.58	0.02
cs2215	6678.622	33.53	1.82	0.48	0.05	cs5998	7080.718	8.15	1.09	0.73	0.06
cs2237	6680.627	15.16	1.25	0.58	0.04	cs5998	7080.727	12.72	1.19	0.70	0.05
cs2242	6678.899	10.96	1.33	0.73	0.04	cs6008	6682.600	12.81	1.29	0.55	0.04
cs2244	6677.710	23.45	6.01	0.58	0.05	cs6039	6682.902	12.58	1.56	0.51	0.04
cs2244	6679.623	26.96	1.24	0.63	0.04	cs6057	6682.833	-13.92	2.02	0.65	0.10
cs2246	6678.645	-17.85	1.31	0.66	0.05	cs6062	6684.874	63.89	2.06	0.44	0.05
cs2252	6684.887	-12.32	1.29	0.66	0.04	cs6085	6678.797	-37.11	2.09	0.41	0.05
cs2262	6684.895	21.62	1.46	0.54	0.05	cs6120	6678.884	69.77	1.79	0.55	0.04
cs2391	6679.730	136.36	1.57	0.69	0.06	cs6193	6680.809	-12.79	1.53	0.64	0.05
cs2391	6684.781	139.95	2.37	0.59	0.08	cs6414	6684.723	43.74	1.40	0.73	0.07
cs2452	6682.696	-10.42	1.88	0.54	0.05	cs6646	6684.636	42.58	1.35	0.58	0.03
cs2996	7074.614	-3.26	0.83	0.56	0.03	cs6653	7080.536	7.07	4.80	0.89	0.04
cs3008	7080.752	-1.94	1.01	0.75	0.06	cs6663	7076.772	32.49	0.80	0.56	0.03
cs3008	7080.766	-1.44	0.89	0.81	0.05	cs6693	6684.832	7.42	1.91	0.25	0.03
cs3019	6684.615	-36.87	1.26	0.55	0.04	cs6831	6682.853	0.45	1.84	0.71	0.06
cs3076	6684.644	61.98	1.84	0.67	0.05	cs6835	6680.878	57.57	2.24	0.56	0.07
cs3148	6678.830	-16.13	9.08	0.36	0.08	cs6906	6679.889	-5.77	1.78	0.64	0.07
cs3881	6684.679	0.73	3.95	0.44	0.04	cs6914	6684.854	23.45	1.65	0.60	0.06
cs3886	7074.797	-1.64	0.76	0.67	0.03	cs7339	7074.643	-5.00	0.72	0.60	0.01
cs3886	7076.720	0.00	0.76	0.80	0.03	cs7405	7080.659	23.11	0.80	0.64	0.03
cs3928	6684.624	44.59	1.28	0.58	0.04	cs7424	6684.877	4.81	1.14	0.70	0.04
cs3936	6684.638	26.18	1.03	0.67	0.03	cs7467	6683.676	-22.00	1.17	0.64	0.04
cs3957	6684.680	14.15	3.18	0.41	0.08	cs7499	6680.659	16.99	1.12	0.73	0.04
cs3965	6682.611	-50.60	1.59	0.42	0.04	cs7500	6681.635	1.05	1.50	0.55	0.04
cs4040	6683.775	34.86	2.46	0.61	0.05	cs7516	6684.772	0.90	1.76	0.64	0.06
cs4099	6681.704	27.02	3.02	0.49	0.06	cs7554	6680.861	14.85	4.27	0.51	0.07
cs4170	6679.696	15.80	1.91	0.69	0.06	cs7561	6681.791	5.59	1.92	0.68	0.07
cs4594	7074.681	-4.60	0.72	0.63	0.02	cs7571	6684.738	-5.27	1.42	0.60	0.05
cs4606	7074.827	11.43	0.72	0.53	0.01	cs7575	6681.828	47.94	2.77	0.55	0.08
cs4630	6684.610	2.56	1.08	0.71	0.04	cs8048	7074.844	-18.48	0.73	0.48	0.02
cs4630	7074.602	2.78	0.75	0.61	0.03	cs8061	7080.650	11.41	0.80	0.80	0.03
cs4638	7076.691	41.92	0.83	0.69	0.03	cs8102	6677.674	-13.46	0.97	0.65	0.03
cs4660	7077.811	8.93	0.76	0.58	0.03	cs8102	6677.684	-12.83	0.91	0.68	0.03
cs4661	6684.741	4.14	1.08	0.58	0.04	cs8102	6684.609	-11.98	1.09	0.72	0.04
cs4725	6684.835	28.49	1.49	0.54	0.04	cs8102	7076.679	-10.27	0.79	0.70	0.03
cs4811	6684.819	69.47	2.43	0.60	0.07	cs8115	6684.722	21.01	1.44	0.54	0.03
cs4875	6682.748	-15.85	1.48	0.71	0.06	cs8140	7077.765	-9.74	0.73	0.69	0.03
cs4895	6681.722	99.33	3.05	0.59	0.07	cs8146	7080.607	-25.51	2.43	0.67	0.03
cs5214	7075.670	4.61	0.74	0.56	0.02	cs8152	6684.792	-14.93	1.14	0.64	0.05
cs5228	6684.592	-13.20	1.10	0.53	0.04	cs8158	6682.620	32.26	1.01	0.69	0.03
cs5228	7074.623	31.34	0.80	0.37	0.02	cs8165	6684.866	31.79	1.18	0.67	0.04
cs5236	6684.714	79.30	1.07	0.56	0.04	cs8168	6684.678	33.78	0.91	0.73	0.04
cs5240	6684.688	83.83	1.28	0.62	0.04	cs8222	6681.661	-15.12	1.34	0.60	0.04
cs5265	6684.647	-1.74	1.14	0.61	0.04	cs8222	6684.898	-17.69	1.61	0.61	0.05
cs5331	6684.751	25.00	1.41	0.63	0.05	cs8228	6684.826	8.64	1.20	0.66	0.04
cs5342	7080.673	-1.03	0.77	0.65	0.03	cs8229	6679.636	-90.54	1.51	0.51	0.04
cs5364	6684.693	49.03	1.38	0.69	0.05	cs8229	6684.638	-93.23	1.51	0.52	0.05
cs5408	6683.808	47.20	1.81	0.56	0.06	cs8250	6684.805	56.58	2.01	0.48	0.05
cs5408	6684.867	46.31	1.54	0.59	0.05	cs8256	6681.845	9.22	2.13	0.55	0.06

Table 5.3—*Continued*

Star	Date[1]	v_r	σ_v	γ	ε_γ	Star	Date[1]	v_r	σ_v	γ	ε_γ
cs8257	6679.806	-7.38	1.86	0.63	0.07	cs11218	6683.748	-5.83	1.43	0.51	0.06
cs8257	6684.811	-12.40	1.83	0.59	0.06	cs11231	6678.764	-12.45	1.48	0.66	0.05
cs8787	6680.599	-16.00	0.89	0.66	0.03	cs11249	6684.838	2.35	1.80	0.52	0.05
cs8787	7075.642	-14.58	0.76	0.56	0.03	cs11814	7074.808	7.40	0.77	0.61	0.03
cs8797	7074.661	-21.65	0.75	0.45	0.02	cs11815	6684.704	9.89	0.88	0.76	0.05
cs8800	6684.640	11.42	0.96	0.69	0.05	cs11827	6684.665	6.78	0.98	0.70	0.04
cs8800	7075.652	9.99	0.73	0.59	0.02	cs11832	6684.696	42.17	1.03	0.54	0.03
cs8857	6684.752	0.94	1.07	0.67	0.05	cs11940	6684.737	8.65	2.43	0.49	0.07
cs8884	6684.670	13.00	1.10	0.61	0.03	cs11958	6678.872	-14.39	1.37	0.65	0.06
cs8896	6684.816	-0.42	1.74	0.55	0.05	cs12039	6679.712	22.36	1.62	0.66	0.06
cs8906	6682.671	18.25	1.24	0.60	0.04	cs12141	6682.713	-33.19	2.28	0.54	0.06
cs8910	6684.739	39.60	1.53	0.60	0.07	cs12436	7074.835	-4.73	0.74	0.47	0.02
cs8990	6682.731	21.41	2.01	0.58	0.07	cs12492	6684.691	19.56	0.97	0.62	0.03
cs9023	6680.791	67.19	1.72	0.53	0.04	cs12503	7080.550	43.99	0.79	0.66	0.03
cs9023	6684.848	63.94	1.78	0.56	0.06	cs12523	6684.604	-13.66	1.23	0.66	0.04
cs9064	6680.843	-25.98	1.71	0.66	0.08	cs12544	6684.872	47.40	2.02	0.58	0.07
cs9064	6684.881	-29.79	1.91	0.72	0.06	cs12557	6684.788	29.62	5.93	0.32	0.06
cs9421	6684.865	11.37	1.03	0.62	0.03	cs12561	6684.696	1.52	2.11	0.50	0.04
cs9439	6684.874	16.83	1.17	0.62	0.04	cs12608	6684.757	4.69	5.45	0.28	0.05
cs9449	7077.742	-3.32	0.75	0.72	0.02	cs12697	6680.722	-35.81	2.00	0.64	0.06
cs9459	7080.617	28.55	0.78	0.74	0.04	cs13114	7076.712	-0.46	0.86	0.71	0.03
cs9515	6681.861	-29.31	2.20	0.65	0.07	cs13121	6684.724	-5.43	0.92	0.64	0.03
cs9549	6678.685	44.97	1.27	0.67	0.04	cs13126	6684.656	4.71	1.00	0.69	0.03
cs9553	6684.803	-2.03	1.37	0.67	0.05	cs13167	7080.636	-6.24	0.77	0.72	0.03
cs9684	6679.791	14.97	2.30	0.58	0.06	cs13261	6684.722	25.53	1.28	0.69	0.07
cs9696	6679.856	28.06	1.87	0.53	0.08	cs13277	6682.783	5.03	2.00	0.56	0.06
cs9720	6679.679	-112.48	1.56	0.53	0.04	cs13350	6679.746	10.12	1.59	0.69	0.06
cs10126	6684.666	-35.02	1.10	0.53	0.04	cs13782	6679.905	46.19	0.90	0.63	0.02
cs10135	6684.905	-29.25	1.11	0.51	0.03	cs13782	7074.581	49.24	0.77	0.45	0.02
cs10147	7080.509	37.08	0.77	0.71	0.03	cs13825	6677.727	-40.54	1.43	0.45	0.04
cs10216	6684.742	-28.22	1.21	0.51	0.03	cs13825	6680.606	-48.20	1.49	0.52	0.04
cs10217	6684.795	35.31	1.44	0.67	0.04	cs13828	6684.731	47.79	1.18	0.66	0.04
cs10230	6681.875	-35.31	1.45	0.72	0.06	cs13883	6683.634	7.47	1.45	0.57	0.06
cs10237	6684.668	11.79	1.45	0.71	0.06	cs13887	6684.648	-11.85	1.28	0.65	0.04
cs10266	6680.895	4.83	1.91	0.66	0.05	cs13917	6681.672	12.55	1.33	0.74	0.04
cs10316	6681.773	-35.77	1.51	0.68	0.06	cs14412	7074.711	28.90	0.74	0.55	0.02
cs10322	6678.747	36.76	3.67	0.68	0.07	cs14449	6684.609	-15.88	1.36	0.52	0.04
cs10361	6684.787	-0.23	1.48	0.60	0.05	cs14466	7080.593	-37.40	0.76	0.71	0.03
cs10371	6681.688	-17.94	2.37	0.66	0.06	cs14497	6684.659	4.20	1.17	0.60	0.04
cs10379	6678.731	8.23	1.65	0.66	0.07	cs14542	6683.649	25.95	1.44	0.62	0.05
cs10972	6684.806	23.10	1.03	0.63	0.03	cs14543	6684.886	12.01	1.70	0.62	0.09
cs10999	6683.698	30.25	1.33	0.64	0.06	cs14555	6684.819	-38.34	1.89	0.43	0.05
cs11000	6683.663	-57.37	1.28	0.57	0.04	cs14601	6682.657	-8.18	1.56	0.51	0.05
cs11001	6681.613	-7.89	1.87	0.68	0.06	cs14607	6683.791	20.37	1.51	0.55	0.05
cs11028	6684.656	4.12	2.60	0.44	0.06	cs15140	7077.823	-21.89	0.78	0.56	0.02
cs11047	6684.884	36.54	1.21	0.66	0.04	cs15152	6677.699	8.44	1.43	0.61	0.05
cs11107	6683.860	-36.92	2.25	0.53	0.05	cs15152	6679.597	9.65	1.20	0.67	0.04
cs11107	6684.831	-37.63	1.71	0.44	0.04	cs15155	6681.622	81.98	1.70	0.62	0.06
cs11125	6684.891	-0.89	1.74	0.56	0.06	cs15155	6684.622	77.84	1.59	0.65	0.05

191

Table 5.3—*Continued*

Star	Date[1]	v_r	σ_v	γ	ε_γ	Star	Date[1]	v_r	σ_v	γ	ε_γ
cs15188	6684.845	75.38	3.54	0.43	0.05	cs17470	6683.686	11.56	1.08	0.82	0.04
cs15229	6682.684	16.79	1.24	0.61	0.05	cs17480	6684.710	15.12	1.80	0.57	0.06
cs15229	6684.704	18.29	1.17	0.67	0.05	cs17494	6680.672	2.79	1.39	0.70	0.06
cs15300	6684.843	2.71	2.02	0.70	0.06	cs17532	6683.846	33.30	1.47	0.65	0.05
cs15967	7076.734	22.73	0.85	0.57	0.03	cs17532	6684.799	32.40	1.54	0.62	0.06
cs15998	6677.736	-11.21	1.06	0.67	0.03	cs17606	6682.869	-37.99	3.38	0.58	0.07
cs15998	6680.617	-8.27	1.13	0.76	0.04	cs17992	7074.672	14.56	1.06	0.20	0.02
cs16042	6684.709	-10.90	1.05	0.69	0.04	cs17993	7074.693	172.31	0.76	0.39	0.01
cs16136	6683.823	11.02	2.25	0.44	0.06	cs17997	7080.799	54.70	0.75	0.61	0.03
cs16266	6678.716	106.29	1.82	0.50	0.05	cs18013	6684.645	16.99	0.92	0.73	0.03
cs16266	6684.690	107.76	1.70	0.52	0.05	cs18013	7074.568	16.42	0.75	0.61	0.02
cs16735	6684.616	-19.46	1.21	0.52	0.03	cs18055	7080.681	-59.04	0.80	0.60	0.02
cs16745	6684.762	-21.48	1.25	0.71	0.03	cs18075	6684.763	32.69	1.62	0.69	0.05
cs16760	6684.600	-9.21	1.11	0.71	0.04	cs18091	6684.849	13.71	1.57	0.42	0.04
cs16778	6684.765	-19.39	1.14	0.62	0.04	cs18105	6684.815	35.02	1.27	0.61	0.04
cs16798	6684.700	-2.31	1.02	0.65	0.03	cs18241	6679.825	-113.78	1.75	0.53	0.05
cs16800	6684.785	-42.35	10.08	0.29	0.04	cs18262	6682.799	34.54	2.27	0.64	0.06
cs16832	6684.778	-33.07	1.38	0.58	0.04	cs18640	6684.623	10.36	0.91	0.72	0.03
cs16856	6677.688	9.62	2.58	0.63	0.05	cs18640	7074.591	9.12	0.73	0.58	0.02
cs16856	6682.633	8.08	1.25	0.61	0.07	cs18647	7074.706	-15.90	0.75	0.50	0.02
cs16859	6680.647	9.04	1.69	0.60	0.05	cs18675	7077.837	-23.68	0.78	0.55	0.03
cs16908	6680.706	1.19	1.43	0.68	0.05	cs18691	6679.612	-25.24	2.19	0.39	0.05
cs16931	6681.807	-2.98	2.14	0.68	0.08	cs18700	6684.804	35.05	2.71	0.31	0.04
cs16940	6681.739	0.55	3.26	0.74	0.08	cs18720	7080.694	-0.61	1.56	0.47	0.04
cs16974	6678.699	-7.13	1.49	0.74	0.07	cs18720	7080.709	-0.80	1.58	0.59	0.05
cs16974	6684.668	-5.39	2.19	0.77	0.06	cs18753	6679.649	-28.93	1.84	0.56	0.04
cs17380	6684.613	64.17	1.30	0.57	0.03	cs18760	6682.643	-1.65	1.21	0.67	0.04
cs17380	7075.661	70.39	0.92	0.42	0.03	cs18760	6684.722	-3.05	1.15	0.73	0.04
cs17386	7074.722	-28.79	0.81	0.53	0.02	cs18837	6680.825	33.98	1.70	0.74	0.07
cs17390	7076.698	-6.11	0.75	0.63	0.03	cs18892	6680.743	5.61	3.23	0.52	0.06
cs17397	6684.630	35.84	1.10	0.64	0.04	cs18897	6679.841	58.73	1.96	0.47	0.05
cs17404	6684.674	12.30	0.96	0.67	0.03	cs19400	6684.831	53.62	2.88	0.61	0.06
cs17414	6680.638	-1.02	1.15	0.63	0.04	cs19475	6678.852	-64.18	2.31	0.44	0.06
cs17439	6684.859	37.85	1.64	0.49	0.04	cs19530	6678.781	-10.48	1.25	0.69	0.04
cs17445	6681.602	-13.22	2.27	0.70	0.05						

[1]Julian date minus 2,440,000

Table 5.4: Coordinates for SGP K Stars

Catalog ID	RA (J2000) Dec		Catalog ID	RA (J2000) Dec	
aux42	00 01 21.7	-25 14 04	cs170	01 00 08.4	-30 02 14
aux46	00 02 30.8	-25 19 04	cs197	00 48 15.7	-30 01 38
aux74	00 19 14.6	-25 13 51	cs213	00 52 23.3	-30 10 07
aux109	00 30 12.3	-25 09 10	cs232	00 54 52.8	-30 03 37
aux130	00 01 49.1	-25 19 00	cs264	01 04 28.6	-30 06 30
aux169	00 25 29.2	-25 14 52	cs268	01 05 22.9	-30 08 04
aux176	00 29 14.8	-25 16 57	cs269	01 05 44.2	-30 05 04
aux185	00 32 15.0	-25 14 46	cs312	00 51 24.3	-30 07 51
aux706	00 01 49.4	-25 04 04	cs339	00 55 15.3	-30 12 44
aux718	00 15 29.1	-25 07 34	cs845	00 48 02.2	-30 00 43
aux803	00 35 08.7	-25 01 34	cs878	00 51 33.6	-29 52 39
aux804	00 35 17.4	-25 02 38	cs898	01 04 30.5	-29 57 21
aux818	00 03 55.5	-25 03 18	cs909	00 49 06.3	-29 57 12
aux851	00 14 17.7	-25 01 43	cs932	00 56 24.8	-29 52 33
aux1438	00 08 23.2	-24 51 26	cs1029	01 00 02.6	-29 52 34
aux1471	00 02 17.5	-24 53 48	cs1051	01 04 05.9	-29 52 42
aux1472	00 02 42.9	-24 49 56	cs1071	00 48 55.6	-29 57 01
aux1475	00 05 00.9	-24 49 22	cs1169	01 04 41.4	-29 59 33
aux1481	00 11 14.1	-24 55 46	cs1536	00 52 58.8	-29 41 27
aux1490	00 18 28.0	-24 56 37	cs1550	00 59 09.2	-29 46 31
aux1491	00 18 31.7	-24 49 39	cs1586	00 50 40.8	-29 50 18
aux1501	00 25 54.0	-24 55 16	cs1598	00 54 52.4	-29 45 29
aux1531	00 08 01.6	-24 54 58	cs1605	00 58 53.9	-29 40 44
aux1560	00 26 09.3	-24 57 57	cs1631	00 46 13.5	-29 43 29
aux1567	00 33 13.0	-24 48 31	cs1688	01 03 09.9	-29 43 17
aux1641	00 23 24.9	-24 48 46	cs1691	01 04 14.6	-29 46 28
aux2203	00 10 17.7	-24 41 42	cs2111	00 54 32.9	-29 33 39
aux2227	00 27 53.0	-24 44 41	cs2140	00 58 33.0	-29 38 41
aux2235	00 33 40.8	-24 41 04	cs2147	01 02 27.1	-29 34 50
aux2236	00 34 08.7	-24 46 28	cs2156	00 47 28.7	-29 31 40
aux2241	00 36 27.0	-24 36 58	cs2206	00 49 05.4	-29 40 04
aux2260	00 08 35.9	-24 44 44	cs2215	00 53 13.9	-29 37 27
aux2265	00 10 06.9	-24 47 06	cs2237	00 58 28.1	-29 33 28
aux2297	00 36 16.4	-24 42 18	cs2242	01 00 00.3	-29 34 04
aux2300	00 36 48.3	-24 46 06	cs2244	01 00 44.3	-29 31 38
aux2940	00 02 01.2	-25 20 09	cs2246	01 00 45.6	-29 32 01
aux2963	00 07 55.3	-25 22 34	cs2252	01 01 59.9	-29 31 58
aux3008	00 33 49.5	-25 24 44	cs2262	01 04 46.4	-29 31 56
aux3197	00 01 37.0	-24 51 50	cs2391	00 50 15.6	-29 31 47
aux3225	00 09 14.3	-24 44 31	cs2452	01 00 19.1	-29 39 07
aux3421	00 10 06.7	-24 31 13	cs2996	01 04 41.8	-29 20 20
aux3432	00 29 14.1	-24 33 08	cs3008	00 49 55.6	-29 24 35
aux3442	00 04 10.4	-24 30 37	cs3019	00 56 31.7	-29 30 08
aux3443	00 05 58.9	-24 35 49	cs3055	00 48 34.7	-29 25 29
aux3443	00 05 58.9	-24 35 49	cs3076	00 55 54.9	-29 29 50
aux3447	00 12 31.3	-24 33 51	cs3148	00 57 26.3	-29 26 45
cs89	00 57 05.4	-30 06 28	cs3881	00 49 05.4	-29 10 27
cs99	00 59 31.9	-30 07 00	cs3886	00 53 37.1	-29 16 57
cs163	00 56 46.0	-30 03 01	cs3928	01 02 30.3	-29 08 51
cs166	00 57 46.6	-30 09 00	cs3936	01 03 50.7	-29 08 59

Table 5.4—*Continued*

Catalog ID	RA (J2000) Dec		Catalog ID	RA (J2000) Dec	
cs3957	00 49 33.5	-29 12 08	cs7516	00 50 55.6	-28 24 43
cs3965	00 52 30.0	-29 12 29	cs7554	00 59 07.0	-28 24 41
cs4040	00 55 13.8	-29 16 26	cs7561	01 00 15.9	-28 26 40
cs4099	00 50 10.8	-29 10 23	cs7571	01 02 34.6	-28 18 14
cs4170	00 59 55.6	-29 18 18	cs7575	01 03 48.7	-28 18 09
cs4594	00 46 19.5	-29 00 50	cs8048	00 56 34.2	-28 15 09
cs4606	01 04 18.6	-29 06 06	cs8061	00 50 43.5	-28 07 41
cs4630	01 02 05.6	-29 08 45	cs8102	00 55 07.9	-28 15 55
cs4638	00 46 44.7	-29 00 21	cs8115	01 00 00.7	-28 08 25
cs4660	01 01 32.4	-29 02 43	cs8140	00 54 32.1	-28 05 52
cs4661	01 01 50.5	-29 08 39	cs8146	00 56 29.9	-28 13 31
cs4725	01 03 55.9	-29 01 17	cs8152	00 57 32.0	-28 14 32
cs4811	00 48 41.9	-29 02 36	cs8158	00 59 31.3	-28 13 23
cs4875	00 59 42.4	-29 00 06	cs8165	01 01 52.4	-28 12 28
cs4895	01 02 19.6	-29 05 28	cs8168	01 02 57.7	-28 08 14
cs5214	01 03 13.6	-28 54 35	cs8222	01 03 37.6	-28 14 16
cs5228	00 54 07.3	-28 51 12	cs8228	01 04 19.9	-28 14 36
cs5236	01 00 50.2	-28 51 14	cs8229	01 04 36.0	-28 11 54
cs5240	01 02 03.2	-28 49 32	cs8250	00 51 06.4	-28 06 32
cs5263	00 54 08.4	-28 50 16	cs8256	00 51 44.7	-28 14 18
cs5265	00 54 41.3	-28 57 45	cs8257	00 51 49.3	-28 15 39
cs5331	01 03 17.6	-28 56 39	cs8787	00 50 58.7	-27 55 39
cs5342	01 05 38.9	-28 53 51	cs8797	01 00 26.0	-27 57 24
cs5364	00 51 11.5	-28 56 40	cs8800	01 01 28.9	-28 05 46
cs5408	01 00 38.2	-28 52 39	cs8857	00 49 54.8	-28 05 22
cs5915	01 01 38.0	-28 38 29	cs8884	01 03 28.6	-28 00 48
cs5984	01 02 50.0	-28 43 51	cs8896	00 48 00.4	-28 00 19
cs5998	00 48 58.1	-28 40 32	cs8906	00 51 54.7	-28 01 46
cs6008	00 52 05.9	-28 39 29	cs8910	00 53 30.8	-28 03 16
cs6039	01 03 06.2	-28 43 48	cs8990	00 50 00.7	-27 56 40
cs6057	00 49 52.5	-28 47 27	cs9023	00 55 37.9	-27 58 58
cs6062	00 50 31.4	-28 43 41	cs9064	01 03 00.8	-27 57 19
cs6085	00 54 26.5	-28 38 25	cs9421	00 49 18.0	-27 45 16
cs6120	01 04 07.1	-28 42 25	cs9439	00 57 20.9	-27 52 31
cs6193	00 56 32.6	-28 37 50	cs9449	01 04 08.1	-27 51 58
cs6414	00 47 36.6	-28 37 28	cs9459	00 49 37.2	-27 45 09
cs6646	00 47 34.3	-28 34 40	cs9515	00 48 38.7	-27 49 21
cs6653	00 49 15.4	-28 37 09	cs9549	00 59 17.6	-27 47 27
cs6663	00 57 31.6	-28 35 21	cs9553	01 00 44.0	-27 49 44
cs6693	00 53 39.5	-28 30 26	cs9684	00 57 32.9	-27 51 28
cs6831	00 49 41.0	-28 30 30	cs9696	01 00 15.7	-27 47 39
cs6835	00 50 03.4	-28 31 22	cs9720	01 03 57.9	-27 47 02
cs6906	01 02 25.9	-28 36 05	cs10126	00 54 43.2	-27 40 37
cs6914	01 03 37.6	-28 27 34	cs10135	01 00 36.0	-27 42 54
cs7339	00 57 43.8	-28 17 42	cs10147	00 48 15.8	-27 35 10
cs7405	00 52 58.0	-28 23 51	cs10216	00 59 54.3	-27 35 52
cs7424	01 01 46.3	-28 18 45	cs10217	01 00 40.3	-27 39 42
cs7467	00 56 21.1	-28 16 57	cs10230	00 46 38.2	-27 40 28
cs7499	01 04 28.6	-28 18 38	cs10237	00 47 51.8	-27 42 47
cs7500	01 05 02.2	-28 24 27	cs10266	00 54 30.4	-27 39 25

Table 5.4—*Continued*

Catalog ID	RA (J2000) Dec		Catalog ID	RA (J2000) Dec	
cs10316	00 48 44.7	-27 42 20	cs14466	00 53 43.9	-26 37 08
cs10322	00 49 56.0	-27 35 23	cs14497	01 04 57.5	-26 40 06
cs10361	00 59 06.0	-27 34 42	cs14542	00 59 13.0	-26 34 49
cs10371	01 01 50.4	-27 38 19	cs14543	00 59 45.1	-26 36 51
cs10379	01 03 28.7	-27 36 39	cs14555	01 03 51.6	-26 32 52
cs10972	01 00 09.4	-27 30 35	cs14601	00 55 06.3	-26 41 41
cs10999	00 49 50.1	-27 28 17	cs14607	00 56 10.1	-26 38 11
cs11000	00 49 54.7	-27 30 14	cs15140	01 02 17.2	-26 23 22
cs11001	00 50 18.9	-27 25 38	cs15152	00 46 45.6	-26 23 55
cs11028	00 59 51.4	-27 29 54	cs15155	00 47 34.7	-26 29 13
cs11047	01 05 25.7	-27 32 24	cs15188	00 56 05.7	-26 23 56
cs11107	00 57 27.7	-27 33 37	cs15229	00 47 42.0	-26 26 03
cs11125	01 01 10.2	-27 30 21	cs15300	01 02 15.2	-26 23 27
cs11218	00 58 41.0	-27 34 16	cs15967	00 52 12.2	-26 10 59
cs11231	01 00 34.9	-27 34 12	cs15998	00 47 54.8	-26 14 27
cs11249	01 02 27.7	-27 34 02	cs16042	00 59 39.7	-26 12 09
cs11814	00 49 08.1	-27 18 22	cs16136	01 02 12.1	-26 21 34
cs11815	00 50 07.7	-27 20 10	cs16266	01 03 56.6	-26 11 34
cs11827	00 58 48.9	-27 14 41	cs16735	01 04 53.8	-26 10 05
cs11832	01 00 54.1	-27 24 25	cs16745	00 48 53.0	-26 09 45
cs11940	01 01 47.4	-27 24 32	cs16760	00 59 05.3	-26 09 18
cs11958	00 47 59.6	-27 23 41	cs16778	00 50 52.1	-26 09 45
cs12039	01 05 32.8	-27 14 50	cs16798	00 59 20.8	-26 08 31
cs12141	01 02 27.7	-27 14 56	cs16800	00 59 48.4	-26 01 24
cs12436	00 54 35.6	-27 07 52	cs16832	00 52 29.9	-26 02 44
cs12492	01 03 57.3	-27 10 58	cs16856	00 58 45.0	-26 04 45
cs12503	00 49 32.3	-27 12 01	cs16859	00 59 38.5	-26 03 19
cs12523	00 57 43.2	-27 13 01	cs16908	00 53 52.2	-26 05 38
cs12544	00 51 08.0	-27 03 24	cs16931	01 01 11.3	-26 00 28
cs12557	00 55 50.2	-27 06 37	cs16940	01 03 15.0	-26 00 39
cs12561	00 56 41.7	-27 12 35	cs16974	00 51 15.4	-26 06 33
cs12608	00 51 21.9	-27 10 01	cs17379	00 50 23.0	-25 50 43
cs12697	00 54 06.7	-27 09 25	cs17380	00 51 34.4	-25 54 26
cs13114	00 53 07.1	-26 54 42	cs17386	00 55 34.7	-25 50 35
cs13121	00 55 54.6	-26 52 43	cs17390	00 58 07.1	-25 58 58
cs13126	00 58 23.8	-27 01 22	cs17397	01 00 39.0	-25 57 46
cs13167	00 56 28.4	-26 58 60	cs17404	01 03 54.3	-25 50 31
cs13261	00 47 03.3	-26 56 11	cs17414	00 51 43.1	-25 58 05
cs13277	00 49 41.5	-26 56 04	cs17439	00 46 15.6	-25 50 07
cs13350	01 05 03.3	-26 56 23	cs17445	00 47 27.1	-25 55 15
cs13782	00 58 39.3	-26 52 06	cs17470	00 55 38.6	-25 53 27
cs13782	00 58 39.3	-26 52 06	cs17480	00 59 43.4	-25 58 12
cs13825	00 57 26.3	-26 50 54	cs17494	00 47 05.1	-25 52 25
cs13828	00 59 35.3	-26 43 20	cs17532	00 55 15.8	-25 56 25
cs13883	00 58 44.7	-26 42 35	cs17606	00 50 47.5	-25 49 30
cs13887	01 01 12.7	-26 44 45	cs17992	00 55 15.1	-25 38 40
cs13917	00 49 34.7	-26 44 43	cs17993	00 56 09.9	-25 42 44
cs13979	01 03 41.9	-26 44 25	cs17997	01 01 33.0	-25 48 51
cs14412	00 51 13.3	-26 39 01	cs18013	00 53 44.9	-25 46 52
cs14449	00 47 43.4	-26 36 46	cs18055	00 55 17.0	-25 39 56

195

Table 5.4—*Continued*

Catalog ID	RA (J2000) Dec		Catalog ID	RA (J2000) Dec	
cs18075	00 47 13.1	-25 40 46	cs18720	00 58 02.9	-25 34 28
cs18091	00 55 49.7	-25 46 13	cs18753	00 48 49.6	-25 30 12
cs18105	01 02 27.9	-25 44 52	cs18760	00 49 50.6	-25 32 28
cs18241	00 55 35.2	-25 41 24	cs18837	00 50 46.3	-25 36 16
cs18262	01 00 14.8	-25 39 03	cs18892	01 01 31.5	-25 32 31
cs18640	00 59 25.1	-25 33 35	cs18897	01 02 27.6	-25 35 44
cs18647	01 04 36.4	-25 37 42	cs19400	01 00 56.5	-25 21 41
cs18675	01 01 19.7	-25 31 27	cs19475	01 00 56.0	-25 27 54
cs18691	00 48 13.4	-25 28 55	cs19530	00 48 39.5	-25 26 04
cs18700	00 52 17.9	-25 30 45			

Also listed are the line strengths (γ) for each star, measured relative to the template spectrum. Note that since line strengths were measured relative to different spectra, the values are not commensurate between the two seasons; however, only the relative values within a run are needed to make the giant-dwarf separation (see below). Due to the low signal-to-noise level of the spectra, the uncertainties in γ for a single order were ~ 0.1, so we averaged the line strengths of 10 orders centered on the order containing Mg b, and took the larger of the formal error or the internal dispersion as the uncertainty.

Since many program stars were observed in both 1986 and 1987, we can make some checks on the accuracy of our velocities and zero point. In addition, we can use the comparison to estimate the fraction of stars that are binaries, particularly the binaries with large velocity offsets (> 10 km s^{-1}) that could significantly affect our velocity dispersion measurement. Table 5.5 shows a comparison of measured velocities between 1986 and 1987, showing velocity differences, expected error in the difference ε_f, and χ^2. The stars aux2241 and cs5228 are clearly variable, and several other stars exhibit slightly larger velocity shifts than expected given the errors. Eliminating all stars with $\chi^2 > 20$, we find $\langle v_{87} - v_{86} \rangle = 0.17 \pm 0.21$ for the cs and aux stars, confirming the accuracy of our relative zero point between the two seasons. The velocities are compared with unpublished velocities from P. Schechter to further search for velocity variation in §5.3.

Table 5.5: Radial Velocity Comparison

Star	$v_{87} - v_{86}$	ε_f	χ^2
aux109	-1.51	1.02	2.21
aux706	0.35	1.13	0.10
aux803	-1.28	1.07	1.43
aux1438	-0.42	0.99	0.18
aux1471	1.78	3.55	0.25
aux1472	-0.94	1.08	0.75
aux1501	-1.02	1.19	0.74
aux2227	-4.45	0.93	22.91
aux2235	1.09	1.06	1.06
aux2236	1.22	1.20	1.03
aux2241	-21.86	1.67	171.99
aux2260	0.74	2.63	0.08
aux2940	5.77	1.07	28.88
aux2963	0.93	1.07	0.76
aux3225	-0.24	1.02	0.06
aux3421	0.28	1.02	0.07
aux3432	1.33	1.03	1.67
aux3443	-1.12	1.44	0.60
cs2111	6.18	1.21	26.08
cs4630	0.22	1.21	0.03
cs5228	44.53	1.26	1243.16
cs8102	2.49	0.84	8.69
cs8787	1.42	1.06	1.79
cs8800	-1.43	1.10	1.67
cs13782	3.05	1.07	8.06
cs17380	6.22	1.51	16.98
cs18013	-0.57	1.07	0.29
cs18640	-1.23	1.06	1.35
hd42637	0.35	0.91	0.15
hd178126	-0.65	0.90	0.53
hd191514	0.55	0.85	0.41
hd192961	-0.74	1.00	0.55
hd196794	-0.64	0.88	0.53
hd201139	-0.36	0.78	0.21
hd201195	0.46	0.95	0.23
hd203066	0.83	1.10	0.58
hd209742	0.17	0.91	0.03

5.2.4 Giant/Dwarf Separation

To determine a space density for the stellar sample, we need to obtain accurate distances to the stars selected from the CS sample. We can accomplish this by using the relation derived between absolute magnitude and color for stars in the solar neighborhood (Chiu 1980, Reid & Gilmore 1982) to derive an approximate distance modulus to each star based on its (V–I) color and apparent V magnitude, suitably corrected for biases caused by scatter in intrinsic M_V. This assumes, however, that the stars in the color range are main-sequence dwarfs, but many of the stars in the sample are actually giants that are intrinsically $\sim$ 5.5 mag brighter. Though the fraction of giants in a volume-limited sample will be small, a magnitude-limited sample will accept a much larger volume for giants and the contamination can become significant. This is illustrated by KG in a plot of a density distribution derived assuming all of their sample stars are dwarfs, which shows an anomalous excess of stars close to the Sun that are in fact distant giants with erroneous distances. To obtain an accurate depiction of the density as a function of height, one would ideally measure spectral types for each star, and exclude the giants from the final sample. However, since we already have spectra for a subset of these stars, selected randomly from bins in apparent magnitude, we can instead use the spectra to make a giant/dwarf separation between these stars and estimate the fraction of giants in each apparent magnitude bin. Each bin of the full sample can then be adjusted downward by the appropriate fraction, and the density law measured from the resultant apparent magnitude distribution (following KG).

We attempted to find the number of giants in our sample by using the strength of the Mg b absorption lines in the spectrum near 5180 Å. In K stars, these lines are substantially weaker that the lines of dwarfs at the same color. There is a general trend toward weaker lines in both dwarfs and giants as their color gets bluer, but the giants remain substantially weaker over the color range of the CS sample (see KG figures 1–3 for a good illustration of the trend vs. (B–V) color).

Figure 5-3 shows the effectiveness of using the line strengths for this separation. The data are from an unpublished analysis by P. Schechter of low resolution data
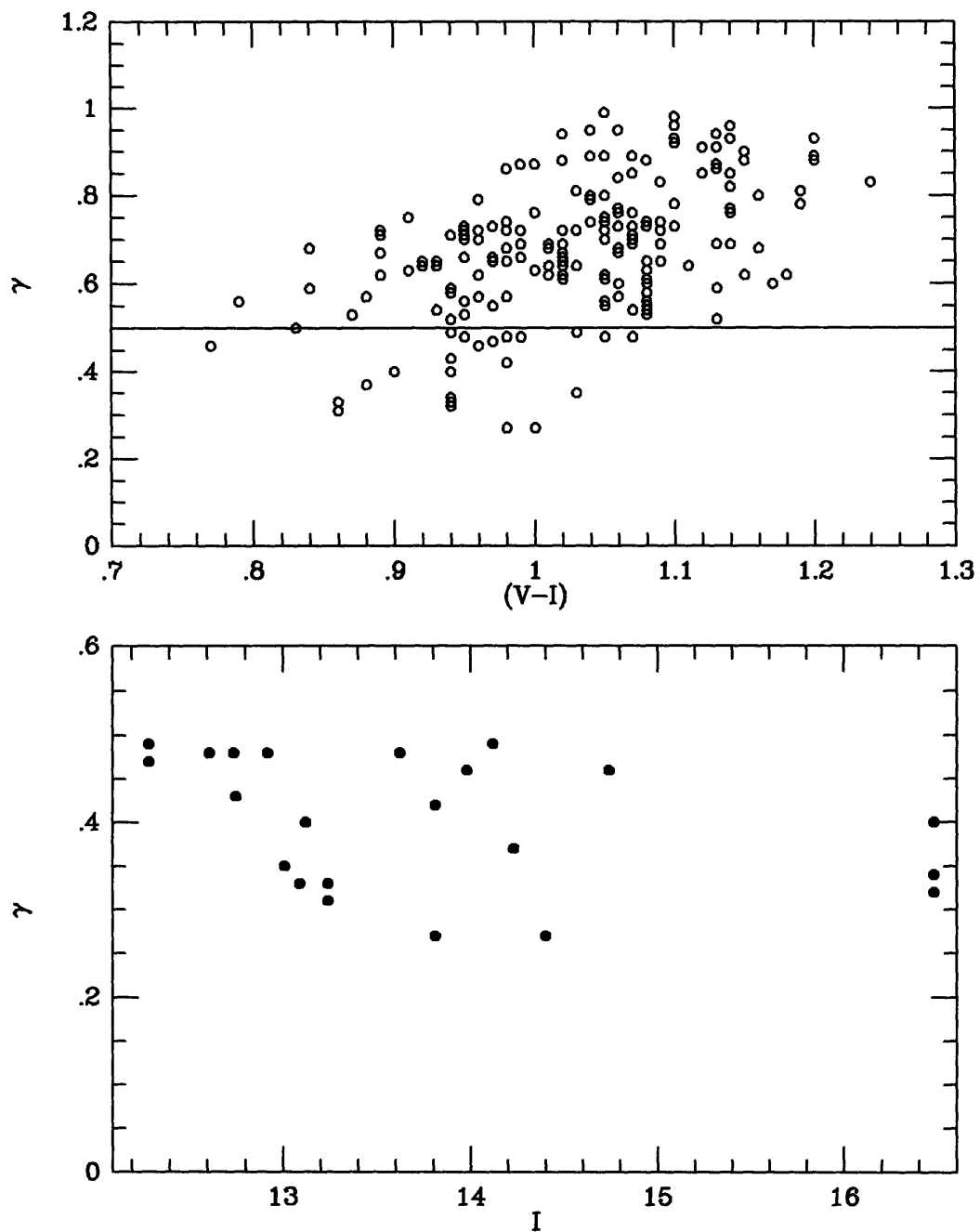
Figure 5-3: Giant-Dwarf separation for the unpublished 1983 data of P. Schechter. The upper panel shows line strength plotted vs. (V-I) color, and a line is drawn to show the separation point used. The bottom plot shows the points below the line plotted vs. apparent I magnitude, indicating that we were successful in selecting out giants.
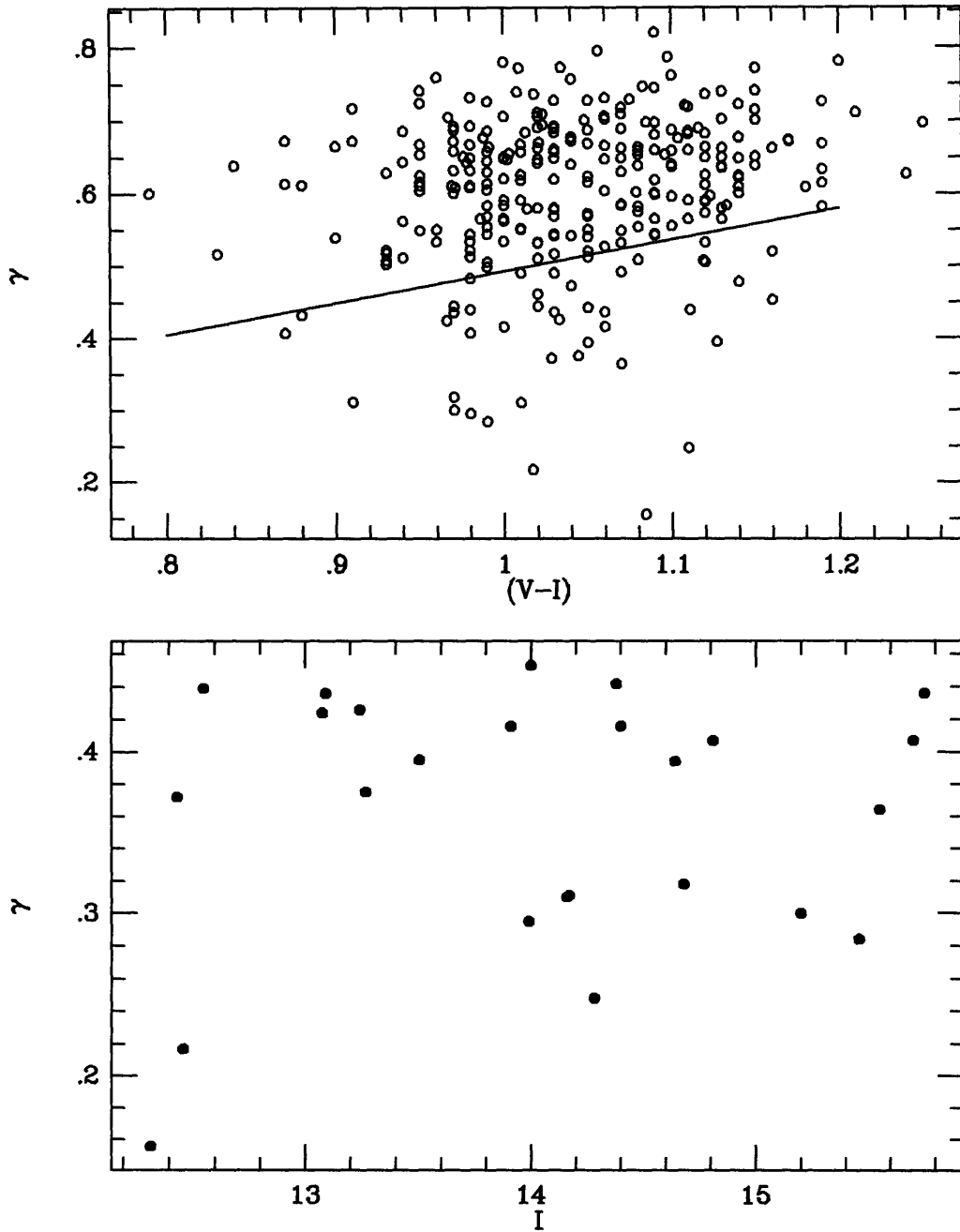
199

Figure 5-4: Giant-Dwarf separation for the data from 1986 given in this chapter. Note the poorer separation in the bottom plot.

taken in 1983 for a subset of the stars we measure. The line drawn is a somewhat arbitrary cutoff of some particular line strength, and all points below the line are labeled as giants. The bottom plot shows the giants alone plotted versus apparent I magnitude. We see that most of the stars are bright, just as we would expect of distant giants: they have $M_V \sim 1$ and fall off in abundance well out of the disk at the distances required to make them apparently faint.

Figure 5-4 shows a similar plot for the present data, and a fiducial line drawn to separate giants and dwarfs. The bottom plot again shows the apparent I magnitude for the "giants", but here the separation does not appear to be nearly as good. Even after moving the cutoff line to (1) flat at 0.4; (2) flat at 0.5; or changing the slope, there are still a significant number of faint stars present in the sample. We attribute this partly to the higher noise level in the faint spectra of our sample, scattering some stars to lower than expected line strength (formal errors for γ reach 0.08 for the fainter stars). The line strength parameter we derived should be correlated with metallicity, however, and can be used to select against contamination from spheroid subdwarfs. While the separation of Figure 5-3 appears significantly better, the number of stars is too small to generate an accurate fraction of giants in the sample.

5.3 Calculation of K_z

The lack of a trend with apparent magnitude in the fraction of stars having low line strength reduces our confidence in the ability to separate giants from dwarfs. If we were truly detecting giants in the full sample, we would expect to find few (if any) stars at faint magnitudes, since the resulting distance modulus would place these giants (with absolute magnitude ~ 1, Egret, Keenan, & Heck 1982; Flynn & Mermilliod 1991) at extreme distances even for spheroid population stars. Figure 5-4 shows that the fraction of stars is more or less equally distributed among the sample, and thus is not performing the separation we want.

Though part of the failure can be attributed to the statistical error of the individual line strengths, a low surface gravity is not the only way to produce weak lines

at a fixed (V–I) color. Stars having low [Fe/H] will also have weak lines. Kuijken & Gilmore (1989) argue that low metallicity (such as that found in spheroid subdwarfs) does not necessarily produce weaker lines in a star at fixed (B–V) color, due to the effectively lower temperature of a metal-poor star at this color from reduced blanketing in B. This effect is likely to be significantly reduced when stars are selected based on (V–I) color (as here) since (V–I) is much less sensitive to metal-line blanketing effects.

The ability to exclude stars from the spheroid population is of great importance for studies measuring K_z. Halo stars carry little information on the mass density in the disk, as they are a kinematically hot population: given a fixed K_z due to mass in the disk, the logarithmic change in density of the population is inversely proportional to the square of the velocity dispersion. Thus in a hot population the change in density due to K_z will be quite small and difficult to measure with the requisite accuracy. Stars from the spheroid can also contaminate a velocity dispersion measurement for disk population stars, as only a few high-velocity stars enhancing the tails will produce an anomalously large σ_z^2 without affecting the density, leading to estimates of the force law that are too high.

The difference in kinematic properties of strong vs. weak lined stars was demonstrated by Roman (1950), and over the next decade the association between weak-lined stars, high velocity stars, and the spheroid Population II was realized (see the review of Blaauw 1963). The substantial metal deficiency of the spheroid stars makes line strength a good indicator of spheroid membership. Another population, the so-called "thick disk", has been recently identified (Gilmore & Reid 1983), and is thought to be differentiated from the standard old disk both chemically and kinematically (Gilmore, Kuijken, & Wyse 1989). Since the thick disk is also significantly hotter than the old disk, the ability to select against this population based on chemical abundance would also aid measurement of the local mass density. Given the prospect that the line strength γ can be used to select against both giants and kinematically hot (spheroid, thick disk) stars, neither of which we desire in our sample, we chose to make a cut from our velocity sample based on this parameter and proceed with a ten-

tative analysis. Note that the cut is not made with direct reference to kinematics, and serves merely to isolate a population that is more closely homogeneous and follows its own equilibrium distribution. The reader is cautioned that the analysis presented below is only meant as a first look at the data and is by no means comprehensive. We proceed in the hope that in the process we can suggest ways to improve the analysis through additional data.

5.3.1   Velocity Distribution

The stars with radial velocities were divided into two groups based on the measured γ parameter for each star. For the 1986 data, stars with $\gamma < 0.6$ were placed in a weak-line group, the others into the strong-lined group. For the 1987 data the division was made at $\gamma = 0.50$, chosen to correspond to approximately the same strength as 1986 data based on stars measured in common. The placement of the division was chosen to eliminate approximately 1/3 of the stars. Making a strong cut may eliminate some fraction of stars that would be useful in the analysis, but we do so to help ensure a more uniform sample in the strong-lined group.

The velocity distribution of the two groups is shown in Figure 5-5. A mean velocity of 7.3 km s^{-1} has been removed from the sample, which corresponds to the Sun's peculiar motion with respect to the LSR and agrees well with other estimates (Delhaye 1965). Note the striking difference in the velocity distributions of the two groups, made without directly using any kinematic selection criteria. The strong-lined group has 198 stars and a velocity dispersion of 22.2 km s^{-1}. We test the hypothesis that this distribution is Gaussian using a Kolmogoroff-Smirnoff test, following Bahcall (1984b); the cumulative distribution of both the data and a normal curve are shown in Figure 5-6 (the abscissa is scaled to units of the 22.2 km s^{-1} measured dispersion). The maximum deviation from the normal distribution is 0.051, and a simple calculation (Press et al. 1986) shows that the probability of exceeding this deviation is 0.68 (a slight overestimate, since μ and σ were calculated from the data, but the correction is small).

Another test that can be applied to the strong-lined velocities is to check for a
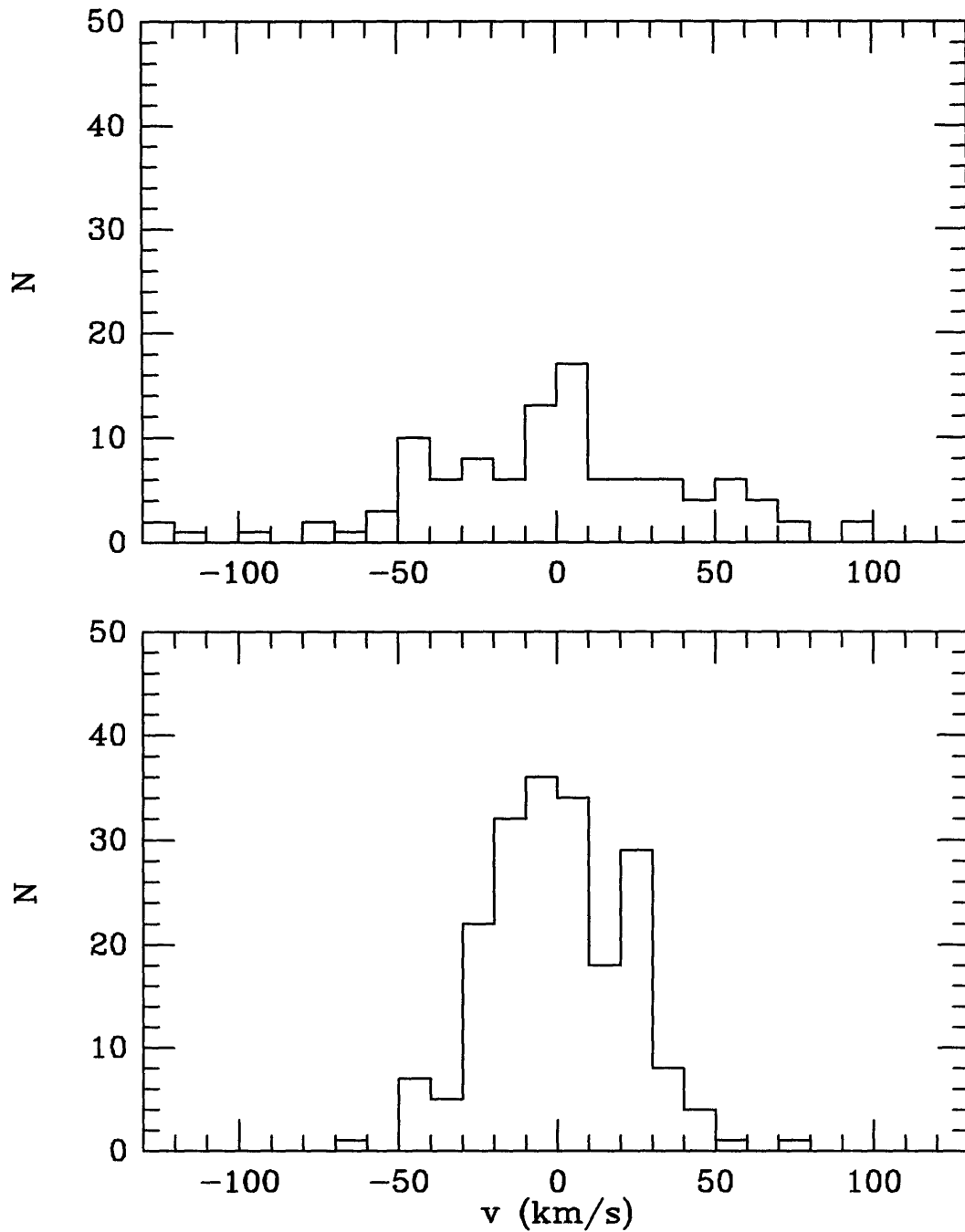
Figure 5-5: The distribution of radial velocities for the two groups of stars divided based on line strength. The upper panel shows the weak-lined group, having a velocity dispersion $\sigma = 45$ km s^{-1}. The bottom panel shows the strong-lined group, with $\sigma = 22.2$ km s^{-1}.
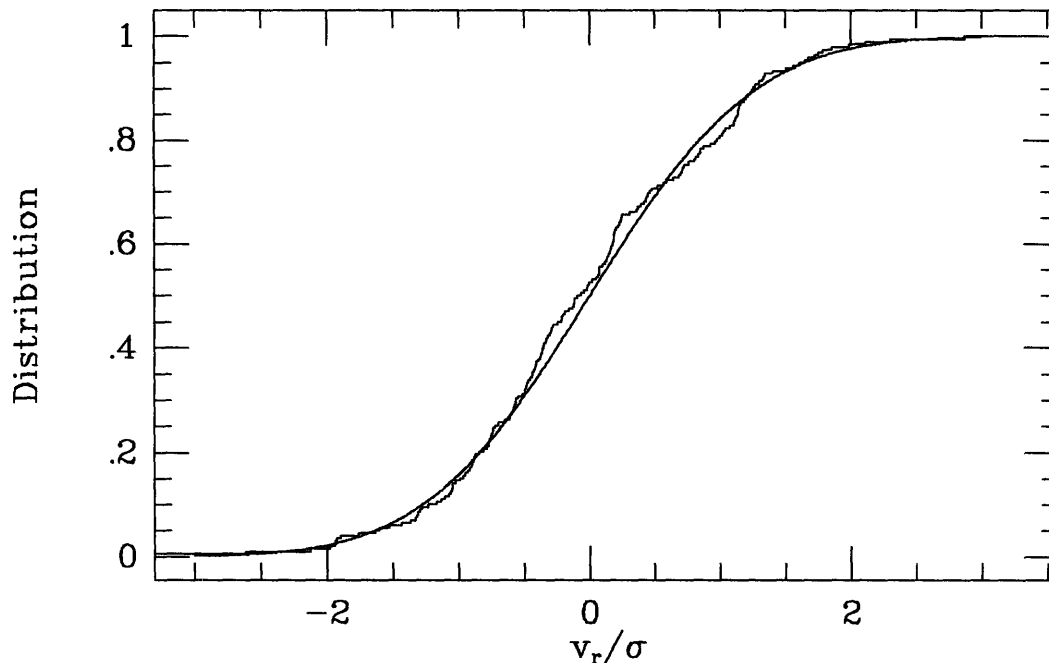
Figure 5-6: The cumulative velocity distribution of the strong-lined sample of stars. The jagged line shows the data, and the smooth line a normal distribution with $\sigma = 22.5$ km s^{-1}.

trend in dispersion with height above the plane. Any residual contamination from hot populations should become evident at greater height above the disk, since the relative density of hot stars will be greater. Figure 5-7 shows the distribution of velocities as a function of apparent magnitude for the strong- and weak-lined samples. Breaking the strong-lined sample into two bins of roughly equal numbers (corresponding to ~ 500 pc), we find $\sigma_{<500} = 22.0$ and $\sigma_{>500} = 22.5$ km s^{-1}, identical to within the error. We therefore conclude that the distribution is consistent with a Gaussian distribution and thus represents an isothermal population. Our result reinforces that of Bahcall (1984b), who found that a metallicity-based selection for K giants could produce an isothermal tracer sample.

It is also apparent from Figure 5-7 that the line strength criterion selects a hot population of stars at all apparent magnitudes. The bright stars can be understood as a thick disk/spheroid population of giants, which we were hoping to separate out from the sample above. The fraction of stars classified as weak-lined actually increases for fainter stars, however, and are also kinematically hot. We interpret these stars to
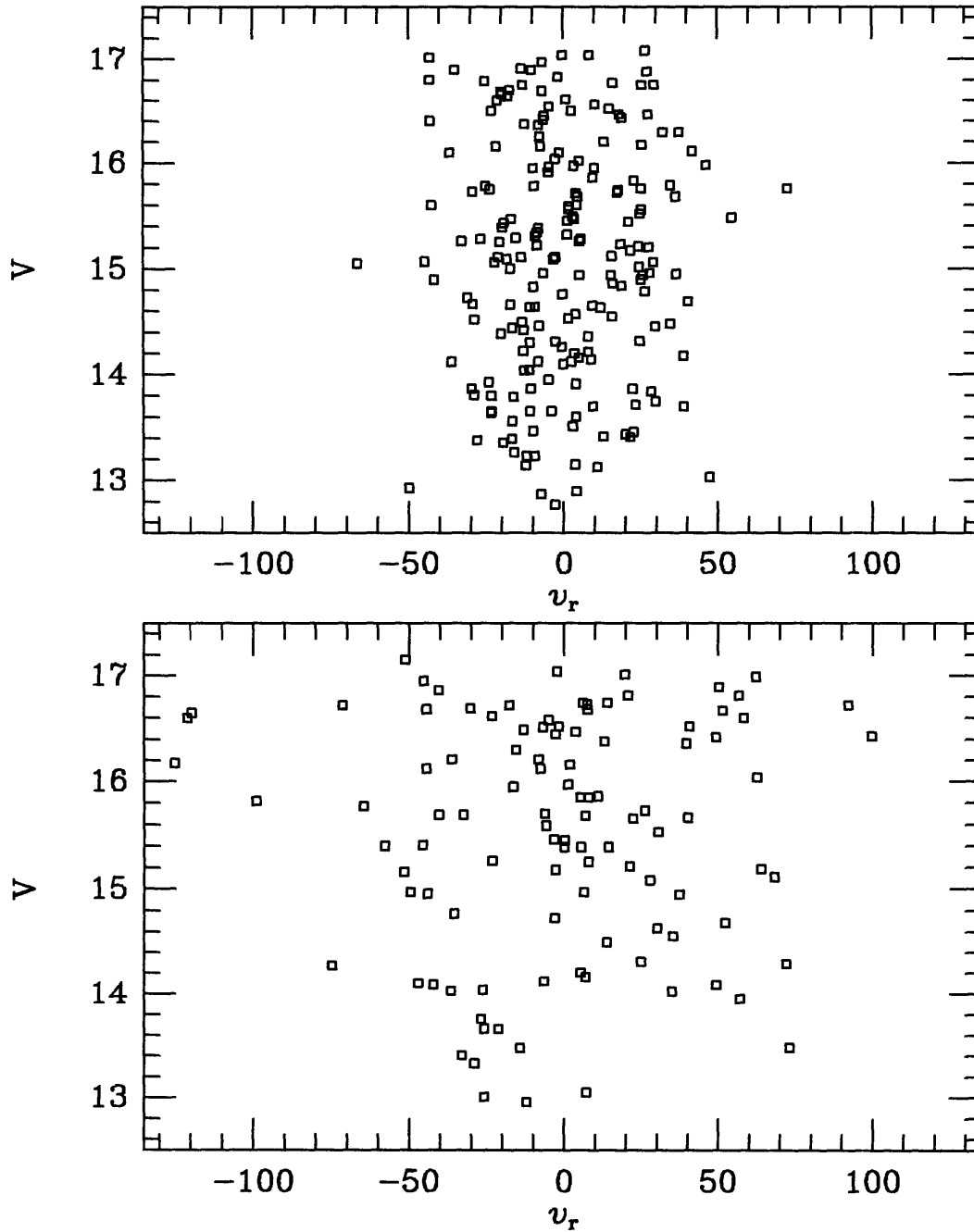
Figure 5-7: Velocities for strong-lined (top panel) and weak-lined (bottom panel) stars, plotted vs. apparent V magnitude.

be dwarfs from the thick disk/spheroid, which begin to provide a significant relative contribution above $\sim 800pc$. Thus our apparent failure to detect giants in §5.2.4 may not be complete: the line strength parameter we generate is probably more closely correlated with metallicity than surface gravity. This is sufficient to find most of the thick disk/spheroid giants contaminating our sample, as they should have low metallicity and hence weak lines (most of the disk giants are avoided by our bright-end magnitude cut, and therefore do not significantly contaminate our sample). However, toward fainter magnitudes we start picking up many more metal-poor dwarfs, which destroys the trend we expected to see in Figure 5-4.

The strong-lined sample is therefore well-suited for use in a study of the matter in the disk in two respects. First, the sample has been selected to represent a cool, isothermal population using a non-kinematic criterion, similar to the procedure used by Bahcall, Flynn, & Gould (1992) for their K giant sample. Second, most of the giants have been eliminated from the sample, via either the bright end magnitude limit (disk giants) or the line strength cut (thick disk/spheroid giants). Since we have removed a subset of the stars to produce a uniform sample, however, we would also need to make some selection to statistically remove the same population from the larger sample in order to measure the density law. As an approximation, we might take the fraction of stars in each half-magnitude bin that were classified as weak-lined and removed the same fraction of stars in each photometric bin of the full CS sample. This would be sufficient as long as there is no bias as a function of distance; unfortunately the errors on the line strength tend to be larger on the fainter stars, and the the faint stars will preferentially scatter into the weak group. This produces an artificial enhancement of the relative number of stars in the faintest bins, due to the larger number of stars in the strong-lined subset.

5.3.2 Density Law

To calculate the density $\nu(z)$ we use the full catalog described by Schechter & Caldwell (1989), using a preliminary photometric calibration provided in advance of publication by J. Caldwell. We select only stars detected in both V and I, and limit the color

range of stars from the sample to $0.97 < (V - I) < 1.13$ as for the velocity sample. The resulting catalog has a total of 1,798 stars. To derive distances, we use the relation between color and absolute V magnitude found by Reid & Gilmore (1982). The narrow range of color allows an accurate approximation of their spline fit using a linear relation, which we take to be

$$M_V = 6.50 + 3.34[(V - I) - 1.05].$$

We use the star counts in magnitude bins to determine an average distance to the stars in each bin. The mean magnitudes for each bin are corrected for Malmquist bias using the relation

$$M_{\mathrm{mag}} = M_{\mathrm{vol}} - \sigma_V^2 \frac{d \ln A}{dm},$$

where the logarithmic count derivative is computed from a smoothed distribution that is linear to good approximation. We take σ_V to be 0.4 mag based on the scatter about the absolute magnitude relation of Reid & Gilmore. The resulting distribution of stars as a function of distance modulus is shown in Figure 5-8. We do not include an explicit correction for a metallicity gradient, as we expect to select a sample of higher metallicity when using line strength as a criterion. Thus the metallicity of our resulting sample should not significantly exceed that in the solar neighborhood, for which the above calibration is accurate. We have also not included an explicit correction for extinction, though we discuss possible effects of such a term below.

The density of the CS catalog stars in the color range $0.97 < (V - I) < 1.13$ is shown in Figure 5-9 as a function of height out of the plane. The tracer sample density appears to follow a linear relation between 300–1000 pc, implying a constant exponential scale height in this range. Since the fraction of stars eliminated in the line strength selection above was essentially constant across the magnitude bins, the density distribution shown should be fairly close to that of the tracer population (at least over the range of distance to which the velocity tracers extend, ~ 1200 pc). We avoid the stars within about 1 scaleheight from the plane, since they may retain some contamination from disk giants; above 300 pc most of the disk mass (at least
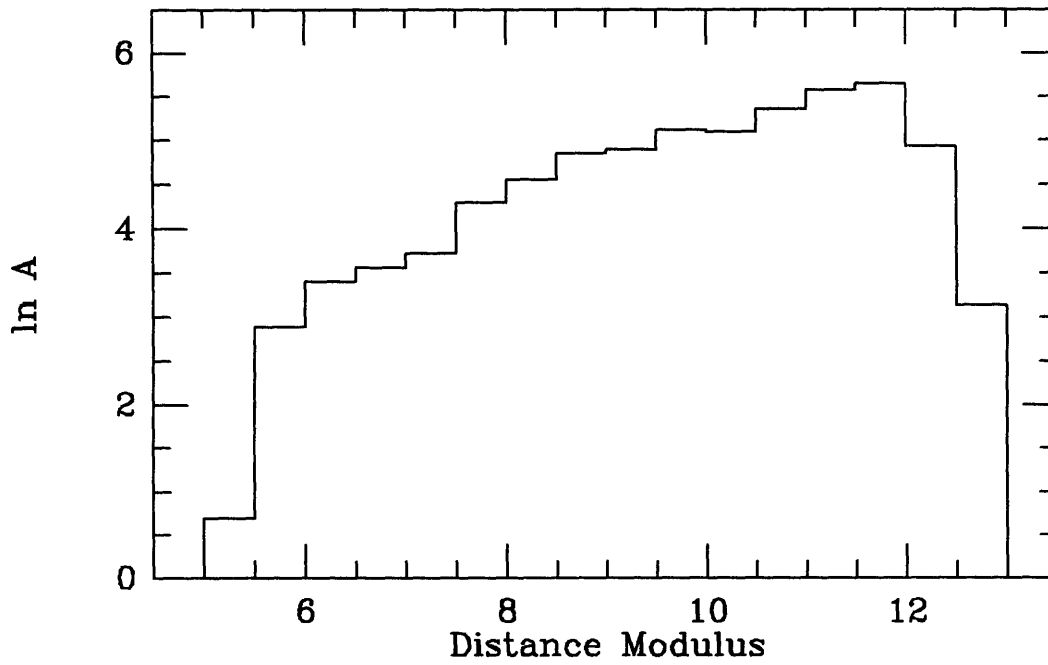
Figure 5-8: The distribution of stars from the Schechter & Caldwell sample in the color range $0.97 < (V-I) < 1.13$ as a function of distance modulus $(= 5\log_{10} d_{pc} - 5)$, corrected for Malmquist bias.
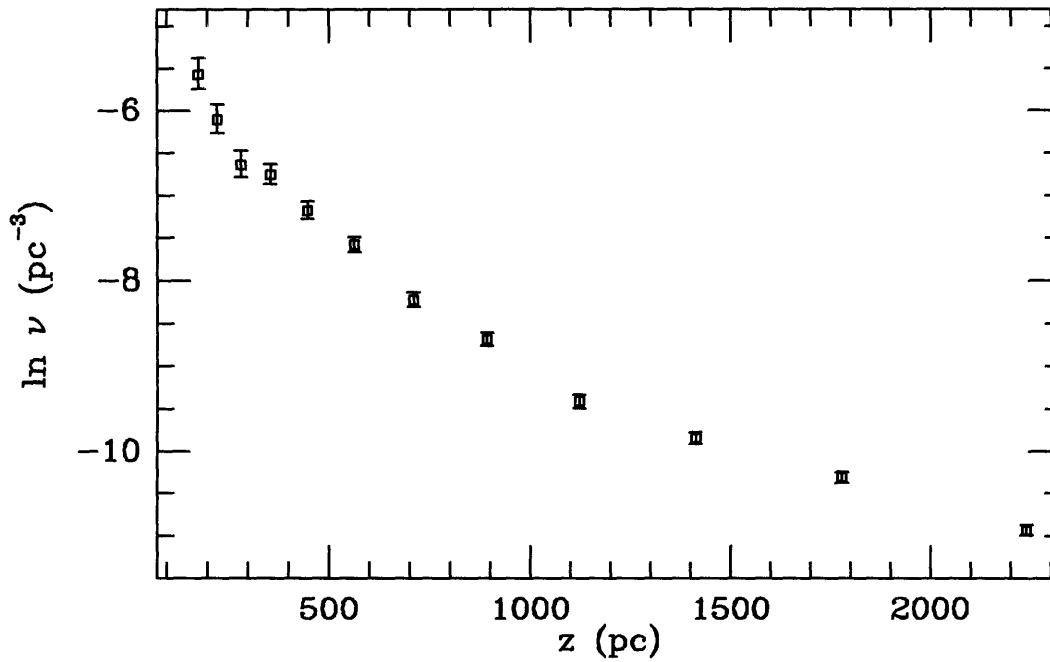

Figure 5-9: Density derived for the stars with $0.97 < (V-I) < 1.13$ in the CS sample.

from visible components) is also below us, and so will be represented in the force law. A linear fit to the density law from 300–1000 pc gives a scale height of 288 ± 10 pc, with $\chi^2_\nu = 1.07$. After accounting for the number of additional stars scattered into the weak-lined bin of the kinematic sample, there is some evidence of an excess of weak-lined stars in the faintest magnitude bins. If we exclude the point at 1100 pc, which would have the most contamination, the deduced scaleheight reduces to 282 ± 14 pc and $\chi^2_\nu = 0.95$. Since both (1) the velocity distribution appears Gaussian and independent of height, and (2) the density of the tracer closely approximates an exponential distribution, the relation for K_z reduces to the simple form

$$K_z(z) = \sigma^2 \frac{\partial \ln \nu}{\partial z} = -\frac{\sigma^2}{z_0},$$

where z_0 is the scale height, independent of z over the range of interest. Under these simple assumptions, we find $K_z = -1.73$ km^2 sec^{-2} pc^{-1}. If we approximate the potential of the disk as a thin sheet, roughly correct well above a scale height, we can determine a surface density $\Sigma = K_z/2\pi G = 64 \pm 5$ M$_\odot$ pc^{-2}. We expect the extinction toward the SGP is < 0.1 mag; under the pessimistic assumption of 0.1 mag of extinction concentrated locally, all distances (including the scale height z_0) decrease by 5%. This has the effect of increasing our derived surface mass density by the same fraction, ~ 3 M$_\odot$ pc^{-2}.

We point out again that due to the simplifying assumptions we have made, these figures are only rough estimates and are meant as a first look at the data. A more detailed analysis, including a careful examination of systematic errors, is left to the future pending additional data on the tracer sample (see below).

5.4   Discussion and Conclusions

Using newly measured radial velocities and line strengths of a sample of K stars, we have isolated an tracer sample based on line strength that is isothermal with $\sigma_v = 22.2$ km s^{-1}, independent of height above the disk. When combined with a larger sample of stars with accurate photometry, we find that the tracer sample follows an exponential

210

falloff above 300 pc with scale height $z_0 = 282$ pc. Using these numbers, we derive a best fit local disk mass density $\Sigma = 64 \pm 5$ $M_\odot$ pc^{-2}.

An important implication of this data is that the disk surface mass density as measured from K_z is roughly constant down to 400 pc, and is fairly well constrained by the data. This significantly reduces systematic effects on surface mass density measurements from contributions to the potential due to the spheroid (Kuijken & Gilmore 1991). Since the local mass surface density of the observed matter is found to be 48 ± 9 $M_\odot$ pc^{-2} (KG), this implies there is some component of matter with relatively low scale height in the disk unaccounted for, but the statistical significance of this result from our data is uncertain as this point.

To fully realize the potential of the CS catalog stars for tracing the disk mass density, we suggest some additional observations to help quantify the systematic errors. The first is to acquire additional data, possibly a MgH index or high-quality spectra, for some portion of the sample to ensure that we are properly excluding giants from the sample. The second would be to obtain spectra of sufficient quality for measurement of velocities and line strengths for a sample of 300-500 stars representative of the total population, in addition to the data with equal numbers in bins of half magnitudes. This should allow for a more accurate calibration of the relative contamination in the faint magnitude bins of thick disk/spheroid dwarfs, to provide an accurate measure of the density profile of the tracer sample itself. If enough spectra are obtained (perhaps using one of the multifiber instruments, such as the CTIO Argus), it will be possible calculate a density law using the same sample of stars used to measure the dispersion, thereby avoiding the additional uncertainty associated with adjusting counts in magnitude bins.

5.5 References

Bahcall, J. N. 1984a, ApJ, **276**, 169

Bahcall, J. N. 1984b, ApJ, **287**, 926

Bahcall, J. N., Flynn, C., & Gould, A. 1992, ApJ, **389**, 234

Bahcall, J. N., & Soneira, R. M. 1984, ApJS, **55**, 67

Binney, J., & Tremaine, S. 1987, Galactic Dynamics (Princeton, NJ: Princeton U.)

Blaauw, A. 1965, in Galactic Structure, eds. A. Blaauw & M. Schmidt (Chicago: U. Chicago), p. 435.

Caldwell, J. A. R. 1994, in preparation.

Delhaye, J. 1965, in Galactic Structure, eds. A. Blaauw & M. Schmidt (Chicago: U. Chicago), p. 61

Egret, D., Keenan, P. C., & Heck, A. 1982, A&A, **106**, 115

Filippenko, A. V. 1982, PASP, **94**, 715

Flynn, C., & Mermilliod, J.-C. 1991, A&A, **250**, 400

Gilmore, G., Kuijken, K., & Wyse, R. F. G. 1989, ARA&A, **27**, 555

Gilmore, G., & Reid, N. 1983, MNRAS, **202**, 1025

Griffin, R. F. 1971, MNRAS, **155**, 1

Hill, E. R. 1960, Bull. Astr. Inst. Netherlands, **15**, 1

Hill, G., Hilditch, R. W., & Barnes, J. V. 1979, MNRAS, **186**, 813

Kuijken, K., & Gilmore, G. 1989, MNRAS, **239**, 605 (KG)

Kuijken, K., & Gilmore, G. 1991, ApJ, **367**, L9

Oort, J. H. 1932, Bull. Astr. Inst. Netherlands, **6**, 249

Oort, J. H. 1960, Bull. Astr. Inst. Netherlands, **15**, 45

Press, W. H., Flannery, B. P., Teukolsky, S. A., & Vetterling, W. T. 1986, Numerical Recipes (Cambridge: Cambridge U.)

Reid, N., & Gilmore, G. 1982, MNRAS, **201**, 73

Roman, N. 1950, ApJ, **112**, 554

Schechter, P. L., & Caldwell, J. A. R. 1989, in The Gravitational Force Perpendicular to the Galactic Plane, eds. A. G. D. Phillip & P. K. Lu (Schenectady, NY: L.

Davis), p. 143.

Shectman, S. A., Price, C., & Thompson, I.B. 1985, in Annual Report of the Director,
Mount Wilson and Las Campanas Observatories, ed. G. W. Preston (Pasadena:
MWLCO), p. 52.

Upgren, A. R. 1962, AJ, **67**, 37